

**Cold, Ion-Neutral, Chemical Reactions in Coulomb
Crystals With Thermal Neutral Sources and Progress
Towards Stark-Decelerated Sources**

by

O. A. Krohn

B.S., California State University, Fresno, 2017

M.S., University of Colorado, Boulder, 2020

A thesis submitted to the
Faculty of the Graduate School of the
University of Colorado in partial fulfillment
of the requirements for the degree of
Doctor of Philosophy
Department of Physics
2023

Committee Members:

Heather Lewandowski, Chair

Eric Cornell

Chuck Rogers

Jun Ye

Ralph Jimenez

Krohn, O. A. (Ph.D., Physics)

Cold, Ion-Neutral, Chemical Reactions in Coulomb Crystals With Thermal Neutral Sources and
Progress Towards Stark-Decelerated Sources

Thesis directed by Prof. Heather Lewandowski

Laser-cooled ions in radio frequency traps provide a unique environment in which to study ion-neutral gas-phase reactions. Such systems form Coulomb crystals, which offer a translationally cold and inherently flexible system for studying reaction kinetics and dynamics. In combination with a time-of-flight mass spectrometer, our linear ion trap has been optimized to monitor gas-phase chemical reactions one molecule at a time with high resolution detection of products. In addition, the low pressures and cold conditions offered by this environment mimic important aspects of the astrochemical environment; this expands the relevance of our studies to chemical dynamics throughout multiple regions of space, including the interstellar medium and planetary atmospheres.

In my dissertation, I present experimental data on three important reactions of interstellar interest studied in our linear ion trap: $\text{CCl}^+ + \text{CH}_3\text{CN}$, $\text{CCl}^+ + \text{C}_6\text{H}_6$, and $\text{C}_2\text{H}_2^+ + \text{CH}_3\text{CN}$. Each of these reactions has demonstrated fast kinetics with branching to multiple products of interest to astrochemical modelers. In two of these reactions ($\text{CCl}^+ + \text{CH}_3\text{CN}$ and $\text{C}_2\text{H}_2^+ + \text{CH}_3\text{CN}$) we were able to demonstrate the reaction dynamics with a full potential energy surface; this also indicated interesting underlying mechanics that influence the outcome of these reactions.

My work also involved development of future directions of this experiment, including a new neutral molecular beam source. This will provide collisional energy and quantum state control over the neutral reactant with a traveling wave Stark decelerator (TWSD). In my dissertation, I describe the characterization and integration of a TWSD with our linear ion trap. I demonstrate detection of a decelerated molecular beam of ND_3 in krypton at the location of the ion trap with tunable final velocities down to 20 m/s. This advance allows future reactions in our linear ion trap to be energy-resolved such that ion-neutral kinetic theories may be empirically compared over the

energy ranges of $\sim 1\text{K} - 50\text{ K}$. This combined setup broadens the astrochemical relevance of our measurements to a critical range of temperatures, as well as providing an excellent opportunity to understand the underlying impacts of collisional energy on reaction dynamics.

Dedication

To my parents, who told me that I could do it

To my husband, who loved that I was doing it

To my coworkers and classmates, who did it with me

And to my friends and family,

who never let me believe that I wouldn't finish it

Acknowledgements

I am grateful to have worked for Heather. I have greatly benefited from her mentorship through many projects, challenges, and life events. My former labmates James, Katherine, and John taught me much about research in AMO physics and physical chemistry; in particular, James and Katherine were mentors to me at a critical time in my professional career and I am very grateful to them. I worked with an excellent group of people that are carrying on the Lewandowski experiments: Chase, Trevor, Stephen, Malayne, Tommy, and Will. Best of luck to you; I am excited to see the incredible physics that you will do. JILA is full of wonderful people that I don't have space to name. Of them, Terry, Hans, and Kyle in the electronics and machine shops have been particularly helpful and instructive to this work. On the admin side, Krista, Agnieszka, and Jeanne have been helpful and patient with my questions. I am also incredibly grateful to Josef Michl and Chuck Rogers for their leadership during the time I was on their projects, and for their goodwill and support when I realized I needed to switch fields and research groups.

I have met wonderful friends from within my program cohort: Daniel, Gayle, Diego, Garrison, Charlie, Brian, Jenny, and Chris, to name only a few. Beyond my cohort, I had amazing roommates: Lindsay, Leng Ying, Rachel and Heidi. They were rocks in early-grad school chaos and pandemic craziness. I am really grateful to my local church and running community, who have supported me in numerous ways. I have wonderful long-time long-distance friends: Charis, Ashley, Sami, Leng Ying, and Esther. They have made the distance between us feel smaller. Thank you to my family, who have been rooting for me all the way: Mom, Dad, Austin, Aubrey, Emmaline and Emily. And of course – my husband Daniel. I love you all so much. Thank you.

Contents

Chapter

1	Introduction	1
1.1	Coulomb crystals for chemistry	3
1.2	The road to energy-resolved ion-neutral reactions	5
1.3	Outline of dissertation	6
2	Experimental tools for observing reactions between trapped ions and thermal neutral gases	8
2.1	Principles of Ion Trapping	9
2.1.1	Ion traps	9
2.1.2	The linear paul ion trap	11
2.1.3	Ion energetics	17
2.1.4	Laser cooling	18
2.1.5	Simulations of Ion Dynamics	22
2.2	Experimental Apparatus	25
2.2.1	Loading the trap	26
2.2.2	Cleaning the trap	31
2.2.3	Exposure to reactant gas	34
2.2.4	Mass spectrometry	36
2.2.5	Full ensemble	38

3	Theoretical tools for calculating ion-neutral gas-phase kinetics and dynamics	40
3.1	An Introduction to Kinetic Rate Theory	41
3.1.1	Introduction to reaction rate theories	41
3.1.2	Capture models for calculating reaction rates	43
3.1.3	Energy in the collision's center-of-mass frame	51
3.2	Potential Energy Surfaces	55
3.2.1	An Introduction to Potential Energy Surfaces	56
3.2.2	Finding a PES: a practical discussion	61
3.2.3	Calculating a PES: self-consistent field methods	63
3.2.4	A glimpse into transition state theory and its relevance to branching ratios	71
4	Isotope-specific reactions of acetonitrile with trapped, translationally cold CCl^+	76
4.1	Introduction	77
4.2	Methods	79
4.2.1	Experimental Methods	79
4.2.2	Computational Methods	82
4.3	Results & Discussion	83
4.3.1	Reaction thermodynamics	83
4.3.2	Reaction measurements	85
4.3.3	Modeling the $\text{CCl}^+ + \text{CH}_3\text{CN}$ reaction	92
4.4	Conclusion and outlook	97
5	Formation of astrochemically relevant molecular ions: reaction of translationally cold CCl^+ with benzene in a linear ion trap	99
5.1	Introduction	100
5.2	Methods	102
5.2.1	Experimental Methods	102
5.2.2	Theoretical Methods	103

5.3 Results & Discussion	104
5.4 Conclusion	113
6 Reactions of Acetonitrile with Trapped, Translationally Cold Acetylene Cations	114
6.1 Introduction	115
6.2 Methods	117
6.2.1 Experimental Methods	117
6.2.2 Computational Methods	119
6.3 Results & Discussion	119
6.3.1 Reaction measurements	119
6.3.2 Reaction thermodynamics	125
6.3.3 Reaction potential energy surface	127
6.4 Conclusion and outlook	131
7 Velocity-tunable beam of neutral molecules produced by Stark deceleration	132
7.1 Stark Deceleration	133
7.1.1 Supersonic molecular beams	133
7.1.2 Stark deceleration of ammonia	135
7.1.3 Phase-space acceptance	144
7.1.4 Detection of neutral ammonia out of the Stark decelerator	149
7.2 Characterization of TWSD output (before integration with LIT-TOFMS)	152
7.2.1 Continuous deceleration of ND ₃ from 385 m/s to 10 m/s	153
7.2.2 Alternative slowing scheme	156
7.2.3 Beam densities and prospects for reactions	160
7.2.4 Summary	161
7.3 Development of the TWSD amplifiers	162
7.3.1 A brief overview of the in-house amplifier design	162
7.3.2 Overview of electrical changes to the amplifiers	167

7.3.3	Overview of structural and cooling changes to the decelerator	171
7.4	Summary	178
8	An integrated TWSD-LIT for energy-tunable ion-neutral reactions	180
8.1	The Combined Apparatus	181
8.1.1	Physical parameters and images of the combined system	182
8.1.2	Shuttering the decelerated beam	186
8.1.3	Configuring an ion trap as a “static TOF”	189
8.2	The hexapole	194
8.2.1	Force on ND ₃ in a hexapole	196
8.2.2	Hexapole Transmission Simulations	198
8.3	To-date output at the decelerator and outlook	205
8.3.1	Calculating center-of mass energies for RT gas or decelerated beams	205
8.3.2	First reaction proposal: NH ₃ ⁺ + ND ₃	210
9	Summary & Outlook	219
9.1	Summary	219
9.2	Outlook	221
	Bibliography	222
 Appendix		
A	TWSD Amplifier Schematics	248
B	Mathematica code for calculating collision energies of NH₃⁺ + ND₃ reaction	256

Tables

Table

2.1	Typical trapping parameters and trap geometry variables. Reproduced from Greenberg (2020). [1]	16
4.1	Rate constants for isotopological variations of $\text{CCl}^+ + \text{CH}_3\text{CN}$ primary products. ‘X’ represents a hydrogen or deuterium from acetonitrile, and corresponds to the isotope used. Rates are in units of $\times 10^{-9} \text{ cm}^3/\text{s}$, and reported statistical uncertainty is the calculated 90% confidence interval.	90
4.2	Branching ratios for primary products by isotopological variations of $\text{CCl}^+ + \text{CH}_3\text{CN}$ reaction. The calculated branching ratio represents the fraction of protonated acetylene rate constant, divided by the total CCl^+ decay rate constant. ‘X’ represents a hydrogen or deuterium, and corresponds to neutral reactant.	91
4.3	Rate constants for isotope variations of $\text{CCl}^+ + \text{CH}_3\text{CN}$ secondary products. ‘X’ represents a hydrogen or deuterium from CH_3CN , and corresponds to the isotope used. Rates are in units of $\times 10^{-9} \text{ cm}^3/\text{s}$, and reported statistical uncertainty is the calculated 90% confidence interval.	93
5.1	Rate constants for isotopological variations of $\text{CCl}^+ + \text{C}_6\text{H}_6$ primary products. Rate constants are in units of $\times 10^{-9} \text{ cm}^3/\text{s}$, and reported statistical uncertainty is the calculated 90% confidence interval.	106

5.2	Branching ratios for the primary products of CCl^+ and C^{37}Cl^+ reacting with C_6H_6 .	
	The numbers are given as percentages and uncertainties are derived from the 90% confidence interval from the pseudo-first-order model fits.	108
6.1	Branching ratios for the primary products of acetylene cations reacting with acetone.	
	The numbers are given in percentages and uncertainties are derived from the 90% confidence interval from the pseudo-first-order model fits.	122
7.1	Geometrical TWSD measurements, as well as typical deceleration parameters and trap geometry variables.	144
7.2	Maximum longitudinal spread in velocities of ND_3 wells at end of decelerator, as calculated by the LPSA model. The full-width half max velocity spread, which is more relevant to collision studies, will be less than this and depends on how the phase-space distribution overlaps with the phase-space acceptance of the decelerator. The velocity spread for $v_f = 385 \text{ m/s}$ is from bunching. Velocity spreads are also converted into kinetic energy uncertainties to facilitate discussion of the energy resolution obtained for collision studies.	154
7.3	Summary of changes to amplifier electronics since Shyur (2018). [2]	168
7.4	Expected and actual performance in 2N6660 FETs. FETs with problematic performance were always characterized by a higher drain-source capacitance and lower threshold V_{GS}	171
8.1	Specified and effective behavior of the 6 mm Uniblitz shutter.	188
8.2	Direct, indirect, and CAD measurements of lengths relevant to TWSD-Hexapole-LIT beampath. Indirect measurements are based on photographs that include features with well-known measurements. All measurements in millimeters.	202

8.3	Velocity distribution standard deviations for ion and hexapole simulation results.	
	The hexapole output fits are shown in Figure 8.15 and the ion fits are shown in	
	Figure 8.16. The uncertainty represents the 95% confidence interval in the Gaussian	
	fit. The x axis corresponds to the decelerator beam propagation, and the z axis	
	corresponds to the trap axial direction.	209
8.4	Maximum longitudinal spread in velocities of ND ₃ wells at end of decelerator, as	
	calculated by the LPSA model. The Gaussian spread, which will be used for final	
	energy calculations, will be less than this and depends on how the phase-space	
	distribution overlaps with the phase-space acceptance of the decelerator.	209
8.5	Final calculated E/k_b “temperatures” for a selection of final decelerated velocities.	
	The uncertainty in the center temperature is included, while the temperature reso-	
	lution is based on the spread of the velocities.	211
8.6	Rate constants at thermal temperatures in a variety of experimental setups. Uncer-	
	tainty is given when reported in source. All measurements and calculations refer to	
	NH ₃ ⁺ + NH ₃ reaction unless stated otherwise	212
A.1	Summary of changes to amplifier electronics since Yomay’s thesis. [2]	248

Figures

Figure

1.1	False-color fluorescence images of two Coulomb crystals, one of pure laser-cooled Calcium ions (left), and the other with co-trapped, sympathetically cooled acetylene ions (right). These images are taken by a CCD camera using microscope objective positioned above the RF trap.	4
2.1	Figure from Paul's original patent. 3 A driving RF voltage is put on the ring electrode (A) and hyperbolic endcaps (B). The ions oscillate between being pulled out axially (z axis) and pushed in radially, and vice versa.	11
2.2	Schematic of the RF fields generated by a linear Paul trap. a) and b) represent an effective radial energy potentials produced at two points separated by 180° of the driving RF frequency. The frequency of the switching between these two potentials is determined by the frequency of the RF. The magnitude of the potential is determined by the amplitude of the driving RF frequency.	12
2.3	Schematic representation of an linear ion trap geometry. An isometric view is given on the left, while the side view is given on the right. The eight outer segments are the endcaps, while the four center sections exert RF trapping fields on the ions. 1 .	13

2.4	Diagram showing the stability regions for the radial and axial directions (a, left). The lowest region of mutual stability is shaded in the left diagram as “A” and is represented at a larger scale in the right figure (b). (c) shows that within this region, only a more constrained region is stable due to the geometrical features of our specific ion trap. Figures (a) and (b) from March (1997), [4] (c) from Greenberg (2020). [1]	16
2.5	Simple schematic of laser cooling. a) A photon and atom propagate in opposite directions. If this photon is absorbed b) the atom is slowed. c) When the photon is remitted, a recoil will be experienced by the atom. [5]	20
2.6	The energy structure of the Calcium ion. Two lasers drive laser cooling, with a primary driver at 397 nm and a re-pump laser at 866 nm.	21
2.7	Plotted positions of a Coulomb crystal within one rf cycle, viewed on end. [6]	24
2.8	End-on view of ion positions in a Coulomb crystal before (left) and after (right) laser cooling is applied. This simulation included 800 Ca ⁺ ions (blue) and 800 <i>m/z</i> 35 ions (red). [6]	25
2.9	Distributions of secular (v_{RMS}) velocities of calcium (left) and dark ion (middle), with a plot of positions from an axial view (right). The top row is for the case with 800 Calcium ions (blue) and 800 <i>m/z</i> 45 dark ion (red). The second row also has equal numbers (800 each) of Calcium (blue) and <i>m/z</i> 35 dark ion (red). [6]	26
2.10	Schematic diagram of the LIT-TOFMS used for ion-neutral reactions. Schematic reproduced from Schmid (2020). [7]	27

2.11 Three common schemes for REMPI ionization of a molecule. Molecular excited states are indicated by Morse-like potentials; periodic lines symbolically indicate internal (ro-vibrational) states. In (2+1) REMPI (left), the first excitation requires two photons to bring the neutral molecule to an excited intermediate state. The ionization occurs with one photon of the same color, depicted here as exceeding the threshold for ionization indicated by the purple line. In (2 + 1'), the ionization photon is a different color. In (1+1) REMPI (right), the initial excitation does not proceed through a virtual state, but rather is directly excited by one photon to an excited state. In this schematic, one photon of the same color ionizes the molecule. Not that the inferred vibrational structure in this diagram will not be relevant for REMPI of atoms, which must solely proceed through resonant excitation of electronic states.	29
2.12 Ion trajectories under the influence of an a) oscillating linear electric field at the resonant secular frequency, and b) oscillating quadrupole electric field applied to the RF electrodes. Inset c) demonstrates the total energy of the ion on a logarithmic scale versus time, where the quadrupole field can be seen to be much more effective at ejecting an unwanted ion. [8]	32
2.13 Mass dependence of the relative energy gain E/E_{res} using parametric excitation (blue solid line) compared to displacement driving (green dashed). [8]	34
2.14 (Left) The <i>pulsed leak valve</i> configuration made of a variable leak valve backed by a three-way solenoid valve. (Right) Ion gauge data from the valve opening and closing which shows excellent stability in gas pressure over time. [1]	35
2.15 a) A graphic rendering of the holes in a microchannel plate, in which signal can be amplified, as shown in b). [9]	37

2.16	Sample TOFMS data from the $C_2H_2^+ + CH_3CN$ reaction. On the top are mass spectra from the loading of ions. Below are after 400s of exposure to CH_3CN . The left traces are zoomed out, while the right shows a “zoomed in” trace recorded on a second channel of our oscilloscope.	38
3.1	a) Schematic for an ion-molecule collision. b) capture cross section of ion-molecule collisions. c) Plot of the effective potential vs. distance from Equation 3.6. Figures from Su & Bowers (1979). [10]	44
3.2	Dipole locking constant vs. μ_D/α from Su & Bowers. [11]	48
3.3	(a) One possible set of dimensions to describe a triatomic molecular complex. This coordinate system is comprised of two bond lengths and an angle. (b) Schematic of three dimensions required to describe a triatomic molecular complex of O_3 isomerization. (c) A representation of the surface in 2-D that is typical to a reaction potential energy surface in higher dimensions. Image from Lewars (2010). [12]	57
3.4	(Top) Full PES for the reaction $CCl^+ + CH_3CN$ with relative energy on the y-axis. Highlighted is the first transition state (TS1). Reactants are denoted by REA, products by PRD, intermediate states by INT. (Bottom) Graphical demonstration of the motion of the reaction coordinate for TS1, found as the imaginary frequency of the computed saddle point.	59
4.1	a) TOF traces demonstrating before and b) after cleaning using secular excitations. After cleaning, only Ca^+ (m/z 40, m/z 42, and m/z 44) and CCl^+ (m/z 47) remain in quantities greater than ~ 5 ions. Also included on the left is a false-color CCD image of fluorescing Ca^+ ions, the resulting Coulomb crystal is deformed primarily in the center section by the heavier CCl^+ ions which sit on the outside of the Ca^+ in the radial direction. This is seen by the deformation of the fluorescing ions from an ellipsoidal shape to one with the appearance of “flattened” sides. The crystal appears truncated because it expands slightly beyond the CCD camera frame. . . .	81

4.2	Reaction model for $\text{CCl}^+ + \text{CH}_3\text{CN}$, noting the reaction order and identity of ions.	
	Each arrow represents a reaction with a neutral CH_3CN molecule. Red number	
	below the molecule denotes m/z ratio. The molecular ions are depicted above, with	
	black indicating carbon, blue for nitrogen, white for hydrogen, and green for chlorine.	84
4.3	Rate reaction data (points) and fits (curves) for pseudo-first order reaction of $\text{CCl}^+ +$	
	CH_3CN . CCl^+ (blue x) reacts with excess CH_3CN resulting in first order products	
	C_2H_3^+ (green circle) and HNCCl^+ (black asterisk). Each of these primary products	
	then reacts with excess CH_3CN to form CH_3CNH^+ (red box).	86
4.4	Figure 4.4: (left) : Rate reaction data (points) and fits (curves) for pseudo-first	
	order reaction of $\text{C}^{37}\text{Cl}^+ + \text{CH}_3\text{CN}$. C^{37}Cl^+ (blue x) reacts with excess CH_3CN ,	
	resulting in first order products C_2H_3^+ (green circle) and $\text{HNC}^{37}\text{Cl}^+$ (black box).	
	Each of these primary products then reacts with excess CH_3CN to form CH_3CNH^+	
	(red asterisk). (right) The same reaction curve fit, here also demonstrating the	
	contaminant population (magenta +).	88
4.5	Figure 4.5: (left) : Rate reaction data (points) and fits (curves) for pseudo-first order	
	reaction of $\text{CCl}^+ + \text{CD}_3\text{CN}$. CCl^+ (blue x) reacts with excess CD_3CN , resulting in	
	first order products C_2D_3^+ (green circle) and DNCCl^+ (black box). Each of these	
	primary products then reacts with excess CD_3CN to form CD_3CND^+ (red aster-	
	isk). (right) The same reaction curve fit, here also demonstrating the contaminant	
	population (magenta +), and protonated acetonitrile formation, CD_3CNH^+ (cyan	
	triangle).	89

4.6	Figure 4.6: (left) : Rate reaction data (points) and fits (curves) for pseudo-first order reaction of $C^{37}Cl^+ + CD_3CN$. $C^{37}Cl^+$ (blue x) reacts with excess CD_3CN , resulting in first order products $C_2D_3^+$ (green circle) and $DNC^{37}Cl^+$ (black box). Each of these primary products then reacts with excess CD_3CN to form CD_3CND^+ (red asterisk). (right) The same reaction curve fit, here also demonstrating the contaminant population (magenta +), and protonated acetonitrile formation, CD_3CNH^+ (cyan triangle).	89
4.7	Potential energy surface for $CCl^+ + CH_3CN$, depicting equilibrium geometries connecting the reactants (REA) to the products (PRD1, PRD2, PRD3, and PRD4). In REA, PRD1, PRD2, PRD3, and PRD4, the bare '+' denotes infinite distance between the ion-neutral pair, while the encircled '+' indicates the ion of the ion-neutral pair. Geometries were calculated at MP2/aug-cc-pVTZ level, with CCSD(T)/CBS//MP2/aug-cc-pVTZ energies. 'INT' refers to intermediate states, while 'TS' indicates transition states. Asterisk denotes a step with an extremely shallow well, the depth of which depends on the level of theory).	94
4.8	Theoretical (RRKM/ME) rate constants for the $CCl^+ + CH_3CN$ reaction as a function of temperature. Values are included for the overall reaction (total) and for the formation of product ions $HNCCl^+$ (PRD1) and $C_2H_3^+$ (PRD2 + PRD3). Included for comparison are the experimental measurements (at the effective temperature of 160 K) and the ADO theory capture rate constants.	96

5.1	Schematic diagram of the LIT-TOFMS used for measuring the reaction of $\text{CCl}^+ + \text{C}_6\text{H}_6$. CCl^+ ions are produced by non-resonant photoionization and sympathetically cooled by the co-trapped laser-cooled Ca^+ . Approximately 2×10^{-10} Torr neutral C_6H_6 (11% in Helium, 300 K) is leaked into the vacuum chamber via a pulsed leak valve scheme for a set duration (0, 10, 90, 170, 240, or 320 s). After each reaction step, the resulting ions are then ejected into the TOF-MS, giving highly resolved mass spectra for each time step. Reproduced with permission from Schmid et al., Phys. Chem. Chem. Phys. 22, 20303 (2020). Copyright 2020 The Royal Society of Chemistry.	105
5.2	Rate reaction data (points) and fits (curves) for pseudo-first-order reaction of $\text{CCl}^+ + \text{C}_6\text{H}_6$. CCl^+ (blue \times) reacts with excess C_6H_6 resulting in first-order products C_3H_3^+ (green \circ), C_5H_3^+ (black $+$), $\text{C}_3\text{H}_2\text{Cl}^+$ (red $*$), and C_7H_5^+ (magenta \square).	106
5.3	Rate reaction data (points) and fits (curves) for the pseudo-first-order reaction of $\text{C}^{37}\text{Cl}^+ + \text{C}_6\text{H}_6$. CCl^+ (blue x) reacts with excess C_6H_6 resulting in first order products C_3H_3^+ (green circle) and C_5H_3^+ (black $+$), $\text{C}_3\text{H}_2^{37}\text{Cl}^+$ (red asterisk) and C_7H_5^+ (magenta box).	107
5.4	(a, left) Energetic limits for reactants $\text{CCl}^+ + \text{C}_6\text{H}_6$ and four products: $\text{C}_7\text{H}_5^+ + \text{HCl}$, $\text{C}_5\text{H}_3^+ + \text{C}_2\text{H}_3\text{Cl}$, $\text{C}_3\text{H}_2\text{Cl}^+ + \text{C}_4\text{H}_4$, $\text{C}_3\text{H}_3^+ + \text{C}_4\text{H}_3\text{Cl}$. Product energies are noted and appropriately scaled to y-axis scale as calculated at [CCSD(T)/CBS//CCSD/aug-cc-pVDZ] level of theory. The geometries appropriate for labeled energy are shown. Other explored isomers for each product can be found in the original manuscript.	109
5.5	Calculated isomers of $\text{C}_3\text{H}_2\text{Cl}^+$ (numbers [1-5]) and C_4H_4 (letters [A-D]). Energies are given in eV at the CCSD(T)/CBS//CCSD/aug-cc-pVDZ level of theory and are relative to the lowest energy isomer for each species. Isomers [1] and [A] correspond to PRD4 in Fig. 5.4].	110

5.6	Calculated isomers of $C_5H_3^+$ (numbers [1-8]) and C_2H_3Cl (letters [A-C]). Energies are given in eV at the CCSD(T)/CBS//CCSD/aug-cc-pVDZ level of theory and are relative to the lowest energy isomer for each species. Isomers [1] and [A] correspond to PRD2 in Fig. 5.4. The ‘*’ next to Isomer [2] is used because one negative harmonic vibrational frequency was found at the CCSD/aug-cc-pVDZ level of theory. This isomer was verified to be a minimum structure at other levels of theory (including CCSD/aug-cc-pVTZ) and has been calculated in other computational studies. ^[13] ^[14] ^[15] Even with 0.04 eV uncertainty at the CCSD(T)/CBS//CCSD/aug-cc-pVTZ level of theory isomer 2 should not be energetically viable product for this reaction.	110
5.7	Calculated isomers of $C_3H_3^+$ (numbers [1-2]) and C_4H_3Cl (letters [A-I]). Energies are given in eV at the CCSD(T)/CBS//CCSD/aug-cc-pVDZ level of theory and are relative to the lowest energy isomer for each species. Isomers [1] and [A] correspond to PRD3 in Fig. 5.4.	111
5.8	Calculated isomers of $C_7H_5^+$ (numbers [1-7]) and HCl ([A]). Energies are given in eV at the CCSD(T)/CBS//CCSD/aug-cc-pVDZ level of theory and are relative to the lowest energy isomer for each species. Isomer [1] and HCl [A] correspond to PRD1 in Fig. 5.4.	112
6.1	Measured ion numbers of $C_2H_2^+$ (blue \circ), $C_3H_4^+$ (magenta $+$), $C_2NH_3^+$ (green \square), $c-C_3H_3^+$ (black \times), and $C_2NH_4^+$ (red $*$) as a function of time. Data are normalized by the initial ion number of $C_2H_2^+$ (~ 200). Each data point represents the mean and standard error from twelve experimental runs per time point. The averaged data are fit using a pseudo-first-order reaction rate model (solid lines).	120
6.2	Model for reaction of $C_2H_2^+ + CH_3CN$, m/z ratio (blue number) and determined chemical formula below the molecule. The reaction order of each molecule is located at the bottom of the figure. Each arrow represents a reaction with a neutral CH_3CN molecule.	121

6.3	Potential energy surface (PES) for acetylene cation addition to acetonitrile to form $\text{CH}_2\text{CCH}^+/\text{H}_3\text{C}_3\text{H}^+ + \text{HCN}$. Geometries were computed at the M06-2X/6-31G(2df,p) level, with energies calculated at the G3X-K level of theory. The energy values are 0 K enthalpies presented in eV.	129
6.4	Potential energy surface (PES) diagram for the reaction channel forming $\text{H}_2\text{CNCH}^+ + \text{C}_2\text{H}_2$. Geometries were computed at the M06-2X/6-31G(2df,p) level, with energies calculated at the G3X-K level of theory. The energy values are 0 K enthalpies presented in eV.	130
6.5	Potential energy surface (PES) diagram for the reaction channel forming $\text{c-C}_3\text{H}_3^+ + \text{CH}_2\text{N}$. Geometries were computed at the M06-2X/6-31G(2df,p) level, with energies calculated at the G3X-K level of theory. The energy values are 0 K enthalpies presented in eV.	130
7.1	(left) a thermalized reservoir has a Gaussian distribution of velocity in each dimension. (right) After supersonic expansion through a small aperture of size d , the gas has a narrowly-defined forward velocity that is skimmed.	134
7.2	Energy of a NH_3 versus the umbrella angle. This forms a double well potential with two parities are separated by a small, nonzero barrier. The peak of this barrier is the planar configuration. Figure adapted from Fitch (2013). [16]	137
7.3	Stark effect for hydrogenated ammonia (red) and deuterated ammonia (blue). At zero field difference in energy of the two parities is separated by the inversion splitting. The Stark shift of ND_3 becomes linear quite early, while the Stark shift of NH_3 is of second order until nearly 3 kV/mm. Figure adapted from Fitch (2013). [16] . . .	138
7.4	Photos of the hardware of a (left) pulsed-pin Stark decelerator and a (right) traveling-wave Stark decelerator. In the case of a PPSD, cylindrical rod pairs are orientated transverse to the molecular beam. For TWSD, rings are stacked along the molecular-beam axis. Left photo is from Fitch (2013). [16]	138

7.5	(a) Schematic of switching sequence in pulsed-pin stark deceleration. The top and bottom panels depicting alternating voltage sequences that are switched between nearly instantaneously. The timing of switching determines how far a molecule climbs a potential hill before the configuration switches. This determines how much kinetic energy is removed per stage. (b-d) graphs of energy versus movement in the beam propagation direction. The black curve represents the potential experience by the synchronous molecule as it travels through two potentials (red and blue). This shows the cases for (b) no deceleration, or bunching, deceleration characterized by a phase angle of (c) $\phi_0 = 30^\circ$, and (d) $\phi_0 = 60^\circ$. A $\phi_0 = 90^\circ$ phase angle would switch configurations at the peak of the potentials. (a) is adapted from Fitch (2013), [16], (b-d) from Shyur (2018). [2]	140
7.6	A Effective electric potential on eight rings with sinusoidal, phase-shifted voltages (electric potential scale is given by top legend). B The resulting effective potential over a central cross-section along the z-axis of A. C the effective potential energy experienced by an ND ₃ molecule due to electrical potential in B. (Scale for energy given by bottom legend.) Schematic adapted from Fitch (2013). [16]	142
7.7	Electric potential energy given for multiple phases of ωt , demonstrating the movement of a well due to the frequency of the sinusoidal potential on each ring. Schematic adapted from Fitch (2013). [16]	143
7.8	Transverse separatrix for TWSD a transverse dimension. The three separatrices denote extremities of transverse phase-space acceptance as dependent on the phase of ωt . Figure adapted from Fitch (2013). [16]	145
7.9	Effective potential energy in Kelvin as a function of longitudinal position in the decelerated well for the different final velocities measured in the experiment. $v_f = 385$ m/s is also evaluated to show the maximum well-depth experienced by the molecules during bunching, where the potential well moves at a constant speed. Figure adapted from Greenberg (2021).	147

7.10 Longitudinal separatrices resulting from the effective potentials in Fig. 7.9. Figure adapted from Greenberg (2021).	148
7.11 (2+1) REMPI scheme for ND ₃ at 317 nm. Figure adapted from Fitch (2013).	149
7.12 Schematic for production and detection of a decelerated ND ₃ beam with traveling-wave Stark deceleration. Figure adapted from Shyur (2018).	150
7.13 Cross-sectional view of the end of decelerator and detection region with the propagation of the molecular beam shown in blue. The molecular beam propagates from the exit of the decelerator to the detection laser, spreading from an initial radius r_{decel} to radius r_{det} at the detection region. Depending on the amount of transverse spread, there may be clipping due to the radius of the TOF aperture, r_{TOF} . Figure not to scale and adapted from Greenberg (2021).	151
7.14 Deceleration data for multiple final velocities ranging from 300 m/s down to 10 m/s. Time is the delay between the molecular beam valve trigger and detection laser pulse. The solid black trace is the free-flight data, scaled to match the baseline of the deceleration data. The free-flight background is essentially zero by 6 ms. The inset plot shows the 10 m/s data. The discrete peaks at each final velocity correspond to multiple, filled potential wells all with the same longitudinal velocity.	154
7.15 Measured and modeled number of molecules, normalized, as a function of final velocity. The black circles represent the data scaled by the reduction in the number of molecules from the exit of the last decelerator ring to the position of the laser due to transverse spread. The red squares represent the total area of the LPSA model, normalized to the area of the LPSA model at 300 m/s. Note the decreasing velocity axis and the lines connecting the points are just to guide the eye.	156

7.16	Deceleration data for a final velocity of 250 m/s using the alternative slowing scheme.	
	The time axis represents the delay between molecular beam valve and detection laser triggers. The free-flight data are scaled to match the baseline of the deceleration data.	
	As the number of bunching stages increase, more aggressive deceleration is applied to the molecular beam, which reaches the final velocity in a shorter distance. This leads to a time delay in the arrival of the slowed packets of ND ₃ 157
7.17	Measured and modeled number of molecules, normalized, as a function of the number of bunching stages. The black circles are the integrated ND ₃ signal, normalized to the integrated signal using zero bunching stages. The red squares represent the total area of LPSA model, normalized to the area of the LPSA model using zero bunching stages. All points represent molecules decelerated to 250 m/s. The data at zero bunching stages correspond to the typical deceleration scheme. 157
7.18	The purity of the molecular beam defined as the percentage of decelerated molecules out of all molecules detected within the integrated time-window containing the molecular packet. The number of decelerated molecules decreases at a different rate as compared to the non-decelerated molecular beam with increasing number of bunching stages. For a final velocity of 250 m/s, the maximum purity corresponds to 20 bunching stages. 158
7.19	(a) A n-channel push-pull amplifier. The rating of the FETs (QT or QB) determines the maximum output and rails ($\pm HV$). Arrows denote optical signal input	
	(b) Multiple FETs connected in series increases the maximum output voltage and rails. A resistor network controls the division of voltage equally across each FET.	
	Figure adapted from Shyur (2018). [19] 164

7.20	Schematics for a leader stage of the amplifier. (A) The FETs responsible for the majority of high voltage switching and current flow when the bank is enabled. (B) Circuitry for the driving signal delivery and global feedback. Q11 is the photoresistor of the optoisolator. (C) Local power supply to hold Q1 & Q2 biased open slightly when the amplifier is not enabled (no signal is delivered.) (D) Local feedback for adequate voltage sharing across stages. Figure adapted from [19]	165
7.21	Schematics for a leader stage of the amplifier. (A) The FETs responsible for the majority of high voltage switching and current flow when the bank is enabled. (B) Local power supply to hold Q1 & Q2 biased open slightly when the amplifier is not enabled (no signal is delivered.) (C) Local feedback for adequate voltage sharing across stages. Figure adapted from Shyur (2018). [19]	166
7.22	Traces demonstrating the effect of bad 2N6660 FETs on amplifier output performance. Yellow traces show the output voltage as measured by the control box (1 V=1.5 kV.) Blue traces are the voltage measured across a 10 Ω resistor in between the low side of the capacitor and ground (1 V = 100 mA). The red trace is a fast Fourier transform (FFT) of the current output. As seen in a), there are extremely fast oscillations with amplitudes nearly a third of the full waveform amplitude. With the time division zoomed in b), the oscillation periodicity and profile becomes more apparent. FFT of the signal determined the oscillations to vary between \sim 20-30 MHz in frequency.	169
7.23	Circuit diagram for the first follower of the amplifier bank. Components of the circuit that we modified to troubleshoot the high-frequency oscillations are marked in color. Full schematics are included in Appendix A.	170

7.24	Photos of the amplifier #7 autopsy. Residue from vaporized components are indicated by the white arrows. This residue most likely came from the high-power 10Ω on the drain side of the IXTF1N450 FETs. This amplifier also showed signs of a short between the top bank leader and first follower (circled in blue). The residue and oxidation found on these copper pads was found on multiple other amplifiers.	172
7.25	Example output traces of amplifiers with “floating issues.” This refers to the “float” of the voltage output towards one of the rails when the active feedback is not on. This does not affect the deceleration of molecules, but does indicate damage of the amplifiers.	173
7.26	Signs of heating was found in multiple ways. a) Some banks had faint burn-like outlines. b), c) Blue or black oxidation was found on many top banks. It was sometimes chalky and sometimes semi-liquid. d) In the case of amplifier 7 it was accompanied by signs of a short between stages.	174
7.27	A photograph of two amplifier banks comparing the wall design. The amp in the foreground has the new single-FET copper pads. The amp in the background has the original wall design, with copper pads printed on a PCB board. The amp in the foreground is not potted, while the amplifier in the back is.	175
7.28	Wall fabrication benefits from Loctite ES1001 epoxy being spread on all surface before attached pieces. (a, b) Epoxy is spread on frame and boron nitride first, (c) Then the panels are placed with light pressure. Make sure the bottom has a teflon layer and is laid level.	178
8.1	Rendering of the core components of the combined TWSD-LIT-TOFMS ensemble. Components original to the ion trap are labeled in blue, the Stark decelerator is labeled in green, and the components new to the integration experiment are labeled in purple (the hexapole and the shutter.)	181

8.2	Details of hexapole mounting. Above photos show an end-on view of the downstream end of the decelerator (a) before and (b) after the hexapole mounting is installed. (c) End-on view of the downstream end of the hexapole before integration with the ion trap. The two discs that provide electrical connection between alternating rods are visible. Outside these disks is a glass sleeve that insulates the hexapole rods from the mounting cap. (d) Partially exploded CAD view of the hexapole and mounting structure. Also shown is the direction of the end-on perspective for the prior photographs.	182
8.3	CAD rendering of the integrated experiment, with correlated photos from the construction process. The orange box highlights the end of the decelerator. The purple box shows the coupling of the decelerator and the hexapole. The green box labels the end of the decelerator, with two photos. One is less complete, showing the glass sleeve that protects the hexapole rods from the mounting cap; the photo to the right is later in the construction process, with the hexapole placed inside the reducing nipple, and a cap mounting the end of the hexapole to spherical octagon that encloses the ion trap. Lastly, a top view photograph of the trap with the integrated hexapole is indicated by the blue box.	184
8.4	Side view of the fully integrated experiment during the building process. The first open flange on the left shows the end of the decelerator and the beginning of the hexapole. The ion trap is on the right, with the flight tube extending directly below. Off the side of the flight tube is a titanium sublimation pump.	185
8.5	Top view of the fully integrated experiment during the building process. The open flange on the right shows the end of the decelerator and the beginning of the hexapole. The ion trap can be viewed on the open spherical octagon on the left.	185

8.6	Deceleration data for multiple final velocities ranging from 300 m/s down to 10 m/s.	
	Time is the delay between the molecular beam valve trigger and detection laser pulse. The solid black trace is the free-flight data, scaled to match the baseline of the deceleration data. Figure adapted from Greenberg (2021.) [18]	187
8.7	(a) A Uniblitz shutter in its original housing and (b) with the housing removed. This shutter opens due to electromagnetism, with the speed of opening modulated by the current applied across the coil shown. The manually opened shutter blades are shown in panel (c).	187
8.8	(a) A side view of the downstream end of the decelerator and upstream end of the hexapole, with entry cap missing. This cap is not yet installed, having a shutter (b) mounted on it. This shutter will be installed before a final characterization of the beam output and subsequent reaction studies. An exploded view of the hexapole mounting (c) demonstrates this removable cap and its position on the hexapole mounting structure.	189
8.9	Particle trajectories in the LIT-TOFMS system. Ions are released from a distribution near the center of the trap that is modeled after either a Coulomb crystal (top), or an ionized molecular beam (bottom). This simulations demonstrate a high relative loss of ions when modeled as a ionized molecular beam, and very low losses when modeled as a dense, small, crystal.	192
8.10	Ion trajectories (left) and electric fields (right) for the original rod voltage settings of top/bottom 2000/1860 V (top) and final settings 2000/1480 V (bottom). The figures together demonstrate the field gradients and resulting focusing of the trajectories. This focusing can be tuned with different combinations of voltages on the rods. We found that the 2000/1480 V gave the best transmission through the hole at the top of the flight tube, and paired best with our Einzel lens to achieve maximum signal at the MCP plates (not shown.)	193

8.11 (a) Electric fields simulated by COMSOL [20] for a standard operating of voltages in our linear hexapole. Here, alternating voltages of ± 2 kV and the resulting electric fields, are shown. (b) A graph of the electric field verses distance (mm) along a transverse line across the hexapole (marked in blue on (a)). This plotted field distribution demonstrates the harmonic nature of the field's dependence on r .	197
8.12 Expected and measured relative ND ₃ signal for 160 m/s final velocity at 3.6 kV _{pp} at various voltage turn-on times. Simulations predict peak density within the trap rods when held on (blue), while predicting a single peak in signal at ~ 1.7 ms at the Coulomb-crystal sized (~ 100 μ m by 0.5 mm) center of the trap (yellow.) Empirical measurements (orange) show something somewhat different from either and similar to both.	199
8.13 Results from hexapole simulations. On the right, a 3-D graph showing the number of ND ₃ molecules that successfully reach between the trap rods, as a function of the hexapole peak-to-peak voltage, and turn-on time of that voltage (in this case, the voltage stays on well past the removal of molecules from the fields.) This results predict the highest transmission of ND ₃ molecules with an immediate implementation of voltage. There are two peaks in signal associated with a "fundamental" (at ± 1125 V) and first "harmonic," (at ± 2250 V) as shown by the trajectories sketched on the left. These trajectory graphs are projected against the xz plane, where z represents the long axis of the hexapole (entering on the left and hitting the crystal on the right) and x is represented by the long axis of the trap. On the far right the hexapole cap radii and crystal size are represented by black lines.	203
8.14 Spread in decelerator (blue) and hexapole (yellow) outputs for 160 m/s outputs. Particles are binned in 100 bins and fitted to Gaussian distributions. The average and standard deviation are reported for (a) longitudinal and (b) transverse velocity spreads. The uncertainty represents the 95% confidence interval.	204

8.15	ND ₃ detected at the ion trap for multiple final velocities at their respective empiri-	
	cally optimized hexapole-lensing parameters. Note that the distinct wells that were	
	evident in the decelerator output data are no longer distinct. This is due to the	
	additional ~0.5 m length over which the longitudinal spread in velocities blurs the	
	physical separation of the distinct wells.	206
8.16	ND ₃ detected at the ion trap for multiple final velocities. The distinct shells that	
	were evident in the data from the decelerator output are no longer distinct; this is	
	due to the additional ~0.5 m length over which the longitudinal spread in velocities	
	blurs the physical separation of the distinct wells.	208
8.17	Three prior studies demonstrating energy dependence of the NH ₃ ⁺ + NH ₃ →	
	NH ₄ ⁺ + NH ₂ reaction rate constant. (a) Mass spectrometry measurements from ther-	
	mal energies to 9 eV kinetic energy. Figure adapted from Ryan (1970.) [21] (b) ICR	
	measurements from thermal energies to 3 eV. Figure adapted from Marx (1973.) [22]	
	(c) Free jet flow reactor measurements with rotational temperatures from 12-20 K,	
	and translation temperatures equivalent to 0.4-4 K. The thermal data point is an	
	average of literature values. Figure adapted from Smith (1995.) [23]	213
8.18	(left) Branching ratios for the three products of NH ₃ ⁺ + ND ₃ as they depend on	
	vibrational excitement and kinetic energy. (a) With vibrationally relaxed NH ₃ ⁺ ,	
	the proton transfer product is enhanced at thermal kinetic energies. Conversely, the	
	charge transfer product is significantly enhanced at higher energy. The deuterium	
	abstraction is relatively independent of kinetic energy. (b,c) The aforementioned trends	
	persist with the excitation of the ammonia umbrella mode. Overall, the proton trans-	
	fer mechanism decreases with vibrational excitement, while the deuterium abstrac-	
	tion and charge transfer cross-sections increase with increasing internal excitement.	
	(right) Illustrations of possible direct models for (d) deuterium abstraction, (e)	
	proton transfer, and (f) charge transfer. Figure adapted from Posey (1994.) [24] . . .	216

Chapter 1

Introduction

“We take well understood building blocks – well understood atoms, molecules – and go out looking for trouble. This is AMO physics these days.”

– Eric Cornell, Gordon Research Conference on Atomic Physics, 2023 (cited with permission)

Recent developments in atomic and molecular physics have rapidly expanded the tools available to manipulate and detect molecules. This has presented excellent opportunities to probe the underlying mechanisms of chemical reactions and apply the knowledge gained to relevant contexts. Ion-neutral, gas-phase chemical reactions are a particularly interesting class of reactions to study; they can be used to understand the fundamental reaction mechanisms in charged systems, as well as contribute to the understanding of important chemical environments, such as the Interstellar Medium (ISM).

Historically, the complex astrophysical environment has inspired substantial ion-neutral reaction research, from laboratory measurements, to astronomical observations, to computational modeling of this complex space. The complexity and diversity of the chemical composition of the ISM poses a scientific challenge, with at least two hundred unique molecules that have been found in the ISM. [\[25\]](#), [\[26\]](#), [\[27\]](#), [\[28\]](#), [\[29\]](#) Modeling the numerous, interconnected reactions that contribute to the current composition of these regions of space is a complicated task and requires extensive knowledge of the identity, density, and reaction rates of the molecular constituents of the ISM. [\[30\]](#), [\[31\]](#), [\[32\]](#), [\[33\]](#) Among the pertinent classes of reactions, ion-neutral interactions play a particularly important

role. Ion-neutral reactions often have low or no reaction barriers and are therefore associated with fast reaction rates ($\geq 10^{-11} \text{ cm}^3 \text{ s}^{-1}$). This high reactivity, together with many detected ions and established ionization sources in space, suggests ion-neutral reactions play an important role on the present composition of the ISM. [34, 35, 36]

The significance of ion-neutral reactions has motivated substantial theoretical efforts. [37] Capture models have been largely successful in predicting kinetic trends of ion-neutral reactions. These models assume an ion-neutral reaction is dominated by long-range forces and predict rates by estimating the likelihood a pair of reactants form an adduct. Langevin's calculated reaction rate theory is particularly famous, as it predicts a temperature-independent reaction rate between ions and neutrals that is determined by the neutral molecule's polarizability. [38] Work from Su, Bowers, Chesnavich, and others extended this theory to reflect that long range effects, particularly the dipole moment, enhance the likelihood of capture. This leads to an ion-neutral reaction rate with temperature dependence for many systems. [39, 40] Similar approaches have been taken in assessing reactions from a quantum-mechanical perspective. This has been particularly necessary as pioneering tools have enabled reactions at progressively lower energies. Examples of such theory include adiabatic capture centrifugal sudden approximation (ACCSA) [41] and statistical adiabatic channel model (SACM). [42] Such theoretical advances have contributed to our ability to predict reaction kinetics. These kinetic theories of ion-neutral reactions aid tremendously in ISM modeling, but they are most compelling when used in conjunction with experimental investigations. [31]

The collaborative relationship of theory and experiment is perhaps even more evident in foundational explorations of reaction dynamics. Product branching and reaction mechanisms can elucidate fundamental principles and parameters involved in reaction dynamics. [43, 44] To probe these underlying mechanisms, experiments with extensive control of reactant properties and detection of product characteristics can be very beneficial. One notable frontier for such investigations is the boundary between reactions that can be treated as classical or quantum mechanical. [45, 46, 47] As such, a recent direction of the field has been to study this dichotomy of regimes by controlling and reducing the reaction energy. Investigations of reactions pertaining to chemical composition

have also led to fruitful investigations of chemical reactivity across isomers, conformers, and isotopologues. These avenues of inquiry require fine control over the reactants, detection of the products, and extensive theoretical work to understand and analyze the underlying mechanisms.

The experimental realization of ion-neutral reactions has been achieved with many types of experimental setups, each with different advantages and limitations.^[46, 45, 47] A few historically prominent experimental apparatuses include: selected ion-flow tubes^[48, 49]; uniform supersonic flows (CRESU)^[50, 51]; crossed-beam methods including the use of velocity-mapped imaging^[52, 53]; and Rydberg-Stark deceleration^[54]; as well as trap-based methods.^[55, 56, 57] Some experiments, including the one described in this dissertation, utilize radiofrequency (RF) traps to study ion-neutral chemical dynamics with Coulomb crystals. The term *Coulomb crystal* refers to the three-dimensional order that can be achieved by cold, trapped ions^[1]. Such an environment allows us to have precise control over the reactions to elucidate a new level of understanding of ion-molecule reactions.

1.1 Coulomb crystals for chemistry

To contextualize the work described in this dissertation, I will provide a brief overview of previous studies of reactions in Coulomb crystals to illustrate the diversity and versatility of this experimental design, and to highlight the excellent progress that has been achieved by the field. The main tool used by the field are Coulomb crystals, which rely on laser cooling of an atomic species. Alkaline earth metal ions are a natural choice for laser cooling as there are relatively simple cooling schemes and readily available lasers for these atoms. Doppler laser cooling can cool such ions to μK temperatures; co-trapped ions that are not directly laser cooled can also reach sub-Kelvin secular temperatures due to the Coulomb forces between ions in the trap.^[58, 59, 60, 61] Cold, trapped ions at these temperatures form an ellipsoidal structure as shown in Figure [1.1](#). When these crystals are formed in dynamic RF traps and ultra high vacuum (UHV) environments, ion ensembles can

¹ These cold configurations of ions have been formed in both Penning and linear ion traps; however, I will focus on such crystals formed in linear ion traps such as ours.

be stable for hours and provide abundant opportunities to manipulate and probe the system.

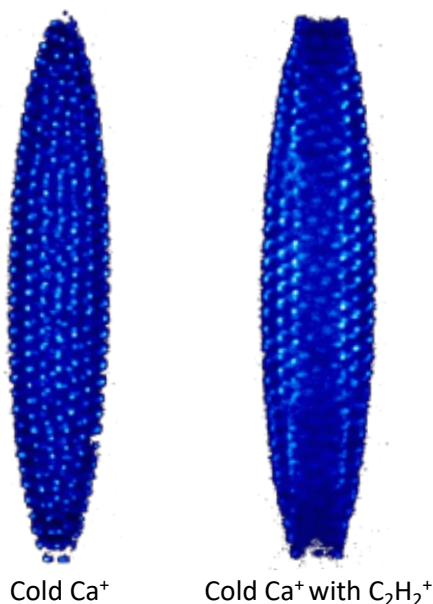


Figure 1.1: False-color fluorescence images of two Coulomb crystals, one of pure laser-cooled Calcium ions (left), and the other with co-trapped, sympathetically cooled acetylene ions (right). These images are taken by a CCD camera using microscope objective positioned above the RF trap.

Because ions can be cooled and trapped for long times, Coulomb crystals have proven to be an excellent environment in which to study ion-neutral, gas-phase reactions with substantial control over reaction parameters.^[62, 63, 64, 65, 66] In one such set of studies in crystals, reactions have demonstrated isotope-specific dynamics. An early example of such an investigation is that of laser-cooled Mg^+ reacted with HD, demonstrating a branching ratio of MgD^+ to MgH^+ of 5 to 1.^[67] A more recent paper reported an inverse kinetic isotope effect (in which reactions with the deuterated neutral are significantly faster than those with the hydrogenated neutral) for ammonia reacting with rare gas ions Xe^+ , Kr^+ , and Ar^+ .^[68, 69] Such isotope effects are unexplained by classical kinetic reaction rate theories, which predict slightly slower reactions in the deuterated case. These inverse cases may be particularly relevant for understanding the greater presence of deuterated molecules in the ISM than is expected from the relative abundances of hydrogen and deuterium (a phenomenon referred to as deuterium fractionation).^[70]

Studies have also demonstrated that chemical dynamics can be fundamentally influenced by

the structural and spatial isomers of the reaction participants. One example from our group is the reaction of $\text{C}_2\text{H}_2^+ + \text{C}_3\text{H}_4$, which is dominated by long-range charge transfer for the allene isomer of C_3H_4 , but is influenced by short-range effects for propyne.[\[7\]](#) [\[71\]](#) Another example of isomer-resolved chemistry includes the work of Yang et al., in which trapped C^+ was reacted with water from a cryogenic buffer-gas beam to form HCO^+ and HOC^+ at cold (~ 20 K) temperatures.[\[72\]](#) The branching ratio of these two product isomers was determined by a second (“titration”) reaction with neutral nitrogen gas, as HOC^+ reacts to form N_2H^+ , while HCO^+ does not.

Another class of isomers with chemical ramifications are stereoisomers, which are distinguished by the same molecular connectivity, but different spatial arrangement. While traditionally difficult to isolate, recent work has succeeded in using high electric fields to deflect stereoisomers dibromobutadiene and 3-Aminophenol by their dipole moments, such that reaction rates can be measured as a function of the relative population of the two isomers. Recent studies have demonstrated an enhanced reaction rate in the isomer with the higher dipole moment; theoretical modeling of the reaction attributed this effect to stronger suppression of the centrifugal barrier and thus greater likelihood of capture for the isomer with the larger dipole moment.[\[73\]](#) [\[74\]](#) Studies of reaction dynamics with control over isomeric and isotopic variables in Coulomb crystal environments have proven productive, and continue to be an avenue of interest. This dissertation will feature an in-depth look at this experimental environment and discuss multiple recent reactions in such an environment that we have investigated.

1.2 The road to energy-resolved ion-neutral reactions

Efforts to tune the energy of the neutral reactant in Coulomb crystals studies have been fruitful as well. With the use of quadrupole guides, several molecules with large Stark shifts have been filtered to lower velocities. This *Stark filtering* has been demonstrated for many molecules, the most common examples of which are CH_3F , ND_3 and CH_3CN .[\[75\]](#) [\[76\]](#) [\[77\]](#) A recent application of this method was demonstrated by Okada et al. in a reaction between cold, trapped Ne^+ and velocity-filtered CH_3CN . The reaction demonstrated an increasing reaction rate with decreasing

collision energy over $20 K \geq T \geq 5 K$ (where $T = E/k_B$, E is energy, k_B is Boltzmann's constant). [78]

There have been many other efforts to incorporate greater control over the collisional energy in cold ion-neutral chemical reactions. [46] Cryogenic traps with buffer gas cooling, [79, 80, 81, 82] and merged beam techniques, [52, 83, 84, 85, 86] have been particularly fruitful avenues for ion-neutral reactions. Zeeman and Stark deceleration of molecules for ion-neutral reactions for ion-neutral reactions has also been a recent emphasis of the field. [87, 118, 88] A portion of this dissertation is dedicated to the description of the preparation and integration of a traveling-wave Stark decelerator to our ion trap to conduct energy-tunable reactions between a decelerated beam and trapped ions in a Coulomb crystal.

1.3 Outline of dissertation

This dissertation will begin with an overview of the experimental tools used to investigate ion-neutral gas-phase chemical reactions between thermal, neutral reactants and cold ions in Coulomb crystals. Chapter 2 will overview ion trapping, laser cooling, and other experimental methods involved in our linear ion trap (LIT) apparatus. In Chapter 3, I will discuss the theoretical tools available to assess the kinetics and dynamics of these reactions. This will include discussions of capture rate theories, quantum-chemical calculations, and potential energy surfaces. Together, these two chapters contextualize the experimental and theoretical tools utilized for three published reaction studies. These are the reactions of $\text{CCl}^+ + \text{CH}_3\text{CN}$ (Chapter 4), $\text{CCl}^+ + \text{C}_6\text{H}_6$ (Chapter 5), and $\text{C}_2\text{H}_2^+ + \text{CH}_3\text{CN}$ (Chapter 6). All three of these reactions are examples of astrochemically relevant reactants that demonstrated fast reaction rates in our LIT. Each reaction will be discussed in conjunction with theoretical work illuminating the thermodynamics of the reaction, as well as aspects of their reaction dynamics.

The last two chapters shift towards the future of the LIT experiment, which is the integration of a traveling-wave Stark decelerator (TWSD) to the LIT as a energy-tunable neutral beam source for reaction studies in Coulomb crystals. The principles of Stark deceleration and the char-

acterization of our TWSD will be outlined in Chapter 7. Chapter 8 will describe our in-progress preparations of the integrated experiment for reaction studies. I will report calculations and literature review that support the scope of planned reactions in this apparatus. A summary of this work and outlook for planned reactions will close this dissertation.

Chapter 2

Experimental tools for observing reactions between trapped ions and thermal neutral gases

“It is the skill of the experimentalist to carry out clear experiments in order to get answers to [her] questions undisturbed by undesired effects and it is [her] ingenuity to improve the art of measuring to ever higher precision. There are many examples in physics showing that higher precision revealed new phenomena, inspired new ideas or confirmed or dethroned well established theories.”

–Wolfgang Paul, “Electromagnetic Traps for Charged and Neutral Particles,” Nobel Lecture, December 8 1989

This chapter concerns the experimental considerations of an ion-neutral gas-phase chemical reaction in our LIT-TOFMS (*linear ion trap coupled to a time-of-flight mass spectrometer*). This chapter will start with a technical overview of ion trapping and Doppler laser cooling to contextualize the cold energies of our trapped ions. This will be put into the perspective of the larger experimental apparatus and I will outline the equipment relevant for a full reaction data acquisition. This together will give a full picture of the experimental methods that define the conditions in which we can do reactions of cold trapped ions with thermal neutral molecules in the molecular flow regime. These are the conditions in which the reactions discussed in Chapters [4](#), [5](#), and [6](#) take place.

2.1 Principles of Ion Trapping

In this section, I will discuss some important principles for trapping ions with a detailed discussion of the electrodynamics of our linear Paul trap. I will overview the physics of Doppler laser cooling and its impact on cooling our trapped ions. This section will end with a reflection on molecular dynamic simulations produced by our group that demonstrate how the trapping and cooling dynamics come together to build a cohesive picture of the ion energies. We will build on this picture of the ion energetics for later characterizations of our reaction thermodynamics.

2.1.1 Ion traps

Ion traps are an excellent environment in which to study ions, both for reaction studies as well as spectroscopy of ions. [89, 90, 91, 92, 93, 94, 95] A key benefit of ion traps is they tend to be quite stable, which provide opportunities to work under low pressures with low loss rates. [55, 56, 57] In our case, this enables excellent opportunities to study two-body reactions in isolation; in addition, this simulates the astrochemical environment, where three-body collisions are usually unimportant. It also allows for more state control, as ions can be manipulated with lasers or allowed to relax from possible excitations from the ionization process with minimal temporal constraints. Both of these benefits contrast with flow methods like flowing-afterglow (FA) or selected ion-flow tubes (SIFT) [48, 49] which rely on high-density flows of gases through a constrained apparatus length. These methods are responsible for a substantial amount of the field's knowledge of ion-neutral chemical reactions and have been extremely effective. Nevertheless, the spatial confinement of ion traps have paired excellently with high fidelity detection schemes, as well as quantum and thermodynamic control to push forward the frontiers of the field.

An important contextualization for the development of ion traps is a constraint of physics itself. Earnshaw's theorem states that a collection of point charges cannot be stably held in equilibrium by static electric fields alone. A stable equilibrium requires that no perturbation can disrupt the equilibrium. This would require that all forces on a trapped particle restore it to its original

position (i.e. the divergence of the field must be negative.) Mathematically this is impossible with static electric fields, as a result of Gauss' law, since the divergence of any electric force field is zero in free space:

$$\nabla \cdot \mathbf{F} = \nabla \cdot (-\nabla U) = -\nabla^2 U = 0 \quad (2.1)$$

Thus, an arbitrary static electric field is insufficient to trap ions as it will only produce a saddle point, not a maxima or minima. Fortunately for us, there are ways around this problem that won the 1989 Physics Nobel Prize. Hans Dehmelt and Wolfgang Paul developed two such solutions, which became the basis of modern ion trapping.

The Penning trap, developed by Hans Dehmelt, was named after F. M. Penning as the technique was inspired by Penning's vacuum gauge design. The Penning trap relies on a quadrupole electric field for axial confinement, with a strong homogenous magnetic field to confine particles radially.[\[96, 97, 98\]](#) These Penning traps (or *ICR cells*) were first used for mass spectrometry and were later developed for ion-neutral reaction studies once ions could be stably trapped in the range of milliseconds to seconds.[\[99, 100, 57\]](#) Building such traps with cryogenic cooling has substantially extended their applications.[\[101, 102\]](#) This trapping method benefits from minimal losses and non-destructive mass detection. A significant drawback of this trap, however, is the large magnetic field required for the trapping. In addition, the geometric setup often complicates access to the trapping region and limits the access of lasers, molecular beams, and/or time-of-flight measurements.

Electrodynamic methods are also quite prevalent. Macroscopic quadrupole and 22-pole traps have historically been the most prevalent, although the more recent designs of traps for quantum information and computer applications usually involve chip-based traps.[\[59, 103, 104\]](#) The 22-pole trap benefits from low micromotion due to a pseudopotential that is flatter than the more harmonic potentials of lesser-poled traps. But note that this also results in a lower density of trapped ions than the harmonic potentials; this leads to lower Coulomb-Coulomb interactions in the trap and thus laser cooling does not effectively sympathetically cool co-trapped ions. Yet they are a great

candidate for cryogenic buffer gas cooling and this type of trap has been particularly productive for studying reactions with H_2 . [81, 105, 106, 107] Higher-order-pole traps can be somewhat limited by the need for cryogenic and buffer gas cooling as these cooling techniques have their own technical challenges, including freeze-out of most neutral reactant candidates at cryogenic temperatures.

2.1.2 The linear paul ion trap

Electrodynamic traps began with Wolfgang Paul's Nobel-winning design, the quadrupole ion trap (also appropriately called a *Paul trap*). [1, 4, 89, 108] This technique utilizes dynamic fields to produce trapping with an oscillating saddle potential. The original design is shown in Figure 2.1. Opposing RF is driven on the ring electrode (A) and the hyperbolic endcaps (B), such that the ions would oscillate between being elongated axially (along the z axis) and radially (x - y).

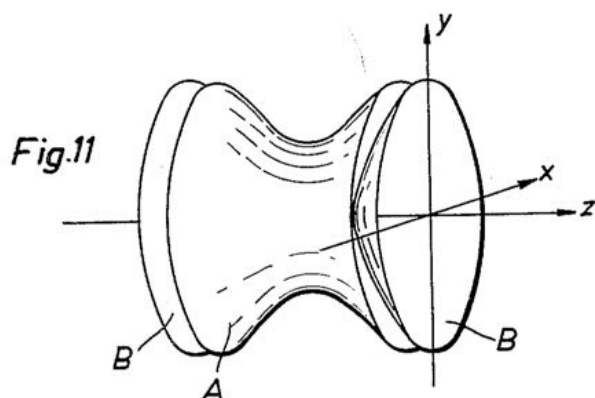


Figure 2.1: Figure from Paul's original patent. [3] A driving RF voltage is put on the ring electrode (A) and hyperbolic endcaps (B). The ions oscillate between being pulled out axially (z axis) and pushed in radially, and vice versa.

A somewhat different geometric design utilizing this principle is the linear quadrupole trap, where four parallel electrodes produce the RF (Figure 2.2). In this configuration, pairs of rods experience RF out of phase to produce the "flapping" saddle point that characterizes the RF trap. These saddle point potentials represent the trapping fields in the radial direction, where the RF

produces a stable well along one axis of the radial direct while simultaneously destabilizing in the other. If the RF is switched between the two fast enough, the ions will be stably trapped. The frequency of the switching between the two saddle point potentials is the frequency of the RF (Ω_{RF}). This linear quadrupole geometry is what we use in our experiment, and the rest of this chapter will explore the mathematical parameters associated with this system's trapping stability and dynamics.

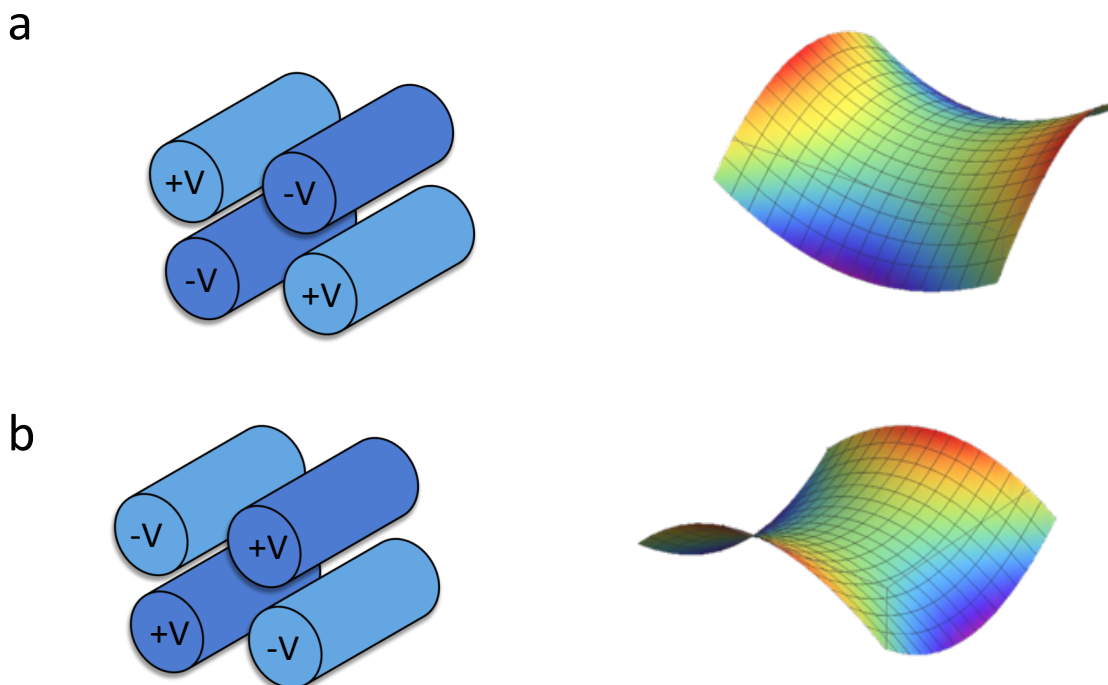


Figure 2.2: Schematic of the RF fields generated by a linear Paul trap. a) and b) represent an effective radial energy potentials produced at two points separated by 180° of the driving RF frequency. The frequency of the switching between these two potentials is determined by the frequency of the RF. The magnitude of the potential is determined by the amplitude of the driving RF frequency.

As mentioned above, this saddle potential (or if you are hungry, Pringle-like potential) represents just the *radial* trapping fields. One more component is required for stable trapping in a linear ion trap: an axial trapping potential. As seen in Figure [2.3](#), a linear Paul trap like the one in our experiment has three segments on each rod, such that the outer components on each can hold a DC voltage for axial trapping, often referred to as the *endcaps*. Ideally all eight endcaps can be

held at the same voltage to produce a harmonic trapping potential in the axial direction. This is schematically shown in Figure 2.3.

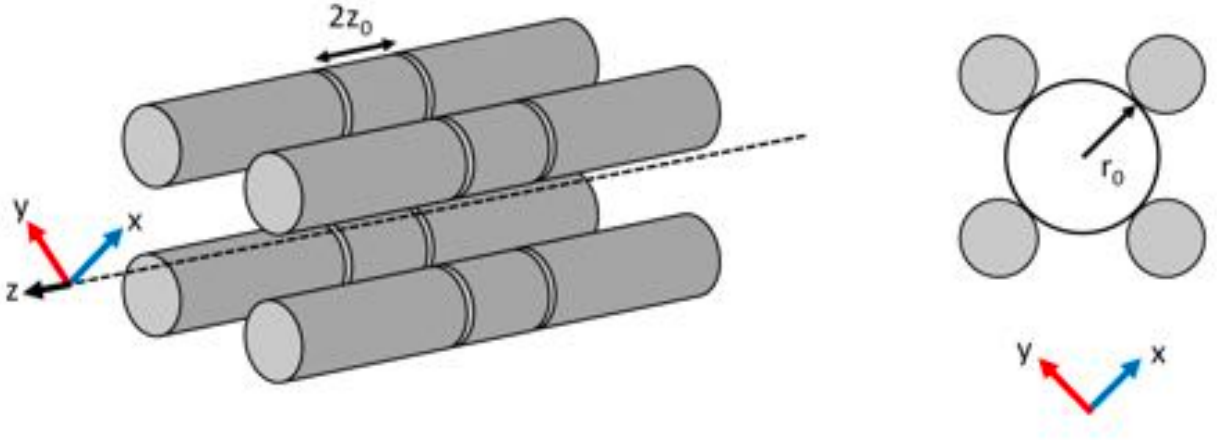


Figure 2.3: Schematic representation of a linear ion trap geometry. An isometric view is given on the left, while the side view is given on the right. The eight outer segments are the endcaps, while the four center sections exert RF trapping fields on the ions. [1]

$$\Phi(x, y, z, t) = \phi_{RF} + \phi_{EC} \quad (2.2)$$

The radial, time-varying potential is described by:

$$\phi_{RF}(x, y, t) = 2V_{RF} \sin(\Omega t) \frac{x^2 + y^2}{2} \quad (2.3)$$

with V_{RF} is the amplitude of the applied RF, Ω is the angular frequency of the RF, and x , y and t are the two radial space components and time, respectively.

A DC voltage on the eight outer electrodes produces an approximately harmonic potential on the axial direction, described by:

$$\phi_{EC}(x, y, z) = \frac{\kappa V_{EC}}{z_0^2} \left(z^2 - \frac{x^2 + y^2}{2} \right) \quad (2.4)$$

with κ (< 1) representing a geometrical factor, V_{EC} is the DC endcap voltage applied, and z_0 is half the length of the center electrode (see Figure 2.3.)

The full combination of both trapping potentials describes the full picture of dynamics in an ion trap. Unfortunately, this equation does not have an analytical solution for multiple ions in the trap. Numerical solutions can solve these system with high accuracy and will be discussed in Section [2.1.5](#). However, there are a few simplifications that can be made that yield substantial insight into the properties of ions in these traps.

The first simplification comes from considering the forces on a *single* positively charged ion of charge q and mass m . In this case, the equations of motion spatially separable and simplify to the so-called Mathieu equation:

$$\frac{\partial^2 u}{\partial \tau^2} + (a_u - 2q_u \sin(2\tau)) = 0 \quad (2.5)$$

where u and τ are generalized coordinates, and a_u and q_u are dimensionless parameters referred to as Mathieu parameters. Equation [2.5](#) describes the equations of motion in the case that:

$$u = \{x, y, z\} \quad (2.6)$$

$$\tau = \frac{\Omega t}{2} \quad (2.7)$$

$$a_x = a_y = -\frac{a_z}{2} = -\frac{q}{m} \frac{4\kappa V_{EC}}{z_0^2 \Omega^2} \quad (2.8)$$

$$q_x = -q_y = -\frac{q}{m} \frac{4V_{RF}}{r_0^2 \Omega^2}; q_z = 0 \quad (2.9)$$

In the case that $q_u \ll 1$ and $a_u \ll 1$, Equation [2.5](#) can be sufficiently approximated by the first term in a Taylor expansion. The ion's equation of motion is then given by:

$$u(\tau) \simeq A_u^{(1)} \cos(\omega_u \tau + \phi_u) \left(1 + \frac{q_u}{2} \cos(\Omega \tau)\right) \quad (2.10)$$

where

$$\omega_u = \frac{\Omega}{4} \sqrt{a_u + \frac{q_u^2}{2}} \quad (2.11)$$

is the radial *secular frequency*. This frequency describes the secular motion of the ion within in the trap. As this frequency depends on the Mathieu parameters, it is also then mass-dependent, as well as dependent on the trap parameters. The amplitude of the frequency is given by $A_u^{(1)}$, and ϕ_u is the phase. Both of these factors depend on the initial conditions of the ion. As will be seen in [2.2.2](#), this can be viewed as a feature of ion traps that will be used to our advantage in reactions studies.

Another interesting result from this approximation considers the stability of an arbitrary mass in an ion trap. The solutions to the Mathieu equation have stable and unstable solutions. Here, stable motion requires that the ions oscillate in the x-y plane with constrained amplitudes that do not hit the trap electrodes. Unstable motion grows exponentially in the x axis, y axis, or both; this leads to trap losses. Clearly, we are interested in stable motion for as wide a range of masses as possible, but note – one application of quadrupole traps is mass filters, which operate by stabilizing only a narrow mass range. This application is particularly appealing as that only certain masses have stable oscillations in the rods and the stability conditions depend solely on a and q and not the initial conditions.

However, we care about the stability regions, which can be mapped generally as seen in [Figure 2.4](#). [Figure 2.4a](#) is a depiction of the overall stability diagram for a two-dimensional quadrupole field. [Figure 2.4b](#) is the lowest possible region for simultaneous trapping in radial and axial directions (shaded ‘A’ region on [Figure 2.4a](#)). The stability is also sometimes represented by the unitless parameter β which is also sketched as continuous lines on [Figure 2.4b](#). This stability parameter, also referred to as the Mathieu characteristic parameter, is defined as:

$$\beta \approx \sqrt{a_u + q_u^2} \quad (2.12)$$

This approximation is true for $a_u \ll 1$; $q_u \ll 1$; $\beta \ll 1$. Stability in this region requires $0 < \beta_u < 1$,

as is also noted on Figure 2.4b.

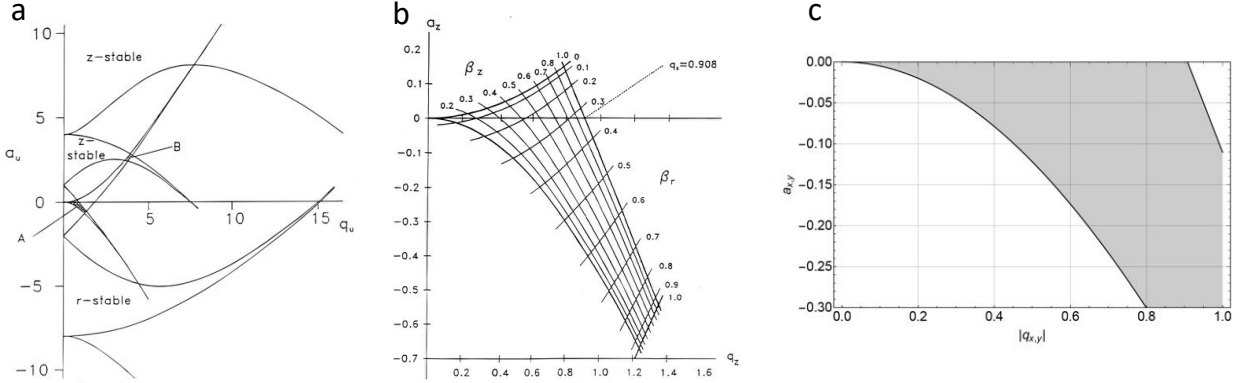


Figure 2.4: Diagram showing the stability regions for the radial and axial directions (a, left). The lowest region of mutual stability is shaded in the left diagram as “A” and is represented at a larger scale in the right figure (b). (c) shows that within this region, only a more constrained region is stable due to the geometrical features of our specific ion trap. Figures (a) and (b) from March (1997), [4] (c) from Greenberg (2020). [1]

However, the a_u and q_u parameters are further constrained by the geometrical parameters of the trap. The geometrical parameters of the trap are given in Table 2.1, and the resulting effective stability diagram for our specific linear ion trap is shown in Figure 2.4c. Note that all the aforementioned results come from the assumption of a single ion in the trap.

Table 2.1: Typical trapping parameters and trap geometry variables. Reproduced from Greenberg (2020). [1]

Trap parameters			Calculated trap values for Ca^+		
RF frequency	Ω_{RF}	$2\pi \cdot 3.552 \text{ MHz}$	Mathieu q param	$ q_{x,y} $	0.25
RF voltage	V_{RF}	200 V	Mathieu a param	$ a_{x,y} $	0.0012
endcap voltage	V_{EC}	3.5 V	radial frequency	$\omega_{x,y}$	$2\pi \cdot 162 \text{ kHz}$
endcap separation	$2z_0$	7 mm	radial trap depth	$D_{x,y}$	12.6 eV
inscribed radius	r_0	3.91 mm	longitudinal frequency	ω_z	$2\pi \cdot 43.8 \text{ kHz}$
geometric factor	κ	0.22	longitudinal trap depth	D_z	0.77 eV
rod radius	R	4.5 mm	ion density	n_0	$4.58 \cdot 10^7 \text{ cm}^{-3}$

2.1.3 Ion energetics

Another approximation that is quite useful in its applications and insight is the *pseudopotential approximation*. In the limit that $a_u \ll 1$ and $q_u \ll 1$, we see from equation [2.11](#) that $\omega_u \ll \Omega_u$. In this case the trapping potential can be modeled as a harmonic, [\[1, 109\]](#) mathematically described by

$$\phi^*(x, y, z) = \frac{qV_{RF}^2}{m\Omega^2 r_0^4}(x^2 + y^2) + \phi_{EC}(x, y, z) \quad (2.13)$$

The potential energy of an ion due to radial trapping fields can then be related back to the Mathieu parameter:

$$PE_{x,y} \leq \frac{q_{x,y}V_{RF}}{4} \quad (2.14)$$

$$PE_{x,y} \leq \frac{qV_{RF}^2}{mr_0^2\Omega^2} \quad (2.15)$$

Notice that this approximation effectively averages over each RF cycle, “blurring” the impact of the micromotion on the ion’s kinetic energy. Thus the energy and velocity from the flapping of the trap is not accounted for, although the motion from cycle-to-cycle is. Nevertheless, these so-called *secular* energies are a very useful metric for the energy of a Coulomb crystal. Further intuition can be gained by calculating the actual kinetic energy, or *secular* energy of the ion by combining equations [2.10](#) and [2.11](#):

$$KE_u = \frac{1}{2}m\langle\dot{u}^2\rangle = \frac{1}{4}mA_u^{(1)2}(\omega_u^2 + \frac{1}{8}q_u^2\Omega_u^2) \quad (2.16)$$

$$KE_u = \frac{1}{2}mA_u^{(1)2}\omega_u^2 \quad (2.17)$$

if $a_u \ll q_u$, as in the case of stable trapping in our linear ion trap. This is of course heavily dependent on the amplitude of secular excitation A_u , which in practice initial conditions in the trap in the absence of any damping force.

There are a few key results from this derivation. Firstly, the masses we can stably trap – as well as the effective trap depth for each mass – are dependent both on our geometrical trap parameters, as well as on our trap parameters. While a faster Ω will allow trapping of lighter ions, it will also contribute to more micromotion heating. We see that the lighter ions will experience a deeper potential than the heavier ions and that the resulting frequency associated with the secular motion will depend on the m/z ratio. We also see that the magnitude of unwanted motion caused by the dynamical fields is dependent on the initial conditions of the trap. However, we may see how quenching of this motion can reduce this magnitude significantly. Thus, introducing a damping force into our trap to cool the ions down can significantly reduce the energy of our ions down to sub-Kelvin effective “temperatures.” In our experiment, we do this with Doppler laser cooling.

2.1.4 Laser cooling

Laser cooling is a technique that has revolutionized the atomic-molecular-optical (AMO) physics community, winning the Nobel Prize in 1997. [5] There are several notable techniques to manipulate atoms with lasers that have developed in the last few decades. [5, 110, 111, 112, 113, 114, 115] These methods have been pivotal to the development of modern AMO physics experiments. Broadly speaking, if an AMO group works with an alkali metal atom or alkali earth ion, odds are extremely high they are laser cooling that atom. These columns of the periodic table are not random, but rather contribute significantly to what atoms can be (at least easily) laser cooled, due to their “hydrogen-like” nature. In this context I will briefly discuss the mechanics of Doppler laser-cooling specifically and discuss the relevant details for cooling the Ca^+ ions we use in our experiment.

Recall that light has momentum, $\hbar k$, where \hbar is Planck’s constant and k is the momentum of light. If a photon is counterpropagating to a particle with velocity v , then the absorption of this photon would necessarily result in a reduction of the velocity of the atom due to momentum conservation. This is shown in Figure 2.5. In the model that a particle could absorb such photons repeatedly with no consequences, this would be sufficiency to cool an atom down indefinitely.

However, an atom is a quantum object and can neither absorb an arbitrary wavelength of light, nor hold on to the absorbed photon indefinitely. If we describe the atom with a simplistic two-state internal energy structure, the absorbed photon must correspond to an internal excitation of the atom and this excited energy state has a finite lifetime, τ . Note that we must red-shift the light in order to simultaneously increase the scattering rate for an atom moving towards the light and decrease the scattering rate for an atom moving away from the light. This aspect gives Doppler cooling its name. After a successful absorption of an on-resonance photon, the probability that the photon energy is re-emitted by the atom between time 0 and t is described by $P(t) = 1 - e^{-t/\tau}$. When this photon is re-emitted, it is spontaneously released in an arbitrary direction. Again conservation of momentum instructs us that this will result in translation velocity “kick” of the atom of magnitude $\hbar k/m$ in the opposing direction to the photon. While this necessary kick will result in a limit to the cooling efficacy, this resonant absorption of laser light followed by stochastic re-emission can provide appreciable cooling in the right atomic systems. For most atoms and ions, this *Doppler laser cooling limit* is on the order of a few hundred microkelvin. In addition, significant work has contributed towards general approaches to laser cooled molecules as well. This has already been achieved for several systems. [\[116\]](#), [\[117\]](#), [\[118\]](#)

But this idealized two-level energy state must be modified to account for the realities of electronic structure in atoms. For a relevantly detailed discussion, consider the electronic structure of calcium ion as shown in Figure [2.6](#). Ground state Ca^+ has nineteen electrons, with three filled (*closed*) shells of electrons with one electron in the final 4s shell, which can be spin up or down. This gives us effective shielding of the eighteen electrons in lower orbits; thus, we can model the one lone electron as participating in a “pseudo-hydrogen” atomic structure (in which selection rules “pseudo-apply.”) The excitation of interest is moving this 4s electron to the p-orbital of Calcium with a ~ 397 nm photon. This photon energy excites the electron specifically to the $P_{1/2}$ state, which has a lifetime of 7.1 ns. However, we break from our two-level model as selection rules do allow decays into the $D_{3/2}$ state as well as the $S_{1/2}$ with a ratio of 1:12, respectively. This D-state decay back into the ground state is mostly forbidden with a lifetime of 1.2 s. Driving a single UV

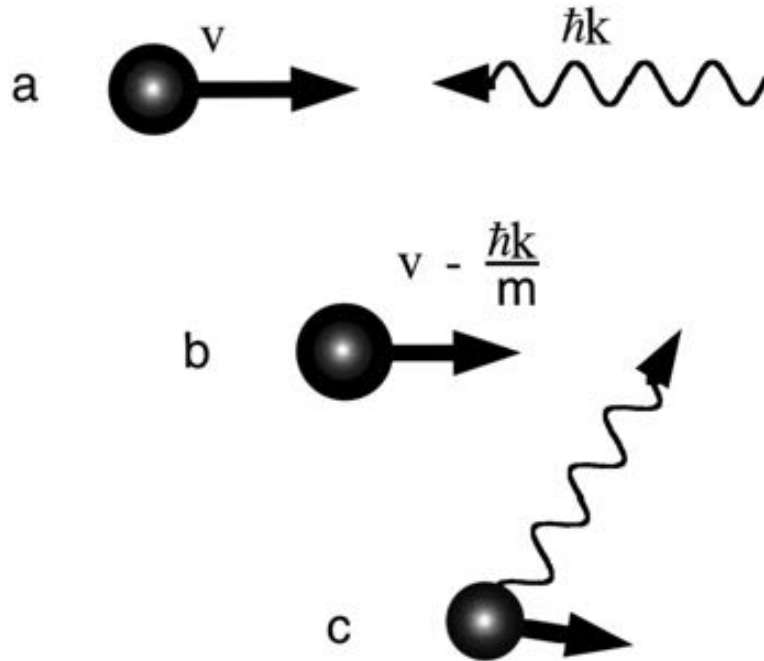


Figure 2.5: Simple schematic of laser cooling. a) A photon and atom propagate in opposite directions. If this photon is absorbed b) the atom is slowed. c) When the photon is remitted, a recoil will be experienced by the atom. [5]

laser would produce an optical pumping into this D-state and render the laser cooling ineffective. However, an ~ 866 nm laser can re-pump the trapped ions into the $P_{1/2}$ state and avoid losing ions from the cooling cycle. A careful examination of dipole selection rules for this system will reveal that this still would produce optical pumping into the $\pm 3/2$ D-states by electron dipole selection rules. However with the presence of a magnetic field *perpendicular* to the polarization of the pumping lasers we can re-pump these $\pm 3/2$ states. A sufficient magnetic field provides a quantization axis for the angular momentum in the direction of the magnetic field and leaves the angular momentum of the Ca^+ ill-defined in the two perpendicular directions. In this case m_J is not a good quantum number on the axis of the laser's polarization and we can address all the $D_{3/2}$ states and pump them into the $P_{1/2}$ state. Note that even just earth's magnetic field (~ 50 mT) is enough to mix the states, but the laser cooling efficiency can be further optimized with the addition of an external magnetic field. We do this in our system with a magnetic coil that provides a local

magnetic field along the axis of the Stark decelerator, perpendicular to the axial direction of the trap. The cooling beams propagate along the axial direction of the trap.

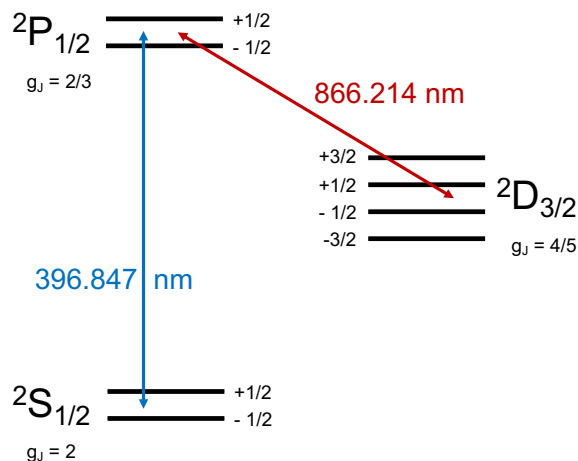


Figure 2.6: The energy structure of the Calcium ion. Two lasers drive laser cooling, with a primary driver at 397 nm and a re-pump laser at 866 nm.

Since our ions are usually loaded at very high energies, as we usually drop the trap RF to effectively *evaporatively cool* the trap, effectively bringing the ions within reach of a decent redshift of our UV laser (~ 70 MHz with a laser linewidth of ~ 10 MHz). The laser frequency can be then moved closer to a redshift of (~ 40 MHz) for the reaction. The detuning is intimately related to the saturation of the cooling transition, the relative populations in different states, the Doppler cooling temperature limit and the damping force felt by the ion. These parameters are not directly relevant to the reactions studied in this thesis and will not be explored in depth here. However, for the interested reader, there are excellent resources that go into these equations and derivations. [\[1\]](#), [\[75\]](#), [\[115\]](#), [\[119\]](#), [\[120\]](#)

While atomic systems are much simpler candidates for laser cooling than molecules, the last few years have seen significant advances in cooling molecules. [\[118\]](#), [\[121\]](#), [\[122\]](#), [\[117\]](#) This has been pursued by bonding a functional group to a commonly laser-cooled atom or ion. If you choose a molecule with one lone electron not participating in bonding (i.e. a radical) you can, in principle, still maintain a relatively simple laser cooling cycle. Leading work has been with M-O-R (metal,

oxygen, and “rest of the molecule”) molecules. However, this is still technically very challenging as molecules necessarily complicate the orbital structure and the rigor of the selection rules (and thus the number of re-pump lasers needed). These advances are currently in a nascent phase, but the next decade may see experiments impacted by this new technique as well as a drastic expansion of interest in molecular spectroscopy. Ultracold molecules are expected to have significant implications in many branches of physics, from precision measurements to quantum information to ultracold chemistry. In the same way that laser cooling of atoms revolutionized the study of atomic physics, these advances can open molecular physics experiments to colder temperatures and open new avenues of investigation.

Within our system, laser cooling plays a foundational role to cool Ca^+ directly in our trap, indirectly damping the motion of the co-trapped “dark” ions. This cold environment of the trap is integral to energetic assumptions we can make about the barrierless reactions that occur in the trap. Since future directions of this experiment intend to study reactions as a function of reaction energy, the aforementioned physics of RF trapping and Doppler laser cooling have been employed to numerically model the energy and dynamics of the trap. The next subsection concerns these simulations.

2.1.5 Simulations of Ion Dynamics

I supervised a former group member, Andrés Villani Dávila, on a project to modify an existing molecular dynamics simulation^[123] for use in our experiment. He did extraordinary work that studied the impacts of the aforementioned mass-to-charge ratio, m/z , on the crystalline structure of Coulomb crystals of our trapping parameters, particularly looking at the impacts of different ion masses on the Calcium ion temperature distribution. The interested reader is directed to his undergraduate honors thesis.^[6] I will present an overview here to demonstrate that these simulations reproduce the dynamics already discussed in this section, as well calculate the velocities and energies of the ions in our trap. These results are critical for accurately modeling the collisional energies with future reactions with Stark decelerated beams. I will discuss the capabilities of these

simulations here, and the calculated results will be discussed in calculations for energy-resolved measurements discussed in section [8.3.1](#).

These simulations use a molecular dynamics simulation package called LAMMPS. [\[124\]](#) This package is an extremely versatile open-source code developed by Sandia National Labs. Recently, a Python/Matlab wrapper for this amazing, but somewhat esoteric, bundle of code was developed by Bentine et al. [\[123\]](#) While the work done was already quite advanced for utilizing features of LAMMPS to simulate laser-cooled ions in an RF trap, there were a few features in need of more work. One of these had to do with the laser cooling, which Dávila re-developed to cool down to only the Doppler limit (previously it acted as an idealized damping force that could reach 0 K in the absence of micromotion, rather than acting like a stochastic force). The second development he added was the processing of the simulation output to mimic our imaging system in order to allow direct comparison between experiment and simulations. He then investigated the feasibility of an energy-resolved study that would look at a charge-transfer reaction as a function of the temperature of the ions; this focused on the relation of ion energies on numerous factors in our trap including the number of *parasitic* or non-reactive, non-laser-cooled ions. [\[6\]](#) Unfortunately, he demonstrated that this proposed experiment was below the signal-to-noise of our setup. However, these simulations have since allowed us to use his simulations for new applications in both understanding and modeling ion dynamics in our trap.

The first thing the simulations allowed us to visualize is the actual motions within an RF cycle. Figure [2.7](#) shows the position of ions in three frames at three different points within one RF cycle. The full video of 20 points along one RF cycle is quite striking, animating the motions of the ions as they oscillate along the x and y directions out of phase. It is worth noting here that the micromotion is not a rotation, but that of a “flapping” or “breathing.” This is perhaps unsurprising, since the RF is indeed flapping between the two orientations, as discussed prior. However, many intuitive pictures of RF trapping present the idea of a “rotating saddle” to envision how trapping occurs and why the frequency of the oscillating RF voltage matters. This picture is perhaps useful for seeing why the secular motion of the ions is a rotation (another result from these simulations),

but within an RF cycle they do not rotate.

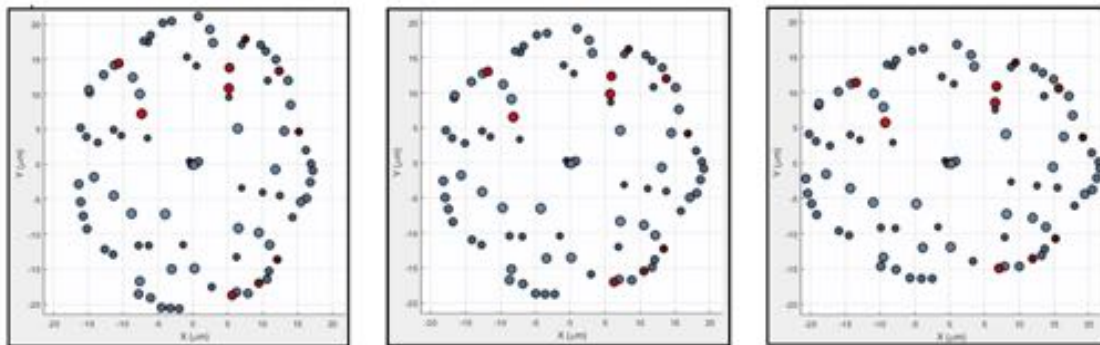


Figure 2.7: Plotted positions of a Coulomb crystal within one rf cycle, viewed on end.[\[6\]](#)

A second result reproduced by these simulations is the effect of laser cooling on the long-range order of ions in the trap. These simulations beautifully reproduced the energies and positions of a hot cloud of ions, and their simultaneous ordering into a Coulomb crystal as a result of simulated laser cooling. This is depicted in Figure [2.8](#). This simulation included 800 Ca^+ ions (blue) and 800 m/z 35 ions (red). Strikingly, the ions form ordered rings along which the ions sit. A qualitative observation over many simulations with a variety of constituents indicates an inverse relationship between ring clarity with temperature. This is perhaps unsurprising if the lowest energy configuration is tightly defined orbits around the center of the trap, as appears to be the case. It should be noted that we are by no means the first group to study these structures computationally and there are many interesting experimental and computation studies of Coulomb crystals that are worth reading. [\[125\]](#), [\[61\]](#), [\[126\]](#), [\[127\]](#), [\[128\]](#), [\[58\]](#), [\[76\]](#), [\[129\]](#)

The most experimentally relevant result of these simulations was the calculation of secular (v_{RMS}) and instantaneous velocities from these numerical simulations. Figure [2.9](#) shows the positions and secular velocities for the different groups of ions in bi-component crystals. In addition, we are able to look at the micromotion energies for any of the ions and can calculate it for a variety of trap constituents, and trapping parameters. These numerical solutions allow us to calculate center-of-mass energies for reaction. Particularly in future experiments, where a neutral beam may be decelerated down to 20 m/s, our neutral reactant will have velocities less than, or on the order

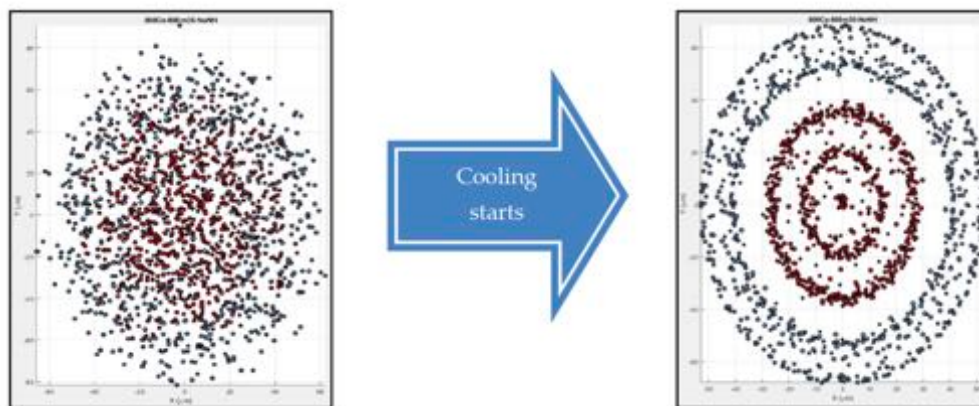


Figure 2.8: End-on view of ion positions in a Coulomb crystal before (left) and after (right) laser cooling is applied. This simulation included 800 Ca^+ ions (blue) and 800 m/z 35 ions (red).[\[6\]](#)

of, the instantaneous velocities of the ions with which they collide. If we indeed want to fully characterize how our reaction kinetics and dynamics depends on the center of mass velocity of the reaction, the ions velocity distribution in the trap will be critical to an accurate and precise analysis.

However, these simulations are not necessary for every estimate of the collisional energy. For experiments in which neutral reactant gas is leaked in at room temperature, the velocities of the neutral reactants are far greater than that of the ions (thermal N_2 is centered at ~ 500 m/s, for example.) For this reason, the center-of-mass collision energy for these reactions is dominated by the neutral gas energy. In the limit that the ions energy is much smaller than that of the neutral molecule, the collisional energy can be approximated without consulting numerical solutions. A general treatment of collisional energy will be discussed in Section [3.1.3](#).

2.2 Experimental Apparatus

This section will briefly walk through the prominent pieces of the experimental apparatus shown in Figure [2.10](#). I will walk through a typical reaction procedure and discuss each important aspect of the experiment as it arrives in the chronology of an experimental run. This will provide an overview of a normal data run and the moving (and non-moving) pieces that are critical to a

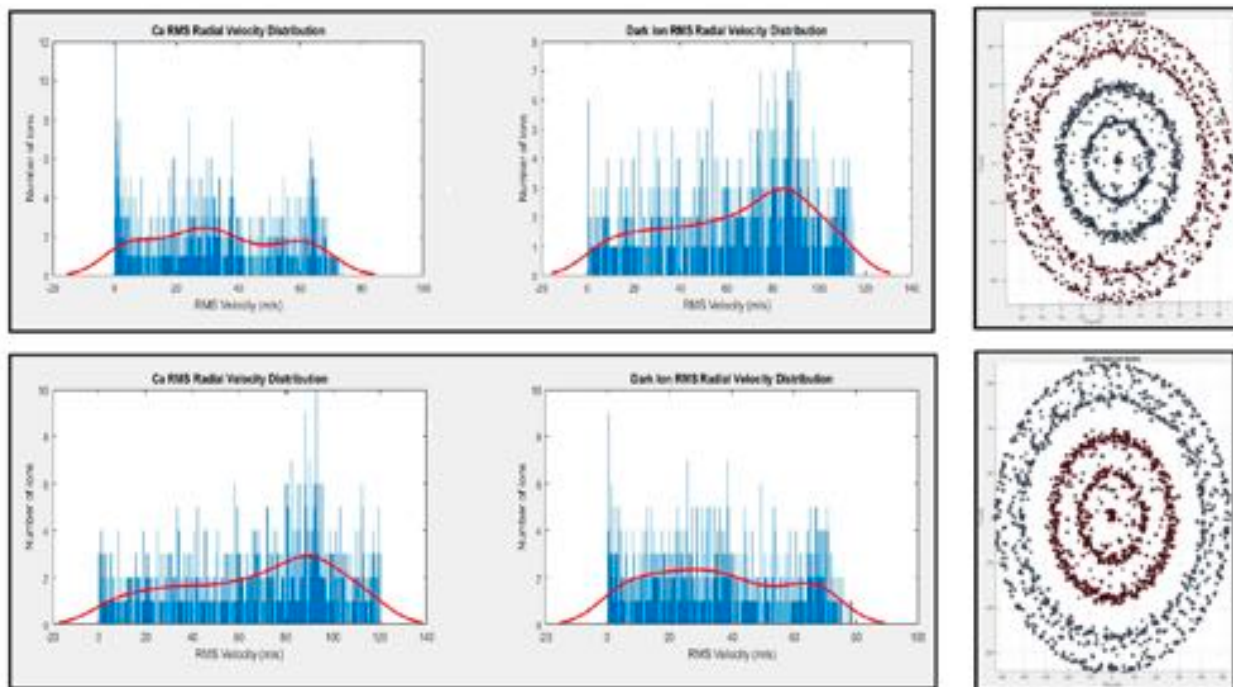


Figure 2.9: Distributions of secular (v_{RMS}) velocities of calcium (left) and dark ion (middle), with a plot of positions from an axial view (right). The top row is for the case with 800 Calcium ions (blue) and 800 m/z 45 dark ion (red). The second row also has equal numbers (800 each) of Calcium (blue) and m/z 35 dark ion (red).[\[6\]](#)

successful reaction study.

Figure [2.10](#) shows the experimental apparatus used for gas phase reactions of trapped ions with room temperature molecules. This entire apparatus is in ultra high vacuum (UHV), typically sitting on the order of $\sim 10^{-10}$ Torr.

2.2.1 Loading the trap

Ions are loaded into the trap by ionizing neutral molecules with pulsed ultraviolet (UV) lasers. In the case of Ca^+ , the atoms are loaded by a diffuse source of calcium, labeled as the calcium oven in Figure [2.10](#). This is comprised of a steel tube filled with solid calcium that is sublimed through a ~ 2 mm hole when current is sent through this tube. A shutter is remotely controlled such that this source has a line of sight to the trap only when we want to load calcium. A skimmer

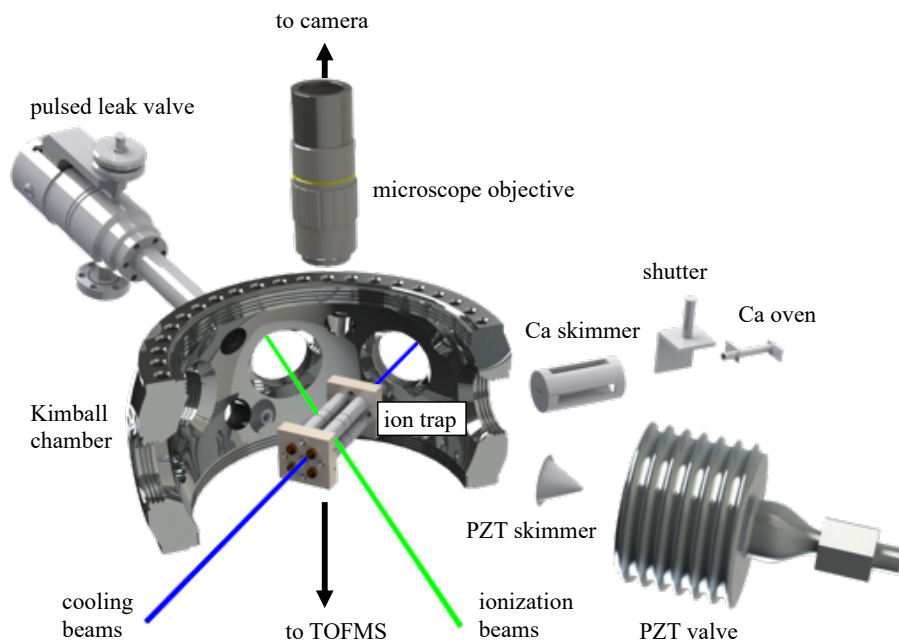


Figure 2.10: Schematic diagram of the LIT-TOFMS used for ion-neutral reactions. Schematic reproduced from Schmid (2020). [7]

aids in the directionality of this source, to allow it to cross paths with the ionization laser in the center of the trap. The ionization laser is a tripled Nd:YAG (355 nm) with a 10 Hz repetition rate of 7 mJ/pulse.

While reactions can be done with the Ca^+ ions themselves, all of the reactions discussed in this thesis involve non-calcium “dark” ions co-loaded into the crystal. Generally, this is done by loading a molecule precursor seeded into an atomic gas at a few percent. This diluted gas backs the piezoelectric (PZT) valve that pulses gas into the chamber in short ($\sim 100 \mu\text{s}$) pulses at high (very roughly, 10^{12} - 10^{13}cm^{-3}) densities. The details of this valve design and operation have been described in detail in Travis Briles’s thesis. [130] We also use a PZT valve for the source of our Stark decelerated molecular beam; the exact properties of the valve and produced beam are more relevant to favorable production of a decelerated beam so more details on this source included in that discussion (Chapter 7). For this context, the relevant details are that the produced beam is

internally cold to allow for efficient resonant ionization processes and is skimmed to provide a high quality beam and good differential pumping between the source chamber and the main chamber. This valve is operated at 10 Hz, producing a molecular beam that can be easily synchronized with a laser to ionize the molecular precursor.

The details of the laser and precursor depends on the reaction studied. One of these is acetylene, which have known techniques by which they can effectively ionized. This technique is referred to as REMPI (resonantly enhanced multiphoton ionization). It refers to a scheme where an atom or molecule absorbs light that resonantly excites it to an electronically (in the case of molecules, usually also vibrationally) excited intermediate state, from which it can be ionized. Usually the excited intermediate state is a metastable (long-lived) state. In the case of molecules, the final state is usually in the electronic ground but vibrationally excited state as shown in Figure [2.11](#). Not that here the details of initial and final states are chosen for pedagogical purposes. The exact initial, intermediate and final states of the process are flexible, restricted only by selection rules and the details of the atom/molecule in question. Also note that this figure includes internal structure (symbolically shown by tiers in a Morse-like vibrational potential) for all the states, which would not be relevant to atoms.

The notation for REMPI indicates the number of photons required and whether one or two colors of light is required. For example, a (2+1) REMPI transition is all one frequency, with two photons required to reach the excited intermediate and one additional photon to ionize. If the process requires two difference frequencies of light, it would be denoted (2+1'). (1+1), then, indicates one photon is required for each and both are of the same frequency of light. The ionization light is often single-photon, but this is not required. In the case of multiple photons required to reach the excited intermediate, this is said to proceed through *virtual states*. The important point here is that those photons must be absorbed simultaneously. Thus, the cross-section of a (3+1) process be less efficient than a (2+1) or (1+1) process, assuming all other things are equal. "All other things" are usually *not* equal though, and the best process for any given molecule also depends on the cross-section of the transitions involved, the power of the laser you are using, the accessibility

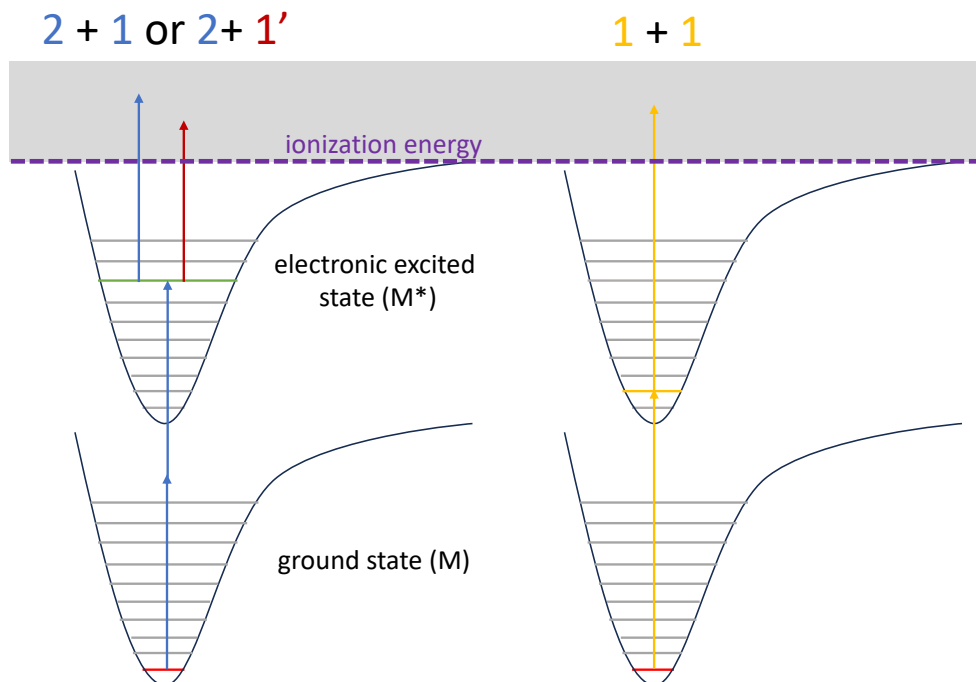


Figure 2.11: Three common schemes for REMPI ionization of a molecule. Molecular excited states are indicated by Morse-like potentials; periodic lines symbolically indicate internal (ro-vibrational) states. In (2+1) REMPI (**left**), the first excitation requires two photons to bring the neutral molecule to an excited intermediate state. The ionization occurs with one photon of the same color, depicted here as exceeding the threshold for ionization indicated by the purple line. In (2 + 1'), the ionization photon is a different color. In (1+1) REMPI (**right**), the initial excitation does not proceed through a virtual state, but rather is directly excited by one photon to an excited state. In this schematic, one photon of the same color ionizes the molecule. Not that the inferred vibrational structure in this diagram will not be relevant for REMPI of atoms, which must solely proceed through resonant excitation of electronic states.

of that wavelength, and other practical considerations.

While REMPI does not always leave an ion in its ground electronic and vibrational states, this is not a barrier for our reaction applications. In the case of ion-neutral reactions, our experimental time scales are much longer than the lifetimes of any electronic and vibrational states (assuming dipolar ions, as is the case for work in this thesis.) The time required to load our reactant ions and calcium is usually sufficiently long (40 s) that we can be confident our ions are fully relaxed by the time we start a reaction. We have used REMPI for many ions, including $C_2H_2^+$, ND_3^+ , O_2^+ , and Ar^+ . Of these, C_2H_2 and ND_3 pertain to these thesis for reaction studies and decelerator output

characterization, respectively. In the case of ND_3 , a REMPI transition was deliberately chosen to detect relative populations of a specific initial state of deuterated ammonia, as will be discussed in more detail in section [7.1.4](#). The REMPI process for acetylene, on the other hand, was chosen for its high cross-section with cold molecules in a molecular beam, and particularly for its accessibility with the dye laser wavelengths accessible to us.

Both isotopologues of acetylene (C_2H_2 and C_2D_2) have multiple available (1+1) REMPI processes. [\[131\]](#) For the reaction of $\text{C}_2\text{H}_2^+ + \text{CH}_3\text{CN}$ (Chapter [6](#)), we excited the acetylene into the $v'_3 = 4$ (trans-bending vibration) of the lowest lying electronic state. This is achieved with 216 nm and 218 nm light for C_2H_2^+ and C_2D_2^+ , respectively. Overall, such resonant processes not only provide higher cross-sections for ionization, but also better “cleanliness” of the outcome ion composition. Non-resonant multiphoton ionization usually has less predictable distribution of the energy into rovibrational modes and causing fragmentation of the molecule into multiple products.

However, sometimes non-resonant ionization is necessary or preferred. In the case of the ion CCl^+ , we used 216 nm light to break apart tetrachloroethylene (C_2Cl_4) seeded in helium. In this case, two or more photons are required to ionize and necessarily fragment the molecule into a CCl^+ fragment. These photons must arrive simultaneously and thus this process is usually not as efficient as most REMPI processes (especially when the product is not purely the sought-after ion). The fragmentation due to non-resonant light absorption is also less predictable and so ionization schemes like that used to make CCl^+ in our group are found through trial and error. This process was found to be most effective in argon (Ar), although we did still see CCl^+ produced in helium (He) and nitrogen (N_2). Argon was also ionized in this process, probably facilitating the formation of CCl^+ with charge transfer reaction with the precursor and subsequent unimolecular fragmentation. However, we do believe CCl^+ was also being directly ionized, as we were able to load CCl^+ when the precursor was seeded in helium, (which has ionization potential of 24.6 eV). However, using Ar loads Ar^+ ions in the trap as well, which can be difficult to clean out since they overlap in mass with Ca^+ ; for this reason, our published data was ultimately taken with CCl^+ produced from (C_2Cl_4) seeded in helium. I will also note that we used chloroform CHCl_3 as a precursor

as well. We generally found that using chloroform with 216 nm light produced less ions overall, particularly of CCl^+ . As far as we are aware, our reaction studies may be the first example of CCl^+ produced with lasers. However, as mentioned prior, this causes fragmentation to multiple different ionic products, including Cl^+ , C_2^+ , CCl^+ , CCCl^+ . In the few other studies looking at CCl^+ , it was studied as a primary product from another reaction, [\[132\]](#), [\[133\]](#), [\[134\]](#) or produced from electron bombardment. [\[135\]](#) Altogether, the effective use of CCl^+ in our apparatus requires us to be able to select only the desired ions for reaction studies and can circumvent the problems of fragmentation. In addition, Chlorine comes in a natural abundance of $\sim 3:1$ of Chlorine-35 to Chlorine-37 such that filtering particular m/z ratios can allow isotope-specific reactions as well. The ion trap provides an excellent way to do this with the use of secular excitations.

2.2.2 Cleaning the trap

The RF driving electronics were developed by prior researchers in our lab. James Greenberg’s thesis is an excellent resource for details on the experimental realization of RF trap electronics. [\[1\]](#) One piece of these electronics that has seen a fundamental change during my time on this experiment is the secular excitation scheme. Excellent work by Schmidt et al. [\[8\]](#) demonstrated that a quadrupole excitation is far more effective in ejecting ions out of a linear Paul trap than a dipolar excitation and we switched to the quadrupolar excitation in response. In this section, I will briefly remind us what a secular excitation is, describe the differences in dipolar and quadrupolar excitations, as well as some commentary on the effect it had on our cleaning schemes.

In section [2.1.2](#), the derivation for a single ion secular frequency was presented. Recall that by equation [2.11](#) this frequency depended on the Mathieu parameters, and indirectly on the ratio of the mass to charge (m/z). This then allows the secular frequency to be used to mass-selectively excite and eject ions in the trap. This use of secular frequency has a historical place in ion trapping, typically used in the past as a rough detection of the contents of the trap. [\[127\]](#), [\[61\]](#), [\[136\]](#), [\[125\]](#) This was accomplished by “tickling” the ion with the secular frequency by exciting it (but not ejecting it from the trap). For a laser-cooled ion, this produces a change in fluorescence due to Doppler broadening.

By sweeping over a range of frequencies, peaks in fluorescence as a function of secular frequency can probe the contents of the ion trap – even for non-laser cooled ions. While this method lacks the number precision and high resolution of mass spectrometry, it is an inherent, non-destructive method in ion traps that allowed significant advances in the field prior to integration of mass spectrometry. Even today, some groups rely on the fluorescence of their ions, often in conjunction with simulations, to infer the contents of their ion traps in reaction studies. [58, 75, 68, 137, 138]

A representation of the different effects of these modulations on the pseudopotential and thus the ion are demonstrated in Figure 2.12. The dipolar excitation (also called “displacement driving”) was enacted by adding the secular frequency, $2\pi\omega_u$, directly on the four trapping rods. This effectively shakes the trap’s center at frequency $2\pi\omega_u$, hence the reference to it as a “dipolar” drive. The quadrupolar drive, or *parametric excitation* and is effectively a modulation in the trap depth caused by variations in the RF amplitude at $2\pi\omega_u$. Effectively, we do this by using an RF splitter/combiner to add our trapping frequency with our secular frequency. This creates a quadrupole-like oscillation of the trap depth.

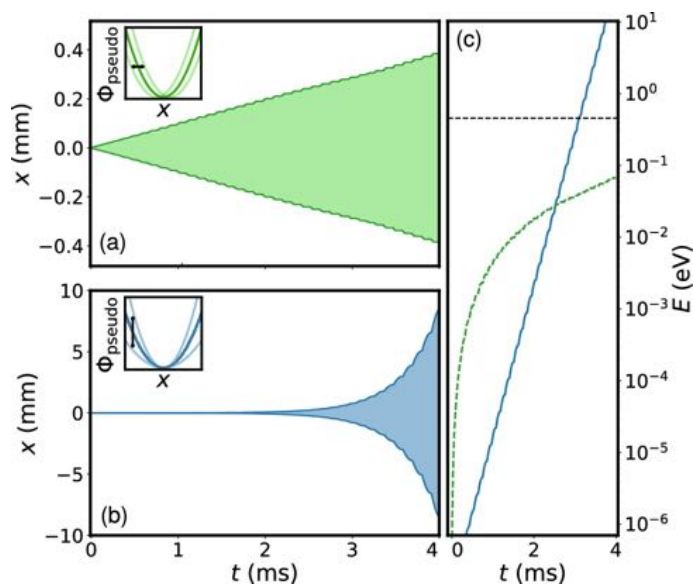


Figure 2.12: Ion trajectories under the influence of an a) oscillating linear electric field at the resonant secular frequency, and b) oscillating quadrupole electric field applied to the RF electrodes. Inset c) demonstrates the total energy of the ion on a logarithmic scale versus time, where the quadrupole field can be seen to be much more effective at ejecting an unwanted ion. [8]

Note that in either case these modulations of the electric fields are felt by all the ions but have a resonant effect for a particular m/z ratio. This resonance frequency is experimentally often slightly different than the frequency calculated by Equation [2.11](#) since that equation was derived for a lone ion in the trap. In reality, we usually excited parasitic ions out of the trap when the ions are in an uncrystallized cloud. In practice, the challenge of an effective use of secular excitation for cleaning often requires investigation of a range of the frequencies, amplitude and time that the secular frequency is enacted. In addition, these excitation often cause losses to neighboring masses if they are not efficient enough.

Empirically, we found the parametric excitation to be far more effective at ejecting the unwanted ions, particularly without ejecting other ions as well. Generally these types of excitations can tend to heat and eject other ions as well. This issue can be particularly problematic when the unwanted ions are quite close to the desired reactant's m/z (this can be particularly problematic when you want to remove $C_2H_3^+$ and leave $C_2H_2^+$, for example). The reason that the parametric excitation is more effective can be seen in Figure [2.13](#). This figure is taken from $t=2.54$ ms in Figure [2.12](#), where the two lines intersect. At this point it is easily seen that for using the excitation for the same amount of time and the same amount of energy gained by the ions, the excitation is much “sharper” for that of the parametric excitation. A potential explanation for this may be in Figure [2.12](#), where the displacement of the ion in the case of displacement driving is much more linear, verses the exponential change in displacement for parametric excitation. In this way, there is far more opportunity for the motion of the ion to couple with that of nearby ions (close in m/z) in the case of displacement driving. [\[8\]](#) Thus the quadrupolar excitation is more selective and thus more efficient in its ejection of only the target ions.

In summary, the use secular frequencies are crucial to effectively cleaning the trap. This upgraded parametric excitation scheme is particularly effective at cleaning our trap and significantly eases our efforts to work with very pure samples of reactant ions. As a result of these schemes, a typical experiment will have less than 10% of “contaminant” ion loaded, with an achievable goal of less than 5% of any one unwanted ion.

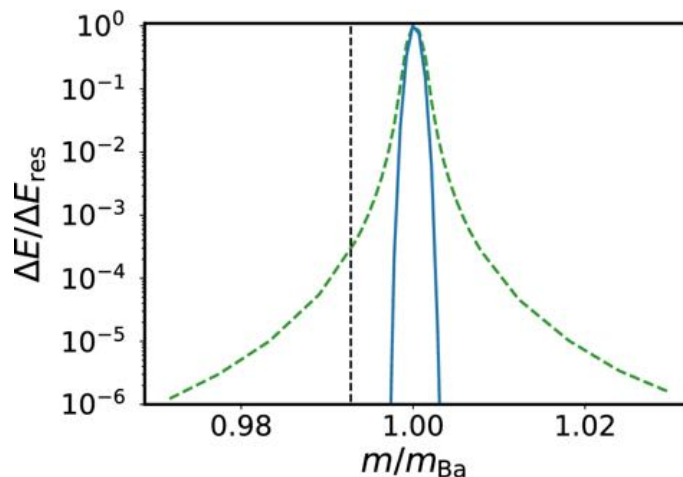


Figure 2.13: Mass dependence of the relative energy gain E/E_{res} using parametric excitation (blue solid line) compared to displacement driving (green dashed). [8]

2.2.3 Exposure to reactant gas

With a cold, clean trap our experiment is now ready to start a reaction. In the trap environment there are only very small partial pressures of trace gases, usually assumed to be atmospheric gases or water. In the case that we are concerned about our ions reacting with trace gases in the 10^{-10} Torr background pressure, we can let the trap sit and see how the contents change over time. Invariably some of our Ca^+ reacts with water to form CaOH^+ , a reliable process that always provides a steady metric to our background water pressure. Such a “background” reaction also allows us to verify that we do not have any trap losses that may be associated with imbalanced RF or inefficient cooling, which is seldom the case, but is good practice to verify.

Reactions take place with the introduction of $\sim 10^{-9}$ Torr of gas through a leak valve backed by a three-way valve, as shown in Figure 2.14. The variable leak valve is a standard UHV tool that is primarily comprised of steel plate with a sharp edge that cuts into a copper gasket when tightened. This can be very precisely loosened, as is an excellent tool for introducing small amounts of gas into the chamber. The leak rate is dependent only on the backing pressure of the leak valve and the amount by which it is opened. However, these are extremely difficult to open and close

reproducibly or quickly. For this reason, we open the valve at the beginning of an experiment and “pulse” the gas flow into the chamber with a three-way valve that backs the leak valve. This three-way valve can be remotely switched between a source of our neutral reactant gas (usually at approximately room pressure), or to a line pumped to rough vacuum (\sim mTorr). This allows for very fast (on the order of seconds) opening and closing, as well as excellent reproducibility in the gas pressure during each exposure to neutral gas. This reproducibility is extremely important, as this reduces the uncertainty in our reaction rate measurements.

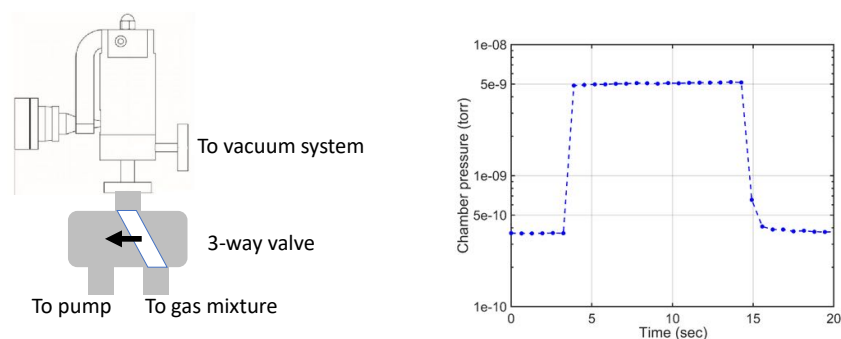


Figure 2.14: (Left) The *pulsed leak valve* configuration made of a variable leak valve backed by a three-way solenoid valve. (Right) Ion gauge data from the valve opening and closing which shows excellent stability in gas pressure over time. [\[1\]](#)

The gas introduced is usually a \sim 5-15% mixture of the reactant gas in Ar, He or N₂. In this thesis, the reactions reported involve either acetonitrile (CH₃CN) or benzene (C₆H₆). Both of these are liquids at room temperature. These mixtures were made by putting either liquid sample in a small steel reservoir and purifying the sample through several rounds of freezing, pumping, and thawing (FPT). These cycles gradually reduce the partial pressures in the lines of anything but the liquid sample. Then we backed the line with the correct amount of buffer gas such that the vapor pressure of the liquid sample made a \sim 5-15% mixture in the buffer gas. Historically, a mixture process was used to reduce issues due to chemical compatibility, such as o-rings swollen by

exposure to ammonia, causing leaks in the three-way valve. This “dilution is the solution” response to chemical incompatibility is less relevant now due to an upgrade in the three-way valve. The new valve installed is a Valcor Teflon 3-way Solenoid valve. The all-teflon body circumvents the issues of chemical compatibility, as teflon is fairly resilient to most gases. Nevertheless, mixing our gases can aid in accurate measurement of partial pressures of our neutral gases since the carrier gases we dilute in are generally better calibrated for measurement by ion gauges and this practice has continued. The resulting partial pressures generally require an exposure time of up to ~ 300 s for a full reaction curve. This is remarkably slow in the grand scheme of ion-neutral reactions and allows us to clearly differentiate between primary and secondary products. To probe the reaction products over time, we choose several time points between 0 s and this ~ 300 s to destructively measure the m/z of the ions in our time with time-of-flight mass spectrometry.

2.2.4 Mass spectrometry

Time-of-flight mass spectrometers (TOF-MS) operate on relatively basic principles. When ions experience an electric field, this produces a force on the ions. This leads to an acceleration that is dependent on the m/z ratio of the ion. If such accelerated ions are allowed a decent amount of “flight” time to spread out, their arrival at a detector is staggered and can be well-resolved. This is implemented in our experiment with a quenching of the RF fields and subsequent pulse of high voltage on the trapping rods. Below the trap is a grounded plate with a small hole for the ions to fly through, into a grounded flight tube that shields stray fields. While the principles are simple, high resolution is technically difficult, as you want to ensure that the arrival time is the same for all ions of a m/z regardless of its exact starting position. An excellent resource for understanding the technical realization of high resolution time of flight mass spectrometers is Wiley and McLaren’s seminal 1955 paper.[\[139\]](#)

Our the TOF-MS in our trap has a resolution of $m/\Delta m \geq 1100$. This metric can be interpreted as the largest mass that can still be resolved from the neighboring mass. Needless to say, this is more than enough to resolve neighboring masses (but alas, not nearly good enough to tell

the difference between C_3H_4^+ 40.0639 and Ca^+ , 40.078, as one reviewer to one of our papers pointed out). This high resolution is largely due to how cold the ions are, but our experiment in particular benefits from excellent RF and high voltage (HV) switches in the trapping electronics. The quick speeds by which the RF is damped, the short time by which the ions are allowed to expand, and the extremely fast hv pulse that sends the ions down the flight tube are all important influences on excellent resolution. The interested reader can learn more about this in Greenberg (2020).[\[1\]](#)

The ions flight down the flight tube and hit microchannel plates (MCP) that amplify this signal. These plates are designed to have many small holes (order few $\sim \mu\text{m}$). These plates are coated with a thin semiconductor layer. This material is designed to have a high efficiency of second electron emission when struck with a charged particle.[\[140\]](#), [\[141\]](#), [\[142\]](#) The plates are further biased by high differential voltages that accelerate these electrons as in Figure [2.15](#) to produce amplifying cascades of electronic signal. In our trap, these channels are actually at an angle ($\sim 10^\circ$) and we have two plates at alternating angles (*Chevron* configuration).

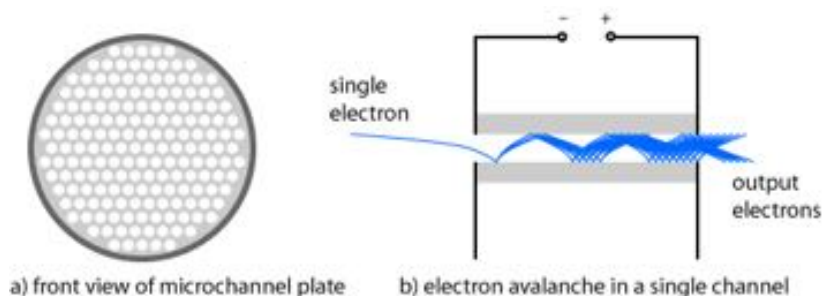


Figure 2.15: a) A graphic rendering of the holes in a microchannel plate, in which signal can be amplified, as shown in b).[\[9\]](#)

The resulting electronic signal can be read out on an oscilloscope. We split our output signal and display it two separate channels of a very fast (1 GHz) oscilloscope, where one channel has vertical resolution optimized for the Ca^+ signal, and the other channel is optimized to record down to single ion signals. In this way, we can accurately count 1000s of ions and single ions simultaneously. Example mass spectra for “zoomed out” and “zoomed in” traces can be seen in Figure [2.16](#). For

reference, the top left figure is showing roughly 200 C_2H_2^+ ions and 800 Ca^+ ions. In the bottom right, one can view ~ 5 ions at the m/z 41 channel, in between the larger m/z 40 Ca^+ and m/z 42 ($\text{C}_2\text{H}_3\text{NH}^+$) peaks.

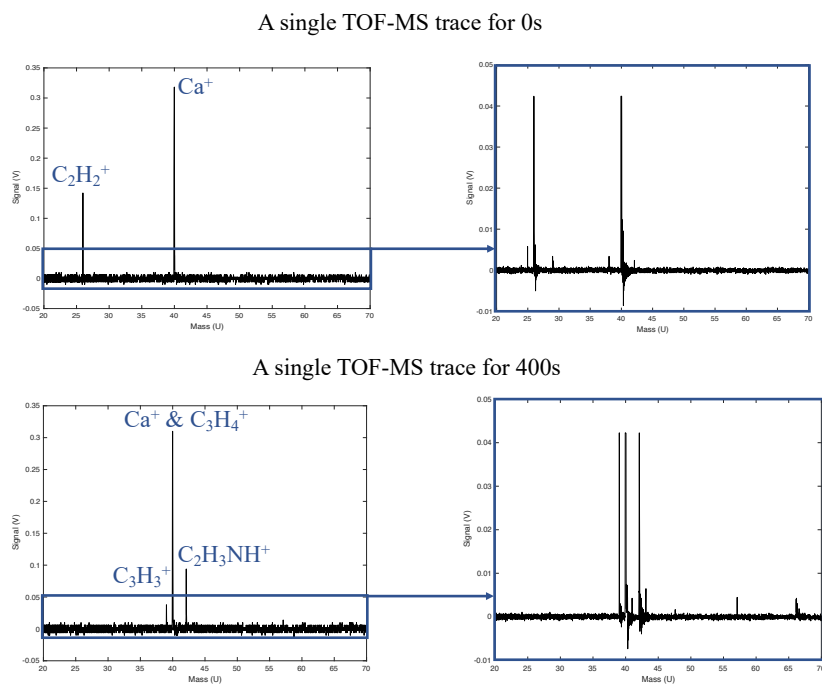


Figure 2.16: Sample TOFMS data from the $\text{C}_2\text{H}_2^+ + \text{CH}_3\text{CN}$ reaction. On the top are mass spectra from the loading of ions. Below are after 400s of exposure to CH_3CN . The left traces are zoomed out, while the right shows a “zoomed in” trace recorded on a second channel of our oscilloscope.

2.2.5 Full ensemble

This full system is automated with Labview-directed drivers that were well described in Greenberg (2020).^[1] The timing triggers for lasers, shutters, valves, and ejection of ions are all produced by a digital input/out (DIO) board. Further, the software allows us to randomize a large set of sequences with different amounts of neutral reactant time preceding the HV pulse that sends the ions to the TOF-MS. Thus, we can randomly scan over multiple reaction times, taking high statistics of mass spectra at different reaction times. A typical experiment will include ~ 10 runs of 5-6 different time points, chosen to show well-distributed points along the reaction curve. Ideally,

we react until a bit after the depletion of the reactant ion. This is the experimental procedure used for the reactions discussed in Chapters [4](#), [5](#), and [6](#).

The environment in which these reactions take place is quite interesting: as we saw, the ions are quite translationally cold. Since we can sit for seconds after ionization, we ensure vibrational relaxation. Exposure to black-body radiation of the room temperature chamber will result in a thermal rotational distribution. Our neutral molecules are translationally and rotationally at room temperature but vibrationally and electronically cold. All these degrees of freedom have varied degrees of influence over the course of an ion-neutral reaction. To understand how these energy states affect the interactions between our ions and neutrals, as well as have a theory comparison for reaction rates in our environment, we must turn to theoretical methods.

Chapter 3

Theoretical tools for calculating ion-neutral gas-phase kinetics and dynamics

“Molecules are smarter than us: they solve the Schödinger equation exactly.”

–Roald Hoffman, Georgiana F. Michl Lecture Series at CU Boulder, March 12, 2018

This chapter will review kinetic rate theory from a historical perspective, with an emphasis on capture theories. This will provide context for a detailed discussion of the kinetic rate theories necessary to model the class of reactions investigated in our apparatus. These theories allow comparison of our experimental results to theory and provide insight complementary to the experimental investigations. This will frame a discussion of the thermodynamics of our room temperature neutral gas reactions and a proper derivation of our center of mass energies or “temperature” of the reactions discussed in Chapters [4](#), [5](#), and [6](#). Then this chapter will review potential energy surfaces and transition state theory, exploring how they can further illuminate the actual dynamics of a reaction complex. This will include a study into modern methods of calculating molecular bond energies, from the early formations of molecular orbital theory and Hartree-Fock *ab initio* methods to modern methods such as Density Functional Theory (DFT) and post-Hartree Fock methods.

3.1 An Introduction to Kinetic Rate Theory

Efforts to fully understand the dependence of chemical reactions on all factors in general, but energy and temperature in particular, has long been a pursuit of physical chemistry. The historical evolution of classic kinetic and dynamic rate theories still heavily influence the treatment of modern ion-neutral reactions. A brief overview of this history will set the stage for our analytical treatment of ion-neutral reactions, including the calculation of reaction rates.

3.1.1 Introduction to reaction rate theories

The impacts of temperature on reaction kinetics was first studied quantitatively in 1850 by Ludwig Wilhelmy [143] and in the following decades many researchers proposed an analytical form for this dependence, including particularly influential work by Jacobus Henricus van't Hoff. [144, 145] Most famously, Nobel Laureate Svante Arrhenius pioneered the equation that most see in their high school chemistry textbooks, aptly referred to as the *Arrhenius equation*. This equation relates the rate of reaction k with the magnitude of the *activation energy* or height of an energetic barrier to reaction E_a to the temperature T :

$$k = Ae^{E_a/RT} \quad (3.1)$$

where R is the universal gas constant and A is an experimentally-found prefactor. [146, 145] This simple and empirical dependence of k on $\ln(T)$ was rather controversial in its time – particularly due to the narrow temperature range that was experimentally available – but was generally accepted by the community by 1910. [145, 147] This empirical prefactor A was better understood in the community after parallel efforts by Henry Eyring, Meredith Gwynne Evans and Michael Polanyi in 1935 established equations of similar form to Equation 3.1 that defined and motivated these terms from statistical mechanics arguments. [147, 148, 149, 150] This is considered the beginning of what we call *transition state theory*, which looks at the equilibrium rate constant in terms of the thermodynamics and statistical mechanics of a reaction complex. These approaches are still used, decades later. Transition state theory has some additional relevance to our calculation

understanding potential energy surfaces in reactions and will be discussed in more depth in Section [3.2.4](#)

However, we must first appreciate that the ion-neutral reaction systems of relevance to this dissertation are exothermic, having energetic barriers to the formation of products that are submerged. The traditional Arrhenius picture of a limiting activation barrier does not directly apply and the reaction rate is more often determined by the rate of the formation of the initial reaction complex. Thus, the calculation of an ion-neutral reaction rate is more concerned with the *kinetic theory* or collisional theory of the reaction. A kinetic approach to defining Arrhenius's prefactor A was pursued independently by Trautz[\[151\]](#) and Lewis[\[152\]](#) in the 1910s. This work built off of a simple collision model pioneered by Langevin[\[38\]](#) and considered the collision rate of two bodies (A and B) modeled as hard spheres with number density N , radius r and mass m . A calculation for the number of collisions per unit time and unit volume yields:

$$Z_{AB} = N_A N_B (r_A + r_B)^2 \sqrt{8\pi k_b T} \frac{m_A + m_B}{m_A m_B} \quad (3.2)$$

where k_b is the Boltzmann constant and T is temperature in Kelvin.[\[147, 149\]](#) This equation had only limited success in predicting warm neutral-neutral reaction rates (an empirical *steric factor* was necessary to accommodate for significant deviations in the value) and it completely ignored long-range interactions in the molecules. However, this was the first example of a reaction rate model based on the rate of reactant collisions.

As experimental investigations progressed in the first half of the 20th century, it became clear that long-range forces created significant deviations from calculated reaction rates. The first calculation of the classic collision cross section accounting for long-range forces was presented by Eyring et al. in 1936 for the system of $\text{H}_2^+ + \text{H}_2$ [\[153\]](#). Beginning in the 1950s, Eyring's solution was generalized with heavy inspiration from Langevin's 1905 work to accommodate for the polarizability of the neutral atom. This led to a series of works to consider the effects of dipole moments and higher order potentials on this rate constant. These reactions comprise *capture rate theories*, still

incredibly useful models for ion-neutral gas-phase reactions.

3.1.2 Capture models for calculating reaction rates

Capture models are united by the assumption that once a reaction complex is formed the reaction will proceed with unit probability. Thus the probability of “capture” or reaction complex formation determines the reaction rate. These methods all account for long-range interactions due to Coulomb forces. We will discuss a few notable models, starting with the simplest and chronologically first model: the *pure polarization* or *Langevin* theory. In this section, I will provide a derivation and discussion of the first capture model and generalize the approach to higher-order long-range forces. Much of this formulation follows the derivations found in Chapter 3 of a book edited by Bowers (1979),[\[10\]](#) as well as a few other excellent resources.[\[95\]](#), [\[154\]](#), [\[37\]](#) The interested reader is directed to these resources for a more exhaustive discussion of the historical details of, and numerous variations on, this collection of models.

We approach the system of an ionic reactant and neutral, polarizable reactant. This derivation begins by assuming that both of the reactants can be modeled as point charges. The long-range force felt by the neutral with polarization α at distance r is then described by:

$$V(r) = - \int_r^\infty F(r)dr = - \int_r^\infty \frac{4\pi\epsilon_0\alpha q^2}{r^5}dr = - \frac{\alpha q^2}{8\pi\epsilon_0 r^4} \quad (3.3)$$

where q is the charge of the ion. Thus we can describe the relative energy of the system, E_r at finite r as the sum:

$$E_r = \frac{1}{2}\mu v^2 = E_{kin}(r) + V(r) \quad (3.4)$$

where μ is the reduced mass of the system v is the relative velocities.

This kinetic energy term can be broken into two components: the $E_{rot}(r)$ describing the energy of relative rotation of the particles, and $E_{trans}(r)$, the translational energy along the line of centers. This rotational term can be considered in terms of classical orbiting angular momentum $l = \mu v b$ where b is the impact parameter, as shown in Figure [3.1a](#). Like the Coulomb potential,

this rotational term also has a dependence on r :

$$E_{rot}(r) = \frac{l^2}{2\mu r^2} = \frac{\mu v^2 b^2}{2r^2} \quad (3.5)$$

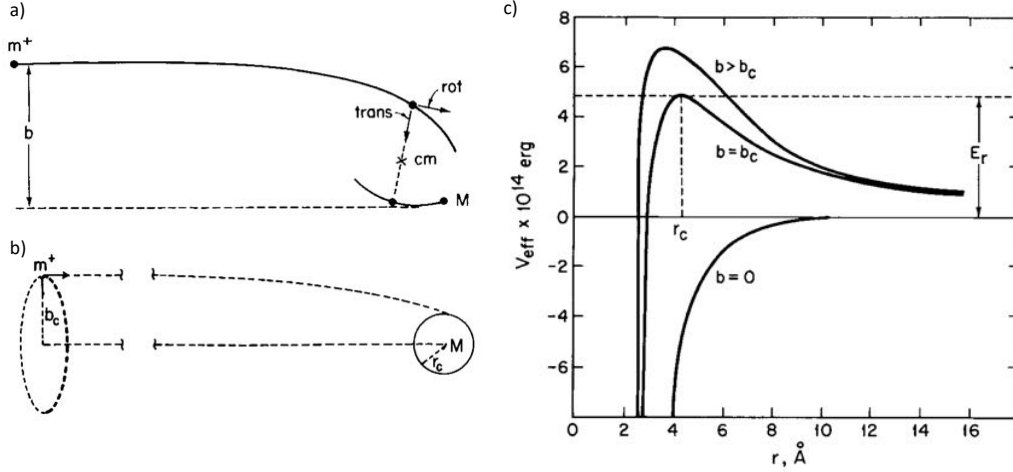


Figure 3.1: a) Schematic for an ion-molecule collision. b) capture cross section of ion-molecule collisions. c) Plot of the effective potential vs. distance from Equation 3.6. Figures from Su & Bowers (1979).[\[10\]](#)

The effective potential of the system is the sum of the Coulomb potential $V(r)$ and the rotational energy term E_{rot} , combining Equations 3.3 and 3.5:

$$V_{eff}(r) = -\frac{q^2\alpha}{8\pi\epsilon_0 r^4} + \frac{\mu v^2 b^2}{2r^2} \quad (3.6)$$

We see now we have competing terms. Below a particular value of r the so-called *centrifugal barrier* will dominate, while at larger distances the induced dipole will dominate. If the complex has enough energy to surmount the centrifugal barrier, capture will occur. This turning point can be associated with a critical impact parameter b_c , as shown in Figure 3.1c. We find this turning point by setting $\partial V_{eff}(r)/\partial(r) = 0$, or where $E_r = V_{eff}(r)$.

$$\frac{\partial V_{eff}(r)}{\partial r} = -\frac{l^2}{\mu r^3} + \frac{q^2\alpha}{2\pi\epsilon_0 r^5} \quad (3.7)$$

$$V_{eff}(r) = \frac{l^2}{2\mu r^2} - \frac{q^2\alpha}{8\pi r^4} = E_r \quad (3.8)$$

These equations yield parameters:

$$r_c = \frac{q}{b_c} \sqrt{\frac{\alpha}{2\pi\epsilon_0 E_r}} \quad (3.9)$$

and

$$b_c = \sqrt[4]{\frac{q^2\alpha}{2\pi E_r}} \quad (3.10)$$

We can re-write this impact parameter in terms of a *cross section* σ as shown schematically in Figure [3.1c](#).

$$\sigma_c(v) = \pi b_c^2 = \pi q \sqrt{\alpha/2\pi\epsilon_0 E_r} \quad (3.11)$$

This cross section can be interpreted as the likelihood of a collision per unit area around the ion, given a neutral reactant of energy E_r . If we multiply this by the speed of neutral reactant we get the reaction rate constant:

$$k_L = v\sigma_c = v\pi q \sqrt{\frac{\alpha}{2\pi\epsilon_0 E_r}} = q \sqrt{\frac{\pi\alpha}{\epsilon_0\mu}} \quad (3.12)$$

a velocity-independent reaction constant in SI units of $[\frac{m^3}{s}]$. This is known as the *Langevin rate constant*. This can be related to a reaction rate when the density of the reactants are known. Note that several assumptions were made here, including that particles are point charges. The finite size of the particles will introduce an inverse dependence on v^2 at high energies (“high energy” meaning a few electron volts or so, much higher than our system).[\[10\]](#) On the extremely cold end, we have to consider quantization of the momentum, as well as short range effects such as tunneling and scattering resonances. However, for our cold (~ 10 - 150 K) ion-neutral studies, these regimes are not applicable. For many systems, the Langevin rate constant has been a successful method for predicting most systems involving ions with non-polar, but polarizable, molecules.

Nevertheless, this is not the full story for many systems. In particular, one can easily see that a permanent dipole moment in the body-fixed frame can introduce a much larger long-range effect. A dipole will have an additional interaction with the ion governed by the term $q\mu_D \cos(\theta)/4\pi\epsilon_0 r^2$, where θ is the angle between the dipole and the line of centers of the collision and μ_D is the neutral molecule dipole moment. However, the velocity- and time-dependent interaction of the dipole with the charge can be treated several different ways. The simplest approach is to assume that the dipole perfectly aligns and “locks in” ($\theta = 0$) for the entirety of the reaction. [155, 156]

From this approach, treating it much like the case of polarization already discussed, you get an additional term on the rate for this locked dipole (LD) approach:

$$k_{LD}(v) = q\sqrt{\frac{\pi\alpha}{\mu\epsilon_0}} + \frac{q\mu_D}{2\mu\epsilon_0 v} \quad (3.13)$$

In the case that the reaction is described by a Maxwell-Boltzmann distribution of gas at temperature T , we can integrate over the v dependence with the Boltzmann distribution $P(v)$ as our weighting:

$$\int_0^\infty \frac{P(v)}{v} dv = \sqrt{\frac{2\mu}{\pi k_b T}} \quad (3.14)$$

Then our equation becomes:

$$k_{LD}(v) = q\sqrt{\frac{\pi\alpha}{\mu\epsilon_0}} + \frac{q\mu_D}{\epsilon_0} \sqrt{\frac{1}{2\mu\pi k_b T}} \quad (3.15)$$

This LD reaction rate constant can clearly be seen as the Langevin rate constant with an addition term dependent on the dipole moment. Indeed, in the case that μ_D approaches zero, we recover Equation [3.12]. However, this LD rate constant usually overestimates a reaction rate by a significant amount. Considering that we assumed a perfectly locked dipole at all times, this is perhaps not so surprising. A common correction to Equation [3.15] is to add a *dipole locking constant* c to the strength of the ion-dipole interaction. This essentially is assuming that there is some empirically determined factor that affects the ability for the dipole to lock. This can be

thought of as either a constant orientation that is imperfect, or a consistently changing orientation with an average orientation with $\theta' \neq 0$. This so-named *Average Dipole Orientation (ADO)* theory has the form:

$$k_{ADO}(v) = q\sqrt{\frac{\pi\alpha}{\mu\epsilon_0}} + \frac{cq\mu_D}{\epsilon_0} \sqrt{\frac{1}{2\mu\pi k_b T}} \quad (3.16)$$

with

$$c = \cos \theta' \quad (3.17)$$

Here c is experimentally determined, usually by comparing a nonpolar and polar isomer if possible. Again, in the limit $\theta' = 0$ this is our LD approximation, and for $\theta' = \pi/2$ it recovers Langevin's equation.

A key aspect that allows Equation 3.16 to be useful in modern ion-neutral reaction analysis is the semi-empirical calculation of c versus $\mu_D/\alpha^{1/2}$ for constant temperature, as shown in Figure 3.2.11. An important impact of this work by Su and Bowers was that it demonstrated the temperature dependence of systems with dipolar neutral reactants. This inverse temperature dependence is quite fascinating, particularly as it is opposite from the Arrhenius equation. However, a simple intuitive picture makes some sense of this: the faster a neutral molecule is going, the less time it has to "lock" effectively, assuming its response to turn towards the electric field is uncoupled to its translational energy.

The last modification of this theory we will discuss are the *parameterized trajectory equations*, also eponymously referred to as the Su-Chesnavich (SC) method.39 The SC approach is the most widely-used capture theory model for ion-dipole systems in our cold, classical regime.37 In this methodology, the dependence of c (Equation refADO) on α and μ_D is empirically fit with classical mechanics and *trajectory calculations*157, 158. It also built off of work with transition state theory for calibrating the equations, unifying the two approaches.159 These trajectory calculations begin

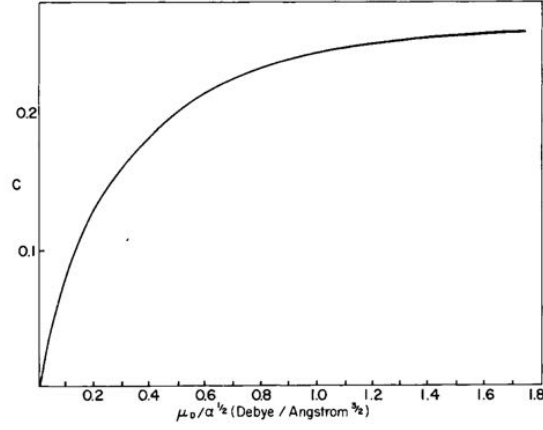


Figure 3.2: Dipole locking constant vs. μ_D/α from Su & Bowers. [11]

with a model Lagrangian describing the ion-dipole system:

$$L = \frac{1}{2}\mu(\dot{X}^2 + \dot{Y}^2 + \dot{Z}^2) + \frac{1}{2}I(\dot{x}_1^2 + \dot{x}_2^2 + \dot{x}_3^2) + \frac{q\mu_D}{4\pi r^2} \cos(\theta) + \frac{q^2\alpha}{8\pi r^4} \quad (3.18)$$

where the first term is the translational energy of the system, the second is the rotational energy of the system (the ion is assumed to be a point charge), and then we have our dipolar and polarization term, respectively. This equation can be numerically solved for an infinite combination of initial positions and dipole angles. These numerical calculations demonstrate that the divergences of ion-dipole systems from Langevin's equation depend only on,

$$x = \frac{\mu_D}{\sqrt{2\alpha k_B T}} \quad (3.19)$$

such that,

$$\frac{k_{SC}}{k_L} = \begin{cases} 0.4767x + 0.6200 & x \geq 2 \\ \frac{(x + 0.5090)^2}{10.526} + 0.9754 & x \leq 2 \end{cases} \quad (3.20)$$

in cgs-esu units. Again, this approach is unified in assumptions and form as the ADO formulation, but approaches the determination of the dipole locking from a numerical standpoint using trajectory

calculations.

This discussion of capture models is not exhaustive, nor does it mean to be. Many scientists have contributed approximations, corrections and efforts through the last hundred years, resulting in many variations on these equations. For example, two useful extensions I did not discuss here are models accommodating higher multipole moments and a more rigorous treatment of conservation of angular momentum, leading to AQO [160] and AADO [161] theory, respectively. [95, 110, 37] Nevertheless, I have attempted to outline the foundational works for ion-neutral theories in our region of interest. On a practical note, we used Langevin and ADO theories for the analysis of our $\text{CCl}^+ + \text{C}_6\text{H}_6$ and $\text{C}_2\text{H}_2^+ + \text{CH}_3\text{CN}$ reactions, respectively. The SC and ADO methods were both used to look at our expected rate constants over a span of temperature in the $\text{CCl}^+ + \text{CH}_3\text{CN}$ reaction. Note that all of these treatments are classical in nature, reflecting the ~ 100 K translation temperatures and room-temperature distribution of rotational energies for the reactions discussed in this thesis. In the case of very cold collisional velocities and small numbers of rotational states, a more quantum mechanical approach must be taken. I will very briefly mentioned such quantum mechanical treatments.

Very nice reviews of the state-of-the-art in theoretical and experimental ultracold chemistry have been presented elsewhere. [59, 37, 46, 45] In particular, Heazlewood & Softley’s 2021 review (reference [46]) is a very nice contextualization of the different theoretical treatments appropriate for different energy regimes in collisional chemistry. In addition, nice reviews of elastic and inelastic collisions from a first-principles quantum mechanical approach can be found elsewhere. [95, 154, 37, 162] For this subsection, I will overview the principles that make these formulations distinct.

The primary defining difference in the treatment of a reaction scattering from a quantum mechanical perspective is the quantization of angular momentum, $|L| = \hbar\sqrt{l(l+1)}$, with l constrained to non-negative integers. A prominent example of the application of this principle is the *adiabatic centrifugal sudden approximation (ACCSA)*. [41, 163] This formalism calculates the rate constant as it depends on the quantum numbers (J, j, K, Ω) . Here, J is the total angular momentum of the system, j the rotational angular momentum of the neutral molecule, K is the projection

of j onto the molecule-fixed axis, and Ω is the projection of J and j onto the body-fixed axis. If coupling between different Ω states is ignored (the centrifugal sudden approximation, CSA), then cross section $\sigma(j, K, E)$ can be determined by diagonalizing the Hamiltonian in the basis of the rotational wave functions. Ultimately, this cross section can be used to determine a reaction rate dependent on quantum numbers j and K : k_{jK} . The overall rate constant is obtained by weighting these state-dependent reaction rate with the quantized density of states:

$$k_{ACCSA} = \frac{\sum_{j,K} g_{jK} \exp[E_{jK}/(k_B T)] k_{jK}(T)}{\sum_{j,K} g_{jK} \exp[E_{jK}/(k_B T)]} \quad (3.21)$$

Where g_{jk} is the state degeneracy and E_{jK} is the barrier height for the corresponding potential curve. An important prediction from this method is that the reaction rate increases with lower rotational states and lower energy. Like ADO theory, this is attributed to an enhancement of the dipole alignment. Another similar method is the *statistical adiabatic channel model (SACM)*,[\[42\]](#) which is very similar in formulation and assumptions. A primary difference between these two leading theories is that SACM treats the problem more analytically, whereas ACCSA more numerically.

Experimentally testing such theories with reaction rates determined by single- or few-rotational state reactions is a frontier of the field. The observation of enhanced and suppressed reaction rates due to Feshbach and shape resonances has been recently seen in atomic collisions[\[164, 165, 166, 167, 168\]](#) with future prospects for ultracold bimolecular (neutral) reactions [\[169\]](#). Ion-neutral reactions have likewise been pushing to colder temperatures, albeit not as cold, but often with more opportunities for control. Two methods approaching these energy scales are crossed beams of metastable atoms (ion-like) with neutral molecules [\[170, 171, 172\]](#) and combined MOT-ion traps [\[173, 174, 138\]](#). As our tools for cooling and controlling such systems improve, this regime is expected to expand in scope, allowing rigorous comparisons of experimental results with the aforementioned theories.

3.1.3 Energy in the collision's center-of-mass frame

This section is dedicated to providing a simple derivation to solving center-of-mass velocities and kinetic energies for our reactions. We will first walk through it generally, then discuss the case of cold ions and thermal neutral gas specifically.

First, we need a technical definition of our collision kinetic energy. To do so, we need to work in the center-of-mass (COM) frame of the reaction. To do so requires some simple Newtonian relativity. Let us start with the case of the collision of two particles with mass m_1 and m_2 with velocities v_1 and v_2 , respectively. We find the velocity of the COM frame as follows:

$$v_{COM}(m_1 + m_2) = m_1v_1 + m_2v_2 \quad (3.22)$$

$$v_{COM} = \frac{m_1v_1 + m_2v_2}{m_1 + m_2} \quad (3.23)$$

Within this frame moving at v_{COM} , objects 1 and 2 have velocities v'_1 and v'_2 , respectively:

$$v'_1 = v_1 - v_{COM} = \frac{(m_1 + m_2)v_1}{m_1 + m_2} - \frac{m_1v_1 + m_2v_2}{m_1 + m_2} = \frac{m_2(v_1 - v_2)}{m_1 + m_2} \quad (3.24)$$

and

$$v'_2 = \frac{m_1(v_2 - v_1)}{m_1 + m_2} \quad (3.25)$$

With our frame-shifted velocities we get the total kinetic energy in the COM frame:

$$KE = \frac{1}{2}m_1\left(\frac{m_2(v_1 - v_2)}{m_1 + m_2}\right)^2 + \frac{1}{2}m_2\left(\frac{m_1(v_2 - v_1)}{m_1 + m_2}\right)^2 \quad (3.26)$$

$$= \frac{1}{2}\frac{m_1m_2}{m_1 + m_2}(v_2 - v_1)^2 \quad (3.27)$$

$$= \frac{1}{2}\mu(v_{rel})^2 \quad (3.28)$$

where μ is our reduced mass and v_{rel} the relative velocities in the originally defined (lab) frame of reference. We can further state that if we want the expectation value of this kinetic energy, we will need the expectation value of the relative velocity squared:

$$\langle KE \rangle = \frac{1}{2}\mu\langle v_{rel}^2 \rangle \quad (3.29)$$

We now have our collision energy for two particles with known velocities. Let us generalize this to the case where the probability that m_1 has v_1 described by an arbitrary function $f(v_1)$ and m_2 has a distribution of velocities $g(v_2)$ where,

$$\int_{-\infty}^{\infty} dv_1 f(v_1) = 1 \quad (3.30)$$

and

$$\int_{-\infty}^{\infty} dv_2 g(v_2) = 1 \quad (3.31)$$

So then we re-write Equation [3.29](#) as:

$$\langle KE \rangle = \frac{1}{2}\mu \int_{-\infty}^{\infty} dv_1 \int_{-\infty}^{\infty} dv_2 f(v_1)g(v_2)(v_2 - v_1)^2 \quad (3.32)$$

If we let $v_{rel} = v_2 - v_1$ and $v_1 = v_{rel} - v_2$ we can express this integral as:

$$\langle KE \rangle = -\frac{1}{2}\mu \int_{-\infty}^{\infty} dv_{rel} v_{rel}^2 \int_{-\infty}^{\infty} dv_2 g(v_2) f(v_2 - v_{rel}) \quad (3.33)$$

where the integral over dv_2 may be easily recognized as a convolution, sometimes mathematically denoted as $(f * g)(v_{rel})$. Some consideration shows that this makes good physical sense as a convolution effectively computes the resulting probability distribution of $v_{rel} = v_2 - v_1$ given a function $f(v_1)$ and $g(v_2)$. Note that Equation [3.33](#) is agnostic to the functional form of the velocity distributions, a fact we will need later. However, we will turn our attention to the case of Maxwell-Boltzmann velocity distributions, as this is a useful case with which we can draw more conclusions from this derivation.

Firstly, we will begin by acknowledging everyone's favorite representation of the Maxwell-Boltzmann (M-B) distribution, the probability of finding a particle with velocity v in the three-dimensional velocity space d^3v :

$$f(v)d^3v = 4\pi v^2 \left(\frac{m}{2\pi k_B T}\right)^{3/2} \exp\left[\frac{-mv^2}{k_B T}\right] dv \quad (3.34)$$

with the expected variable dependencies: m is the mass of the particle, T the temperature, and k_B is Boltzmann's constant. However, if we take a step back, we recall that this famous equation is for

the case of an *ideal gas* with *spherical symmetry* in its velocity distribution. Also note that in this context the temperature is a defining feature of the distribution. That is to say, in the case of ideal gases, the meaning of *temperature* is a description of the equilibrium conditions that produce this distribution of velocities. A more general case arises from decomposing each of the three spatial dimensions:

$$u = \{x, y, z\} \quad (3.35)$$

to rewrite Equation [3.34](#) explicitly in three dimensions:

$$f(v)d^3v = \prod_{u=1}^3 \left(\frac{m}{2\pi k_B T_u}\right)^{1/2} \exp\left[\frac{-mv_u^2}{k_B T_u}\right] dv_u \quad (3.36)$$

Now if we use our M-B description of gases from [3.36](#) and use it for the convolution of our two collisional partners in Equation [3.33](#), we get six-dimension integral that is the general calculation for the kinetic energy of collisions between two gases following M-B distributions with each spatial component uniquely defined:

$$\begin{aligned} \langle KE \rangle = & -\frac{1}{2}\mu \prod_{u=1}^3 \left(\frac{m_1}{2\pi k_B T_{u,1}}\right)^{1/2} \left(\frac{m_2}{2\pi k_B T_{u,2}}\right)^{1/2} \\ & \int_{-\infty}^{\infty} dv_{u,rel} v_{rel}^2 \int_{-\infty}^{\infty} dv_{u,2} \exp\left[\frac{-m_1(v_{u,2} - v_{u,rel})^2}{k_B T_{u,1}}\right] \exp\left[\frac{-m_2(v_{u,2})^2}{k_B T_{u,2}}\right] \end{aligned} \quad (3.37)$$

This relationship defines both collisional partners as M-B gasses, but it still allows each component to have a different distribution (i.e. a different characteristic temperature).

For the analysis of the ion-neutral reactions presented in this thesis, we are interested in a thermal neutral gas (let it be m_1 , such that $T_{u,1}$ is the same for x, y, z . This is not true for the trapped ions, which have cylindrical symmetry due to trapping conditions, and are not M-B distributions (as we saw from simulations in section [2.1.5](#)). However, if we approximate the distributions of the ions as Gaussians, we can treat them as effective M-B distributions. We will make another erroneous assumption by imposing spherical symmetry on the ion distribution. As

we will see in a moment, for the case of room temperature distribution of neutral, we will take the limit of the ion temperature to ~ 0 K, so our incorrect assumption will not matter. It will, however, simplify Equation [3.37](#) to:

$$\begin{aligned} \langle KE \rangle = & -\frac{1}{2}\mu\left(\frac{m_1}{2\pi k_B T_{u,1}}\right)^{3/2}\left(\frac{m_2}{2\pi k_B T_2}\right)^{3/2} \\ & \left[\int_{-\infty}^{\infty} dv_{rel} v_{rel}^2 \int_{-\infty}^{\infty} dv_2 \exp\left[-\frac{m_1(v_2 - v_{rel})^2}{k_B T_1}\right] \exp\left[-\frac{m_2(v_2)^2}{k_B T_2}\right]\right]^3 \end{aligned} \quad (3.38)$$

We note that this is a convolution of two Gaussians – a special case that is well-known in mathematics:

$$\int_{-\infty}^{\infty} dt \exp^{-a(x-t)^2} \exp^{-bt^2} = \sqrt{\frac{\pi}{a+b}} \exp\left[\frac{-abx^2}{a+b}\right] \quad (3.39)$$

This can be used to derive an explicit analytical description for the average kinetic energy. However, as this specific case models both collisional partners as a M-B distribution with a definitive temperature, temperature is a nice metric for this energy. If the variance of a convolution of two Gaussians with variances a and b is $ab/(a+b)$, then we can describe two systems with M-B distributions described by variance $T_1 k_B/m_1$ and $T_2 k_B/m_2$ to have an effective variance:

$$\left(\frac{T}{m}\right)_{eff} = \frac{\frac{m_1}{T_1} + \frac{m_2}{T_2}}{\frac{m_1 m_2}{T_1 T_2}} = \frac{m_1 T_2 + m_2 T_1}{m_1 m_2} \quad (3.40)$$

If we let m_{eff} be the reduced mass μ then we get a very nice mass-weighted temperature average for the effective temperature for our center-of-mass collisional temperature:

$$T_{eff} = \frac{m_1 T_2 + m_2 T_1}{m_1 + m_2} \quad (3.41)$$

This equation is valid for any two spherically symmetric M-B gases. But as promised, we take the case where our ion temperatures approach zero, $T_2 \rightarrow 0$. Then Equation [3.41](#) becomes,

$$T_{eff} \rightarrow \frac{T_{neutral}}{1 + \frac{m_{neutral}}{m_{ion}}} \quad (3.42)$$

This is the relationship used to describe the center-of-mass temperature for our ion-neutral reactions with thermal leaked gases described in Chapters [4](#), [5](#), and [6](#). In the true limit of motionless ions, we do have a thermal distribution of center-of-mass velocities, and this use of the word “temperature” is justified. This is a good approximation to the degree that it impacts our treatment of capture rate theories. However, these ions, while extremely cold, *are not actually motionless, do not actually have M-B distributions, and are not in thermal equilibrium*. This is important to keep in mind when temperatures become relevant to transition state theory in Section [3.2.4](#), as well as the case that a decelerated beam of molecules is reacted with ions in future experiments. These reactions of a decelerated beam of molecules will require a more general treatment of the form described by Equation [3.33](#), where the convolution is acted upon more custom functions than M-B distributions. Indeed, we will need the simulations demonstrated in section [2.1.5](#), as well as estimations of the decelerator output distributions, (which are also not described by M-B distributions,) to appropriately describe the collisional energies in this case. We will return to this in section [8.3.1](#).

3.2 Potential Energy Surfaces

Complementary to kinetic calculations, potential energy surfaces are another excellent tool with which to dive deeper into the reaction dynamics and further compare experimental results with theoretical expectations. I will first give a practical discussion for using quantum chemical packages to find critical points on PESs. Then I will give a brief introduction to the theory behind such numerical techniques behind these packages, including a description of *Self-Consistent Field (SCF)* methods to calculate energies and geometries of different reaction complex configuration. Lastly, I will briefly describe how such surfaces can be combined with transition state theories such as *Rice-Ramsperger-Kassel-Marcus (RRKM)* to approximate the branching ratios for comparison against experiment.

3.2.1 An Introduction to Potential Energy Surfaces

First, we must step back and describe what we mean by a *potential energy surface* (PES) and what is involved in finding one. I will give a brief overview here; as always, excellent references exist for more in-depth studies.[\[12\]](#), [\[175\]](#)

The purpose of PESs is to determine the series of bonding and geometric rearrangements required within a molecule to form a pathway from reactants to products. In our specific context of cold ion-neutral reactants, we are further looking for such a pathway with *submerged barriers* such that even with a scant ~ 10 meV of kinetic energy the reaction can proceed. Such a study indicates what products can be formed within the energetic constraints of our system, and can yield information about the expected rates and ratios of such products. In order to find and communicate such a PES in an effective way, we need two things. Firstly, we need a understanding of how to model and communicate the potential energy landscape involved in a reaction. Secondly, we need the means to calculate the energy of this landscape so that we can model the kinetics and dynamics of the system.

A challenge in communicating and visualizing potential energy surfaces of multi-atom systems is the dependence of the internal potential energy on many dimensions. To illustrate this, we will first discuss a simple reaction case: a three-body reaction. As can be seen in Figure [3.3a](#), the electronic potential energy of three-body system requires three variables to describe fully, and all three dimensions must be considered to find a local or global energy minimum. To understand how such systems are understood and communicated, let us further the case $AB + C \rightarrow A + BC$.

Let us imagine that C approaches with the AB bond length held at a local minimum with respect to energy. In this instance, we could draw a 3-D graph with the energy on the z axis, with the x and y axes each showing this dependence on the angle α and interatomic distance BC . An example of such a system is given in Figure [3.3b](#). In the lower left of the 3-D graph, we see an ozone molecule with a large angle α and large AC (O–O) bond length. This is at a local minimum with respect to all dimensions and is colloquially called a *minimum* or *intermediate state*. As this angle

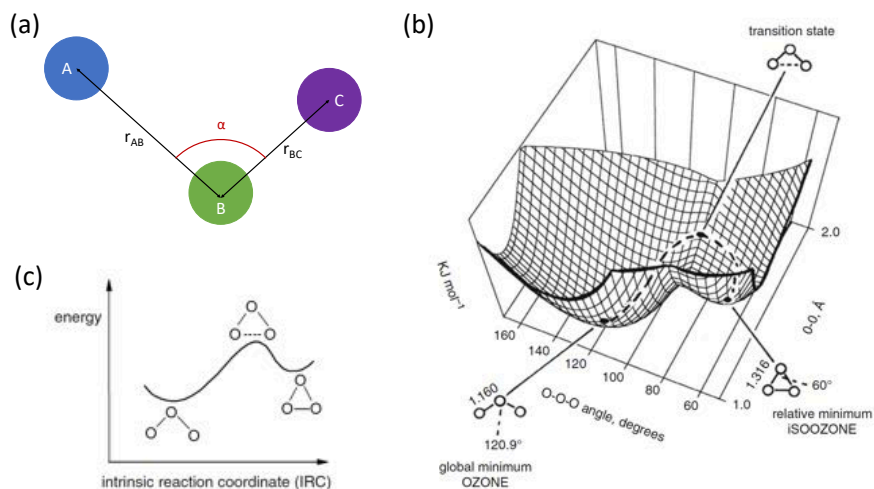


Figure 3.3: **(a)** One possible set of dimensions to describe a triatomic molecular complex. This coordinate system is comprised of two bond lengths and an angle. **(b)** Schematic of three dimensions required to describe a triatomic molecular complex of O_3 isomerization. **(c)** A representation of the surface in 2-D that is typical to a reaction potential energy surface in higher dimensions. Image from Lewars (2010).[\[12\]](#)

closes and the bond shortens, the complex increases in energy until it reaches a local maximum along that particular coordinate of motion. This saddle point is called the *transition state*. Once over this transition state, the local minimum is a stable equilateral triangle configuration – another intermediate state – as shown in bottom right. A common 2-D representation of this 3-D surface (which would be 4-D if we varied AB length also) is given in Figure [3.3c](#). Here, the transition state and intermediate states, (collectively called stationary points,) are plotted versus energy. In this way, the 2-D representation is a slice of the higher-dimension PES that communicates the energetic extremes and geometric details of what changes are happening in the molecule. This is the compromise made to still mathematically treat the system with higher dimensions, even though we cannot represent it graphically in its full dimensionality. This becomes even more relevant as we move to large systems.

I will take this a step further and specifically demonstrate how to interpret a more complicated and more realistic system. Let us consider the reaction $\text{CCl}^+ + \text{CH}_3\text{CN}$. It is a lovely reaction (although I am biased in this matter) and its surface will show up again in the next chapter. This

reaction involves not three atoms, but eight. This corresponds to eighteen ($3N - 6$ for nonlinear molecules) dimensions required to fully express the molecular geometry and calculate its energy. Let us consider the potential energy surface, and in particular what is happening at one transition state.

Figure 3.4a shows the first few steps of the potential energy surface for the reaction of $\text{CCl}^+ + \text{CH}_3\text{CN}$. The energy of the reactants can be determined the limit that they are infinitely far away; this is the relative energy reference for the reaction at 0 eV. Carbon atoms are shown in black/gray, hydrogen in white, nitrogen in blue, and chlorine in green. The first intermediate state is formed via a bond between the carbon of the CCl^+ group with the nitrogen of the CH_3CN molecule. This configuration (labeled INT1 on Figure 3.4a) is stabilized with the geometry requiring about 2 eV less potential energy for such a bonding structure. The methyl group from the original CH_3CN still persists in INT1 but quickly changes when a hydrogen is passed over to the neighboring carbon and forms a planar structure, INT2. There is a saddle point (TS1) in which all coordinates are minimized except those associated with this passing of the hydrogen. This particular coordinate is called the *intrinsic reaction coordinate* (IRC), associated with a vibrational mode of the molecule with an imaginary frequency. This IRC represents the pathway with the largest gradient down either side of the saddle point. Note that the energy is maximized relative to exactly one coordinate, but this coordinate can involve multiple bond lengths and angles. Transition state TS1 is a nice example in which to see the relationship between the vibrational mode and the IRC. Figure 3.4b shows the movement of the vibrational mode associated with the IRC. In this vibrational mode, a hydrogen moves between the two carbons (labeled 1 and 2 in red) with a coupled up-and-down motion of a hydrogen atom left behind on the methyl group of the reaction complex. This vibrational mode is associated with the rearrangement of the reaction complex from INT1 to INT2 as the complex morphs from a bent structure with a methyl group to a planar complex with a hydrogen abstracted to the neighboring carbon.

Consider what it might look like to extrapolate these rearrangement in the 2-D Figure 3.4 to the full 18-dimension figure. We cannot *graph* anything like this for a eight-atom reaction, but

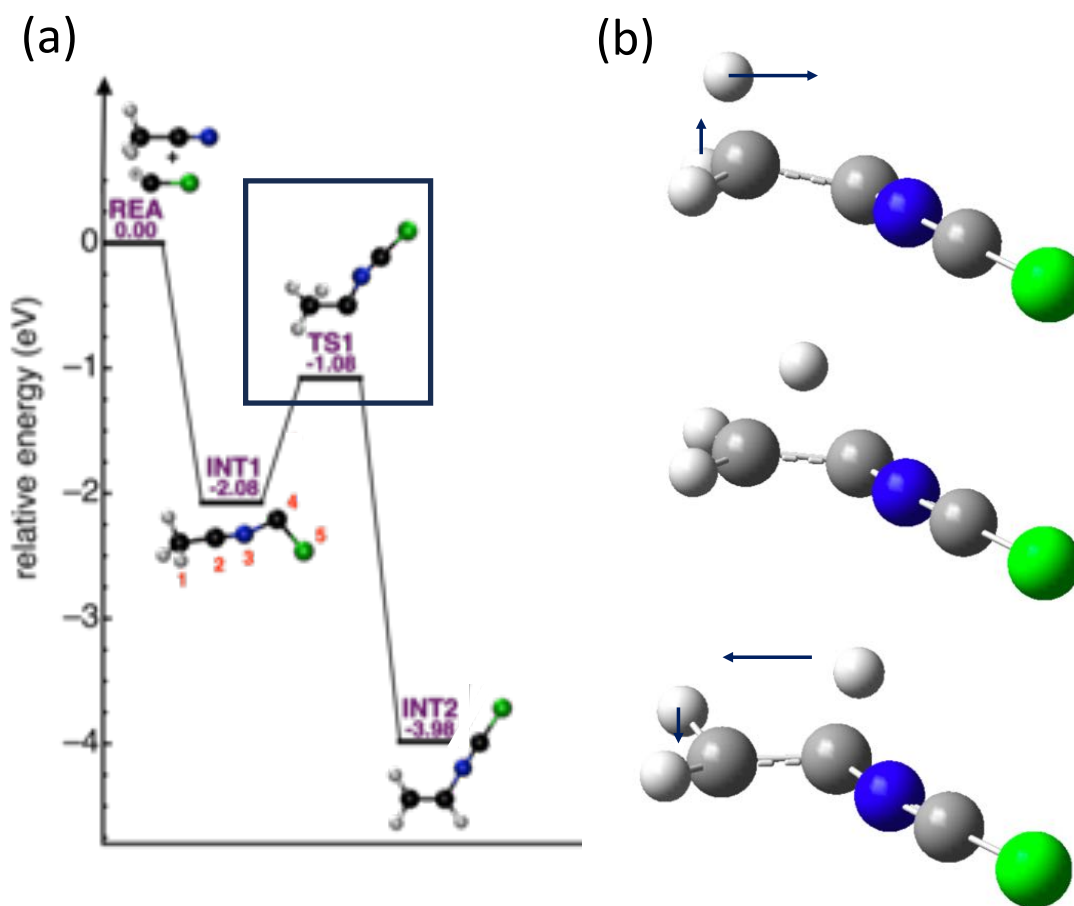


Figure 3.4: (Top) Full PES for the reaction $\text{CCl}^+ + \text{CH}_3\text{CN}$ with relative energy on the y-axis. Highlighted is the first transition state (TS1). Reactants are denoted by REA, products by PRD, intermediate states by INT. (Bottom) Graphical demonstration of the motion of the reaction coordinate for TS1, found as the imaginary frequency of the computed saddle point.

such a surface still exists! This relationship between all 18 dimensions is what we mathematically probe when finding the transition and intermediate states that connect our reactants to products. It demonstrates whether a particular series of rearrangements are energetically viable and often yields insight into the mechanisms involved in the reaction. The high dimensionality of our systems can complicate the communication and understanding of the reaction dynamics. However, with the proper understanding and interpretation of what a PES represents, the full picture can be found, communicated, and understood effectively.

I will include two notes of caution against common misunderstandings. It is tempting to think

of this reaction system as moving “linearly” through these transition and intermediate states, left to right, reactants to products, and actually making these exact geometrical changes. There are two issues with this natural intuition. Firstly, there is no rule that says the molecule has to move left to right. Rather, the movement of the complex depends on the distribution of energy in different modes. As such it is governed by statistical mechanics; this will be discussed more explicitly in section [3.2.4](#). For our reaction interpretation, the important principle here is that once the complex reaches the reactants or products, this is an irreversible process. Every other move on the surface is reversible and probabilistic.

Another interpretation of these graphs I will note explicitly: the molecule doesn’t actually “fall into the wells,” but rather “skims along the top.” This is another way of saying the molecule does not lose its total energy, as there no energy is removed from the system during the duration it spends on the surface (usually on the order of ~ 1 ns, but can be as long as $\sim \mu\text{s}$.) This is not nearly enough time for a reaction complex to radiate away its extra energy, nor for a collision with a third-body collision to quench the energy in a UHV system like ours. Once the reactants join the surface, the total energy remains the same. However, stabilized wells and submerged barriers provide opportunities for the *bond energy* (by which we mean the potential energy due to interatomic forces) to become to *internal energy* (by which we mean energy in the ro-vibrational modes of the molecule) from the transition to intermediate states, respectively. While a PES provides us with the lower bounds for potential energy and the path of highest gradient, the actual complex can proceed pathways that require more potential energy (as long as they stay within the bounds of the total energy of the system.) Thus, the complex is not constrained to the exact geometries that make up the stationary points, nor does it rise and fall in total energy during its time on the PES. It is, however, constrained to the total energy and thus determining pathways that are under this constraint are an important marker for the feasibility of that pathway.

To summarize, potential energy surfaces highlight the pathway of lowest potential or bond energy that connects reactants to products. The process starts with a “capture” (callback to section [3.1.2](#)) to form the initial intermediate complex. Movement within the surface is determined

by the distribution of kinetic energy at any given point on the surface. The total amount of energy is maintained throughout the entire process, such that rovibrational and potential energy is exchanged as the molecule undergoes geometrical rearrangement of its atoms. This rearrangement is what we think of as bond breaking and formation and does not need to follow the lowest energy path. However, finding the energy path between these local minima and maxima verifies that the process is viable under the energetic conditions of the reaction. The process ends when the complex fully breaks a bond and form a two-body product or reactant; this is irreversible and the reaction is over.

Now that we know how to properly interpret a PES, let us move on to our second challenge: how we actually compute one. The next section will discuss some very practical notes on using quantum chemical packages to find the transition and intermediate states already discussed. Then we will discuss the actual quantum mechanics “under the hood” of these packages, to better understand what approximations are being made as well as how to compare trade-offs of accuracy and computational cost.

3.2.2 Finding a PES: a practical discussion

The two quantum chemical packages I worked with in this dissertation are Gaussian 16,^[176] and Psi4^[177]. Gaussian is a proprietary software with a nice graphical user interface that is set up for calculations with a variety of methods, while Psi4 is open-source code that is more optimized for computationally costly methods. We often used Gaussian to find our transition and intermediate state with computationally cheap DFT methods and then used these results as starting points for computations at higher levels of theory in Psi4.

As mentioned, we are interested in reactants, products, intermediate states, and transition states. The first three can be effectively found by inputting a starting geometry and requesting your computational package the minimize the system. It will iteratively move each coordinate and re-evaluate the energy, determining the global minimum once a set perturbation of each coordinate returns equivalent or larger energy. This is a pretty straightforward process, and will of course be

more efficient the closer you are to the minima. Smart guesses on the intermediate state geometry, or using the outcome of other computations, is a nice way to be efficient in this process.

Transition states are a little more fickle. They need to have one coordinate in which the energy is maximized, while the other coordinates are minimized. The closer you are to the saddle point, the more likely the software will be able to find this point. In practice, one can find this by *scanning* over a suspected reaction coordinate. A scan is a function of quantum chemical packages wherein you can calculate the energy of a system as a particular coordinate changes. For example, you could ask it to stretch just one bond by 0.1\AA for 20 steps and it will move the bond accordingly, finding the minima of all the other coordinates with each scanning step. Then you can see the effect of changing this coordinate on your complex. If you choose a coordinate involved in the transition state, there will be a maximum of energy with respect to your chosen coordinate. The actual coordinates associated with a saddle point are (usually) more complicated than a simple bond stretch or an angle variation that can be easily scanned over, so the local maximum found from a scan is (again, usually) not actually the saddle point, but is still close enough that it is a feasible starting point for the software. It is good practice to check the vibrational modes calculated for all geometry optimizations. A complex with all real vibrational modes is a minimum. A complex with one imaginary vibrational mode is a transition state and that vibrational mode is the reaction coordinate of interest.

Another very nice capability of these packages is that these imaginary vibrational modes can be used to find neighboring intermediate states. This is usually referred to as a scan over the intrinsic reaction coordinate (IRC) and effectively uses the vibrational mode associated with the maxima of the saddle point as the scanning direction. This is a convenient way to see the energy of the complex drop as the complex falls off the saddle and towards the closest local minima. Sometimes these IRC scans can take you all the way to the minima, and sometimes they are used to get close to a geometry that can be used as the input for an optimization to a minima.

I have used the term “finding” a PES in this chapter as well as “calculating.” Both are relevant for this procedure: the computer does the calculating, you do the finding. The challenge

of this process (and what comes with experience and skill) is the intuition and thoroughness to look for all the reasonable pathways. There are certain transition states that will certainly be significantly higher than your starting point; there are more reasonable guesses that stem from chemical intuition. This procedure benefits from cultivating an intuition for the reaction mechanism. This intuition is followed up with the aforementioned tools to find potential stationary points, with re-evaluation of the initial guesses as a result of the computational outcomes. One practical note is that when computationally exploring a PES, you can explore from multiple points of the surface simultaneously; this is efficient, but difficult to document carefully. It is difficult to keep track of multiple parallel computations, especially before the full surface has come into focus. Experience helps with both organizational skills as well as intuition for a logical and energetically viable path forward. One benefit of the conditions of our reaction systems is such that anything endothermic to the starting reactants can be immediately abandoned, which nicely simplifies things. A future implementation of such a search may be almost entirely automated: exciting work at Sandia national labs has begun to automate the search of potential energy surfaces. [178], [179] While this does not accelerate individual computations, it is able to immediately take the results of a calculation to begin guesses on the next step of a reaction, drawing on patterns in reaction dynamics for the guesses. While it is unlikely to entirely eliminate the role of a physical chemist overseeing the process, it drastically simplifies some of the tedium.

An input that must be decided in all of these calculations is the *level of theory (LOT)* with which to calculate the structures. The prominent *ab initio* (i.e. non-empirical) LsOT are split into DFT and post-HF. The distinction between the two and their capabilities come down to which approximations are made to calculate the molecular wavefunctions. This is the topic of our next section.

3.2.3 Calculating a PES: self-consistent field methods

This section will overview a few different categories of methodologies to optimize the geometry and energies of atoms and molecules. I will begin by pointing out that many excellent books are

written on the subject of computational chemistry.[\[12\]](#), [\[180\]](#), [\[181\]](#) Many undergraduate physical chemistry textbooks give a nice introduction to this topic as well (of these, I have referenced McQuarrie and Simon’s classic text in this discussion.[\[182\]](#)) In addition, Walter Kohn and John Pople won the 1998 Nobel Prize in chemistry for their contributions to this field. This section is not intended to represent a thorough review of or rigorous derivation for modern computational physical chemistry methods. Rather, it is intended to give a conceptual overview of the core mathematical principles involved in computational quantum chemical methodologies. For this section, I will endeavor to present just the basics necessary to appreciate the complexity and assumptions, strengths and weakness, of different methods that comprise the bulk of molecular geometry and energy calculations required to calculate potential energy surfaces. This discussion arises from the use of such methods for calculating PESs, but note that much of this has applications for spectroscopy of atoms and molecules, solid state physics, and more.

Our discussion begins with the first problem: why not solve the Schrödinger equation exactly for our atomic and molecular systems? With the Born-Oppenheimer assumption, we can treat the atomic and electronic wavefunctions separately, due to their large discrepancy in masses. The result is the electronic Schrödinger equation. Such an equation for helium, with the coordinate system fixed at the nucleus of the atom, is written thus:

$$\left[\frac{\hbar^2}{2m_e} (\nabla_1^2 + \nabla_2^2) - \frac{e^2}{4\pi\epsilon_0} \left(\frac{1}{r_1} + \frac{1}{r_2} \right) + \frac{e^2}{4\pi\epsilon_0 |\vec{r}_1 - \vec{r}_2|} \right] \psi(\vec{r}_1, \vec{r}_2) = E\psi(\vec{r}_1, \vec{r}_2) \quad (3.43)$$

The first two terms are our kinetic energy of the electrons, the next two terms are the potential energy of the electrons, and the last term is electron-electron Coulomb repulsion. Without this last term, we could express the solution as a combination of two, separable, hydrogen-like orbitals. With this term, we do not have an analytical solution. Thus, anything with more than two electrons will need a numerical and/or approximate approach.

One excellent tool on our side is the variational principle. It can be shown that if you take a

trial wavefunction ϕ , and calculate the expectation value of the energy with this wavefunction:

$$\langle E_\phi \rangle = \frac{\int \phi^* \hat{H} \phi d\tau}{\int \phi^* \phi d\tau} \geq E_0 \quad (3.44)$$

Then the calculated expectation energy $\langle E_\phi \rangle$ with any trial wavefunction will be larger than the actual energy, E_0 . This is powerful as we can always know an approximation with this method is an upper bound and the lowest energy calculated with this method is the closest yet. The proof consists of the principle that you can cover all Hilbert space with the ground state wavefunction and all possible excited states. Thus, any trial wavefunction used for this calculation can be written in the basis set of the ground and excited states. This means that unless the guess is the exact solution, it must contain some of these higher energy wavefunctions and necessarily have an expectation value of energy higher than the ground state. A nice feature of this method is that it can be combined with tricks such as adding differentiable parameters in the trial wavefunction or weightings in combinations of possible solutions. After solving Equation 3.44 analytically, you can find the minimum energy as a function of these parameters. If you are really clever about your trial solution you can even converge upon the exact solution. As might be expected, this high accuracy has technical difficulties, such as choosing the right set of trial wavefunctions and finding for the global minimum to Equation 3.44 over multiple variational parameters.

To understand the role of the variational principle, let us return to our Hamiltonian (Equation 3.43). How does the variational principle help us with the $\frac{1}{|\vec{r}_1 - \vec{r}_2|}$ term? It doesn't – yet. It opens the door to using hydrogen-like orbitals to approximate solutions and using approximate waveforms to converge on a solution. The next step in approximating the solution to this Hamiltonian is to modify it. In particular, we let the solution be a combination of two independent (and uncorrelated) electronic densities, ϕ_1 and ϕ_2 , such that the solution in the helium atom would take the form:

$$\psi(\vec{r}_1, \vec{r}_2) = \phi_1(\vec{r}_1)\phi_2(\vec{r}_2) \quad (3.45)$$

Then we express the electron-electron repulsion term as the effect of one electron density on the other, that is to say:

$$V_1^{eff}(\vec{r}_1) = \int \phi_2^*(\vec{r}_2) \frac{1}{r_{12}} \phi_2(\vec{r}_2) d\vec{r}_2 \quad (3.46)$$

and our new Hamiltonian (sometimes called the *Fock Operator*), now becomes

$$\frac{\hbar^2}{2m_e}(\nabla_1^2 + \nabla_2^2) - \frac{e^2}{4\pi\epsilon_0}\left(\frac{1}{r_1} + \frac{1}{r_2}\right) + \int \phi_2^*(\vec{r}_2)\frac{1}{r_{12}}\phi_2(\vec{r}_2)d\vec{r}_2 + \int \phi_1^*(\vec{r}_1)\frac{1}{r_{12}}\phi_1(\vec{r}_1)d\vec{r}_1 \quad (3.47)$$

Now our Hamiltonian is defined by our solutions. This means we will need to iterate over solutions, using a trial ϕ_2 to calculate the V_1^{eff} to solve for ϕ_1 to determine V_2^{eff} to improve ϕ_2 . This iteration continues until the modified wavefunctions change very little through the iteration. This process is aptly referred to as a *Self-Consistent Field (SCF)* method. Particularly as we can start with *linear combination of atomic orbitals (LCAO)* as nice guesses for molecular orbitals, this is a very powerful technique.

There is one more ingredient to make a *Hartree-Fock orbital* or to call this a *Hartree-Fock method*. That is to take these single-electron orbitals and accommodate for Fermi statistics. The Fermi Exclusion principle necessitates that no two spins can occupy the same orbital and that the overall wavefunction must be antisymmetric. This is enabled with a bit of clever mathematics by using determinants. Let us return to helium one last time. Let us assume we have two spatial wavefunctions in the two orbitals; let us call the electron spin either α or β . Now if we set up a matrix where each column has a distinct spatial wavefunctions and the spins progress down the rows like so:

$$\Psi(1, 2) = \det \begin{vmatrix} \phi_1\alpha(1) & \phi_2\beta(1) \\ \phi_1\alpha(2) & \phi_2\beta(2) \end{vmatrix} = \phi_1\alpha(1)\phi_2\beta(2) - \phi_1\alpha(2)\phi_2\beta(1) \quad (3.48)$$

Our resulting determinant will have several key features that obey Fermi statistics. First note that if we swap the labels of electrons 1 & 2 (or calculate $\Psi(2, 1)$) we would get the same solution but with a sign change. Further, if we try to build a matrix with an electron with the same spin and the same orbital, the determinant will be zero. Together, these features of determinant make for an excellent mathematical convention to efficiently assign appropriate combinations of spatial and spin orbitals to produce an antisymmetric wavefunction. When used in this way these

determinants are called *Slater determinants*, and can be generalized to describe larger systems:

$$\Psi(1, 2, \dots, N-1, N) = \det \begin{vmatrix} \phi_1(1) & \phi_2(1) & \dots & \phi_{N-1}(1) & \phi_N(1) \\ \phi_1(2) & \phi_2(2) & \dots & \phi_{N-1}(2) & \phi_N(2) \\ \dots & \dots & \dots & \dots & \dots \\ \phi_1(N-1) & \phi_2(N-1) & \dots & \phi_{N-1}(N-1) & \phi_N(N-1) \\ \phi_1(N) & \phi_2(N) & \dots & \phi_{N-1}(N) & \phi_N(N) \end{vmatrix} \quad (3.49)$$

for a system with N electrons, where each ϕ is an orthonormal spin orbital. A swapped row corresponds to a switched electron and will flip a sign. A repeated column will result in a determinant of 0, appropriate for the forbidden case of two electrons in the same state. The exact convention for naming the orbitals varies, but they are typically labeled in such a way to reflect the system it is calculating (such as a lithium atom have two identical and one distinct s orbitals, etc).

However, there is a major problem with our analysis so far. We took a direct Coulomb repulsion between electrons and replaced it with interactions between “smeared out,” or average, field potentials. This means we will get energies associated with the interactions of the average motions of the electrons, but we have completely omitted their actual correlated motions and positions. While we did account for the fact that two spins cannot occupy the same orbital, our replacement of repulsive pairs of moving electrons with that of each electron in charged clouds is the major deficiency of the Hartree-Fock method. A lovely analogy from Lewar’s book put it this way: “If you walk through a crowd, regarding it as a smeared-out collection of people, you will experience collisions that could be avoided by looking at individual motions and correlating yours accordingly. The Hartree-Fock method overestimates electron-electron repulsion and so gives higher electronic energies than the correct ones, even with the biggest basis sets, because it does not treat electron correlation properly.” [12] Without accounting for electron correlation, HF methods can generally can get within 99% of the actual ground state energy. This 1%, however, is on the order of a chemical bond and is unsatisfactory for our applications. Note that this mention of a “full basis set” implies that we can use the variational principle to get extremely close or arrive at our real

expectation value for our Fock operator. However, this operator is not the true Hamiltonian of the system. That is what we lost by replacing our electron repulsion term with our effective coulomb potentials.

These principles set up our problem: we have a nice way to make our Hamiltonian numerically solvable, but we have lost a physical effect – electron correlation – in doing so. This is what is referred to in the field as the *Hartree-Fock limit*. A (reductionistic) summary of the goal of computational quantum chemistry is to find a spectrum of compromises between computational cost and accuracy to modify our Fock Operator or calculate our electron correlation and add it back. There are two broad categories for dealing with this issue. Altering the Fock operator comprises *Density Functional Theory (DFT)* and calculating the electron correlation back is entailed in *post-Hartree-Fock* methods. We will look just a bit closer at the approach that DFT takes and then mention a few of the predominant post-HF techniques.

Density functional theory receives its name from its emphasis on calculating the electron probability density function rather than the wavefunction. This has a few benefits: for one, electron density is measurable, and thus can be semiempirical and more readily testable; secondly, the electron density is only a function of position and thus is dependent on three variables for the entire system, while a wavefunction requires four variables *per electron*. DFT operates on the two Hohenberg-Kohn theorems, the first of which states that any ground state property of a molecule depends only on the electron density. That is to say that there exists a functional (F) that can calculate energy based on the electron density. The second Hohenberg-Kohn theorem is very similar to the variational principle, stating that any trial electron density function will yield a higher energy than the actual ground state energy. Together these theorems form the basis of a set of equations that can be iterative worked over to simultaneously refine the electron density distribution and the functional F in a Hartree-Fock-like iterative process. Historically, DFT was first popular for solid state physics applications, but considered too inaccurate for molecular physics. This changed when the available functionals were modified to account for electron correlation by Kohn and Sham. [\[183\]](#) These electron correlations come at the price of introducing *Kohn-Sham orbitals* into the electron

density functions – and increasing the dimensionality. However, this increase in complexity is no more computationally intensive than the original Hartree-Fock calculations, with the addition of (approximately) accounting for electron correlation. Such functionals in DFT that accommodate electron correlation in this way are sometimes called *hybrid functionals* and include famous methods such as B3LYP. An important point about DFT functionals is that they are all approximations and models. As such, they always handle some aspects of atomic behavior better than others. Some handle short range interactions well, but not long range interactions. Some do not replicate the behavior of halogens well. Some are calibrated against experimental values (*semi-empirical*). The assembly of DFT functionals that are available is a dynamically growing as computational chemists work on finding the balance of computational cost and accuracy for different applications. Thus, not all functionals are created equal, particularly not for any given system of interest. While some can be quite accurate, they do not approach the accuracy of some of the more expensive post-Hartree-Fock methods.

The first post-HF method discussed here is *Møller-Plesset (MP)* perturbation theory. As the name suggests, this calculation indeed involves perturbation theory. Specifically, MP theory involves treating the real molecule as a perturbation of the Hartree-Fock system. To do this effectively, you also need to involve a large *basis set*. What we mean by this is that the theory works best when unoccupied orbitals (sometimes called *virtual orbitals* or *excited Slater determinants*) are involved in addition to the typical lowest-energy orbitals involved in a HF calculation. Allowing higher-order spatial wavefunctions allows the electrons to avoid each other more effectively. The first correction of Møller-Plesset arrives at the second order of the perturbation theory (MP2) and corrections up to the fourth order can be used (MP4). Note that the variational principle is not used past our HF starting point. The perturbation theory corrections oscillate in sign: MP2 gives an answer that is lower in energy than the actual value. MP3 moves back closer to the HF starting point, MP4 back down again. The actual value is usually anticipated to be between MP3 and MP4. In practice, MP2 with a decently large basis set is commonly used for many applications. [\[12\]](#), [\[180\]](#)

The *configuration interaction (CI)* method also benefits from the use of additional orbitals.

Multiple determinants are written, including that of Equation [3.49](#), but also several combinations with electrons singly or doubly excited into higher orbitals. We take our trial wavefunction to be a linear combination of these ground state and excited determinants. The result is a weighted combination of ground state and electronic excited-state wavefunctions. This linear combination of determinants can now be iterated upon in a HF-like manner and the weighting factors for all the contributing determinants can be minimized with the variational principle. In theory, with an infinitely large basis, this could achieve the exact ground state energy for the system. In practice, large basis sets give excellent results. When single excitations are included this method is denoted as CIS, and when singles and doubles are included it is referred to as CISD.

Closely related to both of these methods is the *coupled cluster (CC)* method, which is generally a gold standard within the community, especially when taken to CCSD(T)/CBS. The primary distinction from CI methods is that the correlated wavefunction is expressed by allowing a series of operators to act on the wavefunction where each of the operators promotes different combinations of electrons into virtual spin orbitals. This is in contrast to building and adding together multiple determinants. The operator is of the form $e^{\hat{T}}$ and must be Taylor expanded to operate on the HF wavefunction. Note that this method is not variational. Depending on the number of terms included, you can get coupled cluster doubles (CCD), singles and doubles (CCSD) or where singles and doubles are included and triplet excitations are added in an perturbative way. A common favorite level of theory is CCSD(T), which is most successful used with a large basis set. The most complete basis set is the *complete basis set* (CBS), where the energy is plotted against progressively larger basis sets and the relationship is extrapolated to its mathematical asymptote. This is more computationally expensive than other post-HF and certainly than DFT methods, but is often considered worthwhile for the improvement in accuracy.

In our theoretical work, we typically started a calculation of a stationary point with geometry calculation using a “cheap” DFT method. For my computational work on the CCl^+ reactions, this was done in the M06-2X functional, as it performs fairly well with small nitrogen- and chlorine-containing molecules.[\[184\]](#) Then, we usually treat the resulting optimized geometry as a starting

point in a higher LOT, such as Møller-Plesset theory (MP2). We usually try to use this optimized structure as a starting point for a final geometry calculations at CCSD and then do fixed energy calculations at that geometry at CCSD(T)/CBS (the first term denotes the method, the second is the basis set.) A nice way to denote a geometry calculation at one level of theory and a single-point energy calculation at a higher level is to label it as [*energy calculation LOT//geometry calculation LOT*]. For example, our $\text{CCl}^+ + \text{CH}_3\text{CN}$ surface was calculated at [CCSD(T)/CBS//MP2/aug-cc-pVTZ] level of theory. We did not do a full surface for $\text{CCl}^+ + \text{C}_6\text{H}_6$, but the reactants and products were calculated to [CCSD(T)/CBS//CCSD/aug-cc-pVDZ.]

As a last practical note, I will address the fact that I have only named a few of many many DFT methods, only the three most prominent post-HF methods, and only a few basis sets. There is an entire spectrum of options for DFT methods and basis sets, as well as a couple other possible HF methods.[\[180, 181, 12\]](#) Exploring other methods and basis sets is something that should be done when approaching a new system. The entire process requires some research that is specific to the system of interest, as well as iterative explorations with different levels of theory and methods. However, it is my hope that this section can at least give an introduction and overview to the “flavors” of options that are available, as well as what makes them distinct.

3.2.4 A glimpse into transition state theory and its relevance to branching ratios

As the title suggests, this section will be quite brief. *Transition state theory (TST)* and *Rice-Ramsperger-Kassel-Marcus (RRKM)* calculations are not used by our group in-house, but we have worked with theory collaborators that have used such theories on our system to help us compare the kinetic and dynamic results to theoretical expectations. In addition, the concepts underlying these theories complements the understanding of how one interprets a potential energy surface, and the effect it will have on branching ratios and rate constants. To develop some of the intuitions given by TST and RRKM, I will give a brief overview of the fundamental concepts and assumptions underlying these methods in order to give a launching point for further reading.[\[147, 175, 185\]](#)

TST starts with the assumption that there is a bottleneck or *point of no return* in a reaction.

This essentially simplifies a reaction rate into a counting of the statistical probability that a reaction complex will pass through that barrier (and thus form products) versus dissociate into reactants. In this sense, the reaction is split up into two sections: from the initial reaction complex to a critical transition state, the dynamics of which determine the reaction rate; and from the transition state to final complex before bimolecular product are formed, the dynamics of which determine the distribution of energy in the products. This essentially simplifies a potential energy surface such as Figure 3.4 to a Arrhenius-like profile. Thus, we come full circle to a rate constant associated with the height of the barrier, $\exp\left[-\frac{E_0}{k_B T}\right]$. In this case, the prefactor for this rate is directly related to the distribution of energy within the molecule. Mathematically, this is calculated by the statistical distribution of energy among the available kinetic, rotational, vibrational, and electronic modes for all but the reaction coordinate, normalized by the distribution of energy among all the modes available in the reactants (or neighboring well.) TST further assumes that the reactants and transition state are in thermal equilibrium – this is to say, we describe their densities of states by canonical ensembles (Q). In the case of a two-body reaction proceeding through a transition state, $A + B \rightarrow AB^\ddagger \rightarrow \text{products}$, we can calculate our reaction rate thus:

$$k = \frac{k_B T}{h} \frac{Q^\ddagger}{Q_A Q_B} \exp\left[-\frac{E_0}{k_B T}\right] \quad (3.50)$$

where Q^\ddagger is our canonical ensemble for the degrees of freedom not involved in the reaction coordinate, and Q_A and Q_B are our canonical ensembles for our reactants. As always, k_B and h are Boltzmann's and Planck's constants, respectively.

A common approach when working at lower pressures (where our reactants and transition state are not necessarily in equilibrium) is to work with microcanonical ensembles ($\rho(E, J)$) instead. This is the primary distinction of RRKM from general TST theory. This formulation is related but distinct:

$$k(E, J) = \frac{N^\ddagger(E - E_0)}{\rho(E)} \quad (3.51)$$

where $\rho(E, j)$ is the density of states of the reactant and where $N^\ddagger(E, J)$ is defined:

$$N(E) = \int_0^E \rho(x) dx \quad (3.52)$$

The primary takeaway here is that TST counts the distribution of states from a *thermal* (constant-temperature) standpoint, while RRKM utilizes an *energy-based* perspective. This allows us to utilize results of quantum chemical calculations to look at the possible rovibrational modes in a well beside a large barrier as a metric for the probability of transmission over a rate-limiting barrier – without assuming that this complex is in thermal equilibrium with our reactants. Nevertheless, there are several assumptions made in both of these formulations that need to be recognized.

The first assumption is that this system behaves classically. All the presented formulations are for classical systems. This can be partially adapted to quantum mechanical systems by treating the partition functions as sums of discrete states, math that is well established in statistical mechanics. However, this formulation will not account for quantum behaviors such as tunneling, which can occur in reactions with light atoms like hydrogen. It also usually assumes harmonic potentials when modeling the density of vibrational states; the actual anharmonicity of the vibrational potentials can and should be accounted for with highly excited complexes.

Further, these formulations simplify the motion over the barrier as being along the reaction coordinate only. These equations separate the reaction coordinates from the other coordinates and use the exact barrier height; this assumes the path over this barrier is along that highest-gradient-lowest-energy saddle point. As I pointed out in section [3.2.1](#), this does not have to be the case.

Another assumption was noted at the beginning, that these formulations assume at their core that there is no re-crossing back over our critical barrier. Physically, this can happen and may reduce the actual reaction rate relative to the calculated one. In this sense, these methods provide an upper bound to reaction rates. Nevertheless, these approximations allow us to have a mathematical model with which to compare the real behavior of the system. In the limit of high barriers, thermal equilibrium, and classical energies, it becomes an excellent model. This must be

taken into account when we compare the results of such theories with the behavior of our system.

Since our group's experimental interest is usually more focused on the accurate reporting of branching ratios rather than rate constants, our primary interest in RRKM theory is in relative formation of products. Some level of intuition can be gained from what has been discussed of RRKM: a large barrier will discourage a fast rate along that path, and a deep well will discourage movements back over what is now a large barrier. However, to truly treat the system properly under these equations and obtain numerical branching ratios for multiple pathways in a real surface like that of Figure 3.4, a more systematic approach is necessary. Common practice is to use a time-dependent, multiple-well *master equation (ME)* to model the full surface. These equations are usually too complex to resolve each energy state, and thus they must be *energy-grained*, that is to say, solved as a function of states with energies between E and $E + dE$. With this assumption, you can yield a set of coupled linear differential equations to describe the energy distribution and chemical transformations that occur on a multiple well potential energy surface. Such methods utilize the stationary points calculated to find such a surface to predict the rates and branching for different products on that surface.^[186, 187, 188] This method was used to compare with our experimentally observed branching ratios in the reaction of $\text{CCl}^+ + \text{CH}_3\text{CN}$, which will be discussed in the next chapter.

Beyond predicting branching ratios, there are many aspects in which PESs can also help us understand reactions better. One example is isotopologue effects. Capture theories predict a very small slowing of a capture rate due to a large mass that would come from isotope substitution such as deuteration. However, there are cases where deuteration has actually increased the rate constant. This behavior has been ascribed, at least tentatively, to the changes in distribution of rovibrational levels in the stationary points of the reaction.^[67, 69, 68] Cases like this require more theoretical study, as there appear to be situations where the isotopologue influences the distribution of energy among internal modes in a way that is not yet understood.

In addition, potential energy surfaces can indicate the importance of energy on the reaction product branching. A specific example of this includes optical stimulation of vibrational modes

critical to a reaction progress. A recent study in a cryogenic 22-pole trap demonstrated that the optical excitation of a particular vibrational mode could hinder the reaction of a $c\text{C}_3\text{H}_2^+ + \text{H}_2$ reaction.^[80] In a crossed-beam experiment of $\text{F}^- + \text{CH}_3\text{I}$, product formation was enhanced by the excitation of a crucial vibrational mode. Together with some tunability in collisional energy, this study was able to present and verify the dominant pathways on their potential energy surface.^[189] Similarly, collisional or kinetic energy can impact the branching ratios in particular systems. One aim of our integrated linear Ion Trap-Stark Decelerator ensemble is to extend our reaction studies to this endeavor. If our system has a branching in products that is sensitive to the starting translation energy, a reaction between cold ions and a decelerated beam may be able to demonstrate an impact of the collisional energy on the branching ratios. This combined experiment and its status will be discussed further in Chapter [8](#).

Chapter 4

Isotope-specific reactions of acetonitrile with trapped, translationally cold CCl^+

“What really is the importance of CCl^+ in the ISM?”

–Reviewer #1, 2021

The following chapter is adapted from a work of the same name that was published in the Journal of Chemical Physics. [\[190\]](#) Of the work presented in this section, I was a primary contributor to the accumulation and analysis of the data presented. Former postdoc Katherine Catani and I contributed equally to the computational calculations of the potential energy surface. The energy grained master equation simulations that were used to produce Figure [4.8](#) were the result of work from theory collaborators Sri Sundar and Gabe da Silva at the University of Melbourne.

4.1 Introduction

Nitriles and nitrogen-containing compounds play a prominent role in the chemical reactions thought to take place in the interstellar medium (ISM). These molecules permeate space: from small cyanides such as HCN and DCN found in the Orion Nebula [191, 192] to larger molecules such as benzonitrile, whose initial discovery in the ISM was relatively recent. [193] Nitriles, defined by their $C\equiv N$ functional group, are of particular interest as pre-biotic molecules and potential precursors of amino acids. Several nitriles have been identified in the atmosphere of Titan using the Ion Neutral Mass Spectrometer on the Cassini spacecraft, and are believed to be important in tholin formation, [194] as well as astrobiology. [195]

Acetonitrile (CH_3CN ; the neutral reactant in this study) has been found abundantly throughout many regions of space since its initial identification in the ISM in 1971. [196] It has been observed in cold dark clouds, [197] low-mass protostars, [198, 199] and is considered an indicator of the presence of hot cores. [200, 201] CH_3CN has also been discovered in dust from comet Halley, [202] Hale-Bopp (C/1995 O1) [203] and, more recently, at the surface of comet 67P/Churyumov-Gerasimenko. [204] These cometary identifications can yield critical glimpses into the past conditions and evolutionary history of the Milky Way. Deuterated variants CD_3CN and CDH_2CN have been identified in hot cores and star-formation regions, [205] and the presence of isotopologues of CH_3CN is used to study relative populations of hydrogen and deuterium in some regions of the ISM. [206]

Halogen-containing compounds have also been identified in the ISM, but their role and evolution are less well understood. In particular, chlorine has been found in the ISM in several small molecules ($NaCl$, $AlCl$, KCl , HCl), [207] as well as in CH_3Cl [208] and H_2Cl^+ . [209, 210] The only halogenated carbocation to be observed thus far in the ISM is CF^+ , [207] whereas CCl^+ has been predicted to occur, although only in low abundances. [211] CCl^+ can be produced from reactions of $C^+ + HCl$, [212] and once formed, has been assumed to be predominantly nonreactive. Specifically, room-temperature Selected-Ion Flow-Tube mass spectrometry (SIFT) measurements demonstrated that CCl^+ does not react with HCN (or CO_2 , CO , O_2 , H_2O , CH_4 , H_2) [133] However, it was shown

to react with NH_3 and H_2CO .^[135] Recent work from our group demonstrated that CCl^+ reacts with acetylene (C_2H_2), producing small fundamental carbocations after losing neutral Cl or HCl.^[213] Predictions and models of chemistry involving CCl^+ , paired with measurements of reaction products and approximate rate constants, can indirectly investigate the potential abundances and plausible locations of this cation. Thus, we believe CCl^+ to be an important molecule to study for understanding astrochemistry, even preceding a conclusion regarding its presence in the ISM.

In contrast to CCl^+ , laboratory reactions of nitriles have been much more widely studied. Ion cyclotron resonance (ICR) spectrometry has been used to measure reactions with HCN and carbocations,^[214] while other ion trap experiments have investigated reactions of CH_3CN with multiple carbocations.^[215] SIFT experiments demonstrated reactivity of CH_3CN with O^+ , H^+ , D^+ , HeD^+ , and HeH^+ ,^[216] as well as with C_2H_4^+ ,^[217] and C_2H_2^+ .^[218] However, very few measurements have reported reactions of halogenated carbocations with any nitrile. The only reported reactions of this type are the reaction of CF_3^+ with CH_3CN and benzonitrile, both of which were shown to produce only the adduct.^[219] The reactions of CF_3^+ were executed in a higher pressure regime than that of the current experiment, where reactive intermediates are unable to be stabilized through collisions with background gas. The reactivity of halogenated carbocations with nitriles is in need of further exploration, particularly in a cold, low-pressure environment. This work seeks to understand more about this reaction class by studying the reaction of $\text{CCl}^+ + \text{CH}_3\text{CN}$ in this regime.

There are multiple useful techniques for studying ion-neutral chemistry.^[220, 221] Of particular interest here is the cold (~ 160 K), low-pressure environment provided by using a linear Paul ion trap (LIT), which is excellent for elucidating ion-neutral chemical reactions.^[62, 45] This experimental setup affords a significant amount of control, including the manipulation of collisional energy,^[173, 222] nuclear spin,^[223] and the measurement of isomer,^[73, 7] isotope,^[171, 68] and quantum state^[224, 225, 226, 227] dependencies. Ions of interest are co-trapped and sympathetically cooled with laser-cooled Ca^+ , forming a mixed species Coulomb crystal, achieving translationally cold, trapped ions. Reactions of these cold ions with room-temperature neutral gas result in colli-

sional energies characterized by temperatures on the order of ~ 160 K. While this is warmer than the coldest regions of the ISM, the energetics of these collisions impede endothermic reactions and interactions with significant barriers, resembling the constraints of the ISM. Furthermore, the addition of a time-of-flight mass spectrometer (TOF-MS) provides detection of ionic reactants and products with high mass resolution – a powerful tool for probing reaction products and kinetics.[\[65\]](#)

The reaction of sympathetically cooled CCl^+ with CH_3CN is studied using our LIT TOF-MS. This work seeks to illuminate the role and reactivity of these novel species in the gas phase under experimental conditions that are approximate to that of the ISM and planetary atmospheres. The primary products are found to be C_2H_3^+ and HNCCl^+ , which are unambiguously assigned through the use of isotope substitutions. Computational modeling also supports these product assignments, suggesting a reaction pathway requiring cleavage of the $\text{C}\equiv\text{N}$ bond of CH_3CN in order to form the observed products. Furthermore, the study of $\text{CCl}^+ + \text{CH}_3\text{CN}$ signifies an initial investigation in reactions of halogenated carbocations with nitriles.

4.2 Methods

4.2.1 Experimental Methods

Reaction data were collected using a LIT radially coupled to a TOF-MS. Detailed descriptions of the apparatus have been outlined previously,[\[65, 213\]](#) and only a brief summary focusing on the specific details relevant to the current experiment will be given here. CCl^+ was produced using tetrachloroethylene (TCE, C_2Cl_4) seeded in a pulsed supersonic expansion of rare atomic gas (1.4% C_2Cl_4 in ~ 1000 Torr He). The skimmed molecular beam was overlapped with a focused beam (216 nm) in the center of the trap. This beam was produced from a pulsed dye laser (LI-OPTEC LiopStar; 10 ns pulse, $100 \mu\text{J}/\text{pulse}$), which was then frequency-doubled using a nonlinear BBO crystal. Non-resonant multiphoton ionization of TCE resulted in several fragments, including C^{35}Cl^+ , C^{37}Cl^+ , $^{35}\text{Cl}^+$, $^{37}\text{Cl}^+$, C_2^+ , and small amounts of $\text{C}_2^{35}\text{Cl}^+$ (hereafter, the more abundant isotope ^{35}Cl will be referred to as simply Cl, while ^{37}Cl will be specified when appropriate).

Unwanted ions were ejected from the trap by sweeping over resonance frequencies of the specific mass-to-charge ratio (m/z) of undesired ions.^[127] This provided a clean sample of either CCl^+ or C^{37}Cl^+ with minimal impurities, as demonstrated in Fig. 4.1.

After removing unwanted ionization products from the trap, Ca^+ was loaded by non-resonantly photoionizing an effusive beam of calcium using the third harmonic of an Nd:YAG (Minilite, 10 Hz, $\sim 7\text{ mJ/pulse}$ at 355 nm). The resulting Ca^+ ions were Doppler laser cooled by two external cavity diode lasers, forming a Coulomb crystal structure, which sympathetically cooled the co-trapped CCl^+ ions via the Coulomb interaction. Ca^+ ion fluorescence was collected using a microscope objective and focused onto an intensified CCD camera located above the trap, allowing for qualitative visual monitoring of the experiment. The heavier “dark” CCl^+ ions arrange themselves in outer shells around the Ca^+ ions, deforming the fluorescing Coulomb crystal as seen in Fig. 4.1b. A typical experiment utilized 150-250 CCl^+ ions trapped with ~ 1000 Ca^+ ions, all of which were translationally cold ($\sim 10\text{ K}$, primarily due to micromotion heating).

After CCl^+ and Ca^+ ions were loaded, neutral CH_3CN (9-10% CH_3CN or CD_3CN in N_2) was leaked into the vacuum chamber (2×10^{-9} Torr or 3×10^{-7} Pa gas pressure at 300 K) for a set duration of time using a pulsed leak-valve scheme.^[228, 224] Typical chamber base pressure is 4×10^{-10} Torr (5×10^{-8} Pa). The measurements of gas partial pressures in the chamber were recorded using a Bayard-Alpert hot cathode ionization gauge. Because ion gauges are not well characterized at pressures below $\sim 1 \times 10^{-8}$ Torr, the partial pressure of neutral gas in the chamber is subject to systematic uncertainty.^[229] For this reason, emphasis will be placed on determination of experimental reaction products and branching ratios, rather than precision measurements of rate constants. The opening of the leak valve (LV) defined the zero-time point; the LV remained open for 0, 10, 30, 60, 90, 120, 150, 180, 210, 240, or 330 s before ejecting the ions into the TOF-MS. This process was repeated about 10 times for every time step and measured ion numbers from each mass were averaged over each time step. The average number of reactant and product ions were then normalized by the initial CCl^+ numbers and plotted against time, forming a reaction curve. These reaction curves were then used to determine the relevant rate constants. Reaction curves

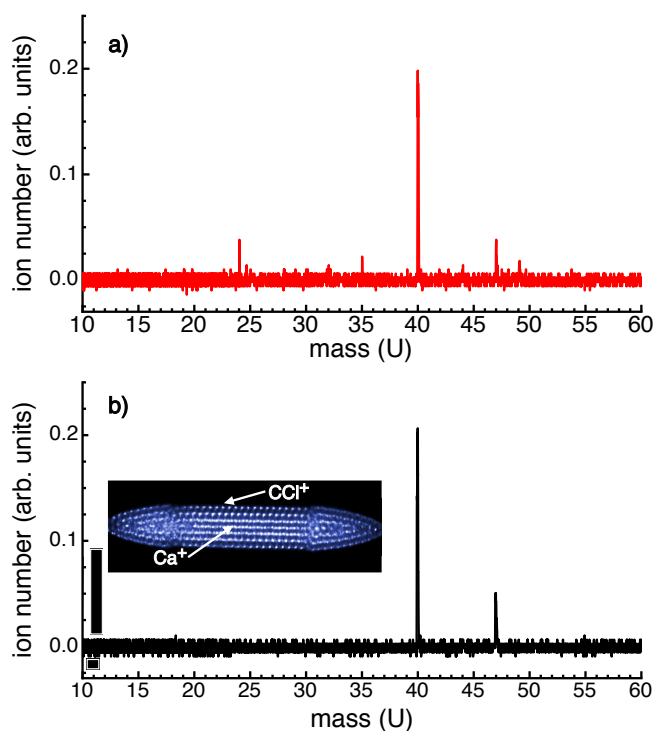


Figure 4.1: **a)** TOF traces demonstrating before and **b)** after cleaning using secular excitations. After cleaning, only Ca⁺ (m/z 40, m/z 42, and m/z 44) and CCl⁺ (m/z 47) remain in quantities greater than ~ 5 ions. Also included on the left is a false-color CCD image of fluorescing Ca⁺ ions, the resulting Coulomb crystal is deformed primarily in the center section by the heavier CCl⁺ ions which sit on the outside of the Ca⁺ in the radial direction. This is seen by the deformation of the fluorescing ions from an ellipsoidal shape to one with the appearance of “flattened” sides. The crystal appears truncated because it expands slightly beyond the CCD camera frame.

were collected in the same manner for isotopologues C³⁷Cl⁺ and CD₃CN, such that all four possible combinations of isotopologues were used. The chemical formula of each mass peak was confirmed by examining the shift in mass spectra as a result of isotopologue substitution (see section 4.3.2), a shift that can be seen due to the excellent mass resolution of the TOF-MS.^[65] In addition, all of the ionic species were tracked via TOF-MS traces. The total number of ions were compared for each time point to ensure that the numbers were constant throughout the experiment; this ruled out systematic losses of ions from the trap. Figures illustrating conservation of charge over each reaction are given with more context in the supplementary material.

4.2.2 Computational Methods

Several theoretical methods were used to explore the potential energy surface for the reaction of $\text{CCl}^+ + \text{CH}_3\text{CN}$. In a previous study, the M06-2X/aug-cc-pVTZ level of theory was found to produce accurate geometries and energies for small nitrogen- and chlorine-containing compounds,^[184] and was therefore chosen to determine possible stationary points. Scans over bond lengths, angles, and dihedrals allowed identification of minima and saddle points. Transition states were verified by visually inspecting the single imaginary frequency and also by using intrinsic reaction coordinate (IRC) analysis. The geometries of the reactants, products, intermediate states, and transition states were then used as starting points for calculations at the MP2/aug-cc-pVTZ level of theory. Zero point energy (ZPE) corrections from calculated harmonic vibrational frequencies (MP2/aug-cc-pVTZ) were added to CCSD(T)/CBS single point energies [CCSD(T)/CBS//MP2/aug-cc-pVTZ nomenclature is used in the subsequent discussions]. Additional higher order calculations were carried out at the CCSD(T)/CBS//CCSD/aug-cc-pVTZ level of theory for reactants and predicted products to provide accurate energetics for the thermodynamic limits of the reaction within 0.04 eV. Even though ^{37}Cl and D isotope substitutions were used experimentally to determine the chemical formulas of the products, calculations accommodating these substitutions are outside the scope of this work. Density functional theory (DFT) calculations and relaxed potential energy surface scans were done using Gaussian 16,^[176] while the higher order MP2 and CCSD computations were done using Psi4 v1.3.2.^[177]

Statistical reaction rate theory calculations were performed to simulate the kinetics of the $\text{CCl}^+ + \text{CH}_3\text{CN}$ reaction. These calculations were carried out using a custom version of the Multi-Well2020 suite of programs,^[230, 231, 232] modified to treat bath-gas collisions using the Langevin model. Simulations followed a general approach that we have used extensively to investigate ion reaction dynamics in a diverse range of instruments, including ion trap,^[233] tandem,^[234] and ion mobility^[235] mass spectrometers. Electronic energies, vibrational frequencies, and moments of inertia were from the CCSD(T)/CBS//MP2/aug-cc-pVTZ model chemistry calculations. Micro-

scopic rate constants were calculated via Rice-Ramsperger-Kassel-Marcus (RRKM) theory, on the basis of rigid-rotor harmonic-oscillator sums and densities of state. For barrierless ion-molecule reactions, association rate coefficients were set at the ADO theory value, with the restricted Gorin model^[236] then applied to fit an effective transition state structure. Energy grained master equation simulations were performed in order to predict the $\text{CCl}^+ + \text{CH}_3\text{CN}$ reaction products. These calculations featured energy grains of 10 cm^{-1} and a single exponential down collisional energy transfer model, with the average energy in deactivating collisions set at 200 cm^{-1} .^[237] Simulations comprised 10^{10} trajectories, and in each case a reaction was predicted to be complete within less than the time required for one bath-gas collision (i.e., effectively collisionless). Simulations were performed at a pressure of 2×10^{-9} Torr N_2 , where acetonitrile was assumed to be infinitely diluted in N_2 . Temperature was varied between 40 and 400 K in order to examine predicted rates from atmospheric down to astrochemically relevant conditions. These simulations assumed statistical behavior, something that can be tested for in the future, when greater control over the energy of the neutral reactant becomes possible.

4.3 Results & Discussion

For the sake of clarity, the reaction thermodynamics will be discussed with the concluded chemical formula assignments in Section [4.3.1](#), followed by experimental support in Section [4.3.2](#). Finally, in Section [4.3.3](#) the modeled potential energy surface, branching ratios, and rate constants of the reaction are discussed.

4.3.1 Reaction thermodynamics

Overall, the reaction of $\text{CCl}^+ + \text{CH}_3\text{CN}$ forms the primary ionic products C_2H_3^+ and HNCCl^+ , which proceed to react with excess CH_3CN to form the secondary product protonated acetonitrile (CH_3CNH^+). This model is illustrated in Fig. [4.2](#).

Neutral CH_3CN was introduced into the vacuum chamber as a room temperature gas (300 K). Therefore, when reacting with translationally cold CCl^+ ($\sim 10\text{ K}$), the calculated collision energy

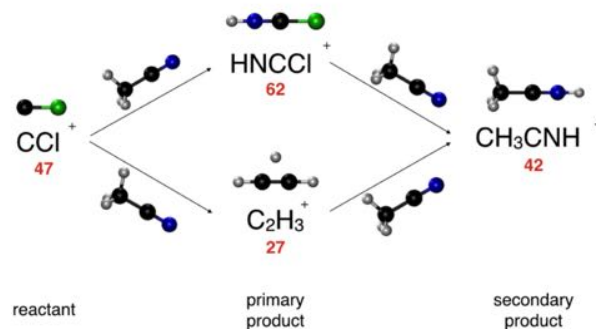
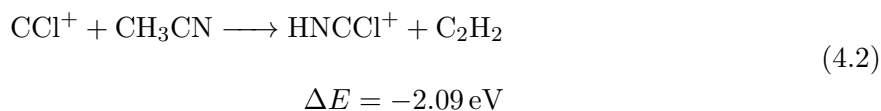
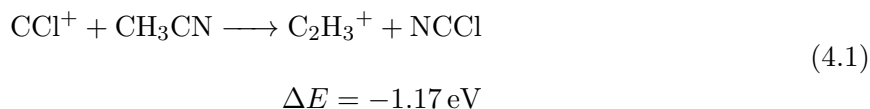


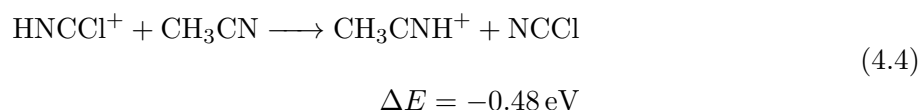
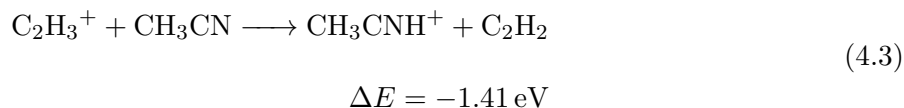
Figure 4.2: Reaction model for $\text{CCl}^+ + \text{CH}_3\text{CN}$, noting the reaction order and identity of ions. Each arrow represents a reaction with a neutral CH_3CN molecule. Red number below the molecule denotes m/z ratio. The molecular ions are depicted above, with black indicating carbon, blue for nitrogen, white for hydrogen, and green for chlorine.

for the reaction is characterized by a temperature of about 160 K (~ 15 meV). This provides an approximate upper limit to the reaction energetics. The observed products are all significantly exothermic and well below the upper limit provided by the calculated collision energy, as shown by Equations [4.1](#)[4.4](#) [CCSD(T)/CBS//CCSD/aug-cc-pVTZ; accurate within 0.04 eV].

Primary products:



Secondary products:



These calculated limits assume the lowest energy isomers. For example, in Eqns. 4.2 and 4.3, the $C_2H_3^+$ energy refers to that of the non-classical “bridge” isomer (see Fig. 4.2 or PRD2 in Fig. 4.7). This non-classical isomer is where the third H hovers between the two carbons, as opposed to the “classical” or “Y” structure ($H_2C_2H^+$, see PRD3 in Fig. 4.7). Other possible isomeric products are discussed in Section 4.3.3

4.3.2 Reaction measurements

One consideration here is that Ca^+ reacts with acetonitrile[77] to produce $CaCN^+$ (m/z 66) with no further reactions. This was verified by reacting $Ca^+ + CH_3CN$ – without loading CCl^+ ions – and demonstrating the growth of the m/z 66 mass channel concurrent with the equivalent loss of ions in the m/z 40 channel. We compared the modeled reaction rate with and without the presence of CCl^+ and concluded no statistically significant differences between the two cases. Furthermore, if $CCl^+ + CH_3CN$ had products that overlapped with this single $Ca^+ + CH_3CN$ product channel, there would be ions missing from the final CX_3CNX^+ channel (where X denotes the appropriate H or D), which is not the case for any of our isotopologue combinations. For this reason, we believe we can fully delineate the products of the two reactions.

Curves that are produced from the reaction of $CCl^+ + CH_3CN$ are shown in Fig. 4.3. Here, CCl^+ (m/z 47; blue) reacts to form two primary products: $C_2H_3^+$ (m/z 27; green) and $HNCCl^+$ (m/z 62; black). The reduction of the CCl^+ population (blue) is concurrent with the growth of $C_2H_3^+$ (green) and $HNCCl^+$ (black). Both of the primary product populations then reduce over time as the secondary product CH_3CNH^+ (m/z 42; red) population grows from reactions with excess CH_3CN . CH_3CNH^+ is confirmed as a second order product because its maximum slope coincides with the maximum number of primary products.

Experimental reaction rates are determined by fitting the reaction data to a pseudo-first order model. CCl^+ was modeled to branch into primary products $C_2H_3^+$ and $HNCCl^+$. These primary products were then modeled to react again with CH_3CN to form CH_3CNH^+ . This model

corresponds to the follow set of differential equations:

$$\begin{aligned}
 \frac{d[N_{\text{CCl}^+}]}{dt} &= -[N_{\text{CCl}^+}] \cdot (k_{\text{CCl}^+ \rightarrow \text{C}_2\text{H}_3^+} + k_{\text{CCl}^+ \rightarrow \text{HNCCl}^+}) \\
 \frac{d[N_{\text{C}_2\text{H}_3^+}]}{dt} &= [N_{\text{CCl}^+}] \cdot k_{\text{CCl}^+ \rightarrow \text{C}_2\text{H}_3^+} - [N_{\text{C}_2\text{H}_3^+}] \cdot k_{\text{C}_2\text{H}_3^+ \rightarrow \text{CH}_3\text{CNH}^+} \\
 \frac{d[N_{\text{HNCCl}^+}]}{dt} &= [N_{\text{CCl}^+}] \cdot k_{\text{CCl}^+ \rightarrow \text{HNCCl}^+} - [N_{\text{HNCCl}^+}] \cdot k_{\text{HNCCl}^+ \rightarrow \text{CH}_3\text{CNH}^+} \\
 \frac{d[N_{\text{CH}_3\text{CNH}^+}]}{dt} &= [N_{\text{C}_2\text{H}_3^+}] \cdot k_{\text{C}_2\text{H}_3^+ \rightarrow \text{CH}_3\text{CNH}^+} + [N_{\text{HNCCl}^+}] \cdot k_{\text{HNCCl}^+ \rightarrow \text{CH}_3\text{CNH}^+}
 \end{aligned}
 \tag{4.5}$$

Where “[N]” refers to the number of ions of the denoted chemical formula, and “k” refers to the fitted rate constant from one indicated ion to another. This set of equations reflects the complete model for the unsubstituted reaction, as shown in Fig. 4.3.

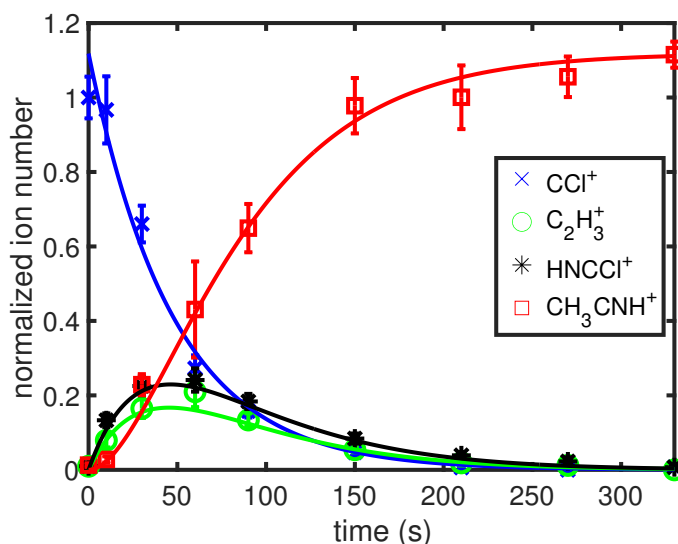


Figure 4.3: Rate reaction data (points) and fits (curves) for pseudo-first order reaction of $\text{CCl}^+ + \text{CH}_3\text{CN}$. CCl^+ (blue x) reacts with excess CH_3CN resulting in first order products C_2H_3^+ (green circle) and HNCCl^+ (black asterisk). Each of these primary products then reacts with excess CH_3CN to form CH_3CNH^+ (red box).

The primary product mass assignments, namely C_2H_3^+ and HNCCl^+ , given by the initial reaction of $\text{CCl}^+ + \text{CH}_3\text{CN}$ were verified by using different combinations of isotopologues. Specifically C^{37}Cl^+ (m/z 49) and CD_3CN (m/z 44) were used to form four possible combinations of reactants. Reaction curves were measured for each of the four unique pairs and mass peak shifts were recorded for each case. Specifically, when the reaction proceeded with $\text{C}^{37}\text{Cl}^+ + \text{CH}_3\text{CN}$, only

one of the primary products shifted, m/z 62 \rightarrow 64 ($\text{HNC}^{37}\text{Cl}^+$), identifying it as the only chlorine-containing product. In the case of $\text{CCl}^+ + \text{CD}_3\text{CN}$, both primary products shifted: m/z 27 \rightarrow 30 (C_2D_3^+), and m/z 62 \rightarrow 63 (DNCCl^+). Furthermore, the secondary product shifted, m/z 42 \rightarrow 46 (CD_3CND^+). In the final case, $\text{C}^{37}\text{Cl}^+ + \text{CD}_3\text{CN}$, the mass shifts were consistent with the aforementioned products. An additional process occurs in reactions involving CD_3CN , which produces a small amount of a tertiary product m/z 45, assigned to CD_3CNH^+ . This tertiary process occurs possibly by either from H-D swapping or from contributions from a small number of contaminant ions remaining from the initial ion loading scheme (any given contaminant constitutes $\leq 5\%$ of 150-250 initial CCl^+ numbers).

Modeling these isotope-substituted reactions was slightly more complicated than the unsubstituted reactions as there was greater incidence of contaminant ions. Namely, the population of ions that were unable to be removed from the trap before the reaction was initiated each represented $\leq 5\%$ of the initial CCl^+ numbers (150-250), but together were more notable in the C^{37}Cl^+ reactions. Many of these (for example, m/z 19, likely H_3O^+ , or m/z 25, C_2H^+) were suspected to be directly or indirectly contributing to the protonated acetonitrile signal, and were modeled as such:

$$\begin{aligned}
\frac{d[N_{\text{CCl}^+}]}{dt} &= - [N_{\text{CCl}^+}] \cdot (k_{\text{CCl}^+ \rightarrow \text{C}_2\text{H}_3^+} + k_{\text{CCl}^+ \rightarrow \text{HNCCl}^+}) \\
\frac{d[N_{\text{C}_2\text{H}_3^+}]}{dt} &= [N_{\text{CCl}^+}] \cdot k_{\text{CCl}^+ \rightarrow \text{C}_2\text{H}_3^+} - [N_{\text{C}_2\text{H}_3^+}] \cdot k_{\text{C}_2\text{H}_3^+ \rightarrow \text{CH}_3\text{CNH}^+} \\
\frac{d[N_{\text{HNCCl}^+}]}{dt} &= [N_{\text{CCl}^+}] \cdot k_{\text{CCl}^+ \rightarrow \text{HNCCl}^+} - [N_{\text{HNCCl}^+}] \cdot k_{\text{HNCCl}^+ \rightarrow \text{CH}_3\text{CNH}^+} \\
\frac{d[N_{\text{CH}_3\text{CNH}^+}]}{dt} &= [N_{\text{C}_2\text{H}_3^+}] \cdot k_{\text{C}_2\text{H}_3^+ \rightarrow \text{CH}_3\text{CNH}^+} + [N_{\text{HNCCl}^+}] \cdot k_{\text{HNCCl}^+ \rightarrow \text{CH}_3\text{CNH}^+} \\
&\quad + [N_{\text{cont}}] \cdot k_{\text{cont} \rightarrow \text{CH}_3\text{CNH}^+} \\
\frac{d[N_{\text{cont}}]}{dt} &= - [N_{\text{cont}}] \cdot k_{\text{cont} \rightarrow \text{CH}_3\text{CNH}^+}
\end{aligned} \tag{4.6}$$

This set of differential equations represents the model used to fit the reaction $\text{C}^{37}\text{Cl}^+ + \text{CH}_3\text{CN}$ (Fig. 4.4).

When deuterated acetonitrile is used, it is assumed that the hydrogen-containing contami-

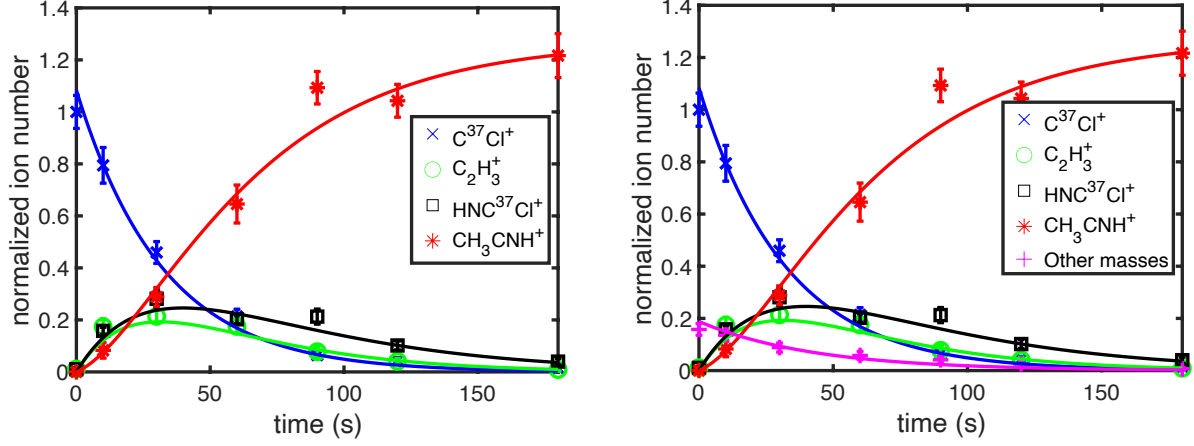


Figure 4.4: Figure 4.4: **(left)**: Rate reaction data (points) and fits (curves) for pseudo-first order reaction of $C^{37}Cl^+ + CH_3CN$. $C^{37}Cl^+$ (blue x) reacts with excess CH_3CN , resulting in first order products $C_2H_3^+$ (green circle) and $HNC^{37}Cl^+$ (black box). Each of these primary products then reacts with excess CH_3CN to form CH_3CNH^+ (red asterisk). **(right)** The same reaction curve fit, here also demonstrating the contaminant population (magenta +).

nants still protonate acetonitrile (producing CD_3CNH^+). In addition, a small turnover seen in the population of CD_3CND^+ is attributed to H-D swapping either caused in the gas delivery lines, or do to small amounts of ambient water in the trap itself. In this case, our model becomes:

$$\begin{aligned}
 \frac{d[N_{CCl^+}]}{dt} &= - [N_{CCl^+}] \cdot (k_{CCl^+ \rightarrow C_2D_3^+} + k_{CCl^+ \rightarrow DNCCl^+}) \\
 \frac{d[N_{C_2D_3^+}]}{dt} &= [N_{CCl^+}] \cdot k_{CCl^+ \rightarrow C_2D_3^+} - [N_{C_2D_3^+}] \cdot k_{C_2D_3^+ \rightarrow CD_3CND^+} \\
 \frac{d[N_{DNCCl^+}]}{dt} &= [N_{CCl^+}] \cdot k_{CCl^+ \rightarrow DNCCl^+} - [N_{DNCCl^+}] \cdot k_{DNCCl^+ \rightarrow CD_3CND^+} \\
 \frac{d[N_{CD_3CND^+}]}{dt} &= [N_{C_2D_3^+}] \cdot k_{C_2D_3^+ \rightarrow CD_3CND^+} + [N_{DNCCl^+}] \cdot k_{DNCCl^+ \rightarrow CD_3CND^+} \\
 &\quad - [N_{CD_3CND^+}] \cdot k_{CD_3CND^+ \rightarrow CD_3CNH^+} \\
 \frac{d[N_{CD_3CNH^+}]}{dt} &= [N_{CD_3CND^+}] \cdot k_{CD_3CND^+ \rightarrow CD_3CNH^+} + [N_{cont}] \cdot k_{cont \rightarrow CD_3CNH^+} \\
 \frac{d[N_{cont}]}{dt} &= - [N_{cont}] \cdot k_{cont \rightarrow CD_3CNH^+}
 \end{aligned} \tag{4.7}$$

This model was used to fit data for the reactions $CCl^+ + CD_3CN$ (Fig. 4.5) and $C^{37}Cl^+ + CD_3CN$ (Figure 4.6)

The measured rate constants for primary products of $CCl^+ + CH_3CN$ are reported in Table

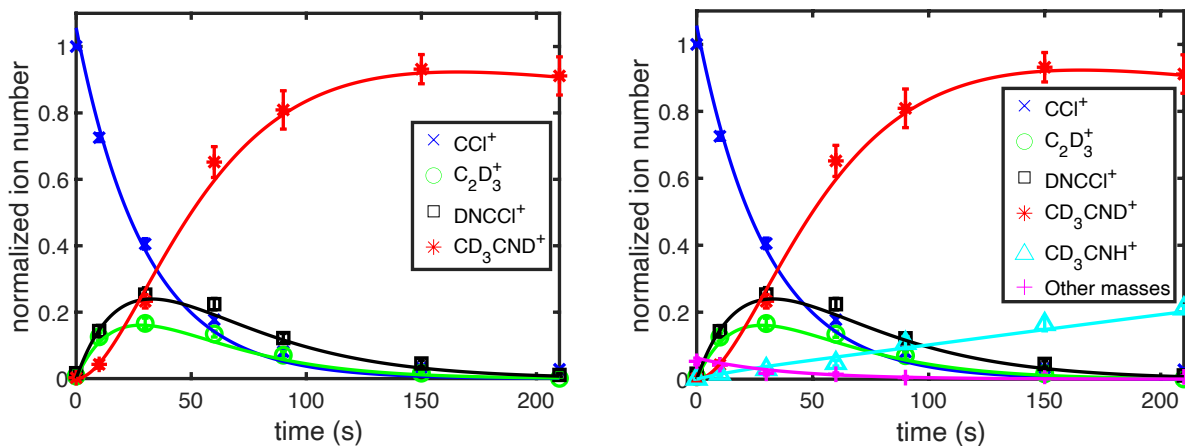


Figure 4.5: Figure 4.5: **(left)**: Rate reaction data (points) and fits (curves) for pseudo-first order reaction of $\text{CCl}^+ + \text{CD}_3\text{CN}$. CCl^+ (blue x) reacts with excess CD_3CN , resulting in first order products C_2D_3^+ (green circle) and DNCCI^+ (black box). Each of these primary products then reacts with excess CD_3CN to form CD_3CND^+ (red asterisk). **(right)** The same reaction curve fit, here also demonstrating the contaminant population (magenta $+$), and protonated acetonitrile formation, CD_3CNH^+ (cyan triangle).

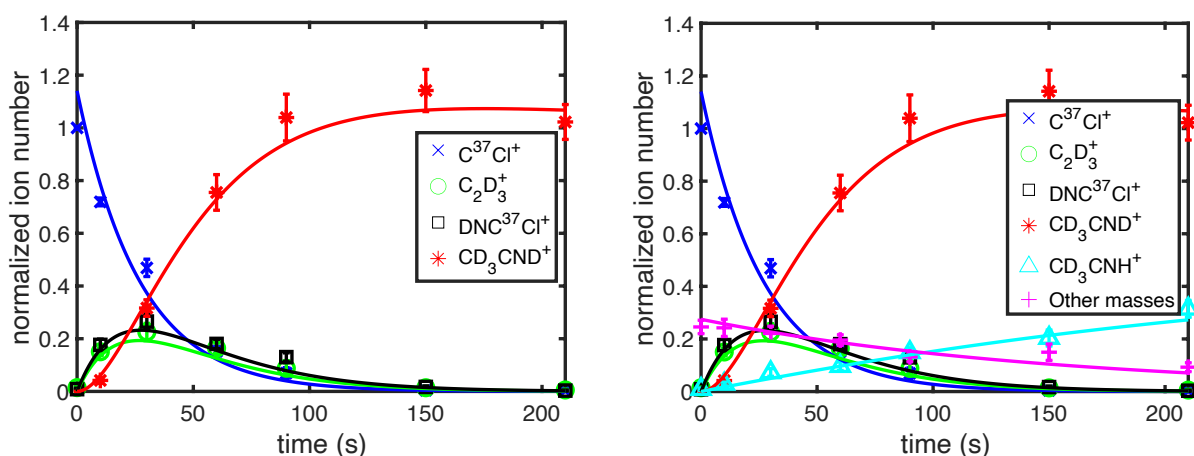


Figure 4.6: Figure 4.6: **(left)**: Rate reaction data (points) and fits (curves) for pseudo-first order reaction of $\text{C}^{37}\text{Cl}^+ + \text{CD}_3\text{CN}$. C^{37}Cl^+ (blue x) reacts with excess CD_3CN , resulting in first order products C_2D_3^+ (green circle) and $\text{DNC}^{37}\text{Cl}^+$ (black box). Each of these primary products then reacts with excess CD_3CN to form CD_3CND^+ (red asterisk). **(right)** The same reaction curve fit, here also demonstrating the contaminant population (magenta $+$), and protonated acetonitrile formation, CD_3CNH^+ (cyan triangle).

4.1. The Langevin capture model is a natural starting place for the analysis of experimental reaction rate constants, as it is the simplest and most general approach for predicting rate constants in

Table 4.1: Rate constants for isotopological variations of $\text{CCl}^+ + \text{CH}_3\text{CN}$ primary products. ‘X’ represents a hydrogen or deuterium from acetonitrile, and corresponds to the isotopologue used. Rates are in units of $\times 10^{-9} \text{ cm}^3/\text{s}$, and reported statistical uncertainty is the calculated 90% confidence interval.

Reactants	C_2X_3^+	XNCCl^+	total
$\text{CCl}^+ + \text{CH}_3\text{CN}$	1.6 ± 0.5	2.2 ± 0.5	3.8 ± 0.4
$\text{C}^{37}\text{Cl}^+ + \text{CH}_3\text{CN}$	2.9 ± 0.7	3.0 ± 0.7	5.9 ± 0.3
$\text{CCl}^+ + \text{CD}_3\text{CN}$	2.4 ± 0.5	3.0 ± 0.5	5.4 ± 0.3
$\text{C}^{37}\text{Cl}^+ + \text{CD}_3\text{CN}$	2.9 ± 0.8	3.4 ± 0.8	6.3 ± 0.3

this regime. Notably temperature-independent, this theory estimates the likelihood of collisions between an ion and a neutral nonpolar molecule. The Langevin rate constant was found to be $k = 1.11 \times 10^{-9} \text{ cm}^3/\text{s}$, 3-6 times smaller than the total reaction rate constant. This underestimation is most likely due to the polar nature of neutral CH_3CN , which is not accounted for in Langevin theory. Average dipole orientation (ADO) theory expands on Langevin theory to account for the polarity of the neutral reactant and should show closer agreement with the measured total reaction rate constant.^[40] This is reflected in the fact that CH_3CN has a rather large dipole-locking constant (c) of ~ 0.25 , leading to $k_{\text{ADO},\text{unsub}} = 3.74 \times 10^{-9} \text{ cm}^3/\text{s}$ (calculated with the reduced mass of unsubstituted reactants). Parametrized trajectory calculations,^[39] a variation on ADO theory, were also carried out for this system, with a calculated rate constant of $k_{\text{traj}} = 5.27 \times 10^{-9} \text{ cm}^3/\text{s}$. The parameterized trajectory theory value agrees with the ADO value within the precision of our experiments, and the subsequent analysis refers only to the ADO values. Our measured total reaction rate constant for $\text{CCl}^+ + \text{CH}_3\text{CN}$, $3.8 \pm 0.7 \times 10^{-9} \text{ cm}^3/\text{s}$ (see Table 4.1), reflects good agreement with ADO theory. This agreement testifies to the high degree of efficiency of the $\text{CCl}^+ + \text{CH}_3\text{CN}$ reaction, where effectively every ion-molecule collision results in the formation of new reaction products, with little reformation of the reactants (*vide infra*). The high reactivity of CCl^+ toward acetonitrile stands in stark contrast to much of the previous work on the reaction kinetics of this ion with neutral molecules.

The isotope substituted total reaction rate constants (also in Table 4.1) agree fairly well with the measured rate constant for $\text{CCl}^+ + \text{CH}_3\text{CN}$, but are somewhat faster, between $5.4 - 6.4 \times$

10^{-9} cm³/s, compared to the unsubstituted total reaction rate constant. This trend is not precisely captured by ADO theory, which predicts a very small ($\leq 5\%$) reduction in the rate constant for both C³⁷Cl⁺ and CD₃CN substitutions. There is precedence for the trend of increased rate constant upon isotope substitution. Indeed, recently, this inverse kinetic isotope effect has been observed using a similar apparatus and Coulomb crystal environment by monitoring the charge exchange reaction between Xe⁺ and NH₃ or ND₃. This effect, which was suggested to be due to intramolecular vibrational redistribution (IVR) occurring at a faster rate, and to a higher density of states in the deuterated ammonia.^[68] It is possible that we are observing a similar effect here. It should be emphasized that we use a Bayard-Alpert hot cathode ionization gauge to measure the partial pressure of CH₃CN gas in the chamber. While sensitivity factors for the gases used in this study have been previously measured, they are not well characterized at pressures of $10^{-9} - 10^{-10}$ Torr (current regime). This systematic uncertainty is difficult to quantify, and is not reflected in our reported uncertainties. For this reason, we do not make a definitive assessment as to whether we are observing an inverse kinetic isotope effect. Instead, more significance is placed on the determination of branching ratios (see Table 4.2) and assignments of chemical formulas and structures of observed reaction products, rather than to individual rate constant measurements.

Table 4.2: Branching ratios for primary products by isotopological variations of CCl⁺ + CH₃CN reaction. The calculated branching ratio represents the fraction of protonated acetylene rate constant, divided by the total CCl⁺ decay rate constant. ‘X’ represents a hydrogen or deuterium, and corresponds to neutral reactant.

Reactants	Branching Ratio ($k(\text{C}_2\text{X}_3^+)/k_{total}$)
CCl ⁺ + CH ₃ CN	0.43 ± 0.16
C ³⁷ Cl ⁺ + CH ₃ CN	0.50 ± 0.17
CCl ⁺ + CD ₃ CN	0.44 ± 0.11
³⁷ CCl ⁺ + CD ₃ CN	0.46 ± 0.17

The branching ratios shown in Table 4.2 are nearly 50% for each of the primary products; here reported as the rate of the C₂H₃⁺ production over the sum of both primary product rate constants. If all products branched from the same final step of the potential energy surface (see

Fig. 4.7), the more exothermic product, HNCCl^+ , might be expected to be favored. However, as will be discussed in section 4.3.3, the potential energy surface is much more complex, with the existence of branching pathways, as well as multiple isomers of products. This necessitates an energy grained master equation approach to obtain quantitative branching ratio predictions.

Secondary reactions with excess CH_3CN are comprised of a proton transfer from either C_2H_3^+ or HNCCl^+ forming CH_3CNH^+ . Analysis of the kinetics for these reactions is more straightforward, and the relative proton affinities of the neutral molecules guide our expectations for the stability of the products. CH_3CN has a larger proton affinity than either NCCl or C_2H_2 and thus both primary products transfer a proton to neutral CH_3CN to form the secondary product CH_3CNH^+ . Reaction dynamics predicted by relative proton affinities has precedence in ion-neutral gas-phase chemistry, and bounds on proton affinities have been determined by examining which proton transfers do or do not take place.^[238] In addition, these reactions are both energetically favorable, as per the reaction thermodynamics reported in Eqns. 4.3-4.4. As for the relative rate constants calculated for the second order reactions, ADO theory predicts a slightly larger rate constant for the $\text{C}_2\text{H}_3^+ + \text{CH}_3\text{CN}$ reaction ($4.3 \times 10^{-9} \text{ cm}^3/\text{s}$) due to its smaller reduced mass as compared to $\text{HNCCl}^+ + \text{CH}_3\text{CN}$ ($3.5 \times 10^{-9} \text{ cm}^3/\text{s}$). This trend is consistent with the reported experimental reaction rate constants in Table 4.3. Overall, there is reasonable agreement within the experimental uncertainty between the ADO calculated rate constants and those measured experimentally.

4.3.3 Modeling the $\text{CCl}^+ + \text{CH}_3\text{CN}$ reaction

The potential energy surface shown in Fig. 4.7 represents a few plausible reaction pathways of the $\text{CCl}^+ + \text{CH}_3\text{CN}$ reaction. It is a result of quantum chemical calculations and is comprised of equilibrium structures that bridge the reactants and the observed products. The experimental conditions are cold ($\sim 160 \text{ K}$) and very low pressure, which therefore means that there is no quenching of the internal energy of any of the intermediate low energy structures. Furthermore, the stationary points along this reaction pathway are all exothermic with respect to the reactants, such that the reaction complex can sample all these intermediary states until it leaves the surface irreversibly.

Table 4.3: Rate constants for isotope variations of $\text{CCl}^+ + \text{CH}_3\text{CN}$ secondary products. ‘X’ represents a hydrogen or deuterium from CH_3CN , and corresponds to the isotopologue used. Rates are in units of $\times 10^{-9} \text{ cm}^3/\text{s}$, and reported statistical uncertainty is the calculated 90% confidence interval.

Reactants	CX_3CNX^+
$\text{C}_2\text{H}_3^+ + \text{CH}_3\text{CN}$	4.2 ± 1.7
$\text{HNCCl}^+ + \text{CH}_3\text{CN}$	4.1 ± 1.2
$\text{C}_2\text{H}_3^+ + \text{CH}_3\text{CN}$	6.2 ± 2.0
$\text{HNC}^{37}\text{Cl}^+ + \text{CH}_3\text{CN}$	3.8 ± 1.1
$\text{C}_2\text{D}_3^+ + \text{CD}_3\text{CN}$	6.0 ± 1.5
$\text{DNCCl}^+ + \text{CD}_3\text{CN}$	4.4 ± 0.9
$\text{C}_2\text{D}_3^+ + \text{CD}_3\text{CN}$	6.2 ± 2.3
$\text{DNC}^{37}\text{Cl}^+ + \text{CD}_3\text{CN}$	5.9 ± 1.9

It is useful to consider the potential energy surface not only because it is an accessible way to explore the pathways to eventual exothermic products presented, but also because it provides a basis for the quantitative master equation-based kinetic modeling presented below. For clarity, the non-hydrogen atoms will be numbered C1, C2, N3, C4, Cl5, as marked on INT1 in Fig. [4.7](#).

In the presented potential energy surface, CCl^+ and CH_3CN initially form the adduct INT1 as a bond is formed between N3 and C4. This structure then undergoes various changes in its bond lengths and angles isomerizing into the lower energy INT2 structure. INT2 can isomerize into INT4, which can dissociate without a barrier into PRD1 ($\text{HNCCl}^+ + \text{HC}_2\text{H}$), PRD2 ($\text{C}_2\text{H}_3^+ + \text{NCCl}$; where C_2H_3^+ is the non-classical bridge structure), or PRD4 ($\text{HNCCl}^+ + \text{H}_2\text{C}_2$; where H_2C_2 is the vinylidene isomer of C_2H_2). Determining the exact chemical identity of the C_2H_2 isomer is beyond the scope of this study: while the m/z of ionic products is known based on the mass spectra, neutral products are speculative since they cannot be observed experimentally.

INT2 can also isomerize to INT3, which leads to the barrierless dissociation into PRD3, the classical ‘‘Y’’ C_2H_3^+ structure and NCCl . The isomerization barrier between the two isomers of C_2H_3^+ has been the subject of rigorous computational and experimental studies, and was found to be 4.8 meV as calculated at the CBS-APNO level of theory.[\[239\]](#), [\[240\]](#), [\[241\]](#) Regardless of which

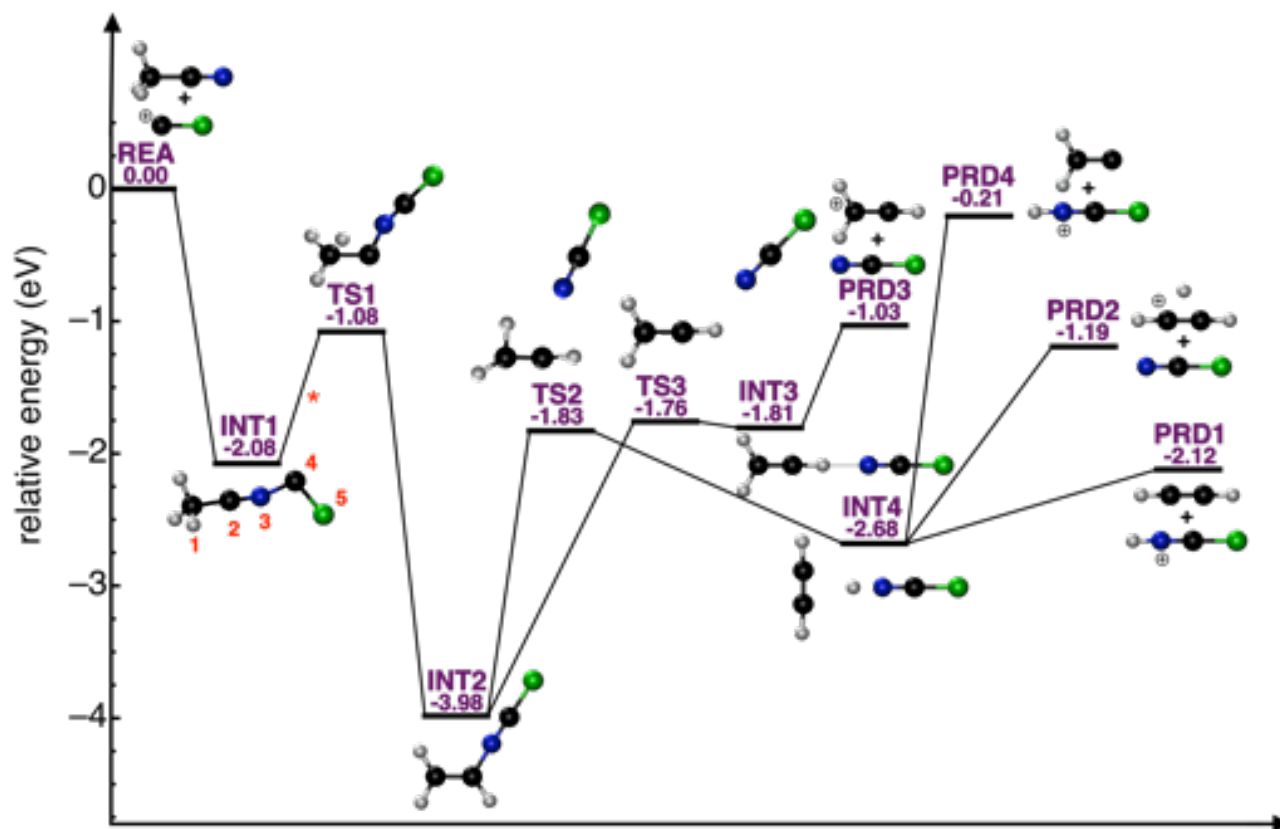


Figure 4.7: Potential energy surface for $\text{CCl}^+ + \text{CH}_3\text{CN}$, depicting equilibrium geometries connecting the reactants (REA) to the products (PRD1, PRD2, PRD3, and PRD4). In REA, PRD1, PRD2, PRD3, and PRD4, the bare '+' denotes infinite distance between the ion-neutral pair, while the encircled '+' indicates the ion of the ion-neutral pair. Geometries were calculated at MP2/aug-cc-pVTZ level, with CCSD(T)/CBS//MP2/aug-cc-pVTZ energies. 'INT' refers to intermediate states, while 'TS' indicates transition states. Asterisk denotes a step with an extremely shallow well, the depth of which depends on the level of theory).

isomer is produced in this reaction, both isomers are energetically allowed, with exothermicity larger than the isomerization barrier. Therefore, either C_2H_3^+ isomer may be the experimentally observed cation.

All of the outlined products are exothermic with respect to the reactants and there are only submerged barriers in the potential energy surface. This indicates that both products are likely to

form, which is perhaps reflected in the experimentally observed branching ratios being equal. This observation is tested below through RRKM theory/master equation kinetic modeling.

There are no previous measurements for reactions of CCl^+ with any nitriles with which to compare the current results. It does appear to be significant that the elucidated potential energy surface requires cleaving of the $\text{C}\equiv\text{N}$ bond of CH_3CN . However, this is perhaps unsurprising given that once a bond is formed between the two reactants, more electron density will be pulled toward the more electronegative chlorine group. This is demonstrated in the first step of the PES, when INT1 (see Fig. 4.7) is formed. Two C-N bonds are of importance to this discussion: the C2-N3 bond, which originated from CH_3CN , and the C4-N3 bond, where the carbon from CCl^+ attaches to the terminal nitrogen of CH_3CN . The shift of electron density from the C2-N3 bond to the C4-N3 and C4-Cl5 bonds occurs in this first steps of this potential energy surface. On this surface, the shift of electron density between stationary points INT1 and TS1 (Fig. 4.7) suggests the $\text{C}\equiv\text{N}$ functional group pairs with Cl over CH_3 , stabilizing the complex with respect to the reactants. This is perhaps intuitive, as the highly electronegative Cl atom pulls electron density towards itself, forming a strong bond, further assisted by the electron donating methyl group of CH_3CN .

All products that are observed in this study are possibly a result of this shift and subsequent cleavage. Using the $^{13}\text{CH}_3\ ^{13}\text{CN}$ isotopologue as the neutral reactant could possibly provide more convincing experimental evidence of the $\text{C}\equiv\text{N}$ bond cleaving mechanism, however, the cost of the reagent was prohibitive. While unsuccessful attempts were made to find a reaction pathway that did not cleave this $\text{C}\equiv\text{N}$ bond, this did not constitute an exhaustive search of the PES. Regardless of whether a reaction pathway without cleavage of the $\text{C}\equiv\text{N}$ bond exists, this theoretical mechanism is interesting in its own right.

To gain further insight into the $\text{CCl}^+ + \text{CH}_3\text{CN}$ reaction, RRKM theory / master equation simulations were conducted on the basis of the potential energy surface reported in Fig. 4.7 (with PRD4 excluded). Predicted rate constants are plotted in Fig. 4.8 for the overall reaction and for formation of the PRD1 - PRD3 products as a function of temperature. Here, the overall rate constants reflect the ADO theory rates less any reverse dissociation of the ion-molecule complex

back to the reactants. Also included in Fig. 4.8 is the experimental measurement made here and the ADO theory capture rate constants.

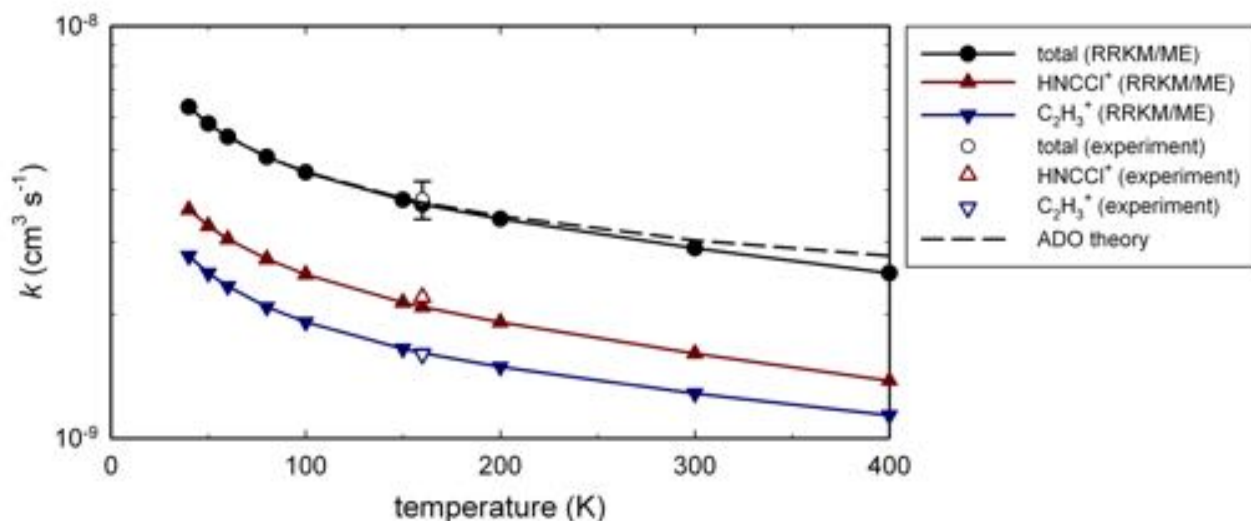


Figure 4.8: Theoretical (RRKM/ME) rate constants for the $\text{CCl}^+ + \text{CH}_3\text{CN}$ reaction as a function of temperature. Values are included for the overall reaction (total) and for the formation of product ions HNCCI^+ (PRD1) and C_2H_3^+ (PRD2 + PRD3). Included for comparison are the experimental measurements (at the effective temperature of 160 K) and the ADO theory capture rate constants.

Fig. 4.8 indicates that the total rate constant is in good agreement with the experimental value, which in turn is similar to the ADO capture value. This reflects the high efficiency of the $\text{CCl}^+ + \text{CH}_3\text{CN}$ reaction, which leads almost exclusively to new products. This is in turn attributed to both the low barriers for $\text{CH}_3\text{CNCCI}^+$ isomerization and the availability of dissociation channels for the subsequent isomers at below the reactant energy. Only at temperatures of around 300 K and above is the reverse dissociation channel significant, resulting in the predicted rate coefficients to fall below the upper limit set by ADO theory.

Branching between the C_2H_3^+ and HNCCI^+ product ions is approximately 50:50, again in accord with the experiments. Interestingly, product PRD3 is predicted to be the dominant pathway to C_2H_3^+ , suggesting that it is formed in the classical, yet slightly higher-energy, vinylum form. This result is attributed to transition states TS2 and TS3 throttling the reaction flux from INT2

to a similar extent. Once TS2 is overcome, dissociation to PRD1 outcompetes all other channels (including PRD2), due to its low energy and high entropy. Following TS3, INT3 prefers to dissociate further to PRD3 than to isomerize back to INT2, presumably due to the loose forward dissociation being highly favored in terms of entropy.

4.4 Conclusion and outlook

The gas-phase reaction of $\text{CCl}^+ + \text{CH}_3\text{CN}$ is presented, with primary products C_2H_3^+ and HNCCl^+ formed in approximately equal yields, and both channels producing a CH_3CNH^+ secondary product. The LIT TOF-MS used in this study enables experimental conditions of low pressures and collisional energies, limiting the reaction dynamics to exothermic pathways without quenching the internal energy of the reaction complex. In addition, the high mass resolution afforded by the TOF-MS yields methodical product identification that is supported by isotope substitution and quantum chemical calculations. The presented potential energy surface pathways indicate a series of equilibrium structures shifting electron density from the original $\text{CH}_3\text{CN C}\equiv\text{N}$ bond to the new $\text{C}\equiv\text{N}$ bond formed with the carbon of CCl^+ . The experimental rate constants were reported and compared to Langevin and ADO theory capture rates, as well as to detailed master equation / RRKM theory-based simulations of the reaction kinetics on a multiple-channel multiple-well potential energy surface. ADO theory, which includes the polarity of the neutral reactant, is in good agreement with the observed experimental primary product rate constants. The master equation modeling indicates that reaction is highly efficient, with the total rate constant predicted to approach the capture rate constant, consistent with capture-rate limited kinetics. Moreover, these calculations reproduce the experimentally observed branching fractions between the primary ionic products C_2H_3^+ and HNCCl^+ . Although CCl^+ has been predicted to not react with several neutrals, here, we see this is not the case, which is consistent with the previously observed reactions with C_2H_2 .[\[213\]](#) This study presents the first example of this class of gas-phase reactions to be studied in a regime more closely comparable to that of the ISM and should aid in predicting the behavior of halogenated carbocations and nitriles in this region.

Future studies could further characterize CH_3CN with analogous reactions of various halogenated carbocations such as the astrochemically relevant ion CF^+ . In theory, a reaction of CF^+ with CH_3CN would behave similarly, and the even more electronegative fluorine might be expected to reproduce chlorine's behavior here. This would be particularly relevant to verify, as the presence of CF^+ in the ISM is more firmly established. It would also be interesting to study the effects of various functional groups (possibly more electron donating or withdrawing) attached to the $\text{C}\equiv\text{N}$ in lieu of the methyl of CH_3CN . For example, benzonitrile $\text{C}_6\text{H}_5(\text{CN})$ with its attached phenyl group could help stabilize intermediates or primary products and thus possibly shift the observed reaction rates. Studying the reaction of CCl^+ with various substituted nitriles might help elucidate a trend in nitrile reactivity in this low pressure and cold ($\sim 160\text{ K}$) regime. Overall, probing the relative $\text{C}\equiv\text{N}$ bond strength across nitriles might contribute to the understanding and predictions of the formation and reactivity of the nitriles present throughout the ISM. Although further isotope tagging is necessary to absolutely verify the experimental reaction mechanism, the computational results are suggestive, and open questions for the role and reactivity of the $\text{C}\equiv\text{N}$ bond in nitriles.

For the LIT-TOFMS apparatus, future directions also include the integration of a traveling wave Stark decelerator [19, 17] to expand control over the internal and external energies of polar neutral molecules. The ability to slow molecules down into the millikelvin regime allows the elucidation of whether quantum mechanical effects play a greater role in ion-neutral chemical dynamics. In this way, it presents an opportunity to both understand this class of reactions at a fundamental level, as well as further our understanding of ISM chemistry.

Chapter 5

Formation of astrochemically relevant molecular ions: reaction of translationally cold CCl^+ with benzene in a linear ion trap

“Speculation and the exploration of ideas beyond what we know with certainty are what lead to progress. They are what makes science exciting.”

– Lisa Randall, “Dangling Particles,” New York Times Op-ed, 2005

The following chapter is adapted from a work of the same name published in Physics Review A.[\[242\]](#) I was the primary contributor to the data acquisition and analysis. I began the initial computational calculations, but the majority of the work was completed by our excellent former postdoctoral researcher Katherine Catani.

5.1 Introduction

Rich chemistry takes place in regions that we still know relatively little about, such as areas of the interstellar medium (ISM) and planetary atmospheres. This chemistry is slowly being understood through a multidisciplinary effort focused on laboratory and theoretical studies, as well as physical measurements from new space exploration missions. [243, 194, 244, 34, 245, 246, 25, 247, 248, 249, 250, 251, 252] Within this larger effort, ion-neutral reactions have been identified as requiring more experimental exploration, especially at lower temperatures. [34] This is because ion-neutral reactions are known to have much faster rates than neutral-neutral reactions, and thus, are predicted to have a more prominent role in the chemistry present in these remote areas. [34, 253] Of particular interest are the ion-neutral reaction pathways that lead to carbon molecular weight growth and perhaps to polycyclic aromatic hydrocarbons (PAHs). Interest in PAHs is fueled by their ubiquity in, and importance to, the chemistry of many regions of the ISM. [254, 255, 256, 257, 258, 245, 259, 260] Interest has also been due to speculation that PAHs could be the carriers for the diffuse interstellar bands (DIBs), the mostly unidentified absorption features seen towards reddened stars and other extraterrestrial objects. [245, 252] Only C_{60}^+ has been confirmed as a carrier, but the PAH hypothesis has fueled many spectroscopic and kinetic studies of potential PAH carriers and formation reactions. [245, 249, 252]. The spectroscopy of several PAHs has been well understood, but it remains to be demonstrated exactly how they form. A promising pathway involves additions of small ions to small aromatics (including benzene). [253, 243, 34, 245, 246, 25, 251] Much work remains to investigate reactions within this category before a clear picture of this process can emerge. This requires exploration of candidate reactions to define their dynamics and potential role in such a process. Controlled, low temperature and pressure terrestrial kinetics and dynamics experiments can reproduce the conditions of the remote areas of the ISM and beyond, providing a clearer understanding of the complex reaction pathways and mechanisms in these environments.

Here, we report on the ion-neutral reaction of $CCl^+ + C_6H_6$, measured for the first time in a low temperature and pressure regime. C_6H_6 has been identified in the atmosphere of Jupiter,

Saturn, and Titan (one of Saturn's moons) [194, 244, 247, 248] and has been tentatively identified in interstellar and circumstellar environments using mid-infrared spectroscopy. [261, 262] Benzenes participation in ISM chemistry is established, including reactivity with highly abundant atomic species such as H, O, C and N+. [243, 263, 264, 265, 266, 267, 268] So far, CCl^+ has not been considered a primary player in interstellar chlorine chemistry because its abundance is uncertain and was thought to be primarily inert to many (but not all) interstellar species. [211, 269, 212, 133, 135] Only recently has the reactivity of CCl^+ been illuminated through experimental efforts by our group. Specifically, its reactivity has been demonstrated with astrochemically relevant molecules acetylene and acetonitrile at low collision energies [213, 190]. These studies support the hypothesis that CCl^+ has a hitherto underrepresented role in the chemistry that is occurring in the ISM. Potential abundances and plausible locations of CCl^+ are inferred with the aid of measured reactions and rate constants, as well as predictions and models of chemistry involving CCl^+ . Thus, we believe CCl^+ to be an important molecule to study, even preceding a definite conclusion regarding its abundance in the ISM. The main ionic products from the reaction presented here include C_7H_5^+ , C_3H_3^+ , C_5H_3^+ , and $\text{C}_3\text{H}_2\text{Cl}^+$, of which C_3H_3^+ has been identified and the rest have been speculated to exist in various areas in the ISM and beyond. [270, 271, 194, 272, 35] Importantly, the reaction results in a carbon growth pathway that could be consequential to chemistry in the ISM, planetary atmospheres, and other remote areas.

The exploration of cold and controlled reactions is a vibrant and growing field. [173, 72, 83, 273] Our experimental apparatus shown in Fig. 5.1 allows for the exploration of ion-neutral interactions under cold conditions. [45, 46, 274, 59, 63] The setup is comprised of a linear Paul ion trap coupled to a time-of-flight mass spectrometer (LIT-TOFMS). While the ultra-high vacuum environment of the apparatus is denser than the sparsest regions of space, it mimics the single-collision conditions of space, in which three-body reactions are extremely unlikely. This apparatus also allows for controlled reactions between translationally cold, trapped ions and neutral reactant gas over long interrogation times. Low collision energies (here 8 meV or ~ 93 K) are achieved by direct laser cooling of Ca^+ , which sympathetically cools the translational motion of the co-

trapped CCl^+ reactant ions. The cold conditions combined with the TOF-MS provide excellent mass resolution enabling clear chemical formula assignments from the resulting mass spectra. The significant energetic constraints on the reaction and identified chemical formulas enable more facile comparison to calculations at the CCSD(T)/CBS//CCSD/aug-cc-pVDZ level of theory, allowing for accurate determination of the thermodynamic limits of the reaction (within 0.04 eV). While temperature conditions in the ISM vary widely (from a few Kelvin to millions of Kelvin), we aim to understand reactions in the coldest conditions that we can achieve. This combination of experimental and computational tools allows for a clearer view of the chemistry of the important, and yet unexplored, reaction of $\text{CCl}^+ + \text{C}_6\text{H}_6$ under conditions comparable to various remote areas of space.

5.2 Methods

5.2.1 Experimental Methods

The linear ion trap coupled to a time-of-flight mass spectrometer (LIT-TOFMS) employed in this study is the same as was recently used to investigate the kinetics and dynamics of several different cations with various neutral species.[\[65\]](#), [\[225\]](#), [\[224\]](#), [\[213\]](#), [\[7\]](#), [\[190\]](#), [\[71\]](#) This section will be dedicated to the experimental details pertinent to the current study. CCl^+ ions are formed by overlapping a pulsed and skimmed molecular beam of tetrachloroethylene (TCE, C_2Cl_4 1.4% in 1000 Torr helium) with a focused 216 nm beam from a dye laser (LIOPTEC Liopstar; 10 ns pulses, $100\mu\text{J}/\text{pulse}$) in the center of the trap. This non-resonant multiphoton ionization scheme produces several ions including CCl^+ and C^{37}Cl^+ . Undesired ions are ejected from the trap by sweeping over resonant frequencies for a specific mass-to-charge ratio (m/z) of the unwanted ion,[\[8\]](#) leaving only CCl^+ or C^{37}Cl^+ (where not specified Cl, refers to more abundant ^{35}Cl). When a clean sample of CCl^+ is achieved, calcium is loaded from an effusive beam and non-resonantly ionized in the center of the trap using the third harmonic of an Nd:YAG (Minilite, 10 Hz, 7 mJ/pulse). Ca^+ ions are then laser cooled, forming a mixed species Coulomb crystal in which the laser cooled Ca^+ sympathetically

cools the co-trapped CCl^+ dark ions. The mixed species Coulomb crystal is monitored visually with a microscope objective and CCD camera. Visual inspection of the deformation of the crystal by CCl^+ and product ions allows for qualitative monitoring of the reaction.

Once a mixed Coulomb crystal is formed, neutral C_6H_6 (mixture of 10.9% in He) is leaked into the vacuum chamber containing the ion trap for a fixed amount of time (0, 10, 90, 170, 180, 240, 320, or 360 s) using a pulsed leak-valve (PLV) scheme.^[228] The base pressure during experiments is about 8×10^{-10} Torr and the leaked-in C_6H_6 in helium raises the pressure to only 1×10^{-9} Torr as the reaction proceeds. After a set interrogation time, the crystal is then ejected into the TOF-MS, and produces a highly resolved mass spectrum for that specific time step. The TOFMS provides clear and quantitative assignments of product masses by their m/z ratio. Each initial Coulomb crystal consists of about 100-200 CCl^+ mixed with about 900-1000 Ca^+ , all translationally cold (~ 10 K). This process is repeated about 12 times for each time step, and the accumulated mass spectra are averaged for each time step. The average number of ions for each mass channel of interest are normalized to the averaged number of the CCl^+ ions at $t = 0$, and plotted against time. This data can be fitted by modeling the reaction as a pseudo-first-order reaction since the neutral reactant is in excess throughout the course of the reaction.

Our experiments employ a Bayard-Alpert style hot cathode ionization gauge to monitor our neutral reactant pressures. These types of gauges are not well suited to measure pressures below 1×10^{-8} Torr, well above the regime we are working in (8×10^{-10} Torr). Therefore, our measurements of the partial pressure of the C_6H_6 reactant are subject to systemic uncertainty. This is mitigated by focusing on determination of branching ratios and actual product masses instead of precision measurements of rate constants.

5.2.2 Theoretical Methods

Electronic structure calculations are a powerful accompaniment to our experimental work. The cold nature of the reactant ions (~ 10 K including micromotion) provides a narrow center-of-mass collision energy ~ 93 K (8 meV) when reacting with room temperature C_6H_6 . This tight

thermodynamic limit allows focused exploration of the ionic and neutral products using quantum chemical computations.

Several theoretical methods are used to determine the possible ion-neutral isomeric pairs for each experimentally observed product mass. The m06-2X/aug-cc-pVTZ level of theory is used as a first step to determine structural isomers for each possible chemical formula. Viable isomers obtained from density functional theory searches are then used as a starting point for higher order CCSD/aug-cc-pVDZ calculations.[\[275\]](#), [\[276\]](#), [\[277\]](#), [\[278\]](#) Zero-point energy corrections from harmonic vibrational frequencies calculated at the coupled cluster singles doubles CCSD/aug-cc-pVDZ level are added to coupled cluster singles doubles and perturbative triples/complete basis set [CCSD(T)/CBS] single point energies.[\[279\]](#) Even though ^{37}Cl isotope substitutions are used experimentally to verify chemical formulas of observed products, calculations of these isotope substituted species are outside the scope of this work. DFT calculations are done using Gaussian 16,[\[176\]](#) while higher order CCSD calculations are done using Psi4 v1.3.2.[\[177\]](#)

5.3 Results & Discussion

Kinetic data for the reaction of $\text{CCl}^+ + \text{C}_6\text{H}_6$ are shown in Fig. [5.2](#). As the reaction progressed, the majority of the trapped CCl^+ reacted away into four products: C_3H_3^+ (m/z 39), C_5H_3^+ (m/z 63), $\text{C}_3\text{H}_2\text{Cl}^+$ (m/z 73), and C_7H_5^+ (m/z 89). These observed products were used to construct a reaction model in order to fit the reaction data and extract reaction rates and product branching ratios (see Tab. [5.2](#)). Under our experimental conditions, C_6H_6 is in excess, allowing for the use of a pseudo-first-order kinetic model, which includes a set of differential equations used to

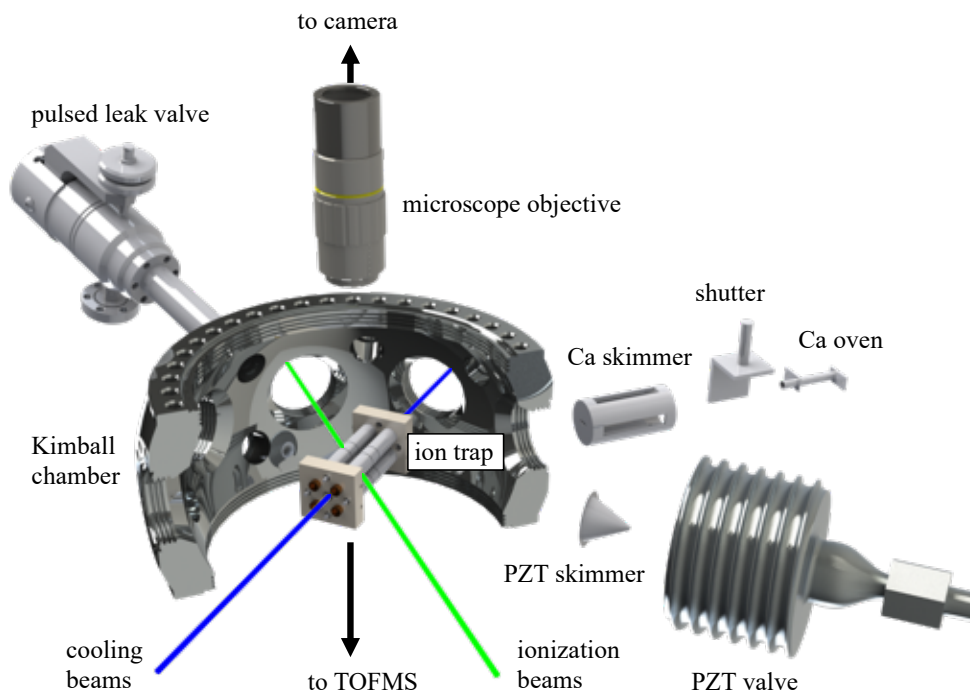


Figure 5.1: Schematic diagram of the LIT-TOFMS used for measuring the reaction of $\text{CCl}^+ + \text{C}_6\text{H}_6$. CCl^+ ions are produced by non-resonant photoionization and sympathetically cooled by the co-trapped laser-cooled Ca^+ . Approximately 2×10^{-10} Torr neutral C_6H_6 (11% in Helium, 300 K) is leaked into the vacuum chamber via a pulsed leak valve scheme for a set duration (0, 10, 90, 170, 240, or 320 s). After each reaction step, the resulting ions are then ejected into the TOF-MS, giving highly resolved mass spectra for each time step. Reproduced with permission from Schmid et al., Phys. Chem. Chem. Phys. 22, 20303 (2020). Copyright 2020 The Royal Society of Chemistry.

fit the experimentally observed ion numbers as a function of time:

$$\begin{aligned}
 \frac{d[\text{CCl}^+]}{dt} &= -(k_{39} + k_{63} + k_{73} + k_{89})[\text{CCl}^+] \\
 \frac{d[\text{C}_3\text{H}_3^+]}{dt} &= k_{39}[\text{CCl}^+] \\
 \frac{d[\text{C}_5\text{H}_3^+]}{dt} &= k_{63}[\text{CCl}^+] \\
 \frac{d[\text{C}_3\text{H}_2\text{Cl}^+]}{dt} &= k_{73}[\text{CCl}^+] \\
 \frac{d[\text{C}_7\text{H}_5^+]}{dt} &= k_{89}[\text{CCl}^+]
 \end{aligned} \tag{5.1}$$

Notably, in this reaction, the majority of CCl^+ reacted away, although in the time frame

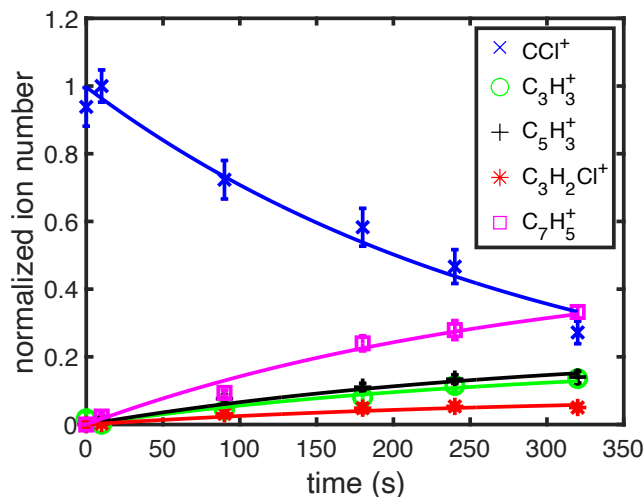


Figure 5.2: Rate reaction data (points) and fits (curves) for pseudo-first-order reaction of $\text{CCl}^+ + \text{C}_6\text{H}_6$. CCl^+ (blue \times) reacts with excess C_6H_6 resulting in first-order products C_3H_3^+ (green \circ), C_5H_3^+ (black $+$), $\text{C}_3\text{H}_2\text{Cl}^+$ (red $*$), and C_7H_5^+ (magenta \square).

of our experiments some remained. This timescale was chosen mainly because the principal focus of the study was to determine the primary products and their branching fractions, as opposed to measuring subsequent reactions of the primary products with benzene. The products shown here can be identified as primary products by the profile of the number of ions measured as a function of time. These product ions have the largest growth rate when the CCl^+ numbers are at their greatest, and continue to grow while the CCl^+ is in the trap. Additionally, secondary ion products are not detected in the trap and the total number of ions (summed over products and reactants) does not change over the course of a reaction, which implies that all ion products are detected.

Table 5.1: Rate constants for isotopological variations of $\text{CCl}^+ + \text{C}_6\text{H}_6$ primary products. Rate constants are in units of $\times 10^{-9} \text{ cm}^3/\text{s}$, and reported statistical uncertainty is the calculated 90% confidence interval.

Reactants	C_3H_3^+	C_5H_3^+	$\text{C}_3\text{H}_2\text{Cl}^+$	C_7H_5^+	total
$\text{CCl}^+ + \text{C}_6\text{H}_6$	0.6(1)	0.6(1)	0.2(1)	1.4(1)	2.8(2)
$\text{C}^{37}\text{Cl}^+ + \text{C}_6\text{H}_6$	1.3(2)	1.0(2)	0.6(2)	2.5(2)	5.5(4)

Kinetic data for the reaction of $\text{C}^{37}\text{Cl}^+ + \text{C}_6\text{H}_6$ was also measured (Figure 5.3), and this reaction was used as a mechanism for the identification of chlorinated products to refine molecular

formula assignments. Indeed, only one observed mass product changed when the heavier C^{37}Cl^+ was used, $m/z\ 73 \rightarrow 75$, confirming its assignment as $\text{C}_3\text{H}_2\text{Cl}^+$. Overall, we can be certain that the products were comprised only of the atoms in the reactants (that is, C, H or Cl), because we begin our reactions with a clean sample of either CCl^+ or C^{37}Cl^+ . Product assignments are further supported by computational modeling discussed below. Although it is not the focus of the current study, it should be noted that the rate of reaction for C^{37}Cl^+ is twice as fast as that for CCl^+ , indicating that a kinetic isotope effect may be at play here, driving the faster rate.

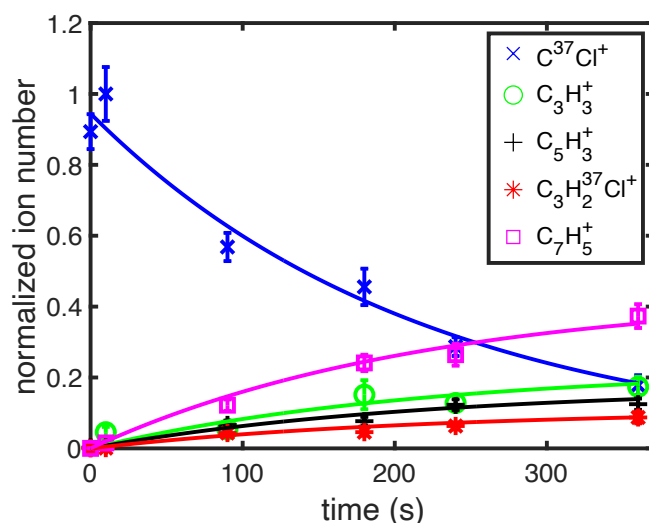


Figure 5.3: Rate reaction data (points) and fits (curves) for the pseudo-first-order reaction of $\text{C}^{37}\text{Cl}^+ + \text{C}_6\text{H}_6$. CCl^+ (blue x) reacts with excess C_6H_6 resulting in first order products C_3H_3^+ (green circle) and C_5H_3^+ (black $+$), $\text{C}_3\text{H}_2^{37}\text{Cl}^+$ (red asterisk) and C_7H_5^+ (magenta box).

Branching ratios for each of the observed products were obtained by dividing the separate product growth rates by the CCl^+ loss rate (see Tab. 5.2). Branching of the $\text{CCl}^+ + \text{C}_6\text{H}_6$ reaction favored the C_7H_5^+ product by about 50% compared to the other observed products. Additionally, we confirmed conservation of trapped ions by monitoring the total ion number as a function of trap time.

The lowest energy structural isomers for each product channel are plotted in Fig. 5.4. The product isomers presented for each observed mass in Fig. 5.4 are significantly more exoergic relative to the reactants at the CCSD(T)/CBS//CCSD/aug-cc-pVDZ level of theory and may all

Table 5.2: Branching ratios for the primary products of CCl^+ and C^{37}Cl^+ reacting with C_6H_6 . The numbers are given as percentages and uncertainties are derived from the 90% confidence interval from the pseudo-first-order model fits.

Reactants	C_3H_3^+	C_5H_3^+	$\text{C}_3\text{H}_2\text{Cl}^+$	C_7H_5^+
$\text{CCl}^+ + \text{C}_6\text{H}_6$	19(2)	23(2)	9(1)	49(4)
$\text{C}^{37}\text{Cl}^+ + \text{C}_6\text{H}_6$	24(2)	18(1)	11(1)	46(4)

be formed. It is assumed that a reaction complex forms as the reaction proceeds, particularly because the $\text{C}_3\text{H}_2\text{Cl}^+$ and C_7H_5^+ products have constituents of both reactants. From such a reaction complex, various steps may be required before fragmentation into the experimentally observed products. Ideally, a potential energy surface would be used to connect the reactants and products and would yield a more rigorous comparison to experimental branching ratios. This would be a large undertaking. Even without a calculated potential energy surface, we are able to demonstrate which isomers contribute to observed experimental products. This is because of the tight energetic constraints of our cold experimental conditions ($\sim 93\text{ K}$, 8 meV). This assumes a room temperature ro-vibrational distribution of the reactants and products. Although we conducted an exhaustive computational search for all possible isomers of each mass channel and corresponding neutral, some higher energy isomers may not have been found.

Multiple possible isomers were explored for each product. Only one ion-neutral pair was found to be exoergic for the $\text{C}_3\text{H}_2\text{Cl}^+ + \text{C}_4\text{H}_4$ and $\text{C}_5\text{H}_3^+ + \text{C}_2\text{H}_3\text{Cl}$ products shown as PRD4 and PRD2 respectively in Fig. 5.4. Because these ions are energetically favorable and the other closest available isomers are $> 200\text{ meV}$ higher in energy, it should be straightforward to assign the m/z 73 product to the PRD4 isomer of $\text{C}_3\text{H}_2\text{Cl}^+$ and the m/z 63 product to the PRD2 isomer of C_5H_3^+ . A schematic showing all the explored isomers for $\text{C}_3\text{H}_2\text{Cl}^+ + \text{C}_4\text{H}_4$ is shown in Figure 5.5; all calculated geometries for $\text{C}_5\text{H}_3^+ + \text{C}_2\text{H}_3\text{Cl}$ are shown in Figure 5.6). For $\text{C}_3\text{H}_3^+ + \text{C}_4\text{H}_3\text{Cl}$, the lowest energy pair for this product is shown as PRD3 in Fig. 5.4. The only energetically favorable ion for this channel is the cyclopropenyl cation ($\mathbf{c}\text{-C}_3\text{H}_3^+$) shown in Fig. 5.4, which we assign to the m/z 39 product. The assignment of m/z 39 to $\mathbf{c}\text{-C}_3\text{H}_3^+$ is consistent with the observed ions

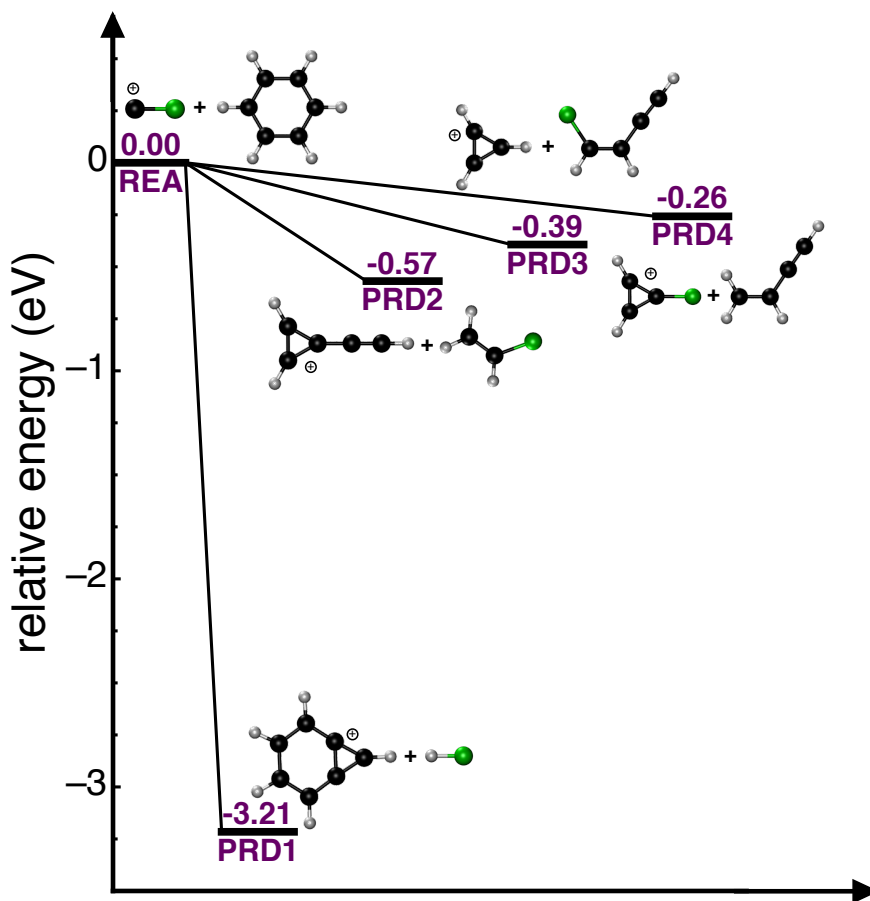


Figure 5.4: (a, left) Energetic limits for reactants $\text{CCl}^+ + \text{C}_6\text{H}_6$ and four products: $\text{C}_7\text{H}_5^+ + \text{HCl}$, $\text{C}_5\text{H}_3^+ + \text{C}_2\text{H}_3\text{Cl}$, $\text{C}_3\text{H}_2\text{Cl}^+ + \text{C}_4\text{H}_4$, $\text{C}_3\text{H}_3^+ + \text{C}_4\text{H}_3\text{Cl}$. Product energies are noted and appropriately scaled to y-axis scale as calculated at [CCSD(T)/CBS//CCSD/aug-cc-pVDZ] level of theory. The geometries appropriate for labeled energy are shown. Other explored isomers for each product can be found in the original manuscript.

not continuing to react with C_6H_6 in the experiment. The reaction of $\text{c-C}_3\text{H}_3^+$ with C_6H_6 is known to be very slow compared to the linear propargyl isomer, further supporting this assignment. [253]

A few neutral $\text{C}_4\text{H}_3\text{Cl}$ isomers are energetically favorable for this channel, as shown in Figure 5.7. However, because the neutral is not trapped in our experiments, it is not possible to know its exact identity.

In contrast to the other products, there are several possible exoergic isomers that could be assigned to the HCl loss product, C_7H_5^+ . In fact, there are seven isomers, all of which are shown in Figure 5.8. The lowest energy isomer, shown in Fig. 5.4 as PRD1, is much more exoergic than

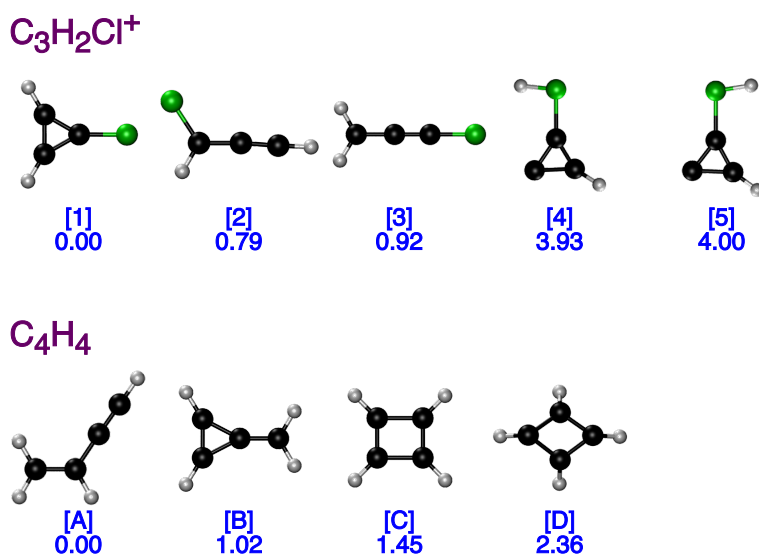


Figure 5.5: Calculated isomers of C₃H₂Cl⁺ (numbers [1-5]) and C₄H₄ (letters [A-D]). Energies are given in eV at the CCSD(T)/CBS//CCSD/aug-cc-pVDZ level of theory and are relative to the lowest energy isomer for each species. Isomers [1] and [A] correspond to PRD4 in Fig. 5.4.

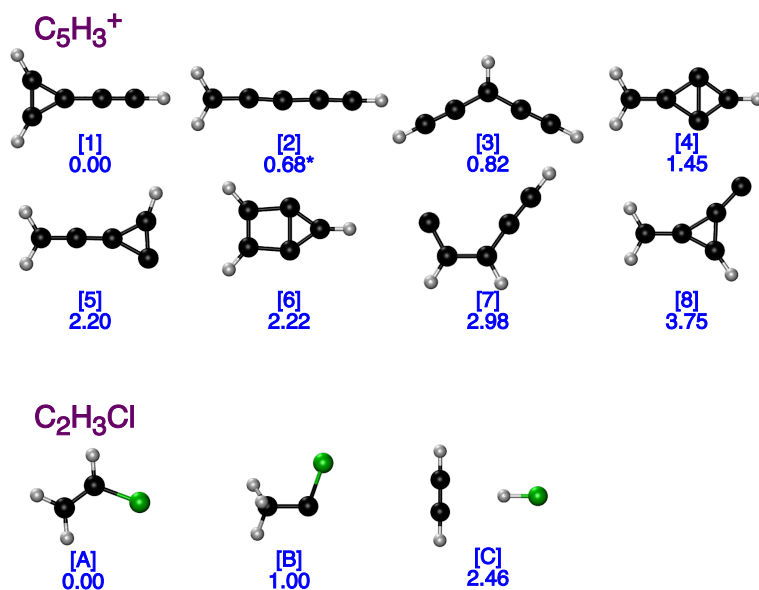


Figure 5.6: Calculated isomers of C₅H₃⁺ (numbers [1-8]) and C₂H₃Cl (letters [A-C]). Energies are given in eV at the CCSD(T)/CBS//CCSD/aug-cc-pVDZ level of theory and are relative to the lowest energy isomer for each species. Isomers [1] and [A] correspond to PRD2 in Fig. 5.4. The '*' next to Isomer [2] is used because one negative harmonic vibrational frequency was found at the CCSD/aug-cc-pVDZ level of theory. This isomer was verified to be a minimum structure at other levels of theory (including CCSD/aug-cc-pVTZ) and has been calculated in other computational studies. [13, 14, 15] Even with 0.04 eV uncertainty at the CCSD(T)/CBS//CCSD/aug-cc-pVTZ level of theory isomer 2 should not be energetically viable product for this reaction.

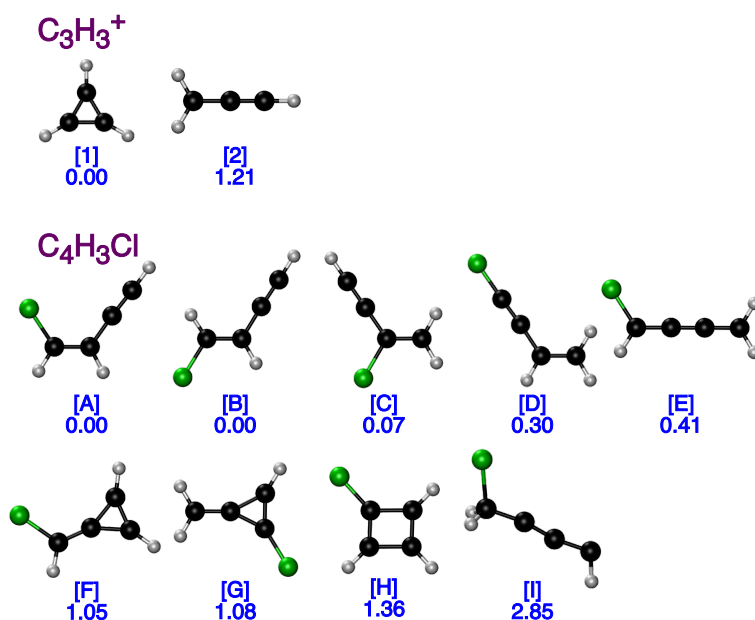


Figure 5.7: Calculated isomers of $C_3H_3^+$ (numbers [1-2]) and C_4H_3Cl (letters [A-I]). Energies are given in eV at the CCSD(T)/CBS//CCSD/aug-cc-pVDZ level of theory and are relative to the lowest energy isomer for each species. Isomers [1] and [A] correspond to PRD3 in Fig. [5.4](#)

any of the other possible products. The increased number of viable isomers, and the exoergicity of the products, might give insight into why this channel is experimentally favored. There may be submerged barriers to some of the energetically favorable isomers of $C_7H_5^+$ that would complicate this simplistic interpretation. Thus, a full potential energy surface and kinetic modeling of this reaction would be enlightening and could be of broad interest to the question of PAH production. We hope that others will continue with these efforts.

There are no experiments with which we can directly compare our results and predicted products. Similar products have been seen before for reactions of $C^+ + C_6H_6$, using ion cyclotron resonance mass spectrometry and a crossed molecular beam apparatus over collision energies of 0.02-12 eV.[\[280, 281, 282, 283, 253\]](#) However, because of the difference in ionization energies between the two reactants, the main product measured was $C_6H_6^+$ and constituted a branching of 67-85%. The $C_7H_5^+$ product was observed, but with only a modest branching of up to 10%.[\[283\]](#) This is in contrast to our observation of $CCl^+ + C_6H_6$, where $C_7H_5^+$ constitutes 50% of the products. The shared carbon growth product between the two reactions is intriguing and even more so that

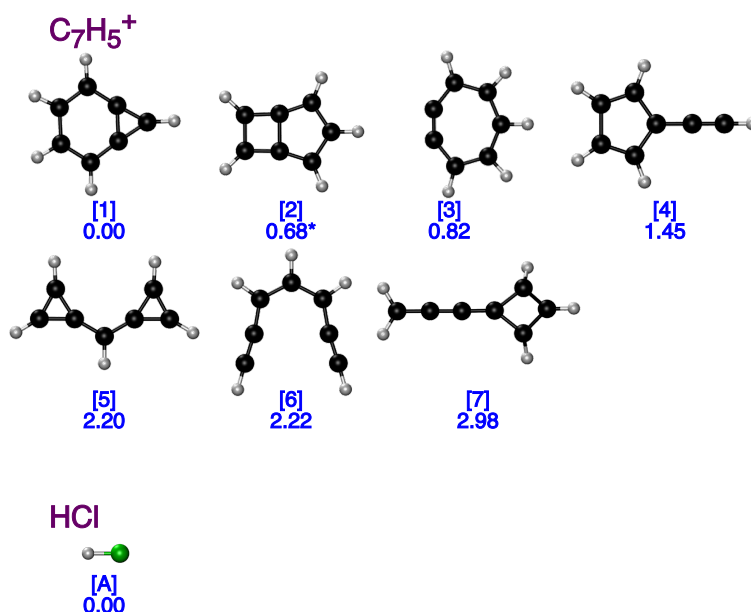


Figure 5.8: Calculated isomers of $C_7H_5^+$ (numbers [1-7]) and HCl ([A]). Energies are given in eV at the CCSD(T)/CBS//CCSD/aug-cc-pVDZ level of theory and are relative to the lowest energy isomer for each species. Isomer [1] and HCl [A] correspond to PRD1 in Fig. 5.4

branching to $C_7H_5^+$ in the reaction with CCl^+ is more heavily favored. Of course, it is likely that the differences in these reactions are at least partially attributed to the presence of the chlorine atom. The high electronegativity of chlorine likely impacts the distribution of electron density in the reaction complex, in which case, the energy landscape of the reaction dramatically changes. Further computational work and reaction studies of this type, including with other halogenated carbocations and C_6H_6 , may illuminate a possible mechanism for this carbon growth.

The experimentally favored HCl loss channel product, $C_7H_5^+$, must be formed by the addition of the carbon atom from CCl^+ to the ring of C_6H_6 . This reaction could provide another mechanism for growth of carbonaceous species and possibly PAH formation in low temperature and pressure environments. As discussed above, because so many of the possible $C_7H_5^+$ isomers are exoergic with respect to the reactants, it is difficult to pinpoint which $C_7H_5^+$ isomer is formed in this reaction. However, this represents an intriguing step to uncovering a possible new pathway to larger carbonaceous species, which might be consequential to chemistry taking place in the ISM, planetary atmospheres, or other environments. Hopefully, this work will inspire further experimental and

theoretical studies towards understanding additional pathways to complex organic molecules and carbon molecular weight growth.

From this and other reaction studies, CCl^+ itself has a growing basis for consideration as an astrochemically relevant molecule. While a positive identification in the ISM is yet to be made, its potential to participate in interstellar chemistry via reactions with other interstellar molecules has been demonstrated [213, 190, 135]. In fact, a high-resolution rotational spectrum of CCl^+ has recently been measured by Asvany et al. [284] and it can be expected that the question of whether it exists in the ISM be answered in the near future.

5.4 Conclusion

This work has outlined the reaction of CCl^+ with C_6H_6 and shows a new pathway to multiple astrochemically relevant carbocations, C_3H_3^+ , C_5H_3^+ , and C_7H_5^+ , as well as $\text{C}_3\text{H}_2\text{Cl}^+$. With the aid of computational work, only one possible exoergic product for each channel was identified, except in the case of C_7H_5^+ , in which several viable exoergic isomers exist. The reactants and products each comprise definite or possible participants in ISM chemistry, and the formation of the favored product, C_7H_5^+ , may illuminate a new pathway to molecular weight growth of carbonaceous species. This could have possible implications for the creation of complex organic molecules and perhaps PAHs in the ISM, planetary atmospheres, and other extraterrestrial environments. The complex chemistry connecting smaller carbocations to larger PAHs is still being understood and more reaction studies with various molecules are required to fully understand the progression from small carbocations to complex molecules like C_{60}^+ . We believe this reaction contributes to this important open question, and presents a very intriguing first step to carbon growth at colder temperatures from CCl^+ reacting with the abundant C_6H_6 .

Chapter 6

Reactions of Acetonitrile with Trapped, Translationally Cold Acetylene Cations

“See first, think later, then test. But always see first. Otherwise you will only see what you were expecting.”

– *Douglas Adams, The Ultimate Hitchhiker’s Guide to the Galaxy, 2002*

This chapter is adapted from the paper of the same name that we published in the Journal of Physical Chemistry A in 2023.[\[285\]](#) I was the primary contributor to the data acquisition and analysis. The potential energy surface is the result of work from theory collaborators from the University of Melbourne, Sri Sundar and Gabe da Silva.

6.1 Introduction

Small carbonaceous species, in both their neutral and ionic forms, are essential building blocks in several diverse chemical environments. Acetylene (C_2H_2) and its cation $C_2H_2^+$ are ubiquitous in fuels, flames, planetary environments, and in the interstellar medium (ISM).[\[194, 286, 287, 253, 246\]](#) Much of the early understanding of $C_2H_2^+$ reactivity was developed from mass spectrometry studies of acetylene-rich flames, motivated by the hypothesis that ion-neutral reactions contribute to soot formation.[\[286, 288, 289, 290, 291, 292, 293, 294\]](#) Far from these hot and dense environments, interest in $C_2H_2^+$ has more recently been focused on its role in colder and less dense regimes like planetary atmospheres and the ISM. Small cations of this type are thought to have a role in ion-neutral condensation reactions that may lead to the formation of larger more complex organic species.[\[253, 246, 295\]](#) Understanding the reactivity of $C_2H_2^+$ in a controlled laboratory setting under low temperature and pressure conditions is crucial to understanding its reactivity in diverse chemical environments such as the ISM and planetary atmospheres.

Nitriles, including acetonitrile (CH_3CN), are pervasive in many regions of space and have been tied to several areas of complex chemistry taking place in the ISM. Particularly interesting are the ion-neutral reactions that form dense haze layers of Titan, which may have implications for prebiotic chemistry.[\[194, 271, 247\]](#) CH_3CN itself has been identified in the ISM,[\[196\]](#) with a notable presence in cold dark clouds,[\[197\]](#) low mass protostars,[\[198, 199\]](#) and hot cores.[\[200, 201, 205\]](#) Furthermore, it has been detected in the dust from several comets, including Halley,[\[202\]](#) Hale-Bopp, (C/1995 O1)[\[203\]](#) and, more recently, 67P/Churyumov-Gerasimenko.[\[204\]](#) Further understanding the reactivity of this prevalent neutral with a fundamental carbocation, like $C_2H_2^+$, is important for many areas of chemistry.

Reactions of $C_2H_2^+$ have been previously studied using several different techniques and neutral reactants.[\[71, 7, 296, 218, 297, 298, 299\]](#) Recent work from our group showed the different mechanisms of $C_2H_2^+$ reacting with two structural isomers of C_3H_4 , and demonstrated how isotopic substitution is a powerful tool for determining chemical reaction processes.[\[71, 7\]](#) The specific

reaction of $\text{C}_2\text{H}_2^+ + \text{CH}_3\text{CN}$ (subject of the current study) was previously measured at room temperature using a selected ion flow tube (SIFT) apparatus.[\[218\]](#) The reported reaction products were C_2NH_4^+ , C_3H_5^+ , C_3H_4^+ , and the C_4NH_5^+ adduct (putatively $[\text{C}_2\text{H}_2\cdot\text{CH}_3\text{CN}]^+$) with nearly equal branching. This study was conducted at high pressure, which can stabilize highly excited reaction complexes through collisions with background buffer gas. Ion-neutral chemical reactions typically produce such unstable complexes, which are unlikely to stabilize in regions like the ISM. The low pressure and collision energy regime of the current study should more closely mimic conditions present in the ISM and yield a better understanding of the reactivity and dynamics of these two species in these remote domains.

In particular, ion traps and Coulomb crystals have been fruitful environments to study a myriad of gas-phase chemical reactions and interesting quantum phenomena.[\[45, 63, 173, 76, 128, 300\]](#) In these experiments, atomic ions (here Ca^+) are trapped and directly laser-cooled, forming Coulomb crystal structures that sympathetically cool co-trapped ions to translational temperatures below 10 K. This type of experimental setup allows for controlled collisions of purified ionic species with neutral molecules, and is particularly suited for long interrogation times. Furthermore, coupling a linear Paul ion trap (LIT) to a time-of-flight mass spectrometer (TOF-MS) allows for the exact determination of the molecular weight and number of the chemical species present in the trap at high resolution. This high resolution is more than enough to detect differences of a single mass unit for the range of masses studied here.[\[65\]](#) The conditions created in these types of experiments are relevant to the cold and low density conditions of space. Additionally, the low collisional energies (~ 100 K) impose stricter bounds on reaction energies, which yield valuable comparisons with quantum chemical computational modeling.

Here, we use a LIT TOF-MS apparatus to characterize the reactions of $\text{C}_2\text{H}_2^+ + \text{CH}_3\text{CN}$ under low pressure and temperature conditions. The primary products are found to be $\text{c-C}_3\text{H}_3^+$, C_3H_4^+ , and C_2NH_3^+ , which are unambiguously assigned using isotope substitutions and quantum chemical calculations. This study provides insight into the reactivity of two astrochemically abundant molecules, C_2H_2^+ and CH_3CN , and additional formation pathways of fundamental carbo-

cations $\text{H}_3\text{C}_3\text{H}^+$, $\text{CH}_2\text{CCH}_2^+$ and $\text{c-C}_3\text{H}_3^+$, which could prove useful for refining chemical models that rely on accurate energetics and electronic structure information. This work also provides useful information on the dissociation of excited $[\text{C}_4\text{H}_5\text{N}^+]^*$ cation, which is relevant to the relatively well-studied decomposition of the pyrrole cation [global minimum on the potential energy surface (PES)] in the photoionization of neutral pyrrole. [301, 302, 303] Observing and studying the interaction of these two important interstellar species in a cold and low pressure regime is consequential to understanding ion-neutral chemistry in extraterrestrial environments.

6.2 Methods

6.2.1 Experimental Methods

Kinetic data are measured using a LIT radially coupled to a TOF-MS. The LIT TOF-MS has been described in detail elsewhere [65, 190, 7, 71] and only a brief summary of the features pertinent to the current experiment are given here. Acetylene cations are produced using a (1+1) resonance-enhanced multiphoton ionization scheme. A $\sim 2\%$ mixture of C_2H_2 or C_2D_2 (CDN isotopes 99% d_2) seeded in He is expanded supersonically to create a molecular beam, which passes through a skimmer into the center of the trap, where it is overlapped with a focused beam from the output of a frequency-doubled pulsed dye laser (216 nm for C_2H_2 or 218 nm for C_2D_2 ; [304, 131] LIOPTEC LiopStar; 10 ns pulse, 1 mJ/pulse). Small amounts of contaminant ions are formed in the ionization process. These unwanted ions are ejected from the trap by sweeping over resonance frequencies of the specific mass-to-charge ratio ($\mathbf{m/z}$) of undesired ions. [127, 8]

Ca^+ ions are subsequently loaded into the trap with the acetylene ions by non-resonantly photoionizing calcium from a resistively heated oven, using the third harmonic of an Nd:YAG (355 nm; Minilite, 10 Hz, ~ 7 mJ/pulse). The resulting Ca^+ ions are laser-cooled using two external cavity diode lasers (397 and 866 nm). The cold Ca^+ sympathetically cool the co-trapped acetylene ions via Coulomb interactions, forming a mixed Coulomb crystal structure. The reaction experiments are visually monitored by collecting Ca^+ ion fluorescence with a microscope objective, which focuses

the light onto an intensified CCD camera located above the trap. The lighter acetylene ions, which do not fluoresce, arrange themselves in the center of the trap as a cylindrical dark core within the Ca^+ ions. A typical experiment utilizes 150-300 acetylene ions trapped with ~ 1000 Ca^+ ions, all of which are translationally cold (~ 10 K), where the temperature of the ions is limited by micromotion heating. This loading process takes about a minute, which allows the acetylene ions sufficient time to relax from any possible vibrational excitation that may have occurred in the REMPI process.

Once acetylene and Ca^+ ions are loaded into the trap, neutral acetonitrile [9-10% CH_3CN or CD_3CN (Cambridge Isotopes 99.8%-d3) in N_2] is leaked into the vacuum chamber (3×10^{-9} Torr or 4×10^{-7} Pa gas pressure at 300 K) for a set duration of time using a pulsed leak-valve (LV) scheme.^[228, 224] The typical chamber base pressure is 6×10^{-10} Torr (8×10^{-8} Pa) and the measurements of gas pressures in the chamber are recorded using a Bayard-Alpert hot cathode ionization gauge. The opening of the LV defines the zero-time point; the LV remains open for several different time steps between 0-400 s before the ions are ejected into the TOF-MS. The TOF-MS has a resolution of $m/\Delta m \geq 1100$, which can resolve neighboring masses with excellent accuracy and precision.^[65] This process is repeated about 12 times for every time step and measured ion numbers from each mass channel are averaged over each time step, including the zero-time point, which measures the initial number of ions in the trap. The average number of reactant and product ions are then normalized by the initial acetylene ion numbers and plotted against time, giving a reaction curve. These reaction curves are then used to determine the relevant rates of the reactions. Reaction curves are collected in the same manner for all isotopologues, such that reactions with all four possible combinations of isotopologues are measured. Due to the excellent mass resolution of the TOF-MS,^[65] we are able to observe mass shifts from these small substitutions. TOF-MS traces are tracked for all of the ionic species present and the total number of ions are compared at each time point to ensure that the numbers are constant throughout the experiment. This rules out systematic losses of ions from the trap. Figures illustrating conservation of charge for each reaction are given in the Supplementary Information (SI).

6.2.2 Computational Methods

Quantum chemical calculations are carried out using the Gaussian 16 program.^[176] Geometry optimizations and harmonic vibrational frequency calculations are performed at the M06-2X/6-31G(2df,p) level of theory. Single point energies are computed using the G3X-K method^[305], which is specifically developed for thermochemical kinetics and is accurate to within 0.03 eV on average for barrier height predictions. Harmonic vibrational frequency calculations of optimized minima and transition states affirm the presence of zero and one imaginary frequency, respectively. The inter-connectivity of transition states is in all cases confirmed by intrinsic reaction coordinate (IRC) calculations.

6.3 Results & Discussion

6.3.1 Reaction measurements

The discussion here is limited to the specific reaction of $\text{C}_2\text{H}_2^+ + \text{CH}_3\text{CN}$. The results of the other three isotopologue reactions are discussed in terms of product identification. Details of these isotopologue reactions are reported in the SI. The reaction of $\text{C}_2\text{H}_2^+ + \text{CH}_3\text{CN}$ produces the curves shown in Fig. 6.1. Here, C_2H_2^+ (blue \circ , m/z 26) reacts away over time to produce the primary products $\text{c-C}_3\text{H}_3^+$ (black \times , m/z 39), C_3H_4^+ (magenta $+$, m/z 40) and C_2NH_3^+ (green \square , m/z 41). The reduction in the ion numbers of C_2H_2^+ coincides with the growth of the three primary products. These primary products reduce over time as the population of secondary product CH_3CNH^+ (red $*$, m/z 46) increases from reactions with excess neutral CH_3CN . C_2NH_4^+ is confirmed as a secondary product as its numbers continue to increase after all the C_2H_2^+ has completely reacted. C_2NH_4^+ is a product from reactions of $\text{C}_3\text{H}_4^+ + \text{CH}_3\text{CN}$ and $\text{C}_2\text{NH}_3^+ + \text{CH}_3\text{CN}$. These observed products are used to construct a kinetic model (see Fig. 6.2) in order to fit the reaction data, as well as extract reaction rate coefficients and product branching ratios. The experimental conditions are such that CH_3CN is in excess throughout the course of the reaction, which is represented by a pseudo-first-order kinetic model. This model uses a set of differential

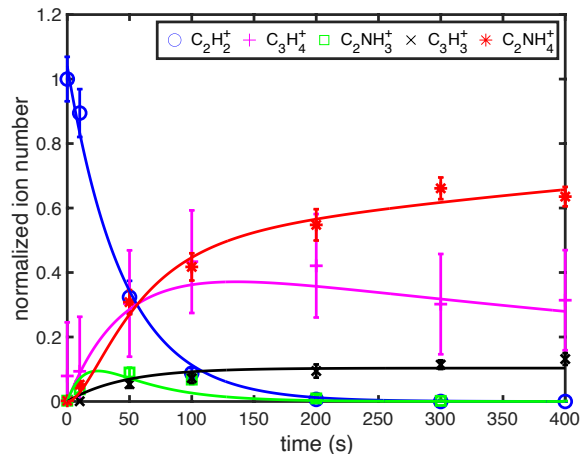


Figure 6.1: Measured ion numbers of C_2H_2^+ (blue \circ), C_3H_4^+ (magenta $+$), C_2NH_3^+ (green \square), C_3H_3^+ (black \times), and C_2NH_4^+ (red $*$) as a function of time. Data are normalized by the initial ion number of C_2H_2^+ (~ 200). Each data point represents the mean and standard error from twelve experimental runs per time point. The averaged data are fit using a pseudo-first-order reaction rate model (solid lines).

equations (given in the SI) to fit the experimentally observed ion numbers as a function of time. The resulting fits are shown as lines in Fig. 6.1. The decay rate of C_2H_2^+ is extracted from this fit and can be used to calculate the reaction rate constant, $k = 4.5 \pm 0.6 \times 10^{-9} \text{ cm}^3/\text{s}$. This value is obtained by measuring the partial pressure of acetonitrile gas with a hot cathode ion gauge close to the trapping region as the reaction proceeds. Hot cathode ion gauges of this type are subject to systematic uncertainties at pressures below 1×10^{-8} Torr associated with the nonlinear sensitivity of ion gauges in this regime.^[229] Reaction rate constants for the isotopologue combinations are similar to that of the fully hydrogenated reaction, with exact values reported Tab. S1 in the SI.

Reaction curves are also measured for the four unique pairs of isotopologue reactants (see SI for these reaction curves). These kinetic data are used to confirm the product assignments from the $\text{C}_2\text{H}_2^+ + \text{CH}_3\text{CN}$ reaction. Primary product mass distributions for each isotopologue combination and branching ratios are given in Tab. 6.1. These branching ratios were determined by dividing the growth rate of each respective m/z channel by the total acetylene ion loss rate.

While an analysis of the branching ratios across the four different reactions would be interesting, masses of the possible isotopic variations coincide for more than one product channel and

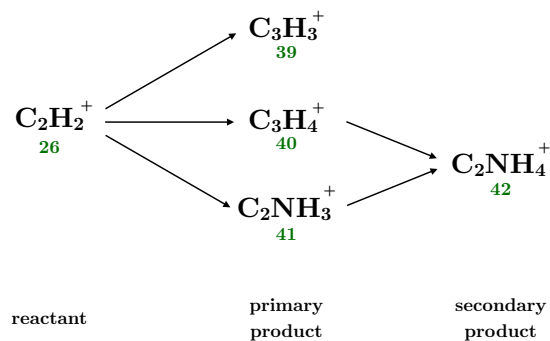


Figure 6.2: Model for reaction of $\text{C}_2\text{H}_2^+ + \text{CH}_3\text{CN}$, m/z ratio (blue number) and determined chemical formula below the molecule. The reaction order of each molecule is located at the bottom of the figure. Each arrow represents a reaction with a neutral CH_3CN molecule.

hinder such analysis. For example, in the $\text{C}_2\text{D}_2^+ + \text{CH}_3\text{CN}$ reaction case, the $\text{C}_3\text{H}_x\text{D}_y^+(x + y = 3)$ reaction product can be found in m/z channel 39, 40 or 41. The $\text{C}_3\text{H}_x\text{D}_y^+(x + y = 4)$ product in this case can feasibly be m/z 41 or 42. Additionally, $\text{C}_2\text{NH}_x\text{D}_y^+(x + y = 3)$ can be m/z 41, 42, or 43. A very similar case emerges for $\text{C}_2\text{H}_2^+ + \text{CD}_3\text{CN}$. Even without the expected splitting in the fully deuterated case, two of the three primary products coincide in the same channel (m/z 44). This overlap in possible product masses precludes any direct comparison of branching for a single *product* across the different reaction sets. Indeed, trying to compare a single *mass channel* for the reaction sets is misleading. For example, in the fully hydrogenated case m/z 41 is solely C_2NH_3^+ . This channel could be C_3HD_2^+ or $\text{C}_3\text{H}_3\text{D}^+$ for the $\text{C}_2\text{D}_2^+ + \text{CH}_3\text{CN}$ reaction and must be C_3HD_2^+ for $\text{C}_2\text{H}_2^+ + \text{CD}_3\text{CN}$. None of our assigned products can be m/z 41 when they are fully deuterated (not seen). The fact that the branching differs in the m/z 41 channel for the four reactions is the natural result of the statistical m/z options available to each product due to hydrogen-deuterium swapping in the reaction complex.

While assessment of the isotopologue effects on branching ratios is not possible for this reaction, these branching ratios are a resource for identifying our products. In the fully deuterated case, $\text{C}_2\text{D}_2^+ + \text{CD}_3\text{CN}$, primary products shift, m/z 40 \rightarrow 44 (C_3D_4^+), m/z 41 \rightarrow 44 (C_2ND_3^+), and m/z 39 \rightarrow 42 (C_3D_3^+). The secondary product also shifts in the fully deuterated reaction,

Table 6.1: Branching ratios for the primary products of acetylene cations reacting with acetonitrile. The numbers are given in percentages and uncertainties are derived from the 90% confidence interval from the pseudo-first-order model fits.

Reactants	m/z 39	m/z 40	m/z 41	m/z 42	m/z 43	m/z 44
$C_2H_2^+ + CH_3CN$	10(2)	43(10)	47(6)			
$C_2D_2^+ + CH_3CN$	3(3)	38(18)	22(15)	14(13)	23(14)	
$C_2H_2^+ + CD_3CN$		26(12)	4(3)	17(11)	53(21)	
$C_2D_2^+ + CD_3CN$		55(14)		10(4)		34(8)

m/z 42 \rightarrow 46 ($C_2ND_4^+$). This analysis can be checked for each reaction set. In each case, mass shifts are consistent with the products observed in the titular reaction. A specific example of this point involves our reassignment of the m/z 41 channel to $C_2NH_3^+$ in the fully hydrogenated case. This channel could theoretically be $C_3H_5^+$. This would require the product masses to shift entirely to the m/z 44 channel in the $C_2H_2^+ + CD_3CN$ case, which is not observed. In addition, this would require a m/z 46 primary product in the fully deuterated case, where we only see the second-order product, CD_3CND^+ . Product assignments are further supported by quantum chemical calculations, in particular calculated reaction thermodynamics discussed below.

The primary product $C_3H_4^+$ is partially obscured by overlap with mass coincident and more abundant Ca^+ signal. Because of this overlap, it is important to understand how calcium is reacting with CH_3CN in order to correctly model the formation and depletion of $C_3H_4^+$. The reaction of $Ca^+ + CH_3CN$ has been previously studied,^[77] and only produces m/z 66 $CaCN^+$.^[190] We verified that there were no interfering mass products with the current reaction by reacting Ca^+ with CH_3CN without any acetylene present, and concluded no statistically significant differences of the formation of $CaCN^+$ to the reaction when acetylene cations are present. In addition to reactions with CH_3CN , some minute amounts of gaseous H_2O are present in our system that react with Ca^+ to form m/z 57 $CaOH^+$. This reaction has also been characterized under similar conditions.^[306] Again, we verified no statistically significant difference between reactions of $Ca^+ + H_2O$ with or without acetylene in the trap. These two reactions, Ca^+ with both CH_3CN and H_2O are included in the model for m/z 40, and details of this model and the specific differential equations for the fits are given in the SI.

Both of these Ca^+ reaction products were taken into account when calculating the reaction rates and branching ratios for the m/z 40 channel.

An insight into the dissociation of excited $\text{C}_4\text{H}_5\text{N}^+$ also comes from numerous prior studies on pyrrole cation dissociation, which is an intermediate in the dissociative photoionization of neutral pyrrole.[\[303\]](#), [\[301\]](#) These studies identify C_3H_4^+ (m/z 40) + HCN and C_2NH_3^+ (m/z 41) + C_2H_2 as the experimentally observed products with their appearance energies at -1.68 eV and -1.81 eV, respectively in the reference to the reactant's energy. As mentioned above, the reaction of C_2H_2^+ + CH_3CN has been previously measured by Iraqi et al. at room temperature and much higher pressures using a SIFT apparatus.[\[218\]](#) They reported primary products C_2NH_4^+ , C_3H_5^+ , C_3H_4^+ , and the adduct $[\text{C}_2\text{H}_2\cdot\text{CH}_3\text{CN}]^+$ with nearly equal branching. In the SIFT study, C_2NH_4^+ was assigned as a primary product, but in the current study, its formation clearly has a late onset that corresponds to the decrease in ion number of primary products m/z 41 and m/z 40 and is therefore re-assigned here as a secondary product. C_2NH_4^+ is not observed in pyrrole cation decomposition studies. Furthermore, m/z 41 is reassigned from C_3H_5^+ to C_2NH_3^+ . This is supported by the absence of m/z 44 ($\text{C}_3\text{H}_2\text{D}_3^+$) in the reaction of C_2H_2^+ + CD_3CN as previously mentioned. Additionally, there appears to be no corresponding first order product at m/z 46 (C_3D_5^+) in the fully deuterated reaction. It could be that, although the formation of C_3H_5^+ is slightly exothermic (~ -0.06 eV), it might be impeded by a small barrier that is surmountable at 300 K (26 meV), but not in the current study with less available energy.

The adduct is not seen in the current study because we are in a low pressure regime and there are no collisions with buffer gas to quench possible intermediates like the adduct. Interestingly, $\text{c-C}_3\text{H}_3^+$ was not reported as a product in the SIFT study but experimentally detected in the pyrrole cation studies.[\[303\]](#) The SIFT study does show m/z 40 as a product, also assigned to C_3H_4^+ , further confirming this assignment without the mass-coincident Ca^+ .

We are confident that we observe the formation of C_3H_4^+ + HCN in the reaction of C_2H_2^+ + CH_3CN , as seen in the previous SIFT and in the pyrrole cation dissociation studies.[\[218\]](#), [\[303\]](#), [\[301\]](#) However, we observe branching into the m/z 40 channel (see Tab. [6.1](#)) in the other data sets

where one or both of the reactants is deuterated. We do expect a small amount of m/z 40 to be present in the mixed data sets based on the observation of the primary product $c\text{-C}_3\text{H}_3^+$ m/z 39 in the fully hydrogenated dataset. No m/z 40 is predicted in the fully deuterated data set, yet a significant amount (about 43%) of C_2D_2^+ is converted to m/z 40. We have dedicated significant effort to understanding the origin and possible identity of the m/z 40 signal, and believe it to be a contaminant in our reactions. We verified experimentally that both reactants need to be present to see growth in m/z 40 and that it is not the result of a reaction with Ca^+ .

Similar contamination issues have been observed before in the reactions of acetylene cations with different isotopologues of C_3H_4 . The contamination was pinpointed as impurities in the deuterated gases.^[7, 71] The current sample preparation of both CH_3CN and CD_3CN included upwards of 10 freeze-pump-thaw cycles that should help to purify the liquid samples, but this technique may not have been successful in eliminating contaminants. We used various samples of different levels of purity from several companies, as well as different mixing gases (Ar, N_2 , and He), without any change in the observed branching into m/z 40 in the fully deuterated data set. We also ran our experiments with trapped C_2H_2^+ and C_2D_2^+ and reacted with 100% of the mixing gas (Ar, N_2 , and He) and saw no growth in the m/z 40 mass channel, indicating there was no contamination from the gas delivery and mixing process. Because both reactants must be present to see this growth, we can rule out reactions between trapped acetylene cations and its neutral counterpart, which may be ambient in the system. Likewise, for the same reasons, we are also able to rule out charge exchange between acetylene cations and ambient neutral Ca.

We considered the possibility that m/z 40 could consist of a different product than C_3H_4^+ . However, the only plausible chemical formula for a primary product would be $\text{H}_2\text{C}_2\text{N}^+$, and all structural isomers for this chemical formula were found to be significantly endothermic ($> 1.5\text{ eV}$) at the G3X-K level of theory. We tested the hypothesis that some m/z 39 product could be HC_2N^+ , which would convert to m/z 40 in the fully deuterated case. However, all viable isomers for this chemical formula were also greater than 1.5 eV endothermic and ruled out. The secondary product CN_2^+ was also considered as a hypothetical constituent of m/z 40, however, it was also

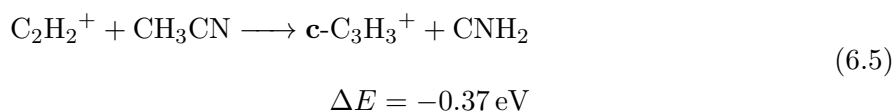
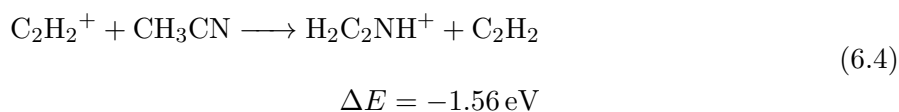
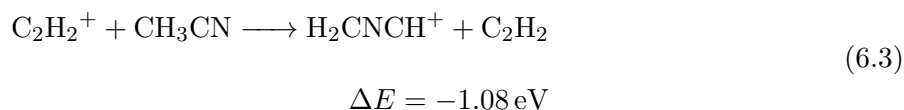
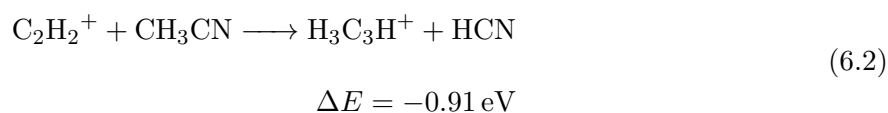
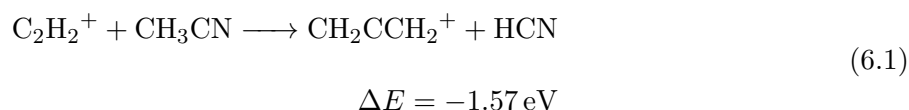
significantly endothermic and eliminated as a possibility. It is possible that the acetylene ions could be electronically excited from the initial ionization laser pulse. However, the lowest-lying electronic states all require two additional photons, with the exception of the lowest-lying doublet $^2\Sigma_g^+$, which lies 5.67 eV above the ground state of $C_2H_2^+$.^[307] This excited state is extremely short-lived (< ns);^[308, 309] the ions have several seconds between loading and the introduction of the neutral reactant. For these reasons, we believe all the acetylene cations are in the ground electronic state. These observations, as well as comparisons with the previous ion trap and SIFT studies,^[7, 71, 218] led us to believe that a contaminant is competing with the $C_2H_2^+ + CH_3CN$ reaction. The previous SIFT experiment showed m/z 40 as a product and it was assigned as $C_3H_4^+$. We remain confident in our assignment of primary products in the reaction of $C_2H_2^+ + CH_3CN$, and have exhausted the available resources in our current experimental set up to further purify or identify the possible contaminant. Unfortunately, this further complicates quantitative analysis of the branching ratios. While the m/z 40 channel in the fully hydrogenated case shows evidence of re-reacting to form a second order product (unlike the m/z signal in all of the other reactions) not all of it reacts in our reaction time. It is possible that the contamination may only be associated with deuterated gasses, but we cannot omit the possibility that this contaminate is also present in the fully hydrogenated case. Nevertheless, the comparison of the reaction across the four isotopologue combinations yields experimental product assignments further verified by quantum chemical investigations and reaction thermodynamics, as will be discussed next.

6.3.2 Reaction thermodynamics

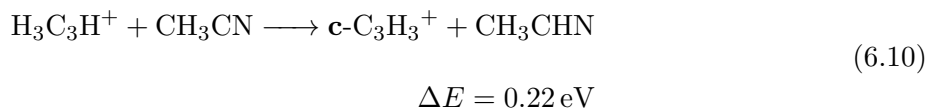
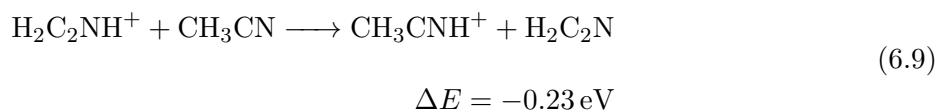
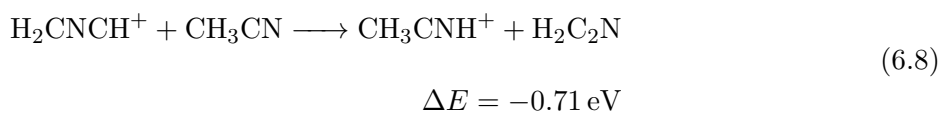
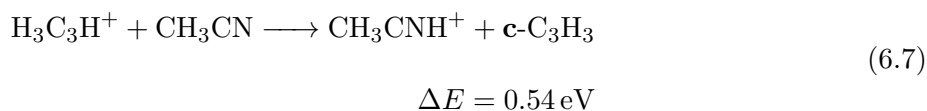
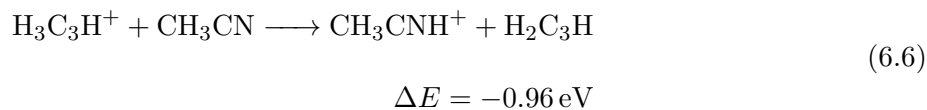
The model of the reaction of $C_2H_2^+ + CH_3CN$ is given in Fig. [6.2](#), and shows that as the two reactants come together, three primary products form, c - $C_3H_3^+$, $C_3H_4^+$ and $C_2NH_3^+$. Two of these primary products then go on to react with excess CH_3CN to form $C_2NH_4^+$, protonated acetonitrile. Since the $C_2H_2^+$ ions are sympathetically cooled to 10 K, reactions with room temperature (300 K) CH_3CN result in a calculated collision energy characterized by a translational temperature of about 116 K (10 meV). It should be noted, however, that the rotational and vibrational energies

will reflect that of the room temperature environment at 25 meV. These energies provide the upper thermodynamic limit to the reaction. Two exothermic isomers were found as a possibility for the $C_3H_4^+$ product, $CH_2CCH_2^+$, the allene cation, and $H_3C_3H^+$, the propyne cation, with hydrogen cyanide (HCN) as the corresponding neutral. This is in accordance with the previous Iraqi et al. SIFT and pyrrole cation dissociation studies. [303, 301] The charge transfer product CH_3CN^+ is not energetically viable compared to the $C_2NH_3^+$ product. However, both isomers of $C_2NH_3^+$, H_2CNCH^+ (Eqn. 6.3) and $H_2C_2NH^+$ (Eqn. 6.4) are significantly exothermic. $C_3H_5^+ + CN$ is also exothermic, but as discussed above, the lack of a m/z 44 product when reacting $C_2H_2^+ + CD_3CN$ indicates that $C_3H_5^+$ is not observed in the current study and therefore is not modeled in the PES. $\mathbf{c}\text{-}C_3H_3^+$ is identified as the cyclic isomer (cyclopropenyl cation) and is determined to be a primary product as all energetic limits for it as secondary product are endothermic (Eqs. 6.5, 6.10). The observed products are all exothermic with respect to the reactants computed at the G3X-K level of theory (see Eqs. 6.1-6.10) and well under the energetic limit of the collision energy.

Primary products:



Secondary products:



6.3.3 Reaction potential energy surface

Quantum chemistry calculations have been used to generate a PES, which connects the reactants to all observed products via multiple saddle points, show in Figs. [6.3](#), [6.4](#) and [6.5](#). In the developed $\text{C}_2\text{H}_2^+ + \text{CH}_3\text{CN}$ reaction mechanism, all transition states, intermediates, and product sets are exothermic compared to the reactants, such that the reaction complex can sample all of the stationary points before exiting the surface without the need for vibrational excitation above what is provided by ion-molecule complex formation. The PES not only identifies reaction pathways to possible product channels, but also provides a basis for understanding the kinetics of product formation.

The section of the PES relevant to $\text{CH}_2\text{CCH}^+/\text{H}_3\text{C}_3\text{H}^+ + \text{HCN}$ formation is presented in Fig. [6.3](#). C_2H_2^+ addition to CH_3CN commences with no entrance barrier to generate an adduct

(W1), located 2.72 eV below the reactants. Two competitive pathways exist from the well W1. The first channel gets to propyne cation by the formation of four membered ring intermediate (W2), by overcoming a 1.86 eV energy barrier (0.85 eV below the reactants). Subsequently, ring opening chemistry (TS2) takes place with a barrier of 1.01 eV to form the intermediate W3. Again, all structures sit below the reactant energies [-1.03 eV (TS2) and -1.25 eV (W3)]. Finally, cleavage of a C-C bond in W3 generates the products $\text{H}_3\text{C}_3\text{H}^+ + \text{HCN}$ at 0.91 eV below the reactant energies.

The second competitive product channel from well W1 initiates via internal H-atom transfer (TS3) with a barrier of 1.81 eV (0.91 eV below the reactants) to generate the intermediate W4. Multiple pathways exist from W4; the pathway to $\text{CH}_2\text{CCH}_2^+$ (allene) + HCN involves ring formation to W5 by crossing an energy barrier of 2.17 eV (TS4). This is then followed by ring opening (TS5), forming W6. A C-N bond homolysis in W6 produces the dissociated products allene cation + HCN, represented in Fig. [6.3](#).

The reaction pathway to the product channel H_2CNCH^+ or $\text{H}_2\text{CCNH}^+ + \text{C}_2\text{H}_2$ is represented in Fig. [6.4](#). W4 undergoes C-C bond formation to produce a five-membered ring intermediate (W7) via a 2.46 eV barrier (TS6). From W7, a series of H-shifts, produces W9 through the transition states TS7 and TS8 lying -1.17 eV and -2.34 eV below the reactants asymptote. The multiple isomer product channels that exist from W9 are represented in Fig. [6.4](#). In the first channel, internal H-shifts occur in W9 through an energy barrier (TS9) of 1.13 eV leading to the deepest well in the entire PES, W10 (pyrrole). The formed pyrrole undergoes an internal H-atom transfer (TS10) within the six-member ring by crossing an energy barrier of 2.73 eV, producing W11. Finally, ring opening reaction in W11 leads to the product channel $\text{H}_2\text{CCNH}^+ + \text{C}_2\text{H}_2$ through the intermediate W12 via the transition state TS11 located -1.95 eV below the reactants asymptote.

The competitive channel from W9 consists of ring opening (TS12), crossing an energy barrier of 1.21 eV, leading to W13. CC bond homolysis in W13 leads to the product set $\text{H}_2\text{CNCH}^+ + \text{C}_2\text{H}_2$.

Another possible product channel from W13 is $\text{c-C}_3\text{H}_3^+ + \text{H}_2\text{CN}$. Whereby, W13 undergoes three-member ring formation leading to W14 through the transition state (TS13) lying -1.65 eV

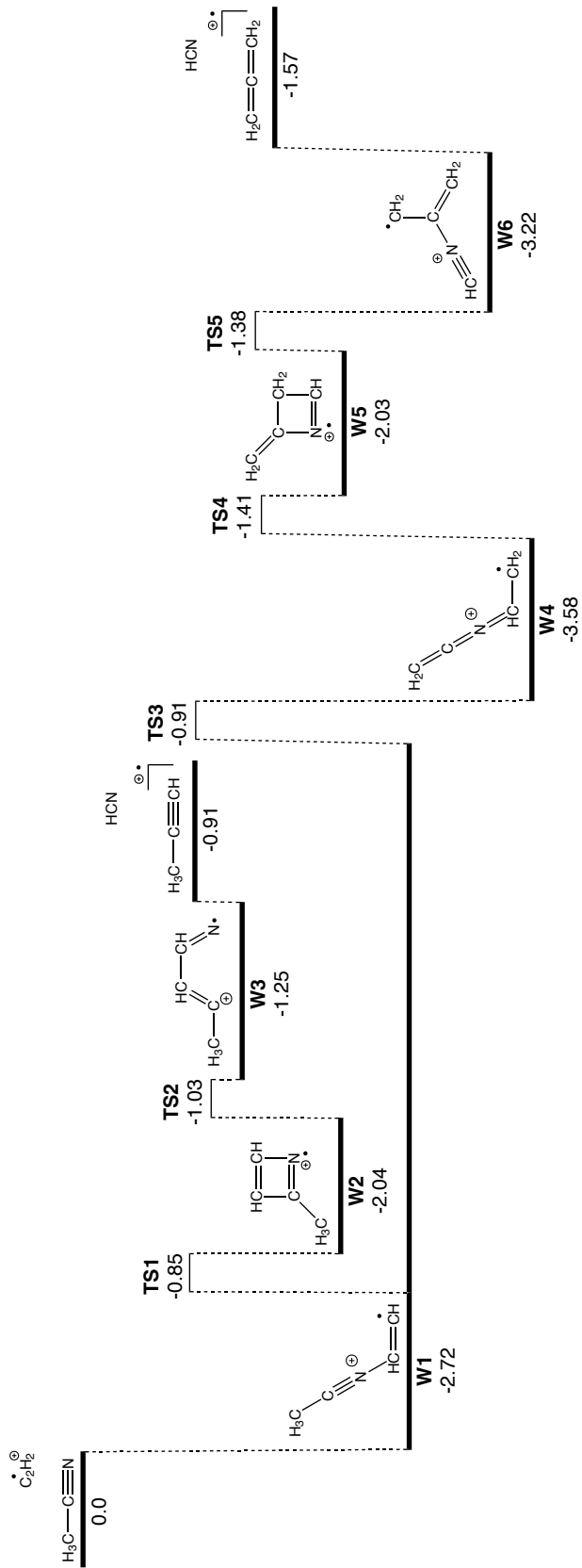


Figure 6.3: Potential energy surface (PES) for acetylene cation addition to acetonitrile to form $\text{CH}_2\text{CCH}^+/\text{H}_3\text{C}_3\text{H}^+ + \text{HCN}$. Geometries were computed at the M06-2X/6-31G(2df,p) level, with energies calculated at the G3X-K level of theory. The energy values are 0 K enthalpies presented in eV.

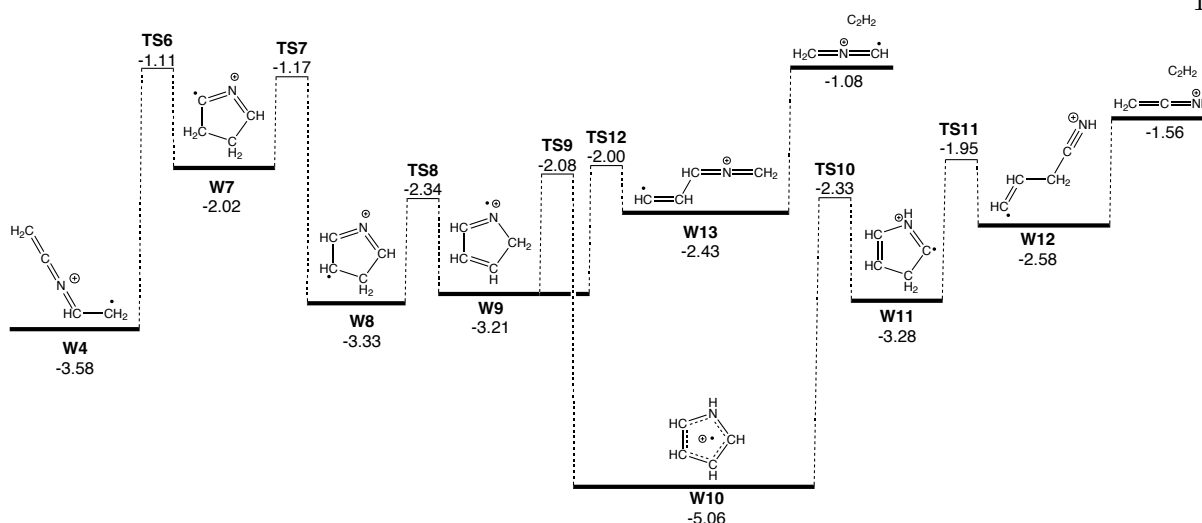


Figure 6.4: Potential energy surface (PES) diagram for the reaction channel forming $\text{H}_2\text{CNCH}^+ + \text{C}_2\text{H}_2$. Geometries were computed at the M06-2X/6-31G(2df,p) level, with energies calculated at the G3X-K level of theory. The energy values are 0 K enthalpies presented in eV.

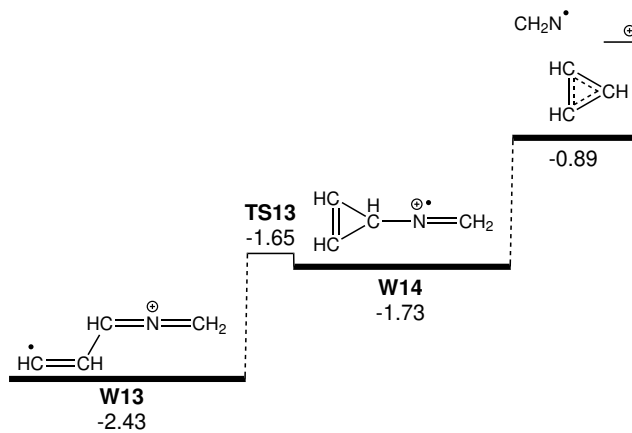


Figure 6.5: Potential energy surface (PES) diagram for the reaction channel forming $\text{c-C}_3\text{H}_3^+ + \text{CH}_2\text{N}$. Geometries were computed at the M06-2X/6-31G(2df,p) level, with energies calculated at the G3X-K level of theory. The energy values are 0 K enthalpies presented in eV.

below the reactants asymptote. CN bond homolysis in W14 generates the product set $\text{c-C}_3\text{H}_3^+ + \text{H}_2\text{CN}$, represented in Fig. [6.5](#).

Comparing the product channels identified here, all of the product sets are exothermic and proceed via transition states with all energies submerged below that of the reactants. For $\text{CH}_2\text{CCH}_2^+ + \text{HCN}$ and $\text{H}_2\text{CNCH}^+ + \text{C}_2\text{H}_2$, the products are below the reactants (by 1.57 eV

and 1.08 eV) respectively, marginally more exothermic than the $\text{H}_3\text{C}_3\text{H}^+ + \text{HCN}$. The highest saddle point along this channel is TS3 (0.91 eV below reactants); this is slightly above the energy of the exit channels. The rate constants and product branching fractions are decided based on the competition between energy and entropy factors. The entire reaction is complex and large parallel pathways exist from pyrrole cation. The dynamics will be the subject of future detailed kinetic studies.

6.4 Conclusion and outlook

The gas-phase reaction of $\text{C}_2\text{H}_2^+ + \text{CH}_3\text{CN}$ is characterized in a low pressure and temperature regime using a LIT TOF-MS apparatus. Experimentally and computationally identified primary products are $\text{c-C}_3\text{H}_3^+$, C_2NH_3^+ and C_3H_4^+ . Two products, C_2NH_3^+ and C_3H_4^+ , react with another acetonitrile to form the secondary product C_2NH_4^+ . The experimental techniques used in this study provide low collision energies and low pressure environments, which limit the reaction dynamics to exothermic pathways and do not stabilize reactive intermediates. Additional reactions of C_3D_4^+ with CH_3CN and CD_3CN would be useful to characterize, as it may provide further evidence that C_3H_4^+ is indeed a primary product of the current reaction and may shed new light on $\mathbf{m/z}$ 40 issues. This reaction has not been studied before in such a controlled manner and could be another important ion-neutral reaction in extraterrestrial environments.

Future plans for the current setup of the LIT TOF-MS involve implementation of a 118 nm light source, which would provide a cleaner ionization procedure for the creation of reactant ions.[\[310\]](#) This vacuum ultra-violet light source would also enable detection of contaminants in reactant samples through photoionization experiments. We have also coupled the current apparatus to a traveling-wave Stark decelerator.[\[311\]](#),[\[312\]](#),[\[19\]](#) This will extend the limits of cold, controlled reaction experiments by enabling control over the neutral reactant, both its quantum state and its velocity, leading to collision energies from 1-300 K.[\[18\]](#) Having such reaction energy resolution and quantum control over both reactants will push the limits of our knowledge of fundamental chemical reactions and may provide new insights into astrochemical reactions.

Chapter 7

Velocity-tunable beam of neutral molecules produced by Stark deceleration

“Born in leaks, the original sin of vacuum technology, molecular beams are collimated wisps of molecules traversing the chambered void that is their theater like companies of players framed by some proscenium arch. On stage for only milliseconds between their entrances and exits, they have captivated an ever growing audience by the variety and range of their repertoire.”

– John B. Fenn, *Forward to Atomic and Molecular Beam Methods*, Volume 1, 1988

As previously mentioned, a significant portion of my time and efforts in the Lewandowski group was devoted to integrating a molecular beam source to the linear ion trap (LIT) system already discussed in Chapter [2](#). This chapter will discuss the traveling-wave Stark decelerator (TWSD) system that will provide a velocity-tunable neutral molecular beam for energy-resolved reaction studies. The integration of this TWSD and the LIT will be discussed in Chapter [8](#).

The discussion of this TWSD is comprised of three parts. First, a general overview of Stark deceleration will highlight the physical principles that govern this beam source. Then, I will discuss the experimental measurements of decelerated molecules, noting parameters relevant to future reactions. Lastly, I will give a summary of the recent electrical and hardware upgrades to the TWSD in our laboratory.

7.1 Stark Deceleration

Stark deceleration is an extensive topic, an entire field of study in its own right. There are excellent resources with which to dive deeper into this topic, [313, 314, 315] including two excellent theses specifically covering traveling-wave Stark deceleration by Noah Fitch and Yomay Shyur, [16, 2] who played instrumental roles in the development of the traveling wave-stark decelerator (TWSD) that will be discussed in this chapter.

This section will primarily focus on the aspects of Stark deceleration that have been relevant to adding a TWSD as a neutral beam source to our LIT-TOFMS system. This discussion will begin by discussing the production of cold molecular beams that seeds the decelerator. This will be followed by a discussion of the Stark effect, and of the suitability of ammonia as an excellent candidate for deceleration. The discussion will focus primarily on TWSD, with a brief discussion of conventional pulsed-pin Stark deceleration for contrast. This will lead into a discussion of the phase space of a TWSD and characterizing the properties of the decelerated beam. Lastly, I will discuss how the decelerated molecules are detected, specifically the REMPI process we use to detect ND_3 .

7.1.1 Supersonic molecular beams

Supersonic molecular beams make an excellent source for a Stark decelerated beam. Such beams tend to have high densities and can achieve a narrow spread in the longitudinal, or forward, velocity with very low translational (perpendicular to beam propagation) velocities.

We produce molecular beams with *piezoelectric (PZT) valves*. Such valves operate *via* a disk of a proprietary material that flexes when high voltage ($\sim 200\text{-}400\text{ V}$) is exerted across it. This flexing motion retracts a poppet that normally seals a $\sim 1\text{ mm}$ hole with an o-ring. This HV-induced flex is quite short ($\sim 100\ \mu\text{s}$) and thus allows a temporally short pulse into the chamber. [316, 317] Such a valve is backed with a relatively large pressure ($\sim 1\text{-}20\text{ psig}$) of the molecule of interest (usually a few percent mixture in an atomic gas), with an UHV environment on the other side. The gas particles undergo a significant number of collisions during the quick expansion through

the small aperture. Especially when the carrier gas is atomic, this causes significant cooling of the vibrational and rotational degrees of freedom in the seeded molecule. The resulting pulsed gas beam is internally cold, with a well-defined forward velocity on the vacuum side of the valve, and is usually skimmed. This is depicted in Figure 7.1. As the gas propagates in the UHV environment, the molecular beam spreads according to its transverse and longitudinal velocities. Skimming the beam selects the section of this expansion with small transverse velocities, which is suitable for deceleration. Skimming also promotes differential pumping on either side of the skimmer, protecting the beam from possible collisions with the gas expansion.

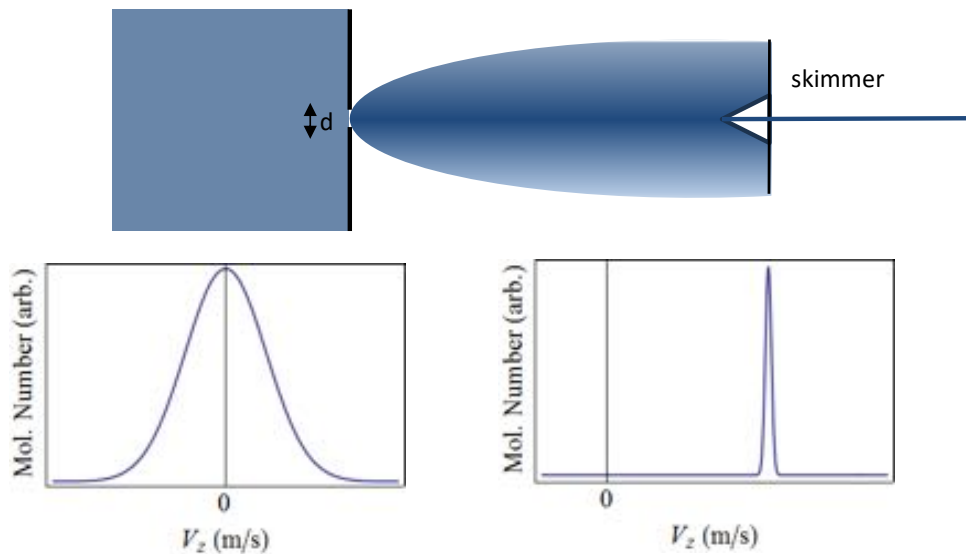


Figure 7.1: **(left)** a thermalized reservoir has a Gaussian distribution of velocity in each dimension. **(right)** After supersonic expansion through a small aperture of size d , the gas has a narrowly-defined forward velocity that is skimmed.

The supersonic beam reaches its ideal forward velocity in the case that all the enthalpy of the gas is converted to kinetic energy:[\[318\]](#)

$$v(T_0) = \sqrt{\frac{2k_B T_0}{m} \frac{\gamma}{\gamma - 1}} \quad (7.1)$$

where T_0 is the temperature of the gas reservoir, m is the mass of the carrier gas and γ is the

adiabatic constant γ is the ratio of the heat capacities of the gas at constant pressure and constant volume (C_p/C_v). This is 5/3 for a monoatomic ideal gas, but is more complicated in practice. C_p and C_v usually depend on pressure and temperature and can be measured and calculated for the gas of interest. And as always, k_B is Boltzmann's constant.

As can be seen by Equation [7.1](#), forward velocity of the beam is inversely proportional to the square root of the mass of the gas. In the PZT valve for the ion trap, we have used helium and argon as our carrier gasses, which have typical beam velocities of 1200 m/s and 560 m/s, respectively. For our decelerator, the velocities we can decelerate are limited by the bandwidth of our amplifiers to ~ 450 m/s or less. Because of this, we use a 2% mixture of ND₃ in krypton, since in our system krypton ideally can produce beams with a peak velocity of 386 m/s. In practice this tends to a bit larger, ~ 390 -400 m/s. There are multiple subtle and often parasitic factors that contribute to the exact quality of a supersonic beam. To better understand some of the principles we do have control over, Travis Briles's thesis is a nice place to start. [\[130\]](#) For our purposes, the important points here are that the use of a pulsed supersonic expansion in principle yields an sufficiently high density beam with a narrow distribution of forward velocity and cooled internal degrees of freedom. This allows deceleration of a low-lying rovibrational state of ND₃ from 400 m/s to multiple final velocities with the highest densities possible. Achieving an optimized starting beam involves tuning of the backing pressure, valve alignment, distance from valve to skimmer, seeding percentage, valve frequency, etc. These parameter optimizations are effectively empirical.

7.1.2 Stark deceleration of ammonia

The discovery of energy shifts and splittings in electric fields earned Johannes Stark the Nobel Prize in 1919. ¹ [\[320\]](#) Stark deceleration, as its name suggests, involves opportunistic manipulation of this field-induced energy shifts in molecules in order to decelerate them. There are two primary ways to do this: the traditional pulsed-pin Stark deceleration (PPSD, described briefly here); and traveling-wave Stark deceleration (TWSD, the emphasis of this section.) Most of this discussion

¹ Italian scientist Antonino Lo Surdo discovered it in the same year, although he did not receive a part of prize. [\[319\]](#)

will focus on the deceleration of ammonia, ND_3 , which was used exclusively for deceleration in this thesis. There exist excellent discussions of the deceleration of OH,^[2] ^[321] as well as many other molecules.^[314]

There are a few reasons that ammonia^[2] is our molecule of choice for this system. Ammonia was the first polyatomic molecule found in the ISM.^[323] Its presence has been established in distant galaxies,^[324] Orion,^[325], Jupiter^[326] and multiple other areas of space.^[327] ^[328] ^[329] ^[330] It is often the subject of studies of the temperature for regions of space.^[331] ^[332] The astrochemical relevance of ammonia is one reason it makes an excellent subject for ion-neutral reactions in our system. From a more practical standpoint, ammonia is particularly susceptible to manipulation by electric fields. As such, it was the first molecule successfully decelerated in a pulsed-pin decelerator,^[333] stored in a storage ring,^[334] ^[335] electrostatically trapped,^[336] and was one of the first molecules used for traveling-wave Stark deceleration.^[312] There are a few reasons for this.

Ammonia has a low-lying inversion state split by a small barrier, as shown in Figure ^[7.2]. This results in a small inversion splitting, U_{inv} , of two opposite-parity states. At relatively low electric fields, there is mixing of the opposite-parity states that results in an effective dipole moment. As a result, there is a Stark shift in the energy of ammonia in DC electric fields. The total energy of the system is described by:

$$U_{\text{stark}} = \mp \frac{U_{\text{inv}}}{2} \pm \sqrt{\left(\frac{U_{\text{inv}}}{2}\right)^2 + (|\vec{\mu}_d||\vec{E}|\frac{MK}{J(J+1)})^2} \quad (7.2)$$

where U_{inv} is the magnitude of the inversion splitting, \vec{E} is the electric field, $\vec{\mu}_d$ is the dipole moment, J is the total angular momentum, K is the projection of J onto the symmetry axis and M is the projection of J onto the electric field. Upper signs are for states in which the electric dipole moment is anti-aligned with the electric field – called *weak-field seeking* states. Lower signs correspond to cases when the energy is inversely proportional to the magnitude of the electric field, or *strong-field seeking* states. Equation ^[7.2] also demonstrates that in the high field limit the stark shift is linear with the magnitude of the electric field – referred to as a *first order Stark shift*. In

² Of interest to the total Nobel Prize count involved in this thesis, Fritz Haber received the 1918 Nobel Prize for the synthesis of ammonia.^[322]

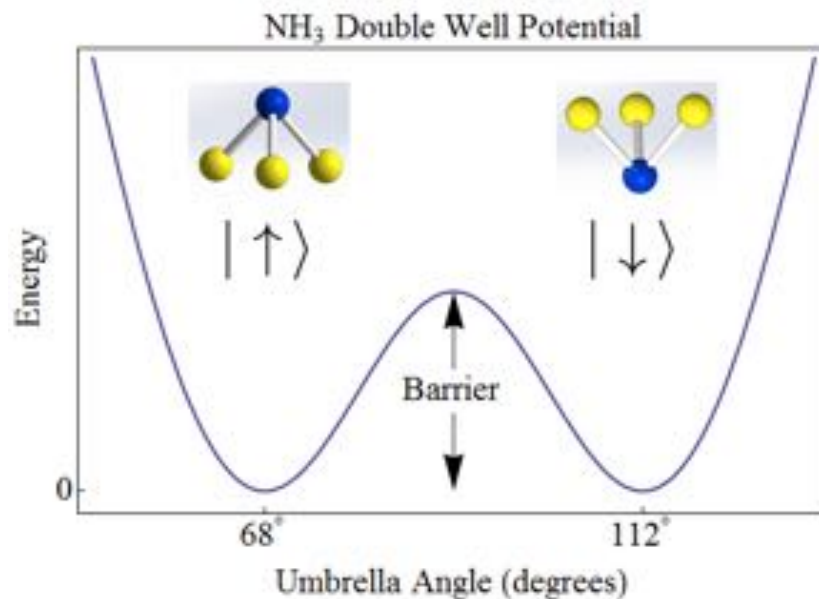


Figure 7.2: Energy of a NH₃ versus the umbrella angle. This forms a double well potential with two parities are separated by a small, nonzero barrier. The peak of this barrier is the planar configuration. Figure adapted from Fitch (2013).[\[16\]](#)

the lower field limit, its dependence scales with the square of the electric field, a *second-order Stark shift*.

An important point here is that due to the smaller inversion splitting of ND₃ relative to NH₃ (0.05 cm⁻¹ versus 0.79 cm⁻¹, respectively), deuterated ammonia reaches the strong field limit sooner, coupling more strongly to the electric fields. This can be seen in the Stark shifts of the $|J = 1, K = 1\rangle$ state of both NH₃ and ND₃ shown in Figure [7.3](#). Note that the $|J = 1, K = 1\rangle$ exhibits the strongest Stark shift and is the target state for our deceleration.

There are two primary modes of using this Stark shift to decelerate a beam of ND₃. The traditional form of deceleration is PSD, a geometry with sets of alternating cylindrical pins that are perpendicular to the beam deceleration axis, as shown on the left in Figure [7.4](#). On the right of Figure [7.4](#) is a photo of our TWSD during its installation to the LIT-TOFMS system. A TWSD has small rings mounted along the beam deceleration axis.

As the name might suggest, a pulsed-pin deceleration scheme involves pulsing high voltage

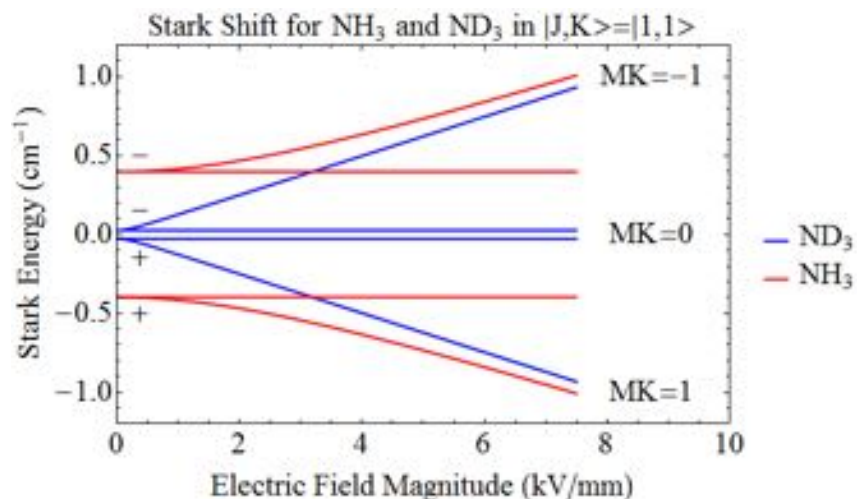


Figure 7.3: Stark effect for hydrogenated ammonia (red) and deuterated ammonia (blue). At zero field difference in energy of the two parities is separated by the inversion splitting. The Stark shift of ND_3 becomes linear quite early, while the Stark shift of NH_3 is of second order until nearly 3 kV/mm. Figure adapted from Fitch (2013).[\[16\]](#)

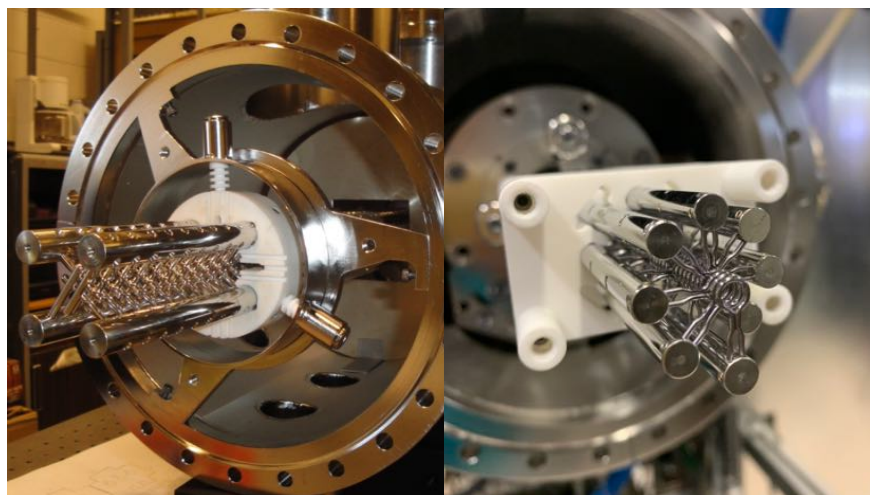


Figure 7.4: Photos of the hardware of a **(left)** pulsed-pin Stark decelerator and a **(right)** traveling-wave Stark decelerator. In the case of a PPSD, cylindrical rod pairs are orientated transverse to the molecular beam. For TWSD, rings are stacked along the molecular-beam axis. Left photo is from Fitch (2013).[\[16\]](#)

on the pins. Deceleration with this technique was first achieved in 2000 (with ND_3),[\[333\]](#) and conventional deceleration relies on the following principles. A single pair of pins can create a strong electric field by placing opposite high negative and positive voltage on the rods. As a molecule

enters into this field, it sees a potential hill. Moving into this region then will require an exchange of kinetic energy for potential energy. If this potential is switched at or before the molecule reaches the top of the electric potential, this kinetic energy in the beam propagation direction will be removed from the molecule. This can be repeated multiple times.³ This is shown schematically in Figure 7.5a, where the dots represent rods at high negative (black), high positive (blue) or grounded (white) potentials. Underneath the rods is demonstrated the effective electrical potential in bold black lines. The top and bottom panels present alternating sets of pins. Recall from Figure 7.4 that alternating pins are perpendicular to each other. Pulsing in this alternating configuration mitigates loss from transverse spreading. The exact time that the rods are switched on for correlates to how “high up the hill” the molecule gets before the potential is switched off. This is mathematically described as the *phase angle*, ϕ_0 . Figure 7.5b-c demonstrate three of many possible phase angles for such a system. The case of $\phi_0 = 0$ results in no deceleration and is referred to as *bunching*. Higher phase angles result in larger deceleration and lower final velocities for a set decelerator length and voltage amplitude. However, more aggressive phase angles will result in large losses in densities. Note that such HV pulsing can be achieved (relatively) easily with commercially available Behlke switches.

However, there are significant issues in deceleration efficiency below 100 m/s. This is primarily due to coupling between the longitudinal and transverse motions that eventually leads to loss of molecules from the decelerator due to high transverse velocities.^[2, 337] There have been nice developments in advanced pulsing schemes to help mitigate this issue;^[337, 338, 339, 340] however, the physical geometry is a fundamental limitation. Nevertheless, PPSD has been a productive mode of deceleration, well-utilized for many scientific studies,^[314, 315, 341, 342] and been the subject of many theses.^[338, 321, 16, 2, 314, 315, 338, 321, 341, 342] The discussion here has barely scratched the surface of the capabilities and applications of this mode of operation. However, the transverse losses are problematic, especially for the purpose of reaction studies in which high

³ Note that this picture just involves one molecule, whereas in reality deceleration will involve a cluster molecules that have a spread in longitudinal *phase space* (i.e. spread in both velocity and position). For clarity and simplicity we model the center of this distribution, calling it the *synchronous* molecule.

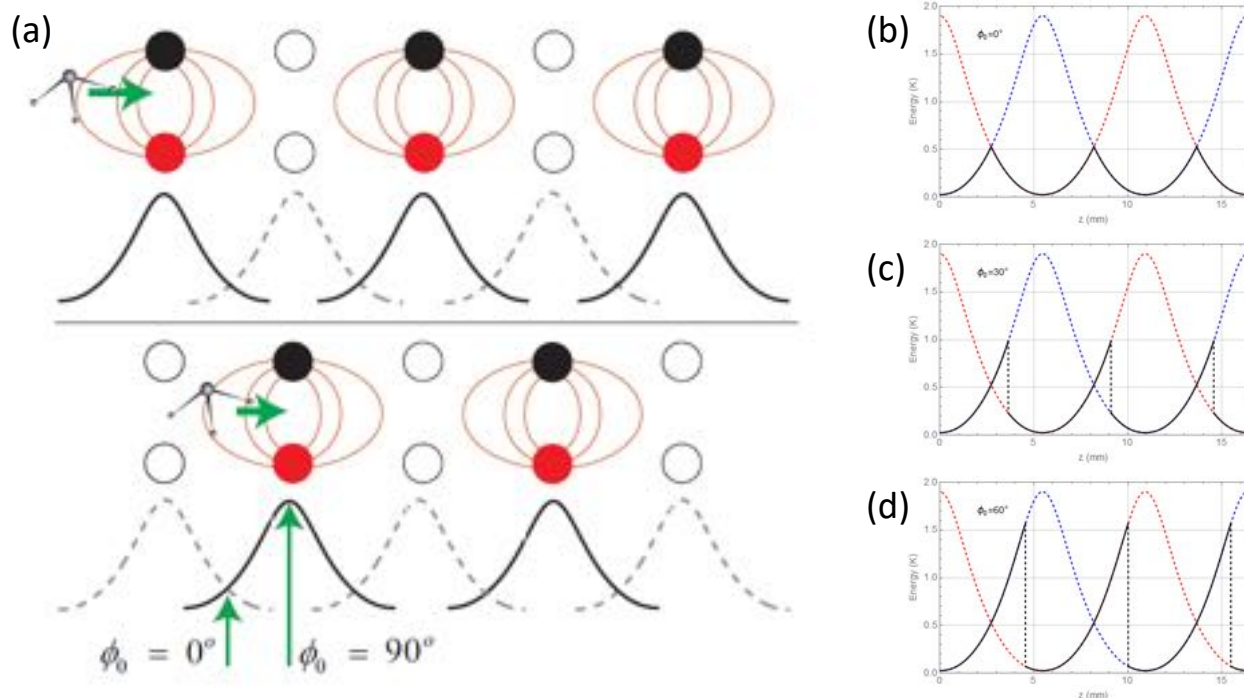


Figure 7.5: **(a)** Schematic of switching sequence in pulsed-pin Stark deceleration. The top and bottom panels depicting alternating voltage sequences that are switched between nearly instantaneously. The timing of switching determines how far a molecule climbs a potential hill before the configuration switches. This determines how much kinetic energy is removed per stage. **(b-d)** graphs of energy versus movement in the beam propagation direction. The black curve represents the potential experience by the synchronous molecule as it travels through two potentials (red and blue). This shows the cases for **(b)** no deceleration, or bunching, deceleration characterized by a phase angle of **(c)** $\phi_0 = 30^\circ$, and **(d)** $\phi_0 = 60^\circ$. A $\phi_0 = 90^\circ$ phase angle would switch configurations at the peak of the potentials. (a) is adapted from Fitch (2013),^[16], (b-d) from Shyur (2018).^[2]

densities are required and low velocities are desired. For the applications of ion-neutral reactions, we need greater densities than can be provided by pulsed-pin Stark deceleration for feasible reaction studies. We thus turn our attention to traveling-wave Stark deceleration.

Traveling-wave Stark deceleration was first demonstrated in 2010.^[311] It utilizes an somewhat different scheme for deceleration. Again, as the name implies, the design is to use sinusoidal wave to produce a potential well that continuously guides and slows the molecules. Typically, the molecules in one such well are called a *packet*. Such guiding and deceleration can be done with sinusoidal potentials, which make an actual 3-D well with decoupled longitudinal and transverse trapping. This nicely addresses the loss issues previously mentioned. Such a potential well can be made with

an arbitrary number of rings. Our system utilizes a periodicity of eight to create sine-wave voltages with voltage:

$$V_i(T) = V \sin\left(\frac{w\pi i}{8} - \omega t\right) \text{ for } i = 0\dots7 \quad (7.3)$$

where V is the amplitude of the potential on the rings, i is the ring number, ω is the speed of translation for this potential wellover time t . As was seen by Figure [7.4](#), the rings on our TWSD are mounted by eight rods that allow independent control of each set of eight rings. The effective electrical potential and the potential energy for ND_3 that this creates is shown in Figure [7.6](#). Now if we want to move such a electric potential well, thus guiding ND_3 , we must choose an ωt that corresponds to an appropriately chosen longitudinal velocity. We are constrained to our potential well moving $8l$ (where l is the inter-ring spacing) over a sinusoidal phase of 2π . We can thus calculate our sinusoidal frequency f :

$$f = \frac{v}{pl} \quad (7.4)$$

Operating the decelerator at a set frequency ωt with eight phase-shifted potentials described in Equation [7.3](#) produces a traveling wave like that shown in Figure [7.7](#). This schematic demonstrates a $\pi/4$ movement of this well. The amount of time that this phase shift takes is the velocity of our moving well. This value of f (Equation [7.4](#)) depends on the geometrical parameters of the built TWSD in our system (see Table [7.1](#).) The starting velocity of our deceleration of ND_3 velocity is around 390 m/s, the empirical velocity of a supersonic expansion of krypton in our system. This corresponds to 24 kHz, with $l = 2.03 \text{ mm}$ for our TWSD. Running at $f = 24 \text{ kHz}$, combined with good timing for turning on the decelerator, can guide, or bunch, such a beam of molecules at the initial velocity. If we want to decelerate, we chirp the frequency. This is done with a simple linear chirp:

$$f(t) = f_i + \alpha t \text{ with } \alpha = \frac{f_f - f_i}{T} (\alpha \leq 0) \quad (7.5)$$

where T is the time-of-flight of the molecular beam through the entire decelerator, f_i and f_f are the initial and final frequencies, respectively.

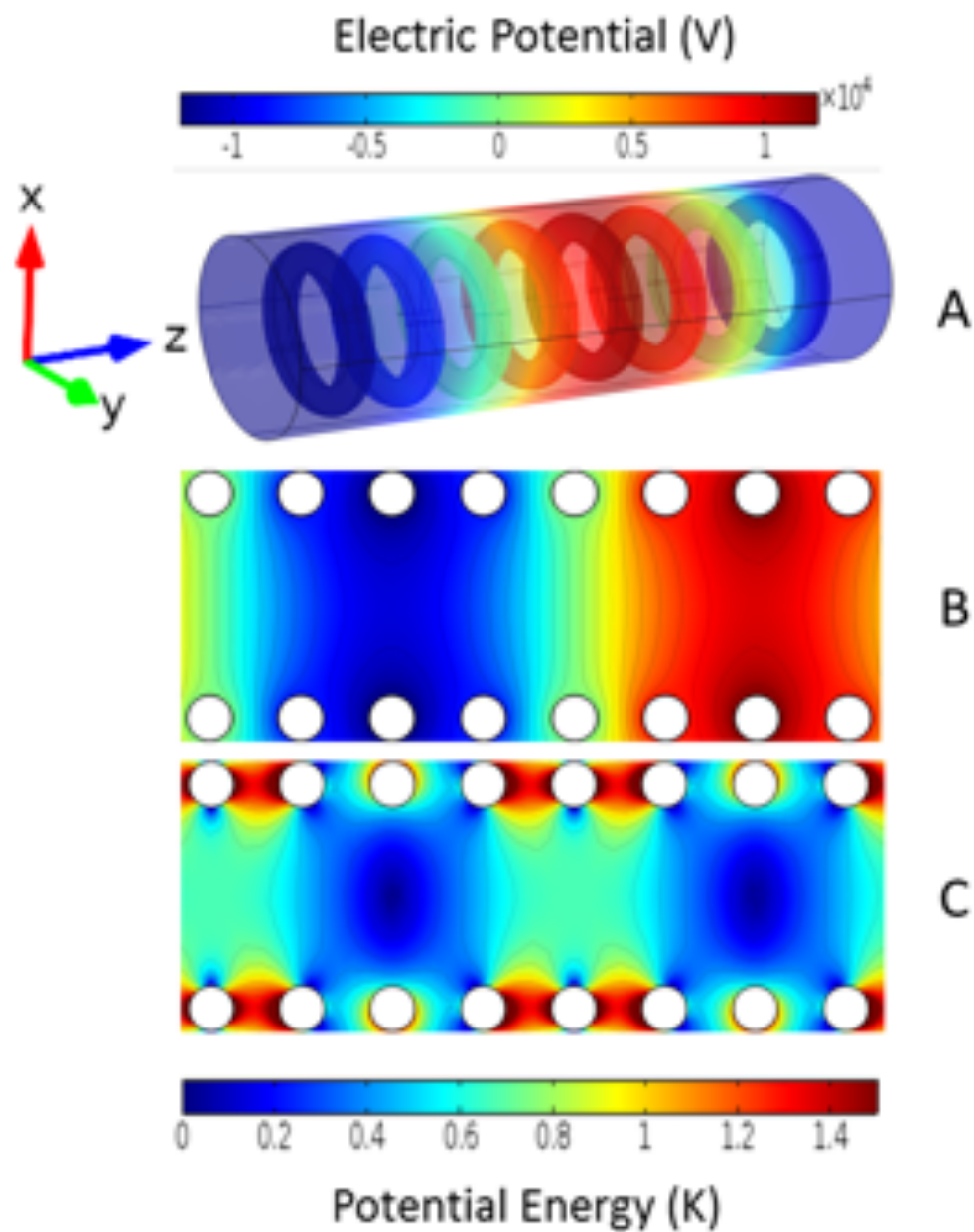


Figure 7.6: **A** Effective electric potential on eight rings with sinusoidal, phase-shifted voltages (electric potential scale is given by top legend). **B** The resulting effective potential over a central cross-section along the z-axis of A. **C** the effective potential energy experienced by an ND_3 molecule due to electrical potential in B. (Scale for energy given by bottom legend.) Schematic adapted from Fitch (2013).[\[16\]](#)

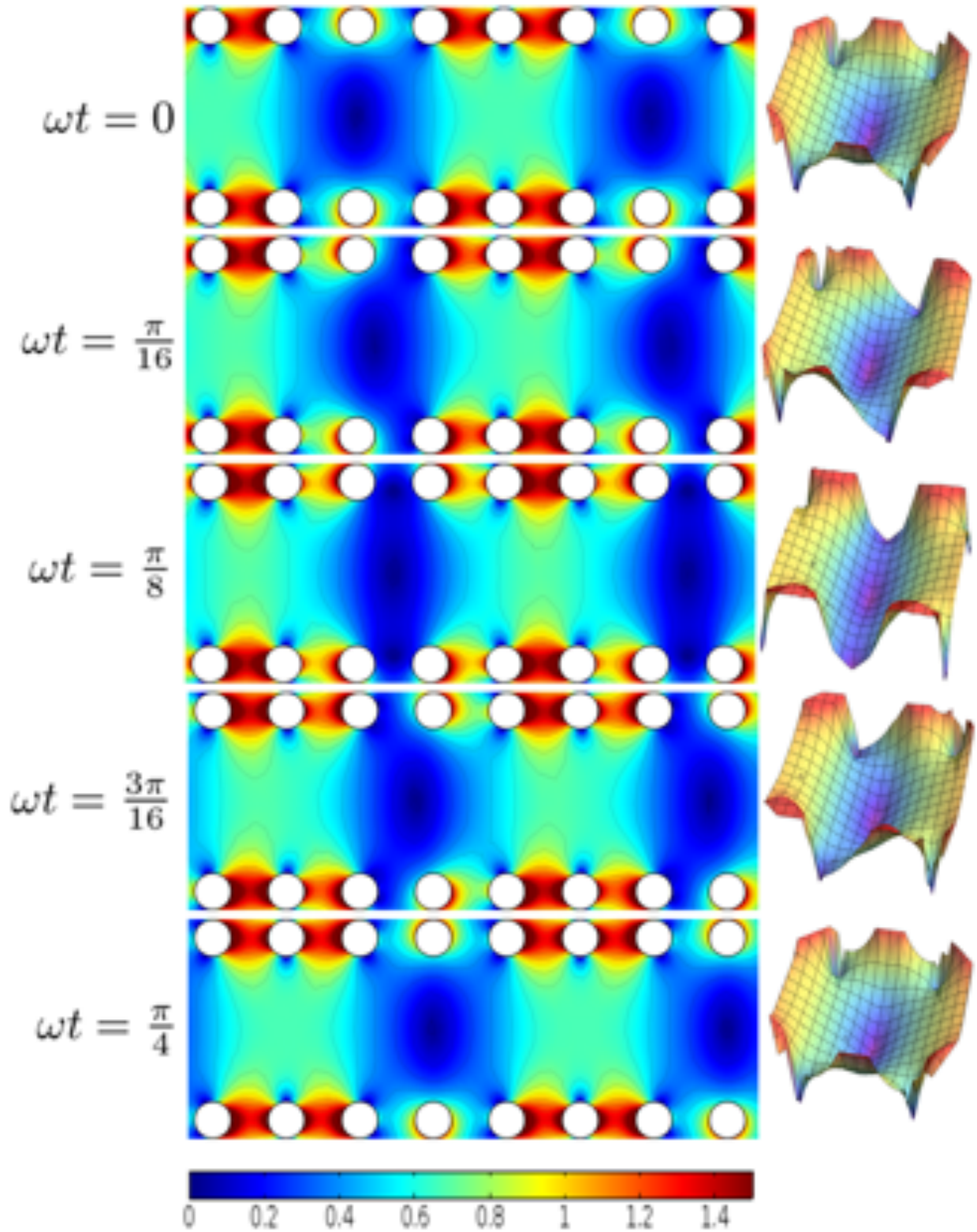


Figure 7.7: Electric potential energy given for multiple phases of ωt , demonstrating the movement of a well due to the frequency of the sinusoidal potential on each ring. Schematic adapted from Fitch (2013).[\[16\]](#)

Table 7.1: Geometrical TWSD measurements, as well as typical deceleration parameters and trap geometry variables.

Decelerator parameters		Typical Deceleration Parameters	
Ring spacing	2.03 mm	Starting gas velocity	385-400 m/s
Ring diameter	4 mm	Frequency bandwidth	25 kHz to DC
Rings per stage	8	Time required to decelerate to rest	6.3 m/s
Number of rings	624	linear chirp, α	$\sim 4000 \text{ s}^{-2}$
Total decelerator length	1.267 m		

It should be noted that while these chirped sinusoidal frequencies are conceptually simple, they are technically difficult. 25 kHz to DC is a significant bandwidth, particularly for high voltage. This is an electrical engineering problem that our group has sought to answer that has necessitated in-house design of specialized amplifiers. A review of these amplifier specifications, challenges, and recent work to improve their performance will be given later in section [7.3](#).

First, we will dive deeper into the principles of traveling-wave Stark deceleration. To understand important details such as initial distribution of molecules that can deceleration, or the characteristics of the decelerated beam, we need to examine what is referred to as the *phase-space acceptance* of the TWSD. This will be discussed in the next section.

7.1.3 Phase-space acceptance

Computational modeling is a critical aspect of understanding the expected performance of a Stark decelerator. This is particularly true for pulsed-pin systems, which must be modeled with numerical methods due to the coupling between transverse and longitudinal modes. Likewise, the modeling of the performance of a traveling-wave Stark decelerator benefits from full Monte-Carlo simulations. However, we can achieve a relatively good approximation of the stable and unstable trajectories of molecules with a more simplistic model. Prior work has demonstrated that the longitudinal phase-space acceptance (LPSA) model compares well with full molecular dynamics simulations. [\[17\]](#) The LPSA model was quite successful in predicting the performance of our TWSD as will be seen in section [7.2](#). LPSA model is also discussed here not just as theoretical calculations with which to compare our system, but also a model also yields some general intuition regarding

the expected characteristics of a successfully decelerated beam.

I will discuss a few practical notes before the model is discussed. Some prevailing themes that will be noticed is the emphasis on the longitudinal potential (as the name might suggest.) This is due to the critical assumption that the transverse potential is decoupled from the longitudinal potential. This feature of traveling-wave Stark deceleration yields transverse guiding of the molecules that is nearly isolated from the magnitude of beam deceleration. Given this assumption, we can model the success of a particular molecule's deceleration as it depends on its position in *phase space*, which is its position and velocity in a particular dimension. Numerical calculations can determine the *separatrix*, or the boundary in phase space between stable and unstable trajectories.[\[16\]](#) A separatrix allows us to calculate the phase-space acceptance, the total area in phase space that results in successful deceleration. An example of the transverse phase-space acceptance for of our TWSD is shown in Figure [7.8](#). Note that the separatrix depends on the position of the well relative to the rings (or the phase of ωt , refer to Figure [7.7](#).) The two extremes for the largest (black) and smallest (red) phase-space acceptance are shown. The narrow acceptance in transverse dimensions is a key motivation for starting with supersonic pulsed beams, which can produce such a distribution in phase space with relatively high densities (see section [7.1.1](#).)

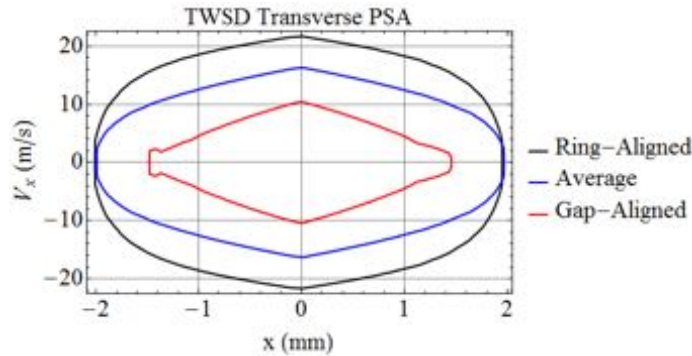


Figure 7.8: Transverse separatrix for TWSD a transverse dimension. The three separatrices denote extremities of transverse phase-space acceptance as dependent on the phase of ωt . Figure adapted from Fitch (2013).[\[16\]](#).

The transverse potential, and the resulting transverse phase space acceptance, is intrinsic to the decelerator geometry. However, the acceptance in the longitudinal direction will depend on the

level of deceleration. In the case of the traveling-wave Stark decelerator this longitudinal potential is not only decoupled from the transverse potential, but also can be modeled analytically. We can model it as a set of toroidal electrodes held at fixed potentials. The potential for a single torus is given by:[\[343\]](#)

$$V(z) = \frac{2V_0}{\pi} \sqrt{\frac{1}{1+z^2/a^2}} \sum_{p=0}^{\infty} (2 - \delta_{0p}) \frac{Q_{p-1/2}(\cosh(\eta_0))}{P_{p-1/2}(\cosh(\eta_0))} \cos\left(p \arccos\left(\frac{z^2 - a^2}{z^2 + a^2}\right)\right) \quad (7.6)$$

with δ_{0p} as the Kronecker delta function, where $a = r_0 \sinh(\eta_0)$ is the effective radius of an equivalent ring of charge, and $V_0 = 10$ kV. The relation, $\eta_0 = \ln\left(\frac{R}{r_0} + \sqrt{\left(\frac{R}{r_0}\right)^2 - 1}\right)$ is that of a toroidal surface with cross-sectional radius $r_0 = 5 \mu\text{m}$ and mean radius $R = 2.5$ mm. $P_{p-1/2}$ and $Q_{p-1/2}$ represent associated Legendre functions of the 1st and 2nd kind, respectively, with $p \leq 2$. ($Q_{p-1/2}(\cosh(\eta_0))$ will necessarily return a complex number for all orders of p , but only the real part contributes to the on-axis potential.)

We can then sum over a set of rings with potential that varies spatially as:

$$V_{\text{tot}}(z) = \sum_{n=-N_0}^{N_0} V(z - n d) \cos\left(\frac{2\pi n}{8}\right) \quad (7.7)$$

with d as the distance between rings, $d = 2.032$ mm, and $N_0 = 6$. Such an model yields quantitative agreement with the full, 3D model of the decelerator generated by numerical calculations with the COMSOL multiphysics package[\[20\]](#). The potential is simply used to calculate the electric field

$$E(z) = -\frac{dV_{\text{tot}}(z)}{dz} \quad (7.8)$$

and used to calculate the Stark energy, which can be used to calculate the energy states in an electric field:

$$U_{\text{Stark}}(z) = -\frac{U_{\text{inv}}}{2} + \sqrt{\left(\frac{U_{\text{inv}}}{2}\right)^2 + \left(\frac{\mu_d E(z)}{2}\right)^2} \quad (7.9)$$

This equation is identical to Equation [7.2](#) for the $|J = 1, K = 1\rangle$ state of ammonia, with the addition of the explicit dependence of the electrical field on the longitudinal coordinate z . With Equations [7.7](#)-[7.9](#), we can calculate the longitudinal well experienced by ND_3 molecules in the decelerator due to the Stark shift.

However, to fully model the longitudinal phase-space acceptance, we must account for a few more things. Firstly, the deceleration will apply a force to the molecules, changing the effective potential energy profile:

$$U_{\text{eff}}(z) = U_{\text{Stark}}(z) + m\alpha z \quad (7.10)$$

with,

$$\alpha = \frac{v_f^2 - v_i^2}{2L} \quad (7.11)$$

As can be seen, the potential energy well depends on the final velocity v_f , the initial velocity $v_i = 385$ m/s, and the deceleration length ($d = 1.266$ m, Table 7.1.) Figure 7.9 shows this effective potential well for different final velocities out of the decelerator.

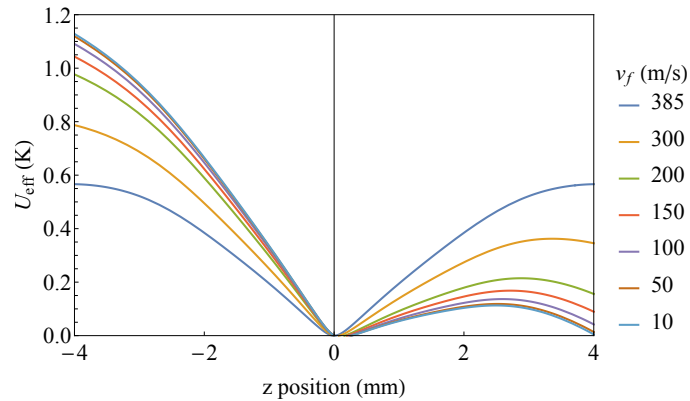


Figure 7.9: Effective potential energy in Kelvin as a function of longitudinal position in the decelerated well for the different final velocities measured in the experiment. $v_f = 385$ m/s is also evaluated to show the maximum well-depth experienced by the molecules during bunching, where the potential well moves at a constant speed. Figure adapted from Greenberg (2021).

Secondly, we need the separatrices for these final velocities. This is calculated using the effective potential well to calculate the classical turning points, where the potential energy and kinetic energy are equivalent. The calculated separatrices that correspond to a handful of final velocities are depicted in Figure 7.10. From these separatrices, we can calculate the relative area enclosed by the longitudinal separatrix to determine the relative signal expected for each final velocity. This calculation was used to compare our experimental data in section 7.2.

There are a few intuitive results to point out here. Note that the 385 m/s separatrix (blue)

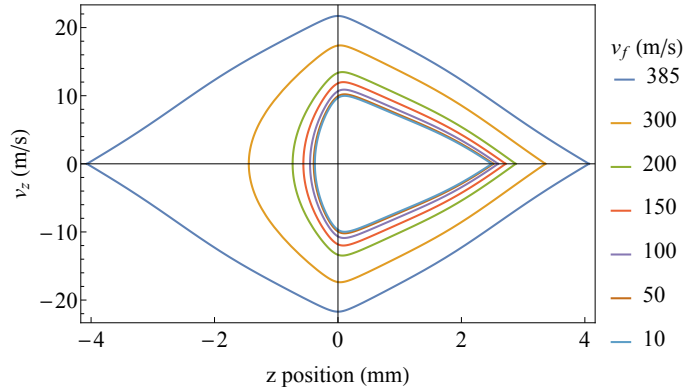


Figure 7.10: Longitudinal separatrices resulting from the effective potentials in Fig. 7.9. Figure adapted from Greenberg (2021).

in Figure 7.10 corresponds to bunching. The lack of tilt in the potential well results in a much larger phase-space acceptance, as well as symmetry in both v_z and z in the separatrix. Of course, the phase-space acceptance decreases significantly as the final velocity gets smaller. As mentioned prior, these results are for a deceleration amplitude $V_0 = 10$ kV. In the case $V_0 = 8$ kV, the well tilts completely over by 100 m/s and there are no stable trajectories.^[2] This is an important point that motivates the high voltages at which we work: deceleration to low velocities, or rest, requires a particularly deep well. This in turn has motivated many of the advances in the electronics necessary to produce such potentials on the decelerator. Another feature to point out is that this model predicts the spread in longitudinal velocities as well. For bunching, this spread is near ± 20 m/s, whereas this approaches ± 10 m/s at the more aggressive deceleration schemes. These are details that are important for modeling reaction collisional energies, as well as predicting the spread of the beam from the output of the decelerator to the trap in the integrated setup.

In summary, the phase-space acceptance of the decelerator can be modeled analytically, with accuracy comparable to full numerical simulations. Such models yield expectations for the relative signal of the decelerator at different final velocities, as well as expectations for the longitudinal and transverse velocity spreads. Such theory can be utilized for comparisons of experimental results.

7.1.4 Detection of neutral ammonia out of the Stark decelerator

As a last point before discussing experimental deceleration results, I will discuss how we detect the neutral ammonia on the output of the decelerator. This involves a brief discussion of the relevant REMPI process, as well a discussion of the geometry of the detection region.

The principles of REMPI (resonance enhanced multiphoton ionization) were briefly discussed in section [2.2.1](#). This was discussed in the context of an efficient ionization process with which to load ions into our ion trap. Here, we are interested in REMPI for its state selectivity as we can choose an ionization scheme with a large cross-section for the $|J = 1, K = 1\rangle$ and $\nu = 0$ state. This state can be resonantly ionized with a (2+1) REMPI scheme at 317 nm. As a reminder, this means two simultaneous photons at 317 nm are required to excited our the ND₃ to an electronically and vibrationally excited intermediate state. Then, another single 317 nm photon ionizes the ammonia, as shown in Figure [7.11](#). The excited intermediate state in this case is the second electric excited state \tilde{B}^1 and the fifth overtone of the second vibrational mode, $\nu_2 = 5$.

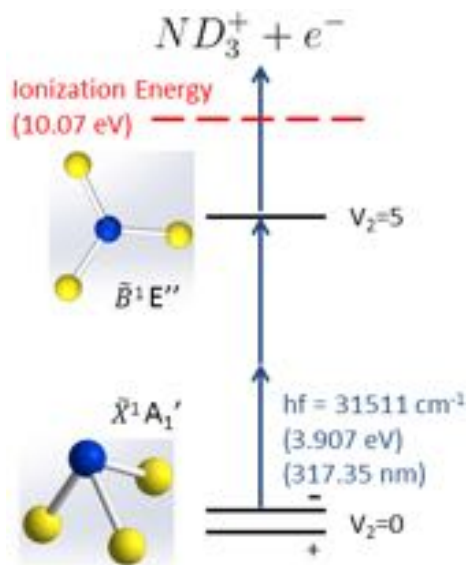


Figure 7.11: (2+1) REMPI scheme for ND₃ at 317 nm. Figure adapted from Fitch (2013).[\[16\]](#)

This REMPI process is used in conjunction with a TOF-MS and MCP to detect the output of the decelerator as shown in Figure [7.12](#). Prior to the integration with the LIT, we detected the

ionized ND_3^+ with a simple-two stage TOF. The REMPI laser beam path was intersected between the two plates of a two-stage TOF to send the newly ionized ND_3^+ into the MCP for detection. While this TOF configuration is not as sophisticated or high-resolution as that used with our ion trap, it is more than sufficient for detecting the relative intensity of resonantly-ionized ND_3 in a molecular beam. This is the detection configuration for the characterization of the decelerator performance described in section 7.2. After the TWSD was integrated with the LIT, we used (are using) the ion trap as our TOF. This will be described in more detail in Chapter 8.

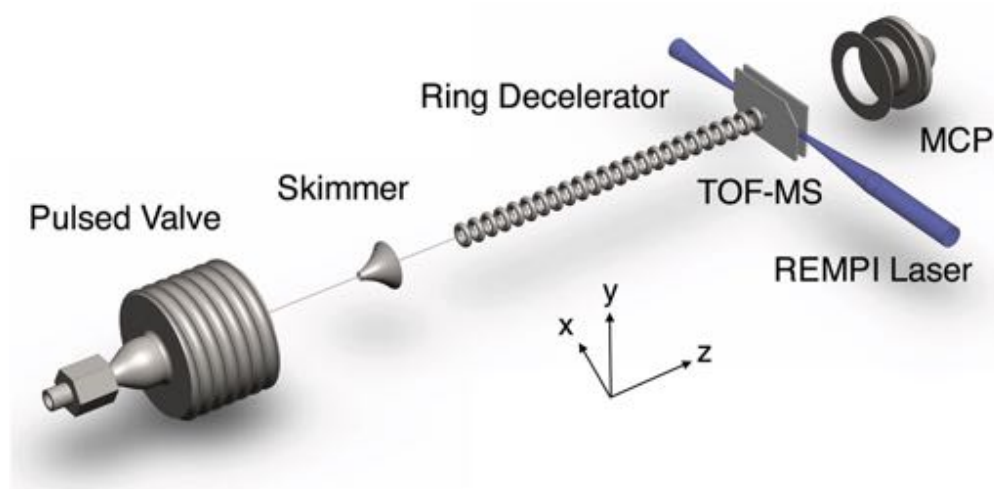


Figure 7.12: Schematic for production and detection of a decelerated ND_3 beam with traveling-wave Stark deceleration. Figure adapted from Shyur (2018).^[17]

One complication that we had to account for when characterizing the output of our decelerated signal is the size of the aperture in the TOF plate shown in Figure 7.12. While the transverse velocity spread of the molecular beam is quite small, it is large enough to cause clipping on the TOF plates at low longitudinal velocities. I will briefly overview the geometry of the detection area to demonstrate how we accommodated this fact in our analysis of the output beam in section 7.2.

First, we must make a few assumptions to estimate the consequences of the transverse spread. One assumption is that the molecular packets have a transverse velocity (v_{\perp}) of 10 m/s regardless of forward velocity, as motivated by LPSA theory discussed in the previous section. Then we can

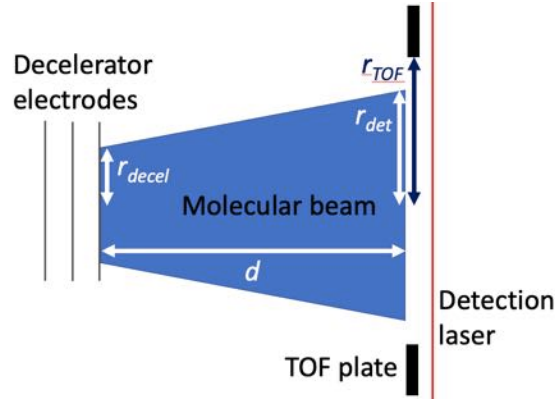


Figure 7.13: Cross-sectional view of the end of decelerator and detection region with the propagation of the molecular beam shown in blue. The molecular beam propagates from the exit of the decelerator to the detection laser, spreading from an initial radius r_{decel} to radius r_{det} at the detection region. Depending on the amount of transverse spread, there may be clipping due to the radius of the TOF aperture, r_{TOF} . Figure not to scale and adapted from Greenberg (2021).[\[18\]](#)

calculated the transverse radius of the packet at the detection region, r_{det} with:

$$r_{det} = r_{decel} + \frac{v_{\perp}}{v_{\parallel}} \cdot d, \quad (7.12)$$

where d is the 7 mm distance from the exit of the decelerator to the ionization laser, v_{\parallel} is the mean longitudinal speed of the packet, and r_{decel} is the radius of the packet at the end of the decelerator, which is taken to be 2 mm. (All of these variables are labeled schematically in Figure [7.13](#)) Secondly, we assume the REMPI laser has a beam waist with a diameter much smaller than that of the molecular packet and that it has a Rayleigh length long enough that it can ionize molecules along the diameter of the molecular packet. This results in a ratio of molecules at the output the decelerator to those in the detection region (N_{decel}/N_{det}) that scales with the inverse of ratio of the radius of the molecular packets as described by the following equation:

$$\frac{N_{decel}}{N_{det}} = \frac{r_{det}}{r_{decel}} = \frac{r_{decel} + \frac{v_{\perp}}{v_{\parallel}} \cdot d}{r_{decel}} \quad (7.13)$$

We also need to consider that the aperture in the TOF plates is 2.5 mm. In some cases the molecular packet will expand and be clipped by this aperture. We can calculate the loss of detected

molecules:

$$\frac{N_{\text{decel}}}{N_{\text{det}}} = \frac{r_{\text{det}}}{r_{\text{decel}}} \cdot \frac{r_{\text{det}}}{r_{\text{TOF}}} = \frac{(r_{\text{decel}} + \frac{v_{\perp}}{v_{\parallel}} \cdot d)^2}{r_{\text{decel}} \cdot r_{\text{TOF}}}, \quad (7.14)$$

where r_{TOF} is the radius of the aperture.

This clipping will occur when the molecular packets have a longitudinal velocity:

$$v_{\parallel} \leq \frac{d \cdot v_{\perp}}{r_{\text{TOF}} - r_{\text{decel}}} \quad (7.15)$$

For this detection system, $v_{\parallel} \leq 130$ m/s.

These equations guided our analysis of the output relative signal at different final velocities, by compensating for effects of the detection scheme. Such analysis allowed us to compare our decelerator output to theoretically calculated expectations, and to accurately characterize the beam prepared for future reaction applications. The next section discusses the experimental measurements of the decelerator performance for reaction studies. This includes a description of the transverse and longitudinal spread, the success and limitation of relevant deceleration schemes, and deceleration efficiency. All of these aspects are critical to the TWSD's role as a molecular beam source for reactions with trapped ions.

7.2 Characterization of TWSD output (before integration with LIT-TOFMS)

Section [7.2](#) is devoted to describing the experimentally measured output of our traveling-wave Stark decelerator (TWSD), as detected by a REMPI laser and two-stage time-of-flight mass spectrometer. This was our final characterization and publication of this decelerator's performance before it was integrated with our linear ion trap (LIT). Section [7.2](#) is adapted from the work that we published in Review of Scientific Instruments in 2021. [\[18\]](#) I was the second author on this paper; the first author, James Greenberg, and I took all of the data together. He did the bulk of the theory calculations with which we compare the results.

7.2.1 Continuous deceleration of ND₃ from 385 m/s to 10 m/s

Packets of decelerated ND₃ molecules were detected after being slowed from an initial velocity of 385 m/s to multiple final velocities. Different final velocities, ranging from 300 m/s down to 10 m/s, were chosen to demonstrate the tunability of the beam produced by the TWSD. We expect the ND₃ signal to be the sum of the decelerated packet with a background of non-decelerated molecules, which exit the decelerator at the same time. To account for the contribution from the non-decelerated ND₃ molecules, we first measured the signal while the decelerator electrodes were grounded. We refer to this measurement as the free-flight data. We then scale the free-flight data to the background value of the decelerated data to be able to evaluate the portion of the signal from non-decelerated molecules. We must scale the free flight data for two reasons. First, the MCP voltage needs to be a different setting for these different data sets to avoid saturating the detector. Second, the overall number of non-decelerated molecules that reach the end of the decelerator during a deceleration sequence will be larger (than in free flight), as they are transversely guided. Figure 7.14 shows a summary of the deceleration data, as well as the free-flight data, scaled to match the decelerated data baseline. Combined, these data show the contribution from free-flight molecules is negligible for final velocities ≤ 100 m/s. The decelerated packets of ND₃ also show four or five distinct peaks at each final velocity. These correspond to multiple potential wells being filled in the decelerator. We verified that the final velocity of the molecules in each well is the same by comparing the detection time of each peak with the ending time of the deceleration sequence. Using the fixed distance between ring electrodes, and the distance between the final ring of the decelerator and the TOFMS extraction region, we found precise agreement between calculated and measured peak arrival times of each of the peaks in the molecular packets.

As the final velocity of the molecular packet decreases, the measured width of each packet increases (see Figure 7.14). This increase is caused by the spread of velocities of the molecules within each decelerated well. The velocity spread was modeled in a previous study using a longitudinal phase-space acceptance model discussed in section 7.1.3. The model showed quantitative agreement

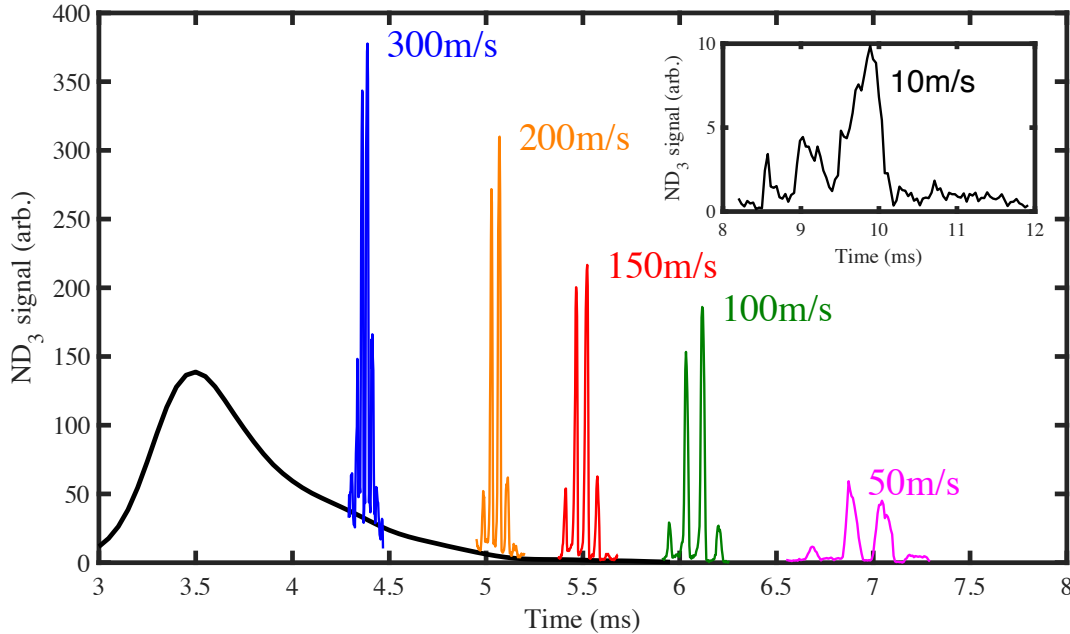


Figure 7.14: Deceleration data for multiple final velocities ranging from 300 m/s down to 10 m/s. Time is the delay between the molecular beam valve trigger and detection laser pulse. The solid black trace is the free-flight data, scaled to match the baseline of the deceleration data. The free-flight background is essentially zero by 6 ms. The inset plot shows the 10 m/s data. The discrete peaks at each final velocity correspond to multiple, filled potential wells all with the same longitudinal velocity.

Table 7.2: Maximum longitudinal spread in velocities of ND_3 wells at end of decelerator, as calculated by the LPSA model. The full-width half max velocity spread, which is more relevant to collision studies, will be less than this and depends on how the phase-space distribution overlaps with the phase-space acceptance of the decelerator. The velocity spread for $v_f = 385$ m/s is from bunching. Velocity spreads are also converted into kinetic energy uncertainties to facilitate discussion of the energy resolution obtained for collision studies.

v_f (m/s)	Δv (m/s)	ΔE (μeV)
385	22	49
300	17	31
200	13	18
150	12	14
100	11	12
50	10	10
10	10	10

with full molecular trajectory simulations [17, 344, 345], so we apply it here to estimate a maximum

velocity spread for each molecular packet. The details of this model were discussed in section [7.1.3](#). The key feature is that the TWSD creates a potential energy well in the radial dimension that is independent of the deceleration applied. Thus, changes in the longitudinal potential impact primarily the dynamics of deceleration. The phase-space acceptance along the axis of the decelerator can be directly calculated as a function of the average force of deceleration. This gives the largest possible spread of phase-stable, and thus decelerated, molecules. The results from the LPSA model are tabulated in Table [7.2](#). The calculations show that the velocity spread of the molecules leaving the decelerator is typically small, ~ 10 m/s. The transverse spread in velocities has been investigated previously [\[17\]](#), and is also on the order of ~ 10 m/s.

We can compare the total number of molecules detected at each final velocity to estimate the overall decelerator efficiency and compare it to the results from the LPSA model. We calculate the total number of decelerated molecules by subtracting the scaled free-flight background from the deceleration data, integrating in time over all of the peaks, normalizing by the final velocity to account for the extended time for slower packets of molecules, and including the impact of detecting the molecules downstream from the exit of the decelerator, (see section [7.1.4](#) for details.) The resulting integrated number of molecules detected as a function of final velocity is shown in Figure [7.15](#) by black circles.

Lastly, we predict how much integrated molecule signal we expect to see based on the LPSA model. The total area of the LPSA should scale the same as the total number of molecules detected, assuming the transverse confinement is entirely decoupled from the longitudinal confinement, and the decelerator phase-space acceptance is filled uniformly. The results of the model calculations, also shown in Figure [7.15](#), show good agreement with the experimental results. Ultimately, we see the decelerator retains nearly half of the molecules all the way down to 10 m/s, which is a very favorable result for collisions studies with trapped ions. The experimental and modeled results are sufficient for planning future reactions with the decelerated beam.

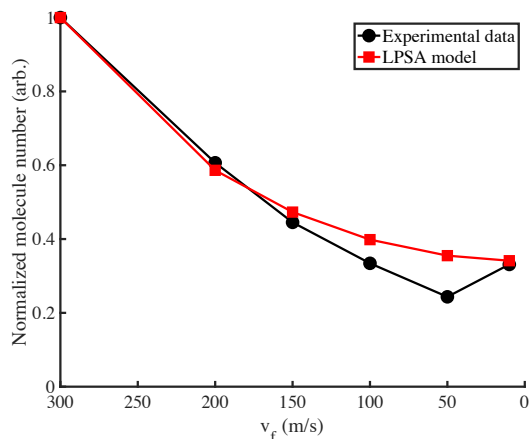


Figure 7.15: Measured and modeled number of molecules, normalized, as a function of final velocity. The black circles represent the data scaled by the reduction in the number of molecules from the exit of the last decelerator ring to the position of the laser due to transverse spread. The red squares represent the total area of the LPSA model, normalized to the area of the LPSA model at 300 m/s. Note the decreasing velocity axis and the lines connecting the points are just to guide the eye.

7.2.2 Alternative slowing scheme

One requirement to make Stark-decelerated beams useful for energy-resolved reaction experiments is for the non-decelerated molecules to be separated from the decelerated packet. If the two distributions of molecules can be sufficiently separated in time, then a molecular beam shutter can be placed in the beam path to allow only decelerated molecules through. For low velocity packets, this time is large enough while running the decelerator in the typical manner. However, for higher final velocity packets, an alternate slowing scheme must be employed.

The typical slowing scheme uses the entire length of the decelerator for slowing, which produces the largest number of slow molecules. Here, we test an alternative slowing scheme that decelerates the molecules more aggressively than necessary, using only a fraction of the decelerator's length for slowing, and the rest of the decelerator for bunching at the final velocity. The end effect is an increase in the time delay between decelerated and non-decelerated molecules (including carrier gas) exiting the decelerator. This alternative slowing scheme has been previously demonstrated with ND_3 in a pin decelerator [340]. Here, we report the time delay and increased energetic

purity of the molecular packets exiting the TWSD as a result of using the alternate scheme.

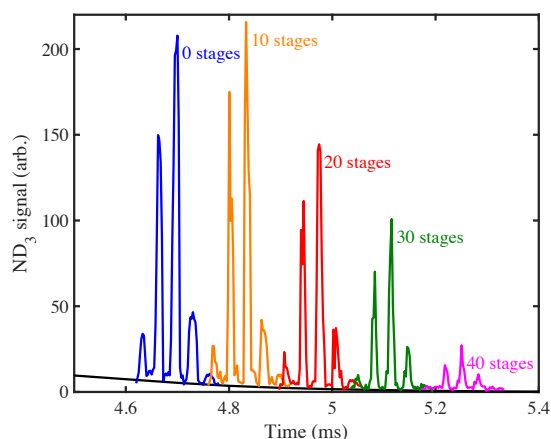


Figure 7.16: Deceleration data for a final velocity of 250 m/s using the alternative slowing scheme. The time axis represents the delay between molecular beam valve and detection laser triggers. The free-flight data are scaled to match the baseline of the deceleration data. As the number of bunching stages increase, more aggressive deceleration is applied to the molecular beam, which reaches the final velocity in a shorter distance. This leads to a time delay in the arrival of the slowed packets of ND_3 .

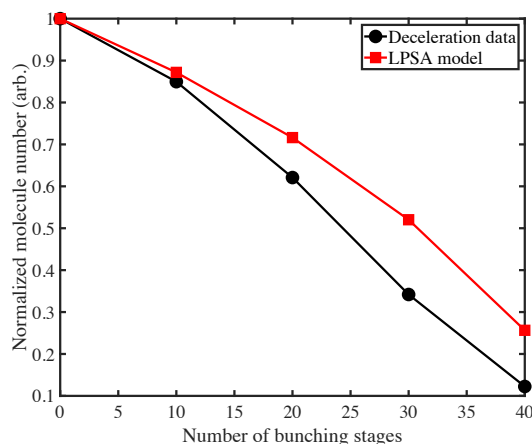


Figure 7.17: Measured and modeled number of molecules, normalized, as a function of the number of bunching stages. The black circles are the integrated ND_3 signal, normalized to the integrated signal using zero bunching stages. The red squares represent the total area of LPSA model, normalized to the area of the LPSA model using zero bunching stages. All points represent molecules decelerated to 250 m/s. The data at zero bunching stages correspond to the typical deceleration scheme.

To test the alternative slowing approach, we vary the the number of decelerator stages (1

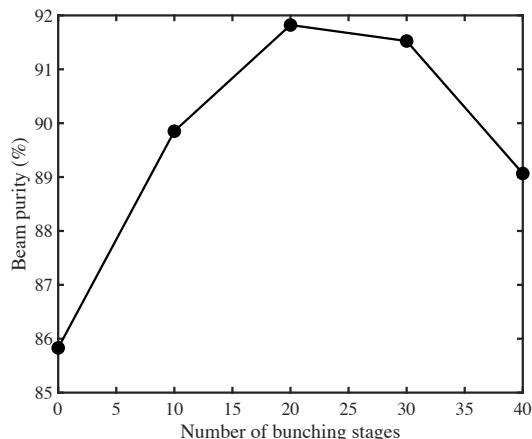


Figure 7.18: The purity of the molecular beam defined as the percentage of decelerated molecules out of all molecules detected within the integrated time-window containing the molecular packet. The number of decelerated molecules decreases at a different rate as compared to the non-decelerated molecular beam with increasing number of bunching stages. For a final velocity of 250 m/s, the maximum purity corresponds to 20 bunching stages.

stage = 8 rings) used for slowing versus bunching to study ND₃ decelerated to a final velocity of 250 m/s. A summary of these results are shown in Figure 7.16. A free-flight background was also measured and scaled to the decelerated data baseline as discussed above. We are able to achieve a time delay from the typical scheme of around 800 μs, which corresponds to a delay between the peak of the molecular beam and the decelerated molecules of 1.7 ms. This is more than enough delay, as typical shutter opening times are around 500 μs (Uniblitz, LS series). We also verified that the final velocity of the molecules were in fact 250 m/s for all molecular packets shown, as discussed in the previous section.

There is, however, a clear trade-off between the amount of time delay gained by increasing the number of bunching stages (i.e., more aggressive slowing) and the integrated ND₃ signal. To quantify this effect, we subtract the free-flight background and integrate the decelerated peaks. The integrated ND₃ signal as a function of bunching stages is plotted in Fig. 7.17 and normalized to the zero bunching stages data point, which corresponds to our typical deceleration scheme. We also calculate the LPSA area to predict the decrease in integrated ND₃ signal. The smallest LPSA calculated used 40 bunching stages, which corresponds to a deceleration aggressive enough

to change the propagation direction of the molecules (molecular packet travels back towards the valve), provided the entire length of the decelerator is used. The well depth associated with such aggressive deceleration is only 0.05 K.

In addition to increasing the time between the peak of the molecular beam and the decelerated signal to allow for a shutter to be implemented, we want to optimize the decelerated beam for velocity purity. For a metric to quantify the velocity purity, we choose the percentage of decelerated molecules that are included in the total integrated signal. To calculate this, we integrate the signal above the free-flight background and divide it by the total integrated signal. Doing this for the alternative slowing data results in the data points shown in Figure [7.18](#). This analysis reveals that 20 bunching stages is the optimal choice for velocity purity of a beam at 250 m/s.

There is a limitation to the application of bunching after the deliberately aggressive slowing scheme. The amount of time delay added per bunching stage is proportional to the final slowing velocity. This means that less time delay can be achieved for higher final velocities. For example, with $v_f = 300$ m/s, only $400 \mu\text{s}$ can be added before the slowed packet signal vanishes, which is predicted by a vanishing potential well. This example, verified experimentally, uses only 8 stages of the decelerator for slowing, and thus 70 stages for bunching. This is unfortunate from a velocity purity standpoint because there is more background at earlier times. However, two possible solutions utilize the TWSD ability to slow ND_3 more aggressively than needed to bring the molecules to rest. Instead of bunching after such a deceleration, one can allow the molecular packet to turn around and be guided back towards the start of the decelerator. Upon arrival at the upstream edge of the decelerator, the packet can be turned around again and accelerated back to the desired final velocity by the time it reaches the end of the decelerator. This scheme (a so called “bounce”) has been demonstrated in a TWSD with CH_3F molecules [346](#). Another solution involves decelerating the molecular packet to rest before the end of the decelerator. There, it can be trapped for the desired delay time and then re-accelerated to the final velocity of choice [312](#), [347](#).

7.2.3 Beam densities and prospects for reactions

Overall, the success of future reaction dynamics experiments hinges on the TWSD beam density. If the density of slowed molecules from the TWSD is too low, reactions will take place on a timescale that is too long to maintain the stability of the experiment. This point is demonstrated by the example reaction from before, $\text{ND}_3^+ + \text{ND}_3 \longrightarrow \text{ND}_4^+ + \text{ND}_2$, which occurs at a rate given by

$$\frac{d[\text{ND}_3^+]}{dt} = k[\text{ND}_3^+][\text{ND}_3], \quad (7.16)$$

where k is the reaction rate constant, $[\text{ND}_3^+]$ is the number of ND_3^+ in the ion trap as a function of time and $[\text{ND}_3]$ is the density of ND_3 passing through the ion trap as a function of time. Eq. [7.16](#) can be separated and integrated to obtain,

$$\ln \left(\frac{[\text{ND}_3^+]}{[\text{ND}_3^+]_{t=0}} \right) = k \int_0^t [\text{ND}_3](t') dt'. \quad (7.17)$$

Since the decelerator delivers $[\text{ND}_3]$ packets at a set repetition rate, Eq. [7.17](#) can be simplified to

$$\ln \left(\frac{[\text{ND}_3^+]}{[\text{ND}_3^+]_{t=0}} \right) = kRI_{[\text{ND}_3]}t, \quad (7.18)$$

where R is the decelerator repetition rate, and $I_{[\text{ND}_3]}$ is given by

$$I_{[\text{ND}_3]} = \int_0^T [\text{ND}_3](t) dt, \quad (7.19)$$

which is the density of the decelerated beam integrated over the time it takes one pulse to pass through the ion trap, T . If we assume an integrated density of $I_{[\text{ND}_3]} \sim 10^6 \text{ s/cm}^3$, then $k \sim 10^{-9} \text{ cm}^3/\text{s}$ and $R = 2 \text{ Hz}$ allow us to evaluate Eq. [7.18](#). The total time it will take for 90% of the reactants to deplete ($[\text{ND}_3^+]/[\text{ND}_3^+]_{t=0} = 0.1$) is $t \sim 10^3 \text{ s}$, which is a reasonable timescale for trapped ion reaction experiments.

Unfortunately, we lack the experimental tools to measure the absolute density of our beam in the current experiment. We do, however, believe we can achieve $I_{[\text{ND}_3]} \sim 10^6 \text{ s/cm}^3$ for a few qualitative reasons. First, densities of this magnitude have been measured out of a pulsed-pin decelerator. One group utilized calibrated laser-induced fluorescence measurements to determine

the peak density of packets decelerated to several hundred m/s, which was found to be $(2 \pm 0.8) \times 10^8$ molecules/cm³ for OH [341]. We expect the deceleration efficiency of the TWSD to show a marked improvement over pin decelerators in this regime because, as Fig. 7.15 demonstrates, the decelerated signal does not exhibit significant losses at low velocities. Second, the guiding hexapole will focus the decelerated beam in the transverse dimensions, which will further enhance the density of neutral molecules within the ion trap [348]. Lastly, the TWSD produces many filled wells for each packet of molecules. These can be seen as the multiple discrete peaks in Figs. 7.14 and 7.16. Each peak in the packet increases the integrated density. These factors combined should allow us to achieve an average ND₃ density of 10^9 cm⁻³ for a duration of 1 ms. The success of the other radical sources considered will depend on the ability to produce comparable decelerated beam densities. Cold buffer gas beam sources may be required for certain radical species [344].

Furthermore, the proposed combined apparatus may allow for lower beam densities than prescribed above. The LIT-TOFMS measures both the depletion of the charged reactants as well as growth of charged products, simultaneously [65]. Under such conditions, bimolecular reaction rates can be determined typically without the need to follow a reaction to 90% completion. Instead, we only need to wait for 10% of the ions to react, which drastically reduces the time of the full experiment for lower density beams.

7.2.4 Summary

In summary, we have characterized a source of neutral polar molecules for use in future low-temperature ion-molecule experiments. Specifically, we achieved continuous deceleration of ND₃ from 385 m/s down to 10 m/s without incurring a significant loss of molecules. We have also shown that the decelerated beam can be separated from the free-flight background in time through the use of an alternative slowing scheme. This led to an enhancement in final beam velocity purity at the cost of a smaller longitudinal phase-space acceptance and thus fewer molecules. We then explored the implications of these results on future proposed ion-molecule reaction studies. Ultimately, the performance of the TWSD indicates low-temperature studies will be possible between many species

of neutral polar molecules/radicals and trapped ions.

7.3 Development of the TWSD amplifiers

The TWSD discussed in this chapter has been developed thanks to the efforts of multiple people. The amplifiers that produce the sinusoidal potentials essential for deceleration have been a particularly challenging engineering feat that has spanned multiple years of work and generations of graduate students. In this section, I will give brief history of the advancements made on these amplifiers to give context to the upgrades applied to the system during my time on this project. This historical review will be extremely brief, primarily summarizing what can be found in Yomay's and Noah's thesis.[\[16\]](#) [\[2\]](#) I will discuss changes made after their tenure in greater detail.

7.3.1 A brief overview of the in-house amplifier design

The traveling-wave Stark decelerator was built to decelerate neutral molecules from a seeded krypton beam at 400 m/s. The sinusoidal potentials required to bring such a beam to rest requires a bandwidth of ~ 30 kHz to DC. The original design had been for 12 kV, (now 10 kV), which allows deceleration of ND_3 and other molecules with relatively low losses. Higher voltage is always better for this application, but 12 kV was chosen as an ambitious but achievable target for an amplifier, requiring a slew rate of 2.3 V/ns, (now 1.9 V/ns, still very fast.) With a driving load around ~ 300 pF, this peak current draw is on the order of 500 mA.[\[16\]](#) Even today, this outperforms any commercially available amplifier. These specifications are met by *eight* amplifiers, one for each of the eight decelerator rings in a deceleration stage.

The amplifiers have to meet several technological challenges. This system needs be able to sink and source a large amount of current, to switch high voltages at a slew rate higher than available components, to insulate the driving signals from HV noise, and to produce a frequency-chirped output with relatively flat gain. In addition, the amount of energy being worked with is substantially: not only are the working voltages lethal, but a catastrophic event is incredibly powerful, loud, and destructive to the electronics. Terry Brown is attributed with saying that,

“electronic design and layout is like doing a jigsaw puzzle, except you don’t have a picture and none of the pieces fit together.” In his thesis, Noah added: “For this design, I would add the constraints that you have to wear a blindfold, and if at any point you put a piece in the wrong place the puzzle may explode!” [16]

The point of this emphasis on the technological difficulty of designing these amplifiers is to highlight the victory of their successful operation, and to contextualize more than decade of work that has brought this project to fruition (including the need for more recent modifications.) The amplifier design is really quite incredible. The interested reader will find Noah’s thesis a detailed and engaging introduction to the electrical engineering of these amplifiers. Yomay’s thesis was written a bit later in the evolution of the amplifiers and also features an excellent perspective on the amplifier design and operation. Thus, I will not attempt a thorough description of the electronics design and function here; this section is intended as follow-up documentation on what are (we hope) the final modifications to these amplifiers. However, I will give an extremely brief overview of the design in order to provide context for the changes made during my time on the project.

A conceptual schematic for the amplifiers is given in Figure 7.19A. Such a design is referred to as a *push-pull amplifier*. This divides the load on the amplifier to one half responsible for sourcing the current (when the output is positive) and to another half responsible for sinking the current (when the output is negative). For these banks to operate out of phase in conjunction with each other, both must be driven with well-coordinated driving signal. This is achieved with optical signals insulated from the HV, usually with optoisolators. This configuration takes advantage of the availability of fast-switching, high voltage MOSFETs (metal oxide semiconductor field-effect transistor) that are best suited for our applications. Even still, MOSFETs that are able to source and sink > 0.5 A of current are limited to handling ~ 4 - 4.5 kV maximum. However, a nice benefit to the push-pull configuration is that it is well-suited to stacking FETs to expand the output voltage capabilities as shown in Figure 7.19B. A well-designed circuit can split the required output among multiple FETs, such that output voltage capacity expands linearly (at least in principle) with the

number of FETs in series.

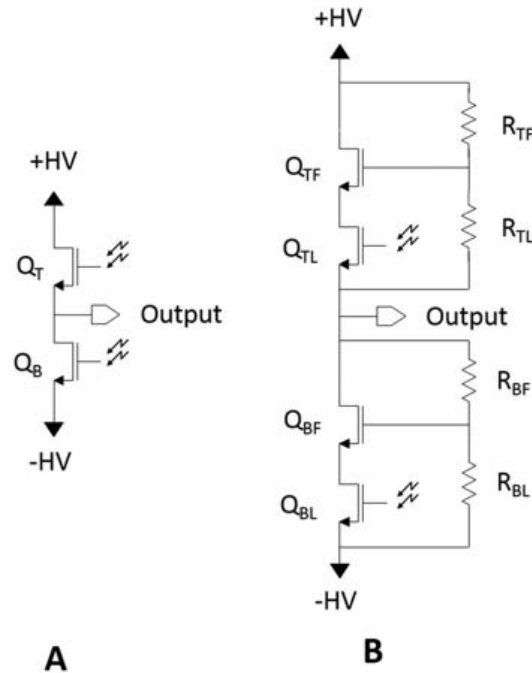


Figure 7.19: **(a)** A n-channel push-pull amplifier. The rating of the FETs (Q_T or Q_B) determines the maximum output and rails ($\pm HV$). Arrows denote optical signal input **(b)** Multiple FETs connected in series increases the maximum output voltage and rails. A resistor network controls the division of voltage equally across each FET. Figure adapted from Shyur (2018).[\[19\]](#)

Our home-built amplifiers have two banks (*top bank* refers to the source/push, *bottom* for sink/pull). Each bank has ten stages, with one *leader* circuit that has global feedback from input signals (Figure [7.20](#)), and nine *follower* stages that serve to divide the high voltage with local feedback to ensure good voltage sharing (Figure [7.21](#)). The “workhorse” of each stage is a 4.5 kV (originally 4 kV) MOSFET (sometimes nicknamed the “HV FET”) placed in a cascode configuration with a lower-voltage FET (sometimes nicknamed the “cascode FET”) as shown by box A in Figure [7.20](#). This configuration reduces the Miller effect, a limitation in the bandwidth of the FET due to inherent junction capacitance. This dual-FET cascode configuration increases the speed and stability of the HV FET. We will get a glimpse of what can happen with this lower-voltage cascode FET when it is not working properly in section [7.3.2](#). (Spoiler alert: it’s not pretty.)

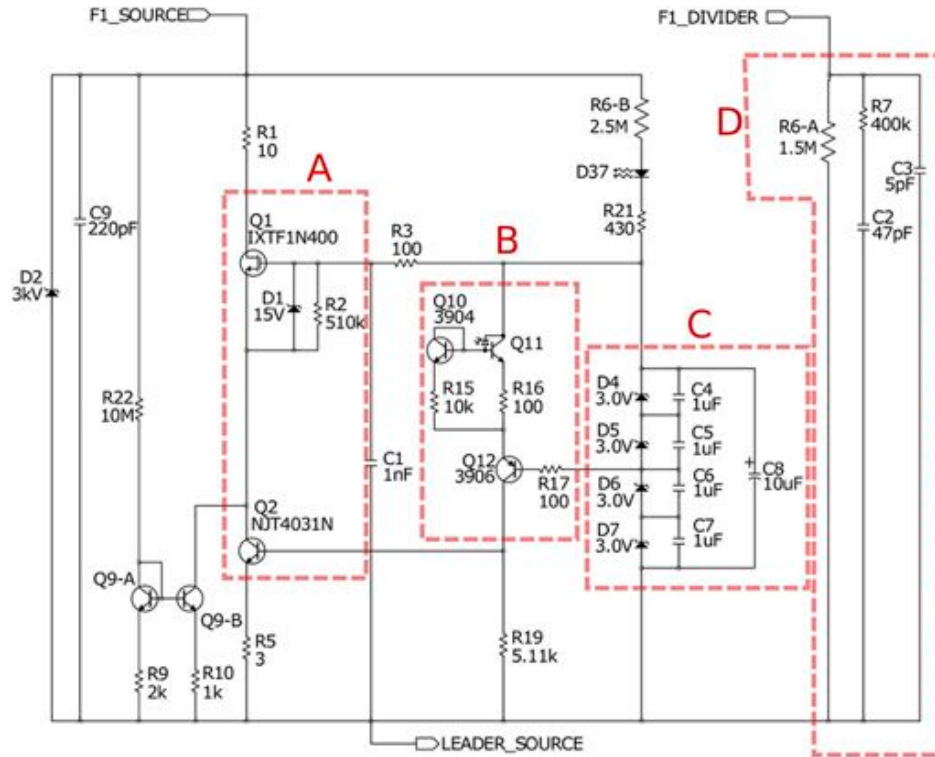


Figure 7.20: Schematics for a leader stage of the amplifier. (A) The FETs responsible for the majority of high voltage switching and current flow when the bank is enabled. (B) Circuitry for the driving signal delivery and global feedback. Q11 is the photoresistor of the optoisolator. (C) Local power supply to hold Q1 & Q2 biased open slightly when the amplifier is not enabled (no signal is delivered.) (D) Local feedback for adequate voltage sharing across stages. Figure adapted from [19]

Both of these FETs benefit from being biased slightly on. This improves their turn-on stability, linearity, and speed. A small *quiescent current* allows the FETs to be open just enough that they will respond quickly and effectively in the presence of signal, without causing inordinate amounts of heating when there is no input signal. However, this biasing on of the FETs requires a local power supply that holds this current at a low and stable value. Such local power supplies are included in the design of each amplifier stage, indicated by box C in Figure 7.20 and box B in Figure 7.21

The multi-stage approach requires that the voltage needs to be shared evenly among the stages. The realities of variations in component performance necessitates local feedback to correct

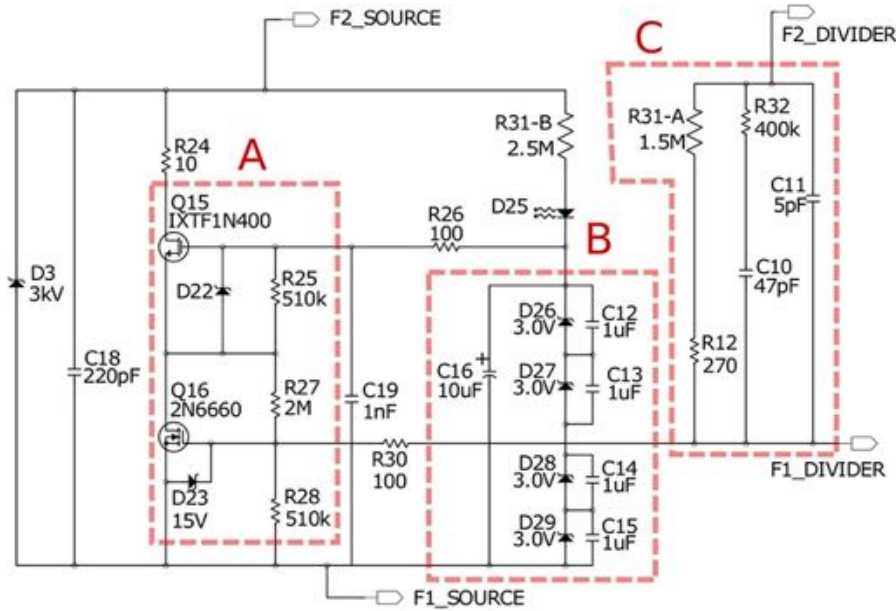


Figure 7.21: Schematics for a leader stage of the amplifier. **(A)** The FETs responsible for the majority of high voltage switching and current flow when the bank is enabled. **(B)** Local power supply to hold Q1 & Q2 biased open slightly when the amplifier is not enabled (no signal is delivered.) **(C)** Local feedback for adequate voltage sharing across stages. Figure adapted from Shyur (2018). [19]

imperfections in the voltage sharing. Such feedback is particularly important at higher frequency outputs. In each stage, a sub-circuit facilitates active feedback to promote good voltage sharing over a larger bandwidth. This is highlighted by box D in Figure 7.20 and box C in 7.21.

The local feedback is not the only source of signal correction. The signal input is stabilized by global feedback with a PID (Proportional/Integral/Derivative) control loop to correct the signal in real time. This signal must be isolated from the noise of the high voltage amplifier, as previously mentioned. It also must be appropriately fast with a large bandwidth. These requirements are met by the circuit shown by box B in Figure 7.20 (the photoresistor of the optoisolator is component Q11) The analog optoisolator provides the input driving signal, while additional BJTs increase the bandwidth and compensate for the low current transfer ratio of the optoisolator.

These described sections of the circuitry are the primary components necessary for the de-

signed multi-stage, high-bandwidth, high-voltage amplifiers. There are many more details that are more thoroughly discussed in other resources. [16], [2] In addition, there have been recent electronic upgrades that have been necessary to reliably run these amplifiers at 10 kV amplitude, which will be discussed in detail in section 7.3.2. One such re-design included the replacement of the original signal optoisolator component and the subsequent alteration of the global feedback electronics to maintain the required bandwidth and gain. I will also discuss the troubleshooting and diagnosis of some puzzling oscillations on our output current signal. Lastly, there have been recent changes in the structural design of the water-cooled boron nitride walls that dissipate heat from the HV IXTF1N450 FETs, which source and sink the majority of the circuit current. The new design and assembly process for these walls is documented in section 7.3.3. In addition, we redesigned the mounting scheme by which these HV FETs are thermally and electrically stabilized. This modification was followed by a retrofit of all of the built amplifiers. Both of these topics will be discussed in more detail.

7.3.2 Overview of electrical changes to the amplifiers

The most substantial electrical change since the amplifier design and performance published in Yomay's thesis is the updated optoisolator component. This upgrade to the circuitry was implemented by Jason Bossert in 2019.

Prior, there were two identical optoisolators in use. One received input from driving circuitry to deliver to the amplifier, while the other sent signals mirroring the current in the amplifier to the low voltage side to provide monitoring of the amplifier current. Both of these optoisolators were component OPI120, rated to ± 20 kV. However, there were regular shorts from the ground to the negative HV rail via the current monitoring optoisolator (D21/Q52) that resulted in destruction of those amplifiers when the output was pushed near or above 8 kV amplitude. To address this problem, the optoisolator used for current mirroring was removed along with the current monitoring circuitry. In addition, the input signal optoisolator was replaced with OPI150, rated to ± 50 kV. This has allowed the amplifiers to reach 10 kV amplitude without destructive events of this nature.

However, this caused a redesign of the circuitry that stabilizes the optoisolator, since OPI150 had a different (i.e. lower) current transfer ratio than the original optoisolator. This was achieved with the change of component R15 to 20 k Ω and R21 to 430 Ω . These changes are noted in Table 7.3. Updated schematics are included in Appendix A.

Table 7.3: Summary of changes to amplifier electronics since Shyur (2018). [2]

Original Component	New Component	Component number	Comment
OPI120	OPI150	Q11/Q51	new optoisolator
10 k Ω RES	20 k Ω RES	R15	new optoisolator driving circuitry
470 Ω RES	430 Ω RES	R21	new optoisolator driving circuitry
	DNI	Q52/D21	current monitor circuitry, no longer in use
	DNI/ optional	LM8261,C17,C175,R61 R159,R160,R161	current monitor circuitry, no longer in use
IXTF1N400	IXTF1N450	Q1,Q15,Q19,Q23,Q27 Q31,Q35,Q39,Q43,Q47	old component is now obsolete

Some additional electrical investigations of these amplifiers resulted from a catastrophic failure of an amplifier in fall of 2021. This failure necessitated the purchase of several components to assemble and test new amplifiers. In the testing process of these new amplifiers, we had a persistent, parasitic oscillation in our output current signal that required significant troubleshooting. This type of oscillation appeared on the top and bottom of the current sinusoidal wave, where the change in voltage is the greatest. The oscillation of these frequencies was ~ 30 MHz and could reach half of the peak current draw in amplitude. These oscillations usually would begin once the output amplitude was around 7 kV. Example measurements of these oscillations on an oscilloscope are given in Figure 7.22.

We investigated many possibilities looking for the cause of these oscillations. We ruled out that the signal could be a picked-up signal from neighboring equipment. For some time we believed it could be due to the new IXTF1N450 HV MOSFETs that replaced the original obsolete component, IXTF1N400. This was supported by the observation that the capacitance between the gate and drain was lower, and the threshold voltage was about 2 V higher. After considerable

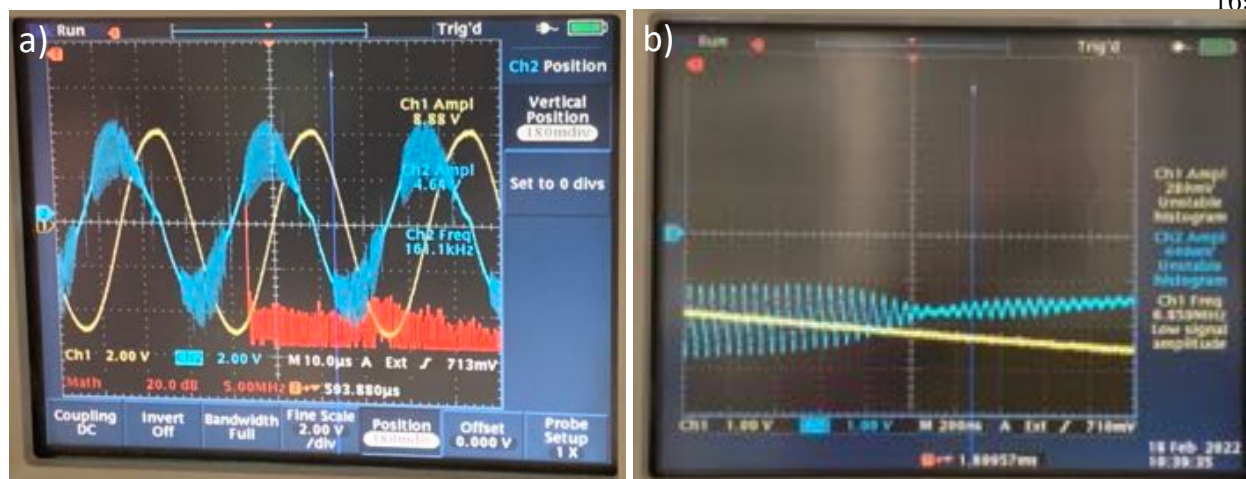


Figure 7.22: Traces demonstrating the effect of bad 2N6660 FETs on amplifier output performance. Yellow traces show the output voltage as measured by the control box ($1\text{ V}=1.5\text{ kV}$.) Blue traces are the voltage measured across a $10\ \Omega$ resistor in between the low side of the capacitor and ground ($1\text{ V}=100\text{ mA}$). The red trace is a fast Fourier transform (FFT) of the current output. As seen in **a**), there are extremely fast oscillations with amplitudes nearly a third of the full waveform amplitude. With the time division zoomed in **b**), the oscillation periodicity and profile becomes more apparent. FFT of the signal determined the oscillations to vary between $\sim 20\text{--}30\text{ MHz}$ in frequency.

time, (trying to procure the obsolete IXTF1N400 FETs,) we eventually established that the new IXTF1N450 HV FETs were not the cause of it⁴. We also determined the $\sim 30\text{ MHz}$ frequency was too large to be within the bandwidth of the global feedback; this ruled out the possibility that it was a problem with the drive circuitry or PID feedback. We also established that the effect did not demonstrate signs of being thermally-induced. The most productive line of inquiry noted that such high frequency oscillations were most likely attributed to some level of instability in the HV IXTF1N450 FET, or the lower voltage FET in the cascode configuration (NJT4031N in the leader stage, 2N6660 in the follower stages.) We attempted:

- (1) Increasing the resistance of the drain resistor of the IXTF1N450 MOSFET (R1, R24, R39..., purple box in Figure 7.23). We tried increasing this from $10\ \Omega$ to $15\ \Omega$ without significant change of the oscillations.
- (2) Increasing the resistance of the gate resistor of the IXTF1N450 MOSFET (R3, R26, R44...

⁴ Actually, they more effectively support voltage sharing than the original component. This is really good news, since the old component is now impossible to acquire.

red box in Figure 7.23). This was increased from $100\ \Omega$ to $200\ \Omega$ without significant change of the oscillations.

- (3) Adding a capacitance to the gate-source of the IXTF1N450 MOSFETs. We tried adding $820\ \text{pF}$ in parallel to the gate and source pins (orange line in Figure 7.23). This created a higher frequency ($\sim 40\ \text{MHz}$) oscillation that began at even lower voltages ($3\ \text{kV}$).
- (4) Decreasing the capacitance of the C branch of the local feedback capacitor (C3, C11, C29... green box in Figure 7.23) from $5\ \text{pF}$ to $2.5\ \text{pF}$. This seemed to work at first, but it moved the threshold for the oscillations to begin just above what we test before encapsulating the amplifier in an insulating potting material ($9\ \text{kV}$ amplitude at $30\ \text{kHz}$.) Thus, we thought we had succeeded, but the oscillations were found during the post-potting final testing.

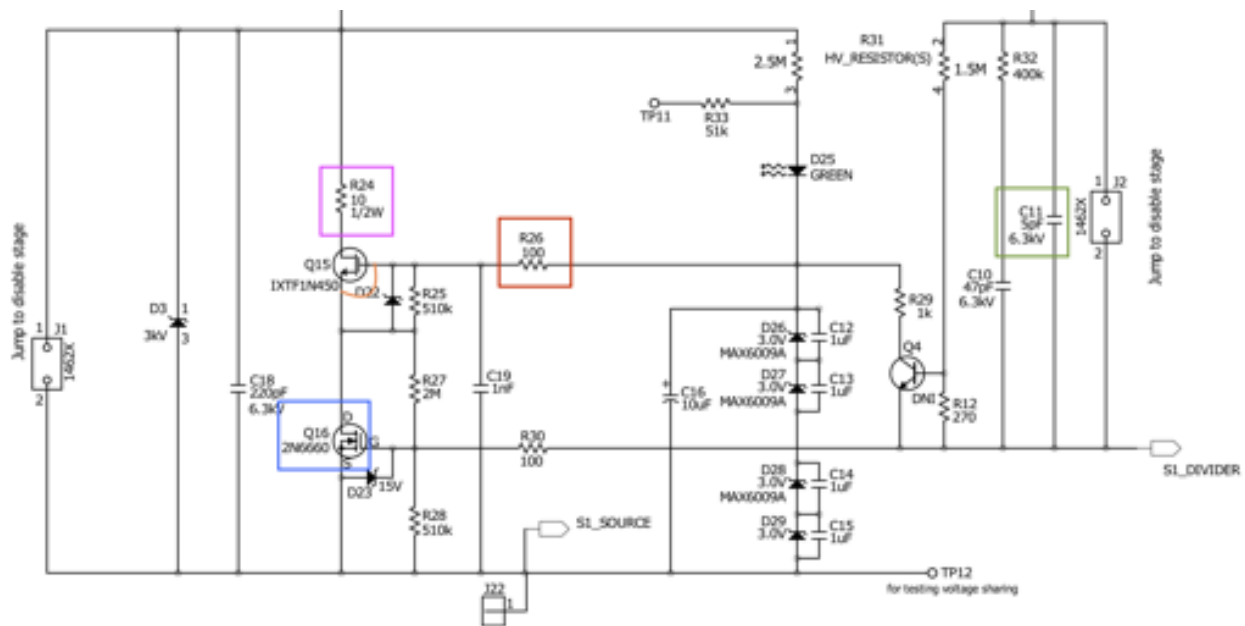


Figure 7.23: Circuit diagram for the first follower of the amplifier bank. Components of the circuit that we modified to troubleshoot the high-frequency oscillations are marked in color. Full schematics are included in Appendix A.

Ultimately, the problem was that the 2N6660 FETs (blue box in Figure 7.23) purchased for this round of assembly were faulty. When we tested these FETs individually, they had quite divergent behavior from the specifications. This behavior is outlined in Table 7.4. This entire “bad

batch” turned out to have very large drain-source capacitances, extremely low threshold gate-source voltages and low drain-source resistances when fully open. Given the typical gate-source voltages that is designed to barely bias these FETs open, these faulty cascode FETs would be effectively fully open at all times in our circuit. This implies these cascode FETs would not mitigate the Miller effect in the HV FETs as per their design, and would also add additional capacitance in the circuit. When we replaced these 2N6660 FETs with components that behaved as specified, the oscillation issue was completely rectified.

Table 7.4: Expected and actual performance in 2N6660 FETs. FETs with problematic performance were always characterized by a higher drain-source capacitance and lower threshold V_{GS} .

2N6660 Measurement	Typical performance	Problematic FET
C_{DS}	70 pF	200 pF
R_{DS} at 2 V_{GS}	8.5 Ω	3 Ω
R_{DS} at 3 V_{GS}	4.3 Ω	1 Ω
R_{DS} at 6 V_{GS}	3 Ω	0.9 Ω

This rather detailed description of this failure mode is intended as a reference for possible future troubleshooting. The unsuccessful attempts to solve the behavior were well-founded. Possibly the solution we found, or the principles guiding the other attempts at a solution to these oscillations, may be helpful to a future reader. In addition, it provides a cautionary tail: always, always, always test your components before assembling a circuit.

7.3.3 Overview of structural and cooling changes to the decelerator

We had two more destructive events with our amplifiers during my time on the project. In fall of 2022, two stages shorted to each other. This was a very quiet failure, only signaled by the tripping of the control interlocks and the subsequent changed output of that amplifier. In winter of 2022, a much more destructive event occurred, heralded by an extremely loud *bang!*, and more destruction on the amplifier itself, as seen in Figure [7.24](#). This failure mode had two primary features. Like the failure in 2021, it was characterized by evaporated resistors on the drain of the HV FETs (10 Ω), resulting in the periodic black char that can be seen on the potting material

and the wall. In this case, there was also a short between two stages, seen as a clear burned path between the leader and first follow of the top bank. This is circled in blue in Figure 7.24. Such events often have a chicken-or-egg problem in determining the actual instigating failure. Such is the case here.

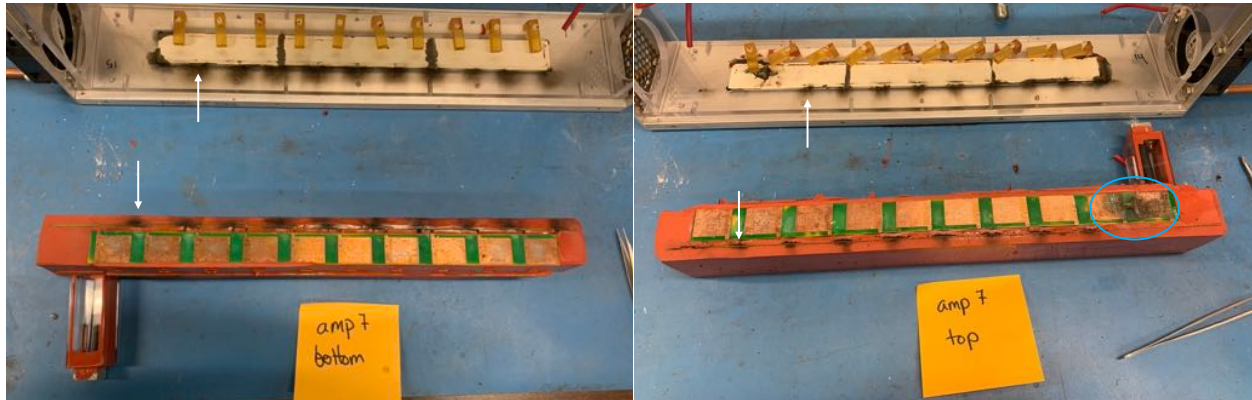


Figure 7.24: Photos of the amplifier #7 autopsy. Residue from vaporized components are indicated by the white arrows. This residue most likely came from the high-power $10\ \Omega$ on the drain side of the IXTF1N450 FETs. This amplifier also showed signs of a short between the top bank leader and first follower (circled in blue). The residue and oxidation found on these copper pads was found on multiple other amplifiers.

An additional question presented in the cause of this failure was the observation that the amps had been slowly accumulating unexpected behavior over time. This unintentional behavior was the “float” of the output voltage of the amplifier when it was not enabled. When an amplifier is enabled, the global feedback will operate to correct an amplifier output to its signal-driven voltages. With a duty cycle of $\leq 2\%$, the amplifiers spend a large amount of time not enabled. During this time, some amplifiers were drifting up or down from zero towards either of the amplifier rails. This affected nearly all of the amplifiers. The drift usually was very negligible at the start of any given day, but increased in magnitude over the course of the day. Over the course of months, the end-of-day drift also slowly increased. An example of the floating signal can be seen in Figure 7.25.

We believe this “floating issue” was thermal in nature. The increasing drift over the course of the day, that resets in the morning, already suggested as much. At higher temperatures the active components — particularly the FETs — tend to have lower resistances at the operating voltages.

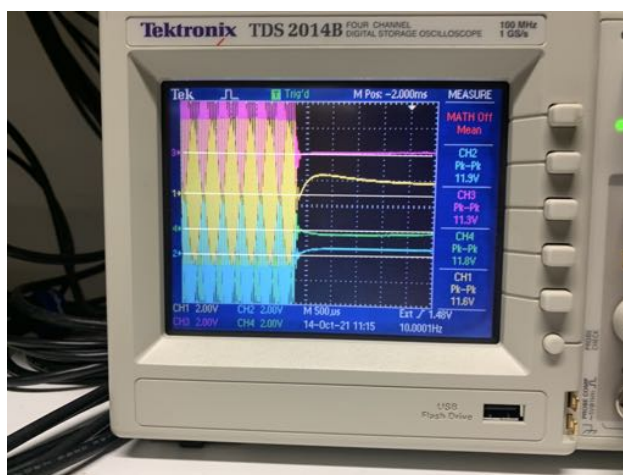


Figure 7.25: Example output traces of amplifiers with “floating issues.” This refers to the “float” of the voltage output towards one of the rails when the active feedback is not on. This does not affect the deceleration of molecules, but does indicate damage of the amplifiers.

This is somewhat mitigated by the circuit design, but can still contribute to constructive cycles in which some heating leads to more heating, etc. However, the largest indication of thermal issues was found when we inspected all the amplifiers in response to the blown amplifier in winter 2022. As shown in Figure 7.26, there were signs of burns, discharge, or a residue on all of our amplifiers that had been in use for over three months. These signs of burning were concentrated entirely on the copper pads that backed the HV (IXTF1N450) FETs. These are designed to dissipate the most heat of the circuit through the copper-plated PCB walls and to the water-cooled boron nitride to which it is clamped. Interestingly, the prominent signs of heating (such as burn outlines in Figure 7.26a and black oxidation on the copper pads in 7.26d) were primarily on the top banks. The greenish residue was entirely localized to the leader and first two followers of the top bank. This is plausibly the largest heat load in the amplifier, perhaps indicating that at least once this stages reached particularly high temperatures. We are still not confident why or how the green-blue oxidation occurred. This oxidation tended to be rather fluid in nature; we suspect heat, copper, oxygen, and some residual solder flux, all contributed to this phenomenon.

This discovery instigated a re-design of the copper backing to which the IXTF1N450 FETs are soldered. It is important to note that the copper-plated PCB walls in the original design served

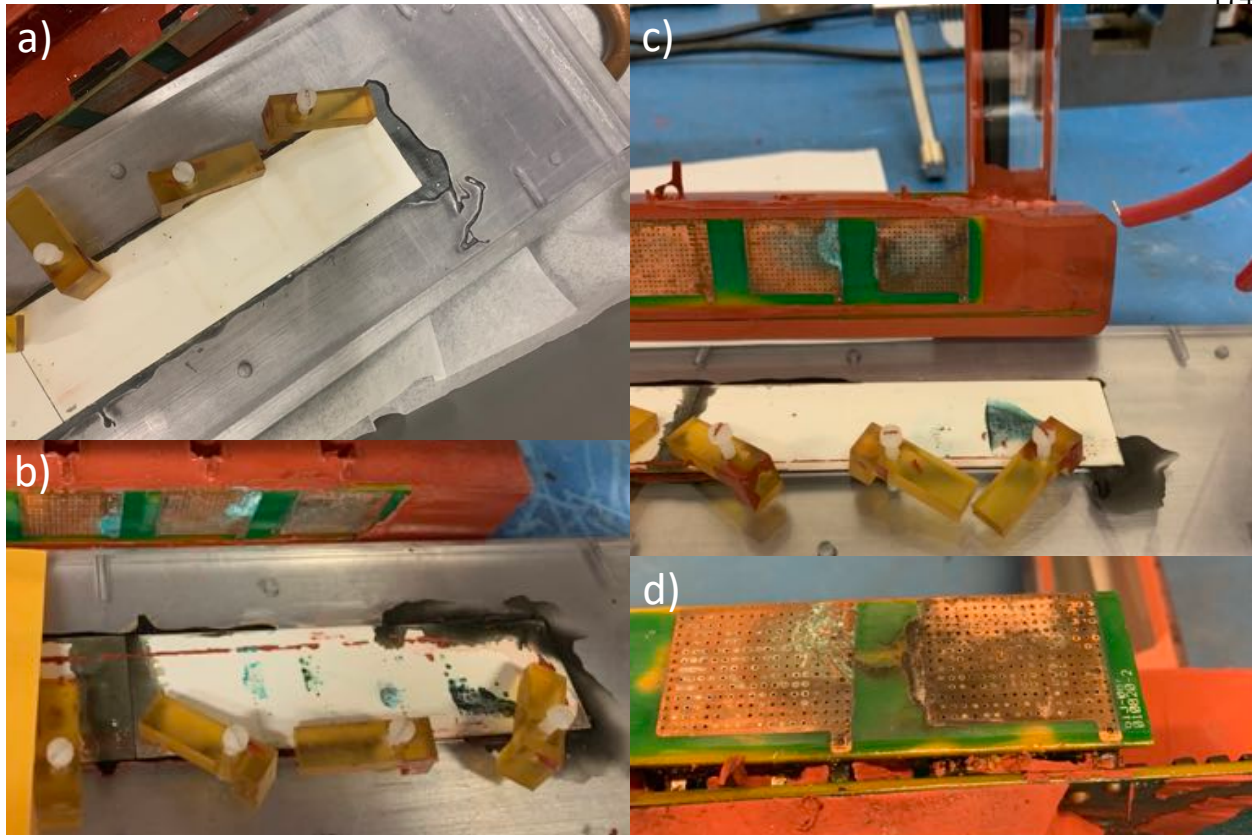


Figure 7.26: Signs of heating was found in multiple ways. **a)** Some banks had faint burn-like outlines. **b), c)** Blue or black oxidation was found on many top banks. It was sometimes chalky and sometimes semi-liquid. **d)** In the case of amplifier 7 it was accompanied by signs of a short between stages.

two purposes. One, the PCB boards had double-sided copper pads with high via density to aid in thermal conductivity between the backside of the FETs and the water-cooled boron nitride. The second purpose of the PCB walls was to electrically connect the electrically isolated back of the FET to the amplifier bank. The motivation behind this was to keep the electrically insulated back pad from floating, possibly inducing unstable behavior in the FET. While the PCB boards addressed this second purpose perfectly, such printed PCB boards are not an ideal thermal conductor, even with the high via density of this original design. The successor to this PCB design were a laser-cut blocks of solid copper designed by Trevor Kieft to connect to the amplifier bank in the same way as the original design, but with improved thermal conductivity. Such blocks of copper did require several steps of smoothing to handle high voltage without corona discharge; however, they solved

this issue nicely, and were verified to bring the average temperature of the FETs down by at least 20°C ($\sim 50^{\circ}\text{C}$ to $\sim 30^{\circ}\text{C}$) during test operation with a test 250 pF load.

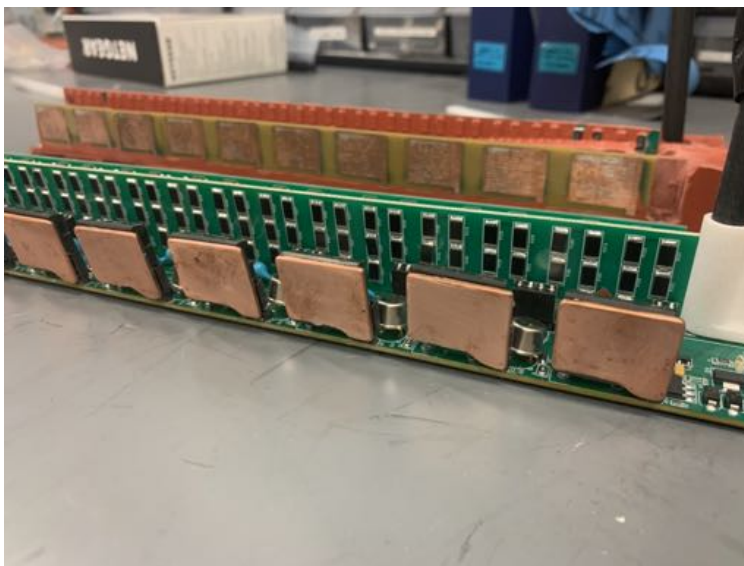


Figure 7.27: A photograph of two amplifier banks comparing the wall design. The amp in the foreground has the new single-FET copper pads. The amp in the background has the original wall design, with copper pads printed on a PCB board. The amp in the foreground is not potted, while the amplifier in the back is.

We retrofit all of our amplifiers with this new design. In addition, we retested all of our amplifiers, in multiple cases removing and testing active components to find possible causes for the floating issues. In multiple amplifiers we found IXTF1N450 or 2N6660 FETs with behavior that indicated some level of damage or deficiency. At the end of this process we had eight working amplifiers, two of which were new, all of which had been recently tested on the bench and showed excellent electrical behavior with no floating issues. In addition, we re-calibrated all of the high voltage probes that are part of the global feedback. We hope that of these upgrades together will increase the lifespan and reliability of the amplifiers. As of summer 2023, all of these amplifiers were re-integrated onto the decelerator and successfully brought to 10 kV at the full range of frequencies relevant to deceleration of ND_3 .

Another aspect of improved amplifier structure was the upgraded design of the previously mentioned boron nitride walls. These walls were originally comprised of three small panels of boron

nitride bonded to a polycarbonate frame bonded with an encapsulant, Super Corona Dope.[\[2\]](#) Later these were modified to be larger panels bonded with epoxy Loctite ES1001. Recently, we were able to procure boron nitride that could be cut into a single panel, which reduces the amount of epoxy-filled seams along which the walls can fail. The process of fabricating these walls with the new, larger, frames and Loctite ES1001 epoxy has not yet been officially documented. I will do so here. This brief description of the assembly process will describe the case that the boron nitride must be placed in three panels. The case of the single panel is a simpler to execute, and as such the description for three panels provides a slightly more comprehensive procedure.

- (1) Before beginning, inspect the polycarbonate frame. Ensure there are no cracks in the frame and that none of the screw holes have been stripped. This step is primarily important for reused frames, but is wise for newly machined polycarbonate frames as well.
- (2) Tape a teflon sheet to the bottom (defined as the side that rests against the aluminum, having with the smaller inset for the boron nitride) of the wall, as shown in Figure [7.28](#). Doing so will allow epoxy to flow through to the bottom without bonding to the surface you are working on.
- (3) Insert nylon screws in the holes intended for the clamps, near where epoxy will be spread. This prevents epoxy from accidentally flowing into these holes.
- (4) Spread the epoxy on all surfaces that need to be bonded, both boron nitride and polycarbonate, as shown in Figure [7.28a](#) & b. I recommend using a syringe with an 18G (or so) needle to spread the epoxy. The commercially available mixing tip for the Loctite ES1001 epoxy is usable, but clumsy to distribute properly.
- (5) Place outer panels in the frame, then the center panel. The goal is to avoid air bubbles in the seams between the two materials. You may need to press down slightly to make good contact, but avoid moving the panel or pressing hard as much as possible. If you press down epoxy will leak out, and if it pulls back up it will likely suck air into the seam.

- (6) You may want to spread some extra epoxy over the top of the seams. The epoxy is quite viscous (close to honey) but will respond to gravity. You will almost certainly need to add more epoxy on the corners after \sim 6-12 hrs. The final results may look something like Figure [7.28](#).
- (7) After about 24 hrs, the epoxy should be firm enough to remove screws and teflon. Most likely there will be some solidified epoxy on the boron nitride surface. Since you need both surfaces to be flat, this will need to be removed. I recommend carefully and gently scraping excess cured epoxy with razor blade that is held nearly parallel to the surface of the boron nitride.
- (8) When screwing the polycarbonate/boron nitride wall the aluminum wall, fasten screws lightly, just tight enough to feel tension. Do not tighten too much, as this can cause the wall the flex and crack.
- (9) Test to static voltages of $\geq 15\text{kV}$, sitting at 15 kV for 5 min or more. A more detailed tested procedure is given in Yomay's thesis. [\[2\]](#)
- (10) Add thermal paste between the boron nitride and aluminum and repeat high voltage test. We use a thermal paste called Thermal Grizzly Kryonaut Extreme. (You read correctly; it is bubble-gum pink and works wonderfully well.)

It took some troubleshooting to dial in this fabrication procedure. Unlike the original assembly with corona dope, there does not seem to be a great way to repair a wall that fails the high voltage test. For this reasons, the assembly was tricky to dial in. However, this assembly had a high success rate for us. The recent acquisition of boron nitride from Saint Gobain in sheets large enough to cut into a single panel also simplified matters, as the seam between the boron nitride panels has been a point of failure in the past.

In the case of a failed wall, the frame can be recovered by soaking the whole assembly in isopropanol (acetone will eat the polycarbonate.) We sometimes recovered larger pieces of boron

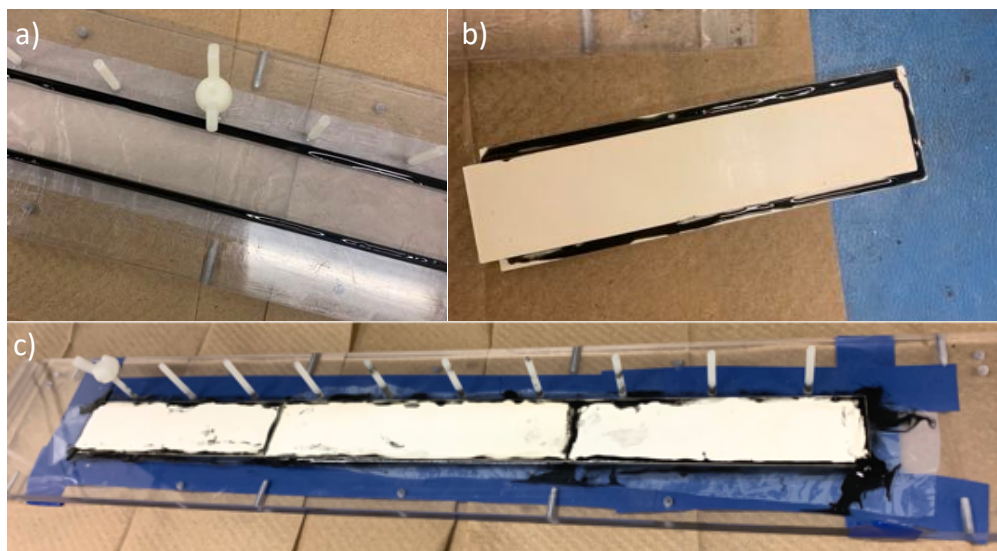


Figure 7.28: Wall fabrication benefits from Loctite ES1001 epoxy being spread on all surface before attached pieces. (a, b) Epoxy is spread on frame and boron nitride first, (c) Then the panels are placed with light pressure. Make sure the bottom has a teflon layer and is laid level.

nitride doing this, but usually not useful pieces. However, with enough gentle force the boron nitride will come out cleanly and leave a reusable polycarbonate frame. As these are a pain to machine, this can be a worthwhile piece to recover.

7.4 Summary

In summary, this TWSD has undergone significant development within the Lewandowski lab. Two thesis have spent significant effort to building the ring decelerator infrastructure and designing state-of-the-art high voltage amplifiers with outputs up to 10 kV from 30 kHz to DC. [16, 2]

A few recent, additional upgrades to these amplifiers have been necessary to attain a 10 KV output with good longevity. Upgrades to the cooling of these amplifier electronics has included design of larger boron nitride walls and better thermal contact between the FETs and these walls with copper pads replacing the original PCB boards. In addition, a new choice of optoisolator for isolation between high voltage and driving electronics has averted a failure mode that original kept these amplifiers from going up to 10 kV amplitude. I also discussed a failure mode associated with damaged or improperly manufactured 2N6660 FETs.

Such technical upgrades have enabled deceleration of a neutral beam of molecules down to 10 m/s as detected with a REMPI laser and TOF-MS. Experimental characterization of the TWSD has verified the velocity-tunable neutral molecule beam source is adequate for applications in collisional chemistry. This preceded integration with our linear ion trap for the study of energy-resolved ion-neutral reactions. This integration process, nicknamed “The Big Build,” is the topic of the next chapter, Chapter [8](#).

Chapter 8

An integrated TWSD-LIT for energy-tunable ion-neutral reactions

“But on the whole, though I was taught that the way of progress is neither swift nor easy, this first trial confirmed in me the taste for experimental research in the fields of physics and chemistry.”

–Marie Curie, *Autobiographical Notes: The Story of My Life, 1923*

This chapter is devoted to the in-progress pursuit of energy-resolved reactions between Stark-decelerated molecules and trapped ions in a Coulomb crystal. This chapter will be split into three sections. First, I will discuss the physical integration of the ion trap (which was described in Chapter 2), and the traveling-wave Stark decelerator (which was described in Chapter 7). This discussion will overview the updated layout of the combined experiment, including the optimized parameters for using trap rods as a TOF and the planned addition of a shutter. Then, the newly added hexapole will be discussed in more depth in a second section. This section will highlight the mathematical principles of hexapole lensing, as well as report on our progress towards modeling and empirically optimizing the operation of this lens for energy-resolved reactions. The third and last section will discuss the center-of-mass collision energy for a TWSD-LIT reaction of $\text{NH}_3^+ + \text{ND}_3$. This will include the definition and estimates of important parameters in both the TWSD and LIT, which contribute to the collision energy of the reaction. I will motivate this first proposed reaction and conclude with an overview of the work that remains to achieve energy-resolved reactions in our TWSD-LIT system.

8.1 The Combined Apparatus

Conceptually, the combined apparatus is quite simple. The traveling-wave Stark decelerator (TWSD) was physically combined with the linear ion trap and time-of-flight mass spectrometer (LIT-TOFMS) in spring of 2021. In order to provide focusing of the output decelerator beam into the center of the ion trap, a hexapole was added to couple the two systems. In addition, a shutter between the decelerator and hexapole will be implemented to block the undecelerated output of the TWSD, while still allowing the decelerated molecules to reach the hexapole. Figure 8.1 shows a schematic of this integrated setup.

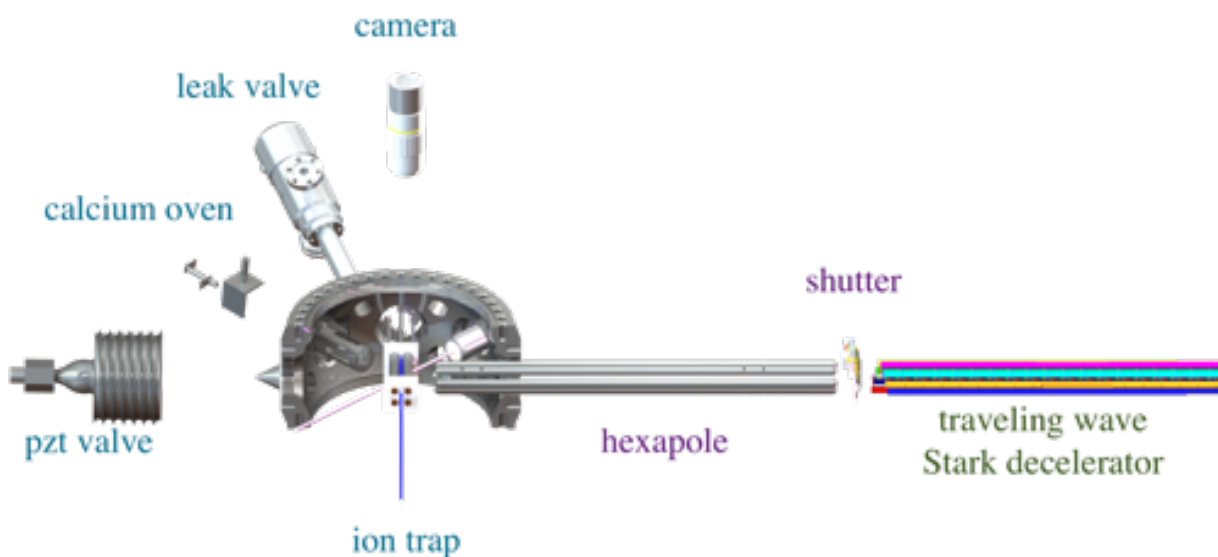


Figure 8.1: Rendering of the core components of the combined TWSD-LIT-TOFMS ensemble. Components original to the ion trap are labeled in blue, the Stark decelerator is labeled in green, and the components new to the integration experiment are labeled in purple (the hexapole and the shutter.)

First, I will describe the combined setup with photographs and CAD drawings. Then I will discuss the beam shutter in more detail, specifically its operation specifications and the procedure for mounting and replacing it. Lastly, I will discuss the challenges of using the ion trap rods for time-of-flight mass spectrometry during beam characterization. This will briefly overview the empirical and computational work we accomplished to optimize the transfer efficiency of ionized

Stark-decelerated molecules to the MCP detector plates.

8.1.1 Physical parameters and images of the combined system

Figure 8.2 shows photos and a CAD drawing of the hexapole mounting structure. The decelerator was designed to receive the mounting poles of the upstream end of the hexapole; Figure 8.2a and b show the end-on view of the decelerator before and after mounting the hexapole, respectively. This mounting design allows the hexapole rods to be insulated from their mounting structure by a glass sleeve around circular discs that hold the hexapole rods in place (Figure 8.2c and d). These discs also electrically connect alternating hexapole rods, with each set of three rods electrically connected to SHV ports on the exterior. On the downstream end of the decelerator, a similar mounting structure insulates the hexapole rods from a mounting cap. This cap attaches to the top of the spherical octagon in which the ion trap resides.

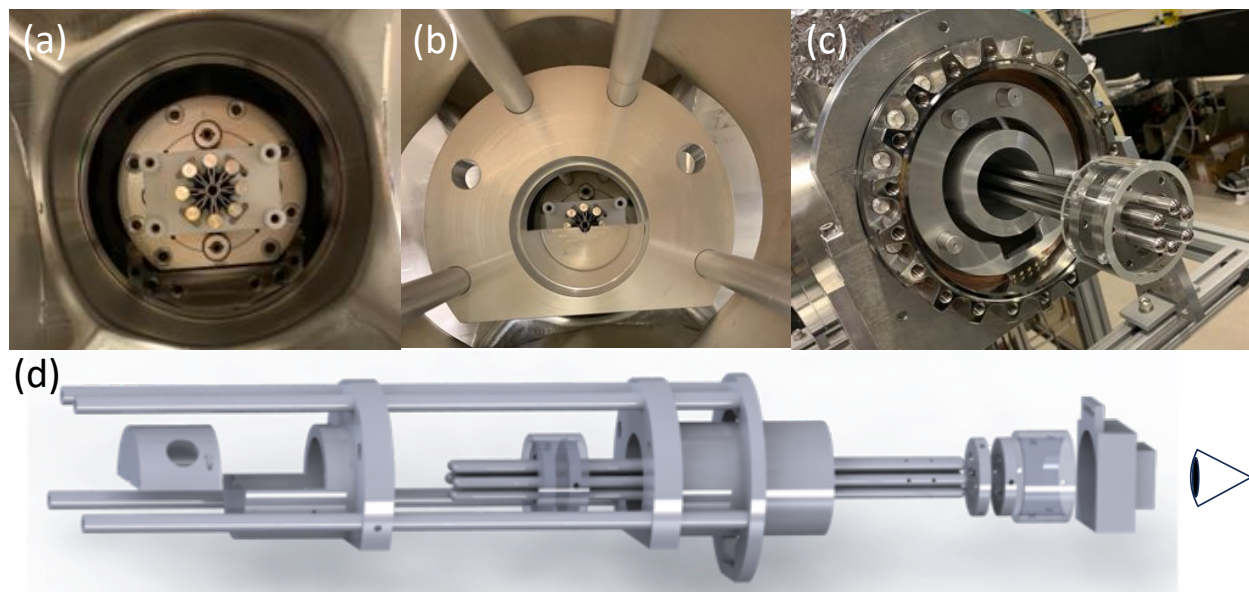


Figure 8.2: Details of hexapole mounting. Above photos show an end-on view of the downstream end of the decelerator (a) before and (b) after the hexapole mounting is installed. (c) End-on view of the downstream end of the hexapole before integration with the ion trap. The two discs that provide electrical connection between alternating rods are visible. Outside these discs is a glass sleeve that insulates the hexapole rods from the mounting cap. (d) Partially exploded CAD view of the hexapole and mounting structure. Also shown is the direction of the end-on perspective for the prior photographs.

A more tangible perspective on the entire ensemble is given by Figure 8.3, which shows a CAD rendering of the decelerator output to the ion trap. This CAD drawing depicts more details of the conflat chamber and mounting hardware, with accompanying photographs. These photos and CAD drawing give an overview of the components and approximate lengths involved in the total beamline. This design was carefully constructed to ensure good alignment from the output of the decelerator to the center of the ion trap.

These photos also yield a nice demonstration of the planned mounting position of the shutter, which has not yet been implemented. In Figure 8.3, the purple box outlines the CAD rendering and photos of the downstream output of the decelerator and the upstream end of the hexapole. Within this section, there is a removable top piece for the upstream hexapole-mounting cap that is not included in the photograph. This will house the mechanical shutter, which will be implemented when we began reaction experiments. Many people have been involved in the design of this shutter and its electrical operation. Excellent work by Andrés Villani Dávila and James Greenberg completed the characterization and the mounting scheme of the shutter, respectively. An overview of the motivation, design, and specifications will be given in the next section.

Lastly, a few pictures from the integration process are quite useful for grasping the full ensemble of this combined experiment. Figure 8.4 shows the side view during the construction process, with key conflat flanges still open. Here, the flight tube below the ion trap can be clearly viewed. The decelerator, hexapole, and ion trap are clearly visible in Figure 8.5 from a top view.

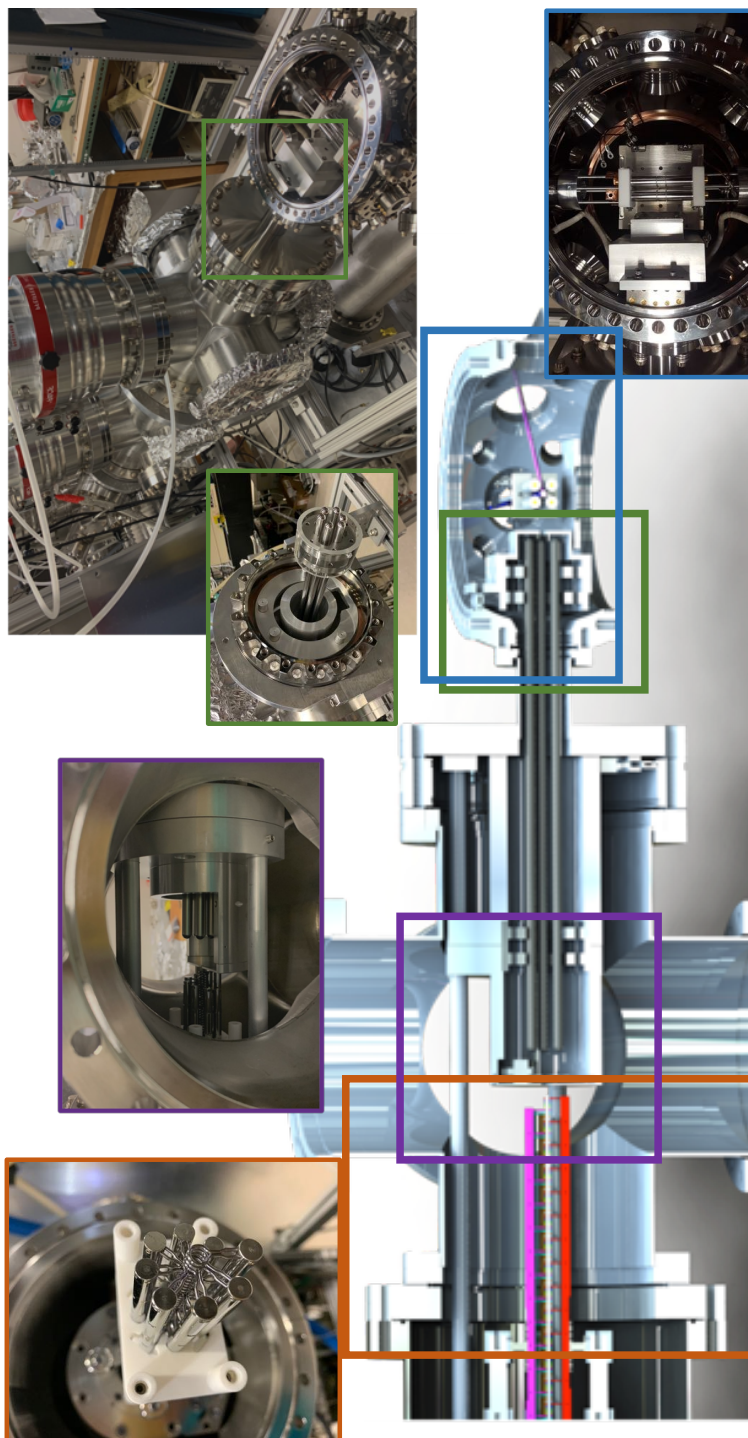


Figure 8.3: CAD rendering of the integrated experiment, with correlated photos from the construction process. The orange box highlights the end of the decelerator. The purple box shows the coupling of the decelerator and the hexapole. The green box labels the end of the decelerator, with two photos. One is less complete, showing the glass sleeve that protects the hexapole rods from the mounting cap; the photo to the right is later in the construction process, with the hexapole placed inside the reducing nipple, and a cap mounting the end of the hexapole to spherical octagon that encloses the ion trap. Lastly, a top view photograph of the trap with the integrated hexapole is indicated by the blue box.

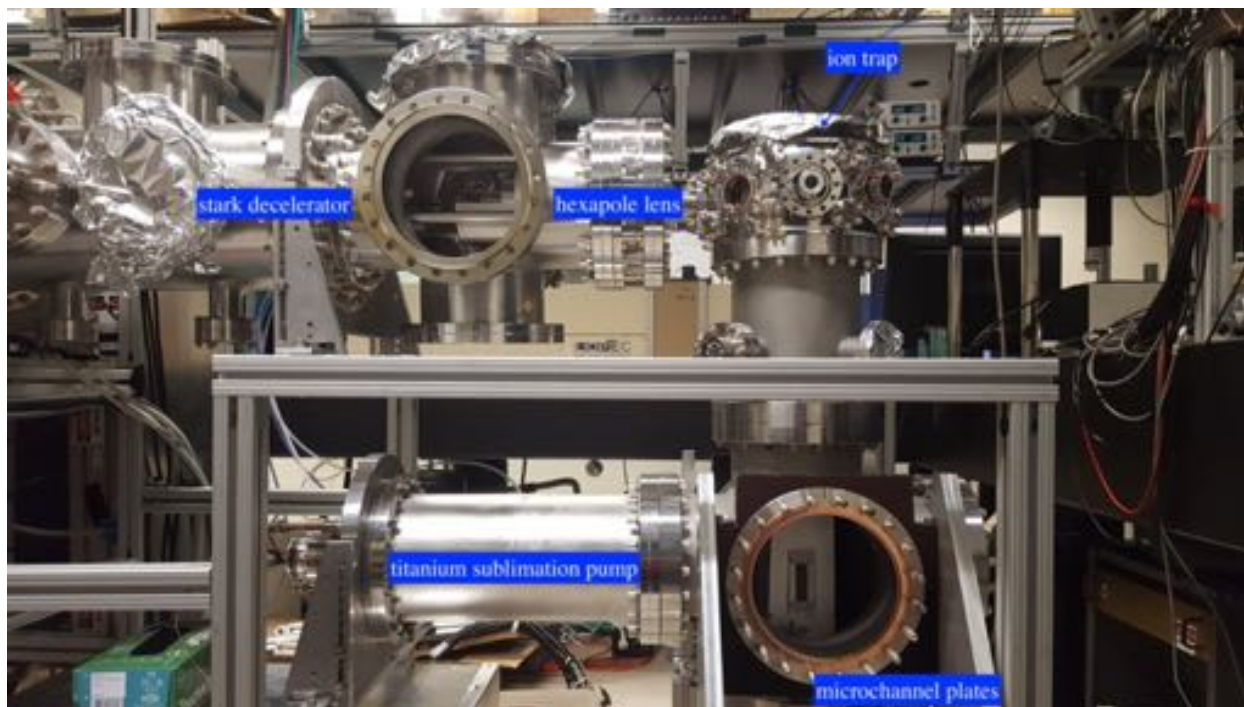


Figure 8.4: Side view of the fully integrated experiment during the building process. The first open flange on the left shows the end of the decelerator and the beginning of the hexapole. The ion trap is on the right, with the flight tube extending directly below. Off the side of the flight tube is a titanium sublimation pump.

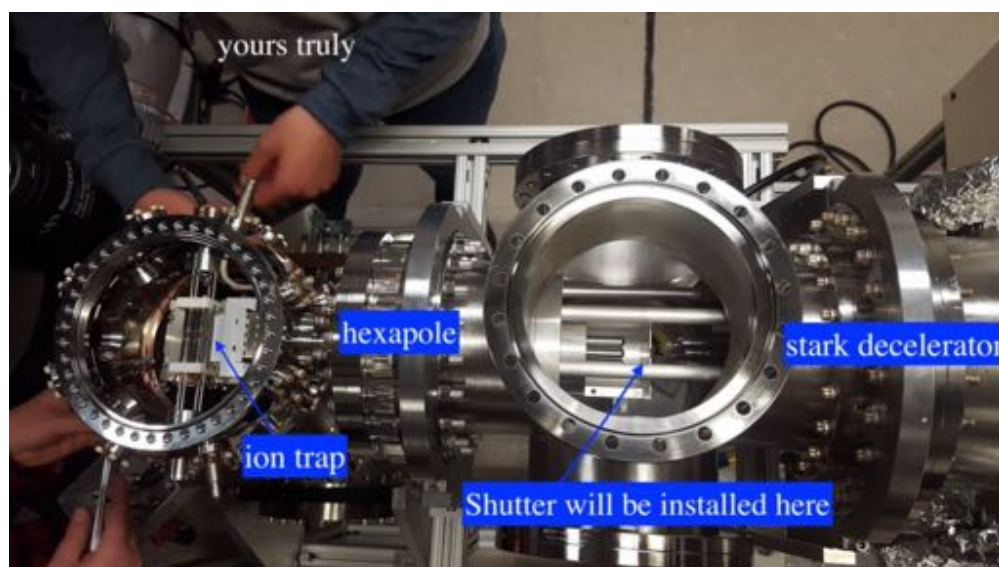


Figure 8.5: Top view of the fully integrated experiment during the building process. The open flange on the right shows the end of the decelerator and the beginning of the hexapole. The ion trap can be viewed on the open spherical octagon on the left.

8.1.2 Shuttering the decelerated beam

A beam shutter is necessary to separate the decelerated molecules from the carrier gas and undecelerated molecules. The undecelerated, molecules and carrier krypton gas will necessarily arrive at the ion trap before the decelerated molecules. The krypton gas may heat or potentially melt the Coulomb crystal, causing uncertainty in the ion energy distribution and possible loss of ions from the trap. In addition, allowing the undecelerated molecules to interact with the trapped ions is problematic, as it defeats the purpose of producing a velocity-tunable source of molecules. Our solution to this problem is to introduce a shutter that can remain closed until the undecelerated molecules and atomic gas have exited the decelerator, which can then open to allow decelerated molecules through. As a reminder of the relevant time scales for such a shutter, Figure 8.6 is reprinted here from section 7.2. As can be seen here, we will need to use the alternative slowing method described in section 7.2.2 to delay the arrival of the faster velocities to fully remove them from the undecelerated background. [340, 18] The highest velocity that this alternative slowing method can be used at without unreasonable loss of molecules is about 250 m/s. However, even with this alternate slowing method, we will need a shutter capable of quite fast opening times, as well as one that can stay open for up to five milliseconds.

The target specifications for this beam shutter is a time to fully open that is within $\leq 500 \mu\text{s}$ and which stays open for 5 ms. In addition, it needs to be vacuum compatible. This will be achieved with modified Uniblitz laser shutters, shown in Figure 8.7.

This laser shutter is designed to open quickly with the use of electromagnetism. The force opening two blades is controlled by the magnitude of current run through the wire coil exposed in Figure 8.7b and c. These blades are spring loaded, which allows them to close quickly after the current is shut off. Andrés conducted research on possible modifications of these shutters. A primary avenue was the stiffness of the springs included on these shutters. However, while using springs with small spring constants allowed a faster the opening speed, they also caused stability issues and unreliable or slow closing speeds.

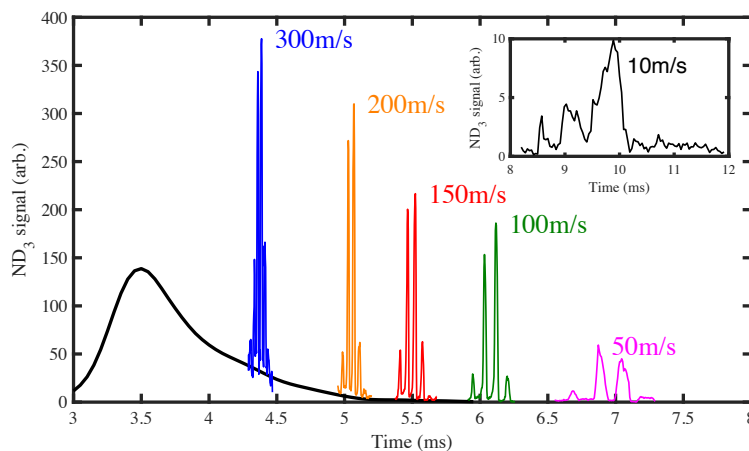


Figure 8.6: Deceleration data for multiple final velocities ranging from 300 m/s down to 10 m/s. Time is the delay between the molecular beam valve trigger and detection laser pulse. The solid black trace is the free-flight data, scaled to match the baseline of the deceleration data. Figure adapted from Greenberg (2021.)[\[18\]](#)

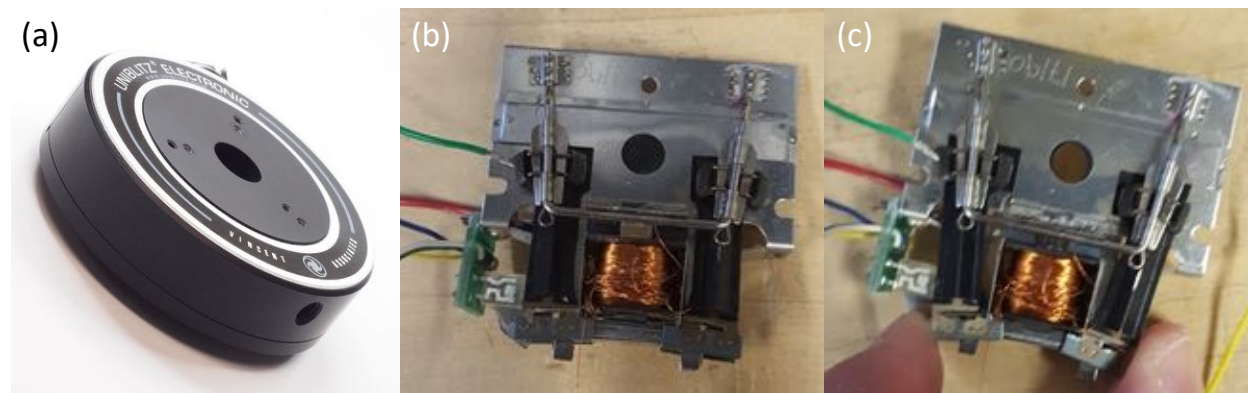


Figure 8.7: (a) A Uniblitz shutter in its original housing and (b) with the housing removed. This shutter opens due to electromagnetism, with the speed of opening modulated by the current applied across the coil shown. The manually opened shutter blades are shown in panel (c).

Research was also conducted on the most efficient currents at which to drive these shutters. One concern regarding this shutter design was its operation in UHV, where there will be no air currents to aid in heat dissipation. To help mitigate this problem, the shutters can be run at higher currents during the opening phase, but with lower currents while the shutter was being held open. This allows a more energy-efficient operation without compromising on opening speed. Andrés further experimented with these values, finding the lowest possible operating currents that meet

our target specifications. The optimized driving voltages are reported below in Table [8.1](#). Andrés found suitable parameters that reduce the heat load by something on the order of ~ 20 . This should aid greatly in the avoiding overheating by this shutter in an UHV environment.

Table 8.1: Specified and effective behavior of the 6 mm Uniblitz shutter.

	Parameters specified by Uniblitz datasheet	Lowest suitable parameters
Open Voltage (VDC)	65	9
Open current (A)	1.35	0.20
Hold voltage (VDC)	10	2
Hold current (A)	0.21	0.05
Open time (ms)		0.440
Close time (ms)		1.240

These heating concerns were also addressed by the mounting structure. As shown in Figure [8.8](#), the shutter is designed to attach to a removable cap on the upstream end of the hexapole. The shutter is mounted to an aluminum cap near the source of the heating, on the other side of the electric coil. This will allow the cap to act as a heat sink for the shutter. This, in addition to the relatively low 2 Hz duty cycle, should allow adequate heat removal from the system. However, it is expected that such a shutter will have a finite lifetime. It is for this reason that the cap was designed to be removable, with a mounting structure that allows spatial access to the shutter mount. The mounting procedure of the shutter to the cap was also designed to be repeatable, and has been documented by James Greenberg.

Because this shutter is expected to have a finite lifetime, it is not planned to be mounted in the beamline until we are ready for reactions. First, we must finish our study of the parameters involved in hexapole lensing. Such studies are accomplished by decelerating the molecules to a particular output velocity, and then altering different timings and voltages on the hexapole to find the highest beam signal. The relative ND₃ signal is measured with a 317 nm REMPI laser (as discussed in section [7.1.4](#)) that intersects the molecular beam at the center of the trapping region. Future applications in reaction studies necessitate precise calibration of the relative beam density of the TWSD at the location the reactions will take place – the center of the ion trap. For this

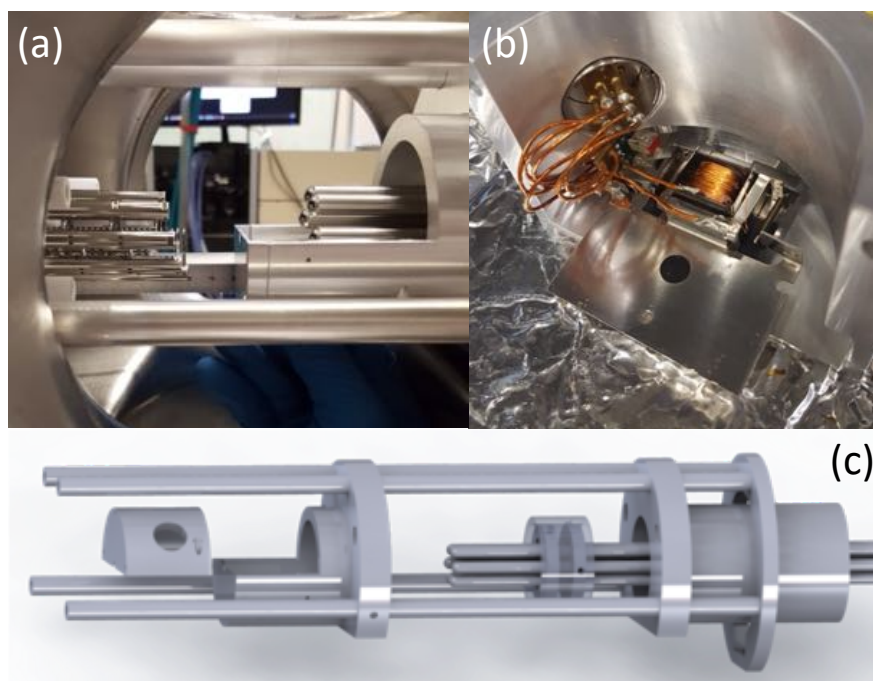


Figure 8.8: (a) A side view of the downstream end of the decelerator and upstream end of the hexapole, with entry cap missing. This cap is not yet installed, having a shutter (b) mounted on it. This shutter will be installed before a final characterization of the beam output and subsequent reaction studies. An exploded view of the hexapole mounting (c) demonstrates this removable cap and its position on the hexapole mounting structure.

reason, as well as the obvious practical one, we decided to use our ion trap as the accelerator of ions to our MCP plates. However, we faced some challenges using a quadrupole trap in lieu of parallel plates, which will be described in the next section.

8.1.3 Configuring an ion trap as a “static TOF”

Coulomb crystals in our ion trap have an excellent transfer efficiency for detection; this has been evidenced by detection of single ions at near the detection efficiency of the MCP plates.^[1] However, ejection of cold, dense ions is a very different regime than laser-ionized molecular beams. This was one of the first challenges of our integrated setup: detecting decelerated (or guided) ions from the Stark decelerator with the ion trap serving as a substitute for traditional parallel plates. In response to difficulties detecting molecules, we looked closer at the transfer of ions from the ion trap to the flight tube with COMSOL simulations.^[20] The top of the flight tube is covered

by a grounding plate with a small elliptical hole for the ions to pass through (with major and minor axes of $2a = 2$ mm and $2b = 1$ mm, respectively.) This grounded plate has an intentionally small hole to reduce the impact of stray fields. As such, we did not want to remove the top grounding plate, but initially pursued COMSOL simulations to investigate the impact of increasing the size of this ion transmission hole. This was extended to an investigation of the impact of the trap rod applied voltages when it became clear that this could improve the transfer efficiency without requiring a permanent modification to the setup (or require a break of UHV.) These results have direct relevance to detecting ions with the integrated setup, as well as demonstrate some general guidelines for utilizing quadrupole trap rods to accelerate ions towards detection plates.

We first modeled the TOF-MS system in COMSOL and computationally compared the expected performance of an ionized molecular beam to the efficiency of Coulomb crystal detection. We modeled the TOF-MS system with a grounded flight tube, which had a grounded entry (top) plate with the aforementioned ellipsoidal hole. The trap rods were modeled to have static voltages, a higher value of positive HV on the top two rods (all three segments of each rod) and a lower value of HV on the bottom two rods. I began by comparing the computed expected efficiency of our standard voltage settings of 2000V on the higher rods, 1860V on the lower rods. This was accompanied by dynamical simulations of ion groups modeled like a Coulomb crystal, or like a laser-ionized molecular beam.

The cold cloud of ions was modeled with a pre-set number of ions (~ 1000) that were released from a rectangular grid of dimensions $0.1 \times 0.1 \times 1$ mm. This was placed at the center of the trapping fields with the long axis parallel to the rods, along the z axis. The ions were given a statistical distribution of velocities with a standard deviation of ~ 30 m/s in all directions and a m/z of 40. This provided a rough model of the spatial distribution and the energies of a calcium Coulomb crystal. All of these ions successfully reach the MCP plates, as shown in the top of Figure [8.9](#).

For the modeling of the ammonia beam, the ions were modeled as a grid of size $1 \times 1 \times 1$ mm

centered at the center of the trapping fields.¹ These particles were given a m/z of 20 and originally given a z -axis velocity of 400 m/s. The mesh was quite dense, with ammonia spaced nearly every $20\ \mu\text{m}$, and a total of $\sim 100,000$ particles modeled. This higher sampling was necessary, as very small proportion ($< 2\%$) of these particles successfully arrived at the MCP, as shown in the bottom panel of Figure 8.9.

Follow-up assessments of the low transfer efficiency for the ammonia model arrived at a few conclusions. We determined that the initial velocity had little to no impact on the transfer efficiency; this was evidenced by minimal change in the simulated detection when the ions began with no velocity as when they began with the 400 m/s directed velocity. This verified that the transfer efficiency was not dependent on the molecular beam velocity, which is a critical result for establishing the comparability of our decelerated molecule signal at different final velocities. This result also indicated that the low transfer efficiency was likely caused by the initial placement of the ions. This was verified by identifying the starting position of the ions that successfully arrived at the MCP. The successfully transferred ions were all very close of the center of the trapping fields, particularly in the x -direction (along the neutral beam propagation direction. See Figure 8.9 for coordinate definitions.) A closer examination at the electric fields caused by these rods illuminated the effective focusing fields that cause this phenomena, shown in Figure 8.10.

The standard TOF-MS configuration used for the original detection of the decelerated beam is comprised of two parallel thin plates. This allows a uniformity of electric field in the direction of acceleration and transverse directions, which depends on the size of the plates. The plate dimensions can be designed to produce a nearly uniform field at the position of the ions. However, by using trapping rods as our TOF field, we introduce deviations from this model. While the cylindrical symmetry yields uniformity along the z -direction (the rod axial direction), neither the x nor y directions are uniform. In the voltage configuration used to eject Coulomb crystals out of the trap

¹ This is not actually physical. The ionization beam comes in along the x/z plane at an angled diagonal to the rods, with a $\sim 100\ \mu\text{m}$ beam waist and $\sim 3\ \text{mm}$ Rayleigh length. These values were chosen as upper limits to the overlap of a focused laser beam and a packet of decelerated molecules. This overlap is not centered by definition, as is the case with a cloud of trapped ions. Overestimating the ionization region was intentionally done to study the best parameters to optimize for the largest region of successful ion transfer. If we were interested in estimating absolute transfer efficiency, we would have to take a different approach.

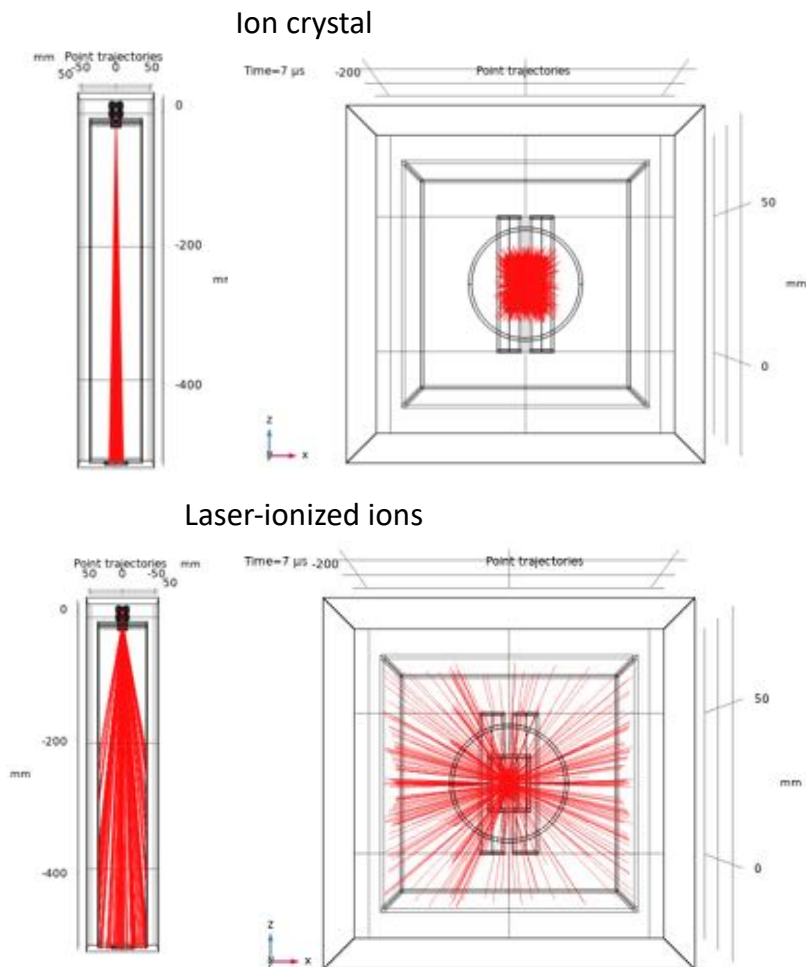


Figure 8.9: Particle trajectories in the LIT-TOFMS system. Ions are released from a distribution near the center of the trap that is modeled after either a Coulomb crystal (**top**), or an ionized molecular beam (**bottom**). This simulations demonstrate a high relative loss of ions when modeled as a ionized molecular beam, and very low losses when modeled as a dense, small, crystal.

(2000/1860 V on top/bottom rods), the fields are relatively uniform between the two rods, but are much less so between the bottom rods and the ground TOF plate. This can be seen by the particle trajectories and electric fields shown in the top left and top right images of Figure [8.10](#), respectively. Here it can be seen that as the ions will defocus slightly before passing through the bottom two rods. Here, they focus sharply before passing through the ellipsoidal hole and into the free-flight region. There are two major source of ion loss here. Most ($\sim 90\%$) of the ions in this 2000/1860 V simulation do not even make it through the ellipsoidal hole. Of those that do, another $\sim 80\%$ hit

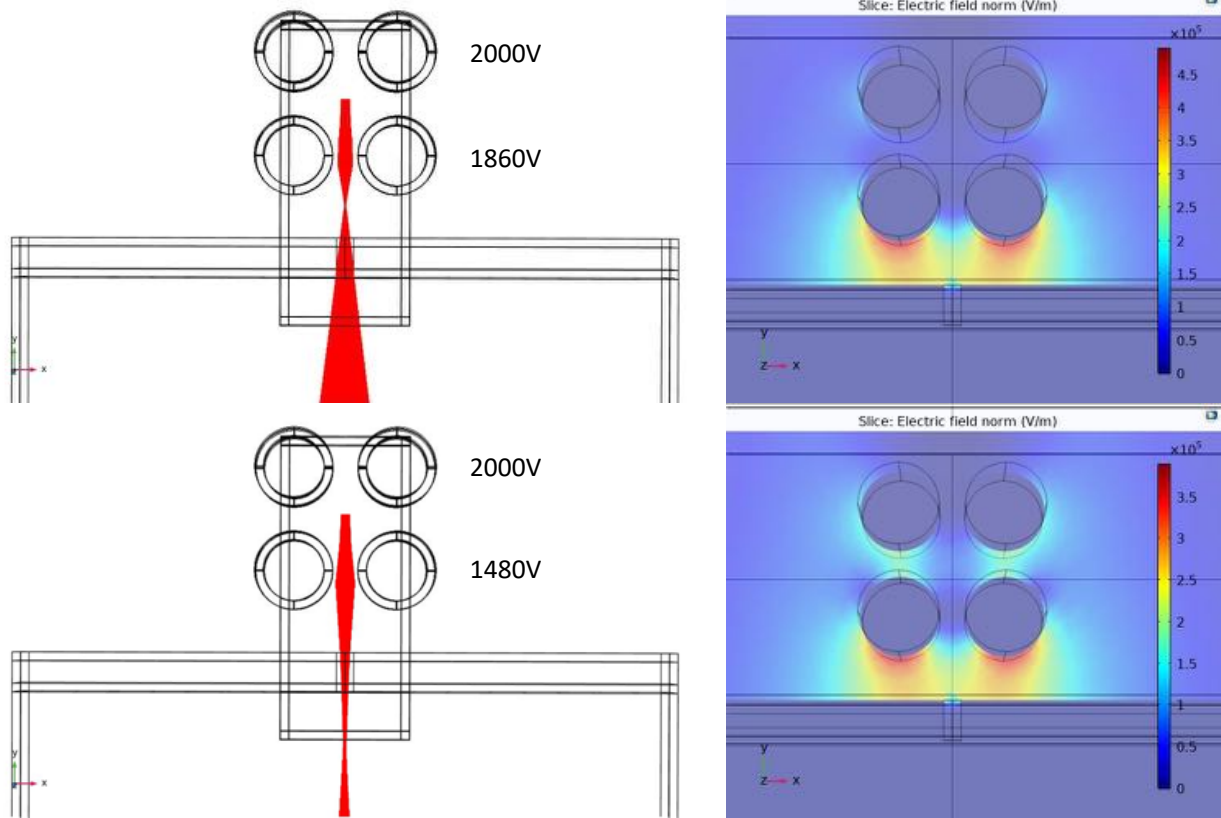


Figure 8.10: Ion trajectories (**left**) and electric fields (**right**) for the original rod voltage settings of top/bottom 2000/1860 V (**top**) and final settings 2000/1480 V (**bottom**). The figures together demonstrate the field gradients and resulting focusing of the trajectories. This focusing can be tuned with different combinations of voltages on the rods. We found that the 2000/1480 V gave the best transmission through the hole at the top of the flight tube, and paired best with our Einzel lens to achieve maximum signal at the MCP plates (not shown.)

the walls of the flight tube, as was shown in Figure [8.9](#) (bottom). The latter problem can be at least partially addressed with an Einzel lens in our flight tub, which was not modeled in this study. The clipping on the grounding plate can be improved by changes in the trap rod voltages.

We modeled the results of drilling a large hole in this plate, as well changing the voltages on both sets of rods. Ultimately, we found by computational simulations that lowering the voltage on the lower pair of rods had the greatest impact on the transmission through the ellipsoidal hole. The relative voltage between the two sets of rods altered the y -direction velocity, and thus the time passing through the fringing fields. We simulated the transmission of the ions with top rod

voltages varied between 1-2.1 kV, and the bottom rod voltage between 0.7-1.9 kV. We found the best calculated transfer efficiency ($\sim 8\%$) at a 2000/1600 V rod voltage combination. Empirically, when we also used the Einzel lens (set to 600 V), we arrived at the optimum configuration of 2000/1480 V.

Another interesting result of these simulations involves the optimum beam path of the ionization laser for ion detection. The sensitivity of the ion placement along the x -direction, but less so along the z -direction, implies that we might have higher detection of our ions if we align our REMPI laser along the z axis. Due to established optics along this path for cooling lasers, we decided to run the laser beam diagonal across the xz direction. However, this does imply that we are complicating this ion transmission process, and likely losing ion signal even with the most effective TOF voltages due to this beam path. This is one reason to change how we align the REMPI laser for neutral beam detection. Another reason relates to the calibration of relative beam density out of the hexapole, a reason which will be discussed in more detail later in this chapter.

An important reminder about these calculations is that they never served to model the absolute transfer efficiency. For that, a much more physical model of the ionization beam parameters, of the molecular beam size and distribution, and the inclusion of an Einzel lens would be necessary. This is beyond the scope of these calculations. The goal of these simulations was to determine how to improve the signal. Indeed, the changes made to the experimental detection in response to these computations brought us from an undetectable signal, to signal large enough to observe and empirically optimize. This investigation and the general principles gained from it may also be useful for other uses of the ion trap as a mass spectrometer, including characterization of contaminants in a gas pulsed in from a PZT valve.

8.2 The hexapole

The hexapole was added to this combined apparatus during the Big Build. Hexapoles are a configuration of six rods symmetrically spaced equidistantly in a circle. When these rods are held at alternating voltages ($-V/2$ and $V/2$, or ground and V), they produce a symmetric electric field with a magnitude of zero on along the center of the symmetry axis and increasing field strength

at larger radii. Such an electrostatic field can be quite useful for guiding molecular beams. These types of symmetric fields can be achieved with any even number of poles, although quadrupolar and hexapolar configurations are the most common. The exact field dependence on the radius, $E(r)$, is determined by the number of poles, and thus the chosen number of poles often depends on the intended neutral molecule.

Historically, hexapolar and quadrupolar guides have been prevalent in beam manipulation. Applications include the orientation of molecules in a beam for reaction studies,[\[349\]](#), [\[350\]](#), [\[351\]](#) focusing of molecular beams,[\[352\]](#), [\[353\]](#) and rotational state-selection of molecules within a molecular beam.[\[354\]](#) Recent applications have also included storage rings or synchrotrons formed by hexapole rods curved into a circular path.[\[335\]](#), [\[355\]](#), [\[356\]](#) Both hexapoles and quadrupoles have been used as beam guides for reaction studies, sometimes introducing energy tunability in a technique referred to as “Stark filtration.” This method utilizes a curved (usually semicircular) multipole guide at a particular voltage. Whether a molecule can be maintained in the guide around a curve depends on the curve radius, the applied voltage, the velocity of the molecule, and the Stark shift of the molecule. Thus, these parameters can be chosen to transmit only the slowest portion of a thermal beam through such a curved multipole guide. Quadrupolar guides, used as Stark filters, have been featured in reaction studies with Coulomb crystals.[\[76\]](#), [\[222\]](#), [\[357\]](#) This technique can be joined with buffer-gas cooling to further enhance the density and degree of control over a velocity-filtered beam.[\[358\]](#), [\[359\]](#)

The preferred number of poles for an application depends on the molecule and application of interest. A $2n$ -pole focuser has an electric field that exhibits a $|\vec{E}| \propto r^{n-1}$ dependence. As such, quadrupoles are preferred for molecules with a quadratic Stark shift, and hexapoles for linear Stark shift.[\[354\]](#), [\[335\]](#), [\[353\]](#) The next section will review the equations that describe fields inside a hexapole, particularly as they relate to the trajectory of ND_3 molecules in our hexapole. This will be followed by a discussion of the computational and empirical work used to optimize the density of the ND_3 beam at the center of the ion trap.

8.2.1 Force on ND₃ in a hexapole

The principles of hexapole lensing, like Stark deceleration, rely upon the Stark effect in molecules.² A more in-depth discussion of hexapole lensing can be found elsewhere; [351, 353, 335] the highlights will be reviewed here.

The force on a molecule at point r is dependent on the gradient of the Stark energy at that point:

$$\begin{aligned} F_r &= -\nabla W_{stark}(r) \\ &= -\left(\frac{\partial W_{stark}}{\partial E}\right)\nabla E(r) \end{aligned} \quad (8.1)$$

where F_r is the force on a molecule, W_{stark} is the energy of the molecule due to the Stark effect at field strength $|\vec{E}|$. The $\frac{\partial W_{stark}}{\partial E}$ term can be easily worked for the case of ND₃ by building off of the equations from section [7.1.2]

$$\frac{\partial W_{stark}}{\partial E} = \frac{E\mu^2\kappa^2}{(\sqrt{U_{inv}/2})^2 - (\mu E\kappa)^2} \quad (8.2)$$

with $\kappa = \frac{MK}{J(J+1)}$, U_{inv} is the inversion splitting, and μ is the dipole moment. Note that $MK < 0$ for low-field seeking states. Further, in the limit that the first order Stark effect dominates ($\mu E\kappa \gg U_{inv}$), this simplifies to,

$$\frac{\partial W_{stark}}{\partial E} = \mu\kappa \quad (8.3)$$

This completes the first term for Equation [8.1]. For the second, we observe that a hexapole produces an ideal electric field magnitude at radius r of: [351, 353]

$$E = \frac{3V_0}{r_0^2}r^2 \quad (8.4)$$

r_0 is the inscribed radius of the rods, and where the rods alternate between voltages $-V_0$ and V_0 . Then we can derive:

$$\nabla E = \frac{6V_0}{r_0}r \quad (8.5)$$

² A discussion of the Stark effect in ammonia can be found in section [7.1.2]

From the electric field strength, we can derive our force,

$$\begin{aligned} F_r &= -\mu\kappa \frac{6V_0}{r_0^3} r \\ &= -\frac{6\mu K M V_0 r}{J(J+1)r_0^3} \end{aligned} \quad (8.6)$$

where J is the total angular momentum, K is the projection of J onto the symmetry axis and M is the projection of J onto the electric field.

The harmonic behavior of this system is sometimes emphasized by relating this force to a radial harmonic frequency ω and mass m . This produces a relationship equivalent to Equation [8.6](#):

$$F_r = -m\omega^2 r \quad (8.7)$$

where

$$\omega = \sqrt{\frac{-6\mu K M V_0}{mJ(J+1)r_0^3}} \quad (8.8)$$

Equation [8.6](#) is based on an ideal hexapole field, which would be created by hyperbolic rods. In our case of cylindrical rods, the deviations from this ideal case are rather small.[\[335\]](#) Simulated results for our own hexapole are shown in Figure [8.11](#) at alternating voltages of ± 4 kV.

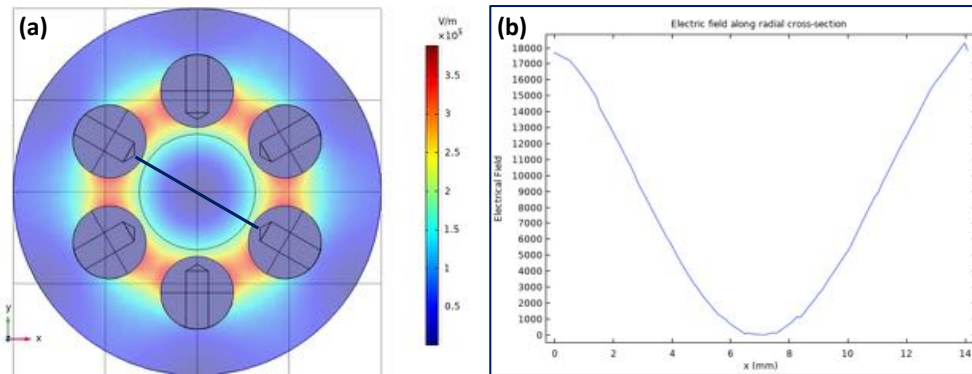


Figure 8.11: **(a)** Electric fields simulated by COMSOL[\[20\]](#) for a standard operating of voltages in our linear hexapole. Here, alternating voltages of ± 2 kV and the resulting electric fields, are shown. **(b)** A graph of the electric field versus distance (mm) along a transverse line across the hexapole (marked in blue on (a)). This plotted field distribution demonstrates the harmonic nature of the field's dependence on r .

8.2.2 Hexapole Transmission Simulations

There are a few reasons to simulate the dynamics of the hexapole lensing on our molecular beam. Firstly, we want to relate the relative ion signal at our MCP for various final output velocities to the relative density that intersects with our Coulomb crystal. Confidence in an accurate assessment of the relative densities at different final decelerator voltages is imperative for an assessment of reaction rate constants. In addition, computational results can yield parameters that are difficult to measure, such as the transverse velocity spread at the center of the trap; this information is required to calculate the energy resolution of our setup. A third reason to simulate the hexapole lensing is more practical in nature: efficient lensing of ND_3 in a hexapole depends on multiple factors, including the peak voltages, the time the hexapole is turned on, and the time it is turned off. This is a wide parameter space to explore, particularly for multiple final velocities. Simulations can help narrow the empirical search for optimized hexapole settings by exploring the optimum parameter space computationally. These computational searches can be done in parallel to empirical studies, and can be faster.

These aforementioned computational simulation software is a MATLAB program initially built by James Greenberg and further developed by Chase Zagorec-Marks and myself. It uses Equation [8.6](#) to calculate the force on the molecules as they proceed through a hexapole of our parameters. The initial spatial and velocity distributions of the ND_3 molecules are taken from results of numerical decelerator simulations.[\[16\]](#) The hexapole simulation program tracks where each molecule ends its trajectory, categorizing the molecules by their “fate,” or where they are lost. We are most interested in the molecules that reach the center of the trap within the expected area of a Coulomb crystal, as well as the molecules that are transmitted between the trap rods. Because we are not yet sure that our laser is detecting molecules at the exact center of the ion trap, it is possible that our experimental measurements of the hexapole output is a combination of the two distributions. We hope to implement a more rigorous alignment procedure of the laser when experimental measurements are resumed, as will be discussed later.

Simulations at multiple final velocities have yet to sufficiently reproduce experimental data. The partial, qualitative agreement that the simulation has shown thus far is best described by Figure 8.12. This figure demonstrates hexapole voltages set to ± 1.8 kV with a variety of times that the hexapole is quickly (< 50 ns) pulsed on. This pulsing technique allows molecules with larger velocities to move closer to the edge of the hexapole before the fields turn on. [335] Empirically, we see two distinct peaks in signal at two different turn on times, 0.6 ms and 1.7 ms. When we simulate the hexapole trajectories at this time, we see a gradual decrease in the ND₃ signal between the trap rods as a function of turn on time. When the scope is narrowed to a Coulomb crystal as a target (~ 100 μ m by 0.5 mm), there is only a single peak in the signal around 1.7 ms after the ND₃ leaves the decelerator.

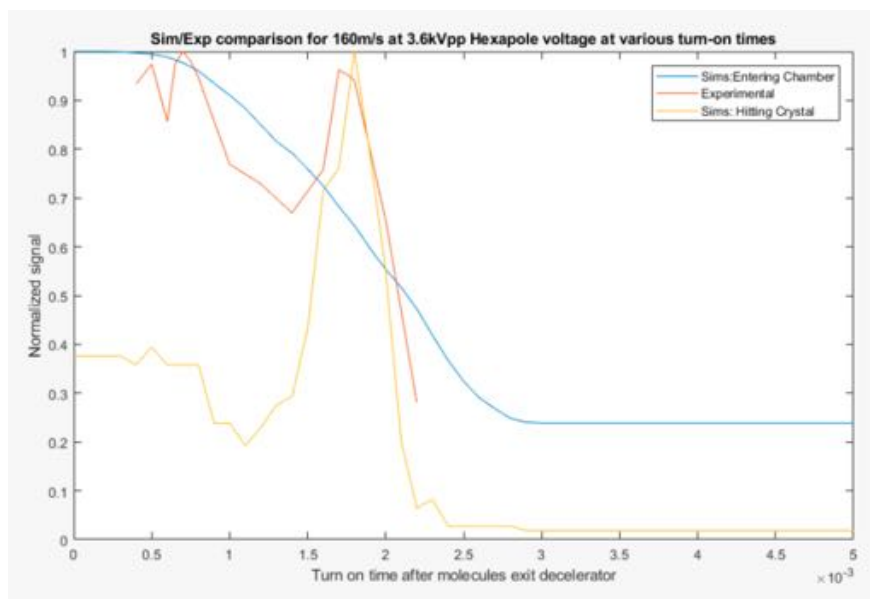


Figure 8.12: Expected and measured relative ND₃ signal for 160 m/s final velocity at 3.6 kV_{pp} at various voltage turn-on times. Simulations predict peak density within the trap rods when held on (blue), while predicting a single peak in signal at ~ 1.7 ms at the Coulomb-crystal sized (~ 100 μ m by 0.5 mm) center of the trap (yellow.) Empirical measurements (orange) show something somewhat different from either and similar to both.

There are a few possible reasons for this discrepancy in the simulated and experimental signal. One possible cause is poor laser alignment to the center of the trap. We have been aligning

the laser to the highest ion signal at the MCP. However, the maximum signal at the MCP is extremely sensitive to the rod voltages and the Einzel lens voltages, as may have been evident from section [8.1.3](#). This presents ample opportunities to find a local maximum of what is effectively five dimensions of parameter space. In this case, we may be effectively optimizing the hexapole settings for peak signal slightly above or below the center of the trap. We propose new alignment procedure to avoid this problem in the future.

During the last amplifier retrofit, Chase Zagorec-Marks and I started developing a plan to align the ND₃ ionization laser to the Coulomb crystal position. This alignment procedure was inspired by that of the sister Lewandowski experiment across the hall, the OHRbIT experiment. [\[321\]](#) This procedure consists in rerouting the 317 nm REMPI laser along a 397 nm beam path, such that we can be assured of our alignment of the ionization laser to the current ion crystal position. Then, the trap rod and Einzel lens voltages will be scanned to optimize the detection of the decelerator signal. This will assure that we are detecting ND₃ signal at the current position of the Coulomb crystal. If this procedure is done without the hexapole lensing, there is further assurance that there is no complications from under or over-focusing the neutral beam by the hexapole. This would achieve the most important result: an assurance that we can know the relative density at the position of our reactant ions.

However, it is possible that the peak decelerator output and the center of the ion trap are not in perfect alignment. Given the long length of the decelerator and hexapoles, as well as slight imbalances in the trapping fields, this is not impossible. A secondary goal could be to also improve the decelerator density at the location of the center of the trap. While the decelerator output cannot be moved in two of the three directions, the DC trap shims allow some movement of trapped ions in all three. A possible extension to the alignment procedure would be to scan the ND₃ REMPI laser from 397 nm path, looking for higher signal. If the signal increases dramatically, the new 317 nm REMPI beampath can be replicated by the 397 nm cooling lasers. Then, the DC shims can be adjusted to move the ions to peak fluorescence along the new cooling laser beampath. This does present some challenges, however. The current DC shim settings are adjusted for the lowest

micromotion, and thus the coldest ion crystal. It is possible that to align to higher decelerated ND_3 may require heating of the ions. This trade-off is difficult to assess until we know more about the approximate density of the decelerated molecular beam.

An additional complication in pursuing a global maximum of the signal is the rather complex multi-parameter optimization incurred by the unorthodox TOF behavior from the trap rods that was discussed in section [8.1.3](#). Every axis has a different sensitivity to the trap rods voltages, Einzel lens voltage, the hexapole lensing voltages, the hexapole voltage timings and the DC shim voltages on the trap. A optimization of the Coulomb crystal position at the maximum deceleration signal would require extreme care and fastidious methodology. At all times, there would need to be care to distinguish between measuring a more dense part of the ND_3 beam and measuring higher transmission from the trap to the MCP; this is not trivial. Unless there are strong indications that the density intersecting with the Coulomb crystal can be improved by at least a factor of 2, I would recommend against pursuing this course of action. The necessity of this level of optimization necessary is unclear, as we have no reason to believe the two systems are misaligned. However, ensuring appropriate detection of the beam at the ion crystal location is critical. This verifies we are measuring the relative ND_3 signal at multiple velocities at the position of the Coulomb crystal. This is to arrive at firm conclusions about reaction rates as a function of collisional energy, as well as arrive at the best hexapole configuration for each final velocity.

Another possible cause for the simulation discrepancy is inaccuracies in the measurements of the beamline. A few of these measurements are very well known, but many are based on CAD simulations or photographs from the Big Build. Any opportunity to measure these numbers more accurately would aid these simulations. The dimensions of the hexapole, as well as the various lengths and radii in the beam path, are critical for accurately simulating the dynamics of the hexapole. These measurements are included with their source in Table [8.2](#).

There are a few other factors that should be considered. A possible reason for the discrepancy could be due to the idealized fields that we are simulating. The equations in section [8.2.1](#) described idealized hyperbolic rods, from which there may be discrepancies, especially near the rods. Another

Table 8.2: Direct, indirect, and CAD measurements of lengths relevant to TWSD-Hexapole-LIT beampath. Indirect measurements are based on photographs that include features with well-known measurements. All measurements in millimeters.

Measurement	Direct	Indirect	CAD
Distance from decelerator to hexapole front cap	22.0		
Hexapole upstream cap thickness	2.0		
Hexapole upstream cap radius	3.8		
Shutter radius	3.0		
Distance from inside of upstream hexapole cap to edge of hexapoles		26.7	
Distance from inside of upstream hexapole cap to shutter	5.0		
Hexapole length	367		
Hexapole inscribed radius	7.0		
Distance from end of hexapole to inside of downstream cap			1.6
Hexapole downstream cap thickness			2.54
Hexapole downstream cap radius			3.8
Distance from downstream cap to edge of trap rods		13.0	
Diameter of trap rods	9.0		
Distance between trap rods	3.0		

idealization is that the forces are experienced on the molecules while in the length of the hexapole, but these fields are modeled as completely absent on either side. It is possible that fringing fields on the input and output of the hexapole could be leading to behavior not modeled by our simulation code. Both of these possibilities could be tested with the simulation of the hexapole fields by cylindrical rods of our dimensions with a finite element simulation program like COMSOL. Another possible issue could be with inaccuracies of the decelerator output simulations, although we have no reason to believe this is the case. A possibility that we have already explored is the integration step size in the hexapole simulations. The calculations are done with a variable-step discrete solver, which reduces the step size until subsequent solutions vary by a value less than a pre-set error tolerance. I manually set the relative and absolute tolerances up to three orders of magnitude smaller than the prior values. The changes in the simulations were no more than the expected of statistical variations already seen at less strict tolerance. At this time, we do not think the inaccuracy of the simulations is due to insufficiently small time step size of the numerical solver in MATLAB.

Although the hexapole simulation program has not quantitatively reproduced our experimen-

tal measurements, they have facilitated insight into the general principles and behavior of a focusing hexapole on ND_3 . One example is that we were able to identify the existence of “harmonics” in the particle trajectories through the hexapole. Because the molecules enter the hexapole with a relatively localized spatial distribution, the path that produces the greatest density at specific point on the other side can be visualized as a standing wave. An analogous “fundamental” mode is reached first, followed by higher harmonics at higher voltages. This is shown in Figure 8.13.

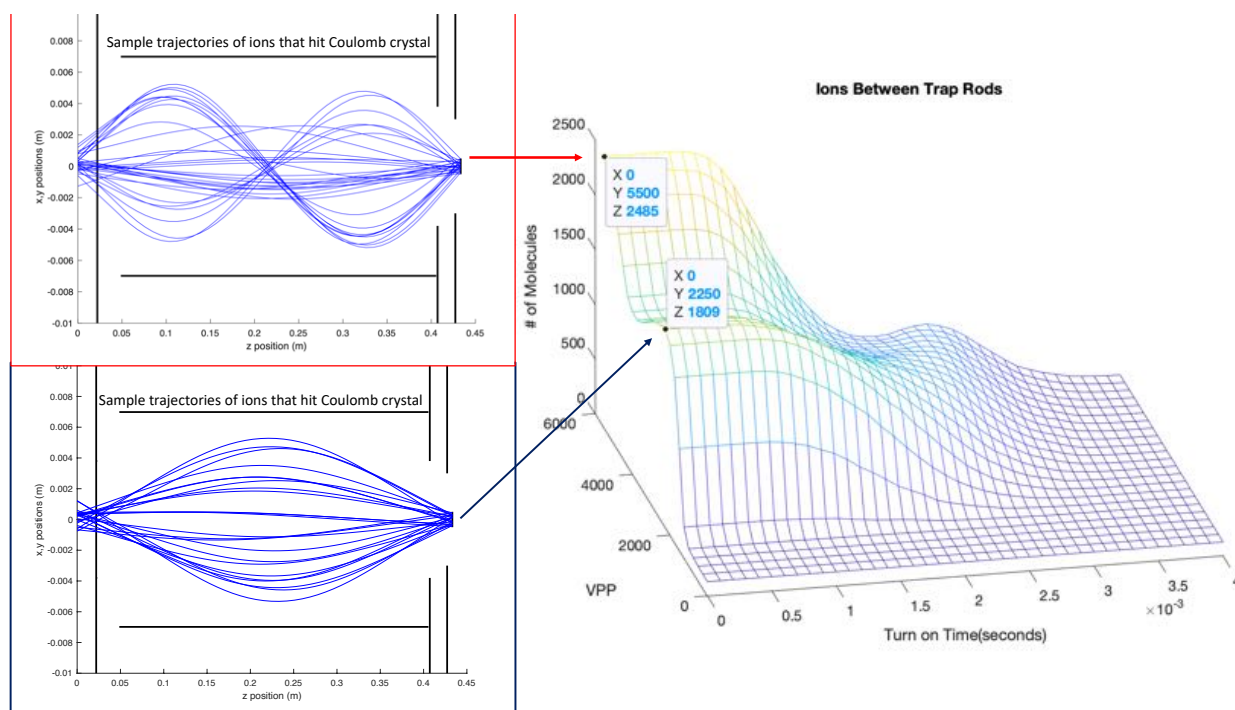


Figure 8.13: Results from hexapole simulations. On the right, a 3-D graph showing the number of ND_3 molecules that successfully reach between the trap rods, as a function of the hexapole peak-to-peak voltage, and turn-on time of that voltage (in this case, the voltage stays on well past the removal of molecules from the fields.) This results predict the highest transmission of ND_3 molecules with an immediate implementation of voltage. There are two peaks in signal associated with a “fundamental” (at ± 1125 V) and first “harmonic,” (at ± 2250 V) as shown by the trajectories sketched on the left. These trajectory graphs are projected against the xz plane, where z represents the long axis of the hexapole (entering on the left and hitting the crystal on the right) and x is represented by the long axis of the trap. On the far right the hexapole cap radii and crystal size are represented by black lines.

These simulations also allow us to examine the transverse and longitudinal spreads of the molecules. These computed velocity spreads will be used to calculate the collision energy and

uncertainty for the different decelerator velocity output. An important result from these simulations is that the velocity spread in the transverse and longitudinal directions for the hexapole output is nearly equivalent to those of the decelerator output. This is shown by the hexapole and decelerator output data and Gaussian fit shown in Figure 8.14. This result has been verified for both harmonics of the 160 m/s output. The longitudinal velocity spread depends on the final velocity, becoming more narrow at more aggressive deceleration (section 7.1.3-7.2.) Once the final hexapole settings are determined, these calculations can be checked for all final velocity outputs that will be used for reactions.

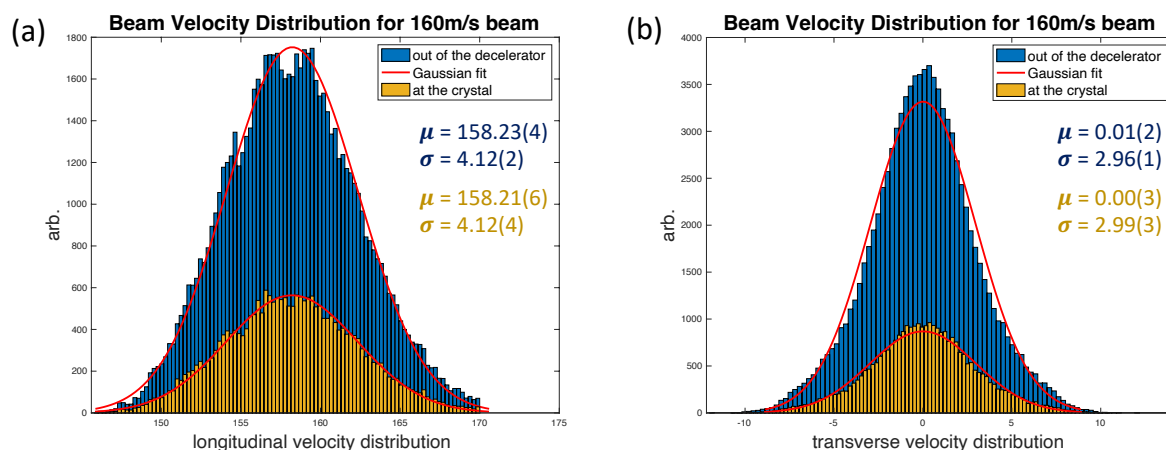


Figure 8.14: Spread in decelerator (blue) and hexapole (yellow) outputs for 160 m/s outputs. Particles are binned in 100 bins and fitted to Gaussian distributions. The average and standard deviation are reported for (a) longitudinal and (b) transverse velocity spreads. The uncertainty represents the 95% confidence interval.

In summary, these simulations have demonstrated qualitative trends in the ND_3 transmission signal as it depends on the timing and magnitude of the voltage on the hexapoles. However, these results are still not yet quantitatively reproduced by experimental measurements. Once the reasons for this are determined, these simulations can be used to support our knowledge of the velocity spreads, and thus energy resolution, in the reaction studies. For the time being, the results we do have from the simulations will be used to approximate the collision energies in section 8.3.1.

8.3 To-date output at the decelerator and outlook

At the time of this dissertation, there has also been significant empirical work to optimize the hexapole lensing. Empirical optimization has been achieved for 200, 160, 120, 100, 80, and 60 m/s. Experimentally detected molecules for each of these velocities is shown in Figure [8.15](#). Exploration of possible voltages and timings were partially complete for 40 m/s and 20 m/s before the last amplifier breakdown. A *bunching after deliberately, aggressively, Stark slowing* (BADASS) scheme for 240 m/s has yet to be determined and optimized. Once characterization of the decelerator output is resumed, the ionization laser should re-aligned to the decelerator beam with the aforementioned laser alignment procedure to ensure proper alignment to the Coulomb crystal. From there, it should be verified that the previous empirically optimized timings and voltages are still the optimum procedure. If this is not the case, then tweaking of these settings will be necessary. Once the hexapole settings are set, then the shutter can be added. Then the integrated experiment will be ready for reactions. The scope and energy resolution of these reactions will be determined by the velocity resolution of both the decelerator and the ion crystal. The next section will review equations that calculate the attainable energy range and resolution in this system, particularly for the first proposed reaction of $\text{NH}_3^+ + \text{ND}_3$.

8.3.1 Calculating center-of mass energies for RT gas or decelerated beams

This section will utilize the equations developed in section [3.1.3](#) to specifically calculate feasible center-of-mass collision energies for the reaction of $\text{NH}_3^+ + \text{ND}_3$. The relevance of this particular reaction will be developed in the following section. These calculations yield expectations for the energy range that will be achievable in this setup, drawing on simulated energy distributions as a resource for calculating the collision energies. In addition, this section should guide similar calculations for other trapped-ion and decelerated-molecule combinations.

In section [3.1.3](#), I demonstrated that the kinetic energy in the center-of-mass frame of a

decelerated ammonia detected at the ion trap with hexapole guiding detected at ion trap

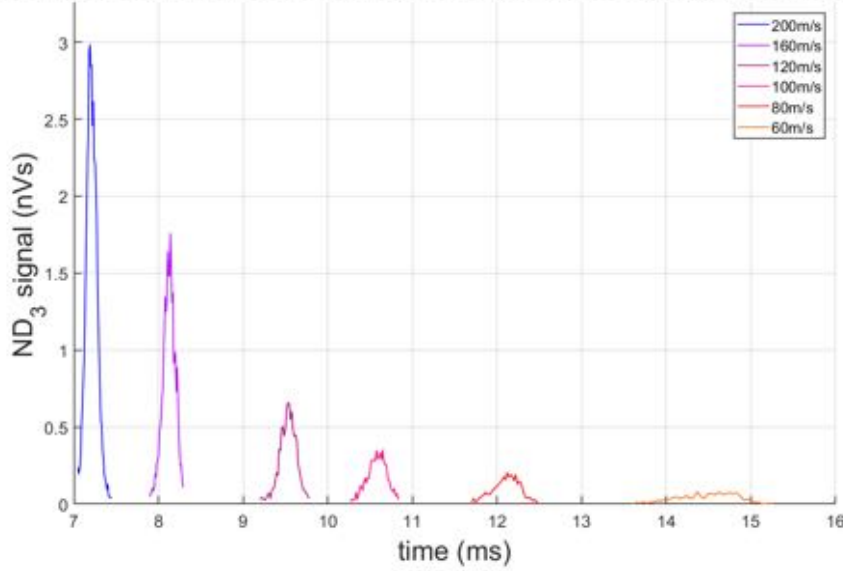


Figure 8.15: ND_3 detected at the ion trap for multiple final velocities at their respective empirically optimized hexapole-lensing parameters. Note that the distinct wells that were evident in the decelerator output data are no longer distinct. This is due to the additional ~ 0.5 m length over which the longitudinal spread in velocities blurs the physical separation of the distinct wells.

collision could be described by the convolution,

$$\langle KE \rangle = -\frac{1}{2}\mu \int_{-\infty}^{\infty} dv_{rel} v_{rel}^2 \int_{-\infty}^{\infty} dv_2 g(v_2) f(v_2 - v_{rel}) \quad (8.9)$$

This can be expanded to three dimensions. In the special case that all three are Gaussian distributions, this convolution takes the form,

$$\langle KE \rangle = -\frac{1}{2}\mu \prod_{u=1}^3 \left(\frac{1}{2\pi\sigma_{u,D}}\right)^{1/2} \left(\frac{1}{2\pi\sigma_{u,I}}\right)^{1/2} \int_{-\infty}^{\infty} dv_{u,rel} v_{u,rel}^2 \int_{-\infty}^{\infty} dv'_u \exp\left[-\frac{(v'_u - v_{u,rel} - v_{u,I})^2}{2\sigma_{u,I}^2}\right] \exp\left[-\frac{(v'_u - v_{u,D})^2}{2\sigma_{u,D}^2}\right] \quad (8.10)$$

Here, the u denotes the cartesian coordinates $\{x, y, z\}$, and $v_{u,I}$ and $v_{u,D}$ are the center velocities for the ion and decelerator distributions for their corresponding coordinate, respectively. Likewise, σ represents the standard deviation of the velocity distribution for ions and decelerated molecules for each coordinate. In this case of convolution of Gaussians, the final distribution will have an

uncertainty that is the square root of the sum of the squares,

$$\sigma_{\text{total}}^2 = \sum_{u=1}^3 (\sigma_{u,I}^2 + \sigma_{u,D}^2) \quad (8.11)$$

I have built a Mathematica code to compute this convolution, which is included in Appendix [B](#). It is currently built to use Gaussian standard deviations to describe the spread of both the ions and decelerator outputs. For the moment, Gaussian distributions are a sufficient approximation for calculating conceivable collision energies. However, once the final reaction settings are determined, the most updated simulations can provide more accurate distributions. The code can be easily altered to accommodate another distribution, or even numerical simulation results, should this be required for sufficient accuracy.

To compute the convolution in Equation [8.10](#), we will need the average value and standard deviation for the ions and decelerated molecules in all three dimensions. Figure [8.14](#) demonstrated the transverse and longitudinal velocity, with a Gaussian fit reporting the mean and uncertainty out of the hexapole lens. These values are reproduced in Table [8.3](#). In addition, we need the velocity distributions for the ions. For this, we turn to the molecular dynamics simulations described in section [2.1.5](#).

Simulations were conducted for 200 NH_3^+ ions trapped within 1000 Ca^+ ions at 400 V_{pp} RF voltage and an endcap voltage of 3 V. The large number of Ca^+ and the large RF trap depth both promote ammonia trapped at a relatively small radius in the trap. Near this center axis of the trap, the micromotion heating is minimal and the ammonia ions accordingly have a narrower range of velocities. The simulated axial and radial velocities are shown in Figure [8.16](#). The top panel corresponds to a crystal with additional heating from the background collisions of $\sim 10^{-9}$ Torr of helium. [\[125\]](#) The bottom panel corresponds to a much more aggressive amount of heating, about one hundred times larger. The particularly cold crystal can be qualitatively seen as moderately sharp crystal image, as seen in the picture on the top panel. This is associated with very orderly structure, such that the radial velocities bunch around three values, associated with three well-defined spatial shells in the ellipsoidal crystal. At higher heating, the image is blurred, and the

crystalline structure of the ammonia is perturbed enough to blur the radial velocity to a Gaussian-like distribution, as shown by the bottom panel. While the top image qualitatively resembles our crystal structure, I will use the results from the warmer crystal as an upper limit to the ion energy spread.³ It is quite possible the final optimum settings for the experiment, and the effective ion temperatures, will be slightly different for the final reaction settings. These simulations have been very well documented by Andés and can be revisited for more accurate simulations when final reaction measurements take place.^[6]

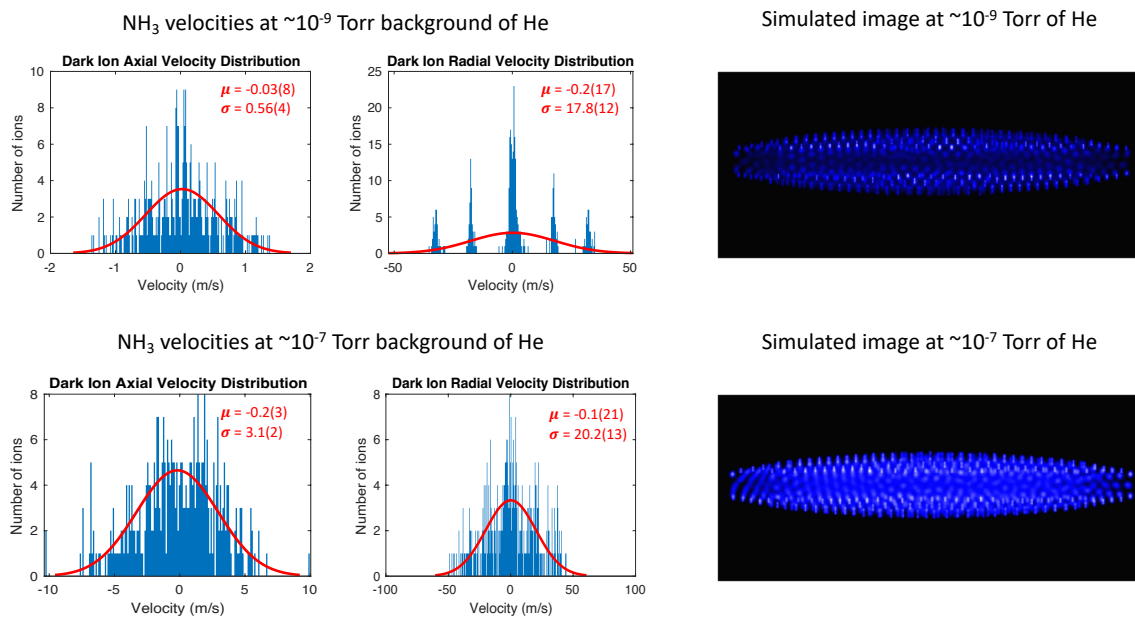


Figure 8.16: ND₃ detected at the ion trap for multiple final velocities. The distinct shells that were evident in the data from the decelerator output are no longer distinct; this is due to the additional ~ 0.5 m length over which the longitudinal spread in velocities blurs the physical separation of the distinct wells.

These Gaussian fits, combined with those already reported for the hexapole, are reported together in Table 8.3. Note that only the 160 m/s results are reported here. The transverse spreads are not expected to vary much for different final velocities. While the longitudinal spreads do

³ While we have empirically seen that pressures at 10^{-7} Torr will melt a crystal, we also notice that the simulations underestimate the time-averaged motion or “blurriness” of the Coulomb crystal at the pressures we read on our ion gauges. Likely we have heating in our trap from imperfect RF trapping fields. This upper limit image and ion energies represents some of the warmest ions we can maintain trapped in a Coulomb crystal, regardless of the heat source.

depend on the final velocity, LPSA models can predict the maximum spread for all final velocities. These spreads for our final velocities suitable for reactions are reported in Table 8.4. For the purpose of this preliminary calculation, I will use longitudinal spreads that were numerically calculated for 160 m/s, normalized by the maximum allowance given by the LPSA model. This is motivated by an assumption that the relative filling of the phase space relative to the LPSA does not depend on final velocity. This is supported by the results in section 7.2, where the relative signal for different final velocities that was measured directly out of the decelerator matched the expectations put forward by this LPSA-based model.

Table 8.3: Velocity distribution standard deviations for ion and hexapole simulation results. The hexapole output fits are shown in Figure 8.15 and the ion fits are shown in Figure 8.16. The uncertainty represents the 95% confidence interval in the Gaussian fit. The x axis corresponds to the decelerator beam propagation, and the z axis corresponds to the trap axial direction.

	v_x	v_y	v_z
Hexapole Lensing at 160 m/s	4.12(2)	2.99(3)	2.99(3)
Ions at 400 V_{pp} with minimal background collisions	17.8(12)	17.8(12)	0.56(4)
Ions at 400 V_{pp} with significant background collisions	20.2(13)	20.2(13)	3.1(2)

Table 8.4: Maximum longitudinal spread in velocities of ND_3 wells at end of decelerator, as calculated by the LPSA model. The Gaussian spread, which will be used for final energy calculations, will be less than this and depends on how the phase-space distribution overlaps with the phase-space acceptance of the decelerator.

v_f (m/s)	Δv (m/s)
240	15
200	13
160	12
120	11
100	11
80	10
60	10
40	10
20	10
10	10

These input distributions were used to calculate the convolution described in Equation 8.10, computed by the code in Appendix B. From this, a center-of-mass average “temperature,” (E/k_b),

can be established. This average temperature and its uncertainty are reported in Table [8.5](#). Note that this uncertainty is for the determination of the average collision temperature, not the resolution associated with the spread in velocities. The most dominant contribution to the standard deviation in velocities is the radial velocities of the trapped ions due to micromotion heating. Equation [8.11](#) demonstrated the total spread associated with this convolution of two Gaussian distributions in three dimensions. The total spread can be related to an effective temperature by using the definition of temperature from the Gaussian profile of M-B gas in one dimension.

$$T_{\text{res}} = \frac{\mu\sigma_{\text{tot}}^2}{k_b} \quad (8.12)$$

In the case of significant background collisions, (as defined by Figure [8.17](#).) this resolution is 1.0 K. In the case of minimal collisions, this number is 0.8 K.⁴ This means that with the current range and approximation of velocity distributions in our system, velocities below 20 m/s will not have distinguishable reaction rates from each other. This limit could feasibly be pushed by considering lower NH_3^+ ion numbers, possibly even a string of ions along the radial trap axis. This would provide a much narrower distribution of ion radial velocities, but at the cost of reactant population. At this time, it is unknown what the density out of the decelerator is, and thus what time scales will be necessary to observe reactions. Reducing the number of ions by at least an order of magnitude will be necessary to produce minimal micromotion. Depending on the TWSD output density and the required reaction times, this avenue may or may not be feasible.

These calculations demonstrate the span of collision energies than can be accessed for this reaction.

8.3.2 First reaction proposal: $\text{NH}_3^+ + \text{ND}_3$

There are a few reasons that the reaction of $\text{NH}_3^+ + \text{ND}_3$ is an excellent first reaction for our setup. We are somewhat constrained by the convenience of using ND_3 as the neutral reactant, and

⁴ Technically this resolutions depend on the longitudinal velocity, but these variations impact the hundredths place of the resolution.

Table 8.5: Final calculated E/k_b “temperatures” for a selection of final decelerated velocities. The uncertainty in the center temperature is included, while the temperature resolution is based on the spread of the velocities.

Velocity	E/k_b
240	35.2(1)
200	24.6(1)
160	15.9(1)
120	9.2(1)
100	6.5(1)
80	4.4(1)
60	2.7(1)
40	1.5(1)
20	0.8(1)
10	0.6(1)

the benefits of an ion with $m/z < 40$ (such that they sit inside the Ca^+ and experience minimal micromotion heating.)

Reactions of ionized ammonia with neutral ammonia has been abundantly studied in a variety of apparatuses, including some capable of temperature-dependent studies. Such a well-studied reaction presents opportunities for comparison, possibly allowing “benchmarking” of our absolute reaction rate constant and densities of the ND_3 beam. There have been multiple measurements of the reaction of $\text{NH}_3^+ + \text{NH}_3$ in a variety of experimental apparatuses This includes ICR, [360, 100, 22] flowing afterglow, [361, 362] free jet flow reactor, [23], SIFT, [363] and mass spectrometry. [364, 365, 21, 366, 367] In some cases, this reaction was explicitly investigated; in others, it was a characterized background reaction. As such, there is wide range of measured thermal, room-temperature $\text{NH}_3^+ + \text{NH}_3$ reaction rate constants from multiple experiments. A selection of these are included in Table 8.6. These values have a distinct spread in the measured values, but are all reasonable close to the value expected by ADO theory, $1.6 \times 10^{-9} \text{ cm}^3 \text{ s}^{-1}$.

These reported thermal measurements and calculations generally show good agreement with each other, all reporting the same ion product, ammonium ion (NH_4^+ ,) and its implied neutral product, NH_2 . The strengths and weakness of these reaction systems complement each other well. The SIFT and FA measurements tend to be at higher ($\geq 10^{-4}$ Torr) pressure. Some of the

Table 8.6: Rate constants at thermal temperatures in a variety of experimental setups. Uncertainty is given when reported in source. All measurements and calculations refer to $\text{NH}_3^+ + \text{NH}_3$ reaction unless stated otherwise

Experiment or theory type	rate constant [$\times 10^{-9} \text{cm}^3 \text{s}^{-1}$]
selected ion flow tube [363]	2.21(42)
mass spectrometry [366]	1.3(1)
mass spectrometry [21]	1.81(10)
ion cyclotron resonance [22]	1.3(4)
ion cyclotron resonance [360]	1.9(2)
ion cyclotron resonance [100]	1.55(8)
flowing afterglow [362]	1.7(5)
flowing afterglow [361]	2.5(5)
Langevin theory	1.16
ADO theory	1.63
Langevin theory ($\text{NH}_3^+ + \text{ND}_3$)	1.16
ADO theory ($\text{NH}_3^+ + \text{ND}_3$)	1.56

early flowing afterglow (FA) measurements may have some contributions to the rate constant from reactions with excited NH_3^+ . Many of the studies report background reactions of co-produced NH_2^+ with ammonia, which forms NH_3^+ and NH_4^+ . [\[360\]](#), [\[21\]](#), [\[22\]](#) A measurement of this reaction in a Coulomb crystal has not been published, which is already a reason it would be interesting to measure and compare. Further, the ability to clean out contaminants in the loading and ensure their ground state relaxation will be a benefit. However, on the whole, this reaction could benefit from comparison to measurements in a Coulomb crystal.

A few studies have reported the temperature dependence of the reaction. Two studies measured reaction rates at energies up to a few eV with distinct ion detection methods. In a mass spectrometry (MS) study, the ion energies ranged from 8 eV down to thermal energies by propelling ions with high voltage from an ionization region into a high-vacuum chamber designed for collisions. This MS study demonstrated a reaction rate constant that was inversely proportion to ion energy, reporting a peak reaction rate constant at the lower limit of the collision energy. [\[21\]](#) These data were fit with an ADO-like cross section to good agreement, as seen in Figure [8.17a](#). A similar measurement was made in an ICR cell, where ions were heated up to kinetic energies of 3 eV. The largest reaction rate constant was found at thermal energies, in correspondence to

the MS experiment. Figure 8.17b shows the reaction rate (k_1) normalized to its values at thermal energies, plotted with the background reactions of $\text{NH}_2^+ + \text{NH}_3$ (k_2 and k_3). The source of the fits are unclear from the original paper. [22] The energy ranges of both of these studies are much higher than the expected effective range of our future experiment. However, these studies do indicate behavior expected from a dipolar molecule by ADO and Su-Chesnavich theory, which were discussed back in section 3.1.2. The suppression of the rate constant at higher velocities is predicted by these theories, which effectively argue that the dipole moment enhances the reaction rate over the expected Langevin rate. However, the ability of dipole moment to “lock” and enhance the rate constant depends on the center-of-mass collision velocity. When applied to Maxwell-Boltzmann distributions, this dependence is a $T^{-0.5}$ dependence.

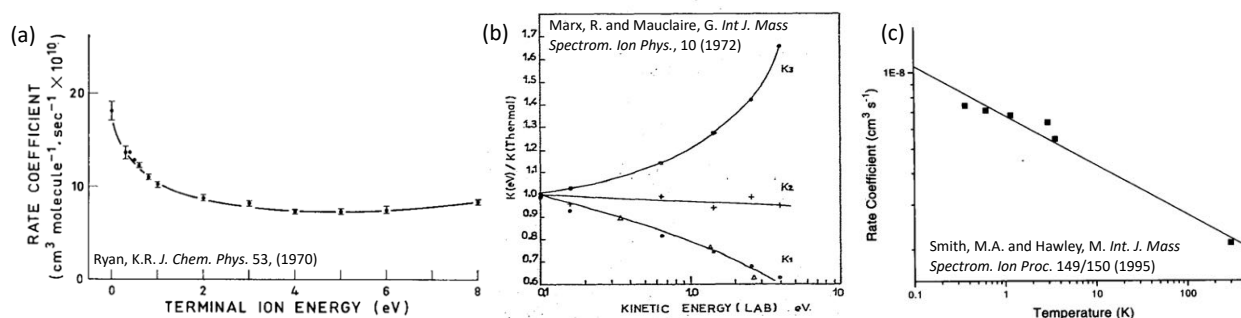


Figure 8.17: Three prior studies demonstrating energy dependence of the $\text{NH}_3^+ + \text{NH}_3 \rightarrow \text{NH}_4^+ + \text{NH}_2$ reaction rate constant. (a) Mass spectrometry measurements from thermal energies to 9 eV kinetic energy. Figure adapted from Ryan (1970). [21] (b) ICR measurements from thermal energies to 3 eV. Figure adapted from Marx (1973). [22] (c) Free jet flow reactor measurements with rotational temperatures from 12-20 K, and translation temperatures equivalent to 0.4-4 K. The thermal data point is an average of literature values. Figure adapted from Smith (1995). [23]

In the case of a free jet flow reactor study by Smith et al. in 1995, measurements of the $\text{NH}_3^+ + \text{NH}_3$ reaction rate constant were conducted by producing supersonic gas expansions of NH_3 seeded in an atomic or molecular buffer gas. [23] These ammonia molecules were ionized with a REMPI scheme that left them in the ground state, after which they flowed undisturbed in a field-free region and reacted with neighboring neutral species. The thermal conditions were determined by those of the free jet core, which was measured to have rotational temperatures equivalent to 12-20 K. The

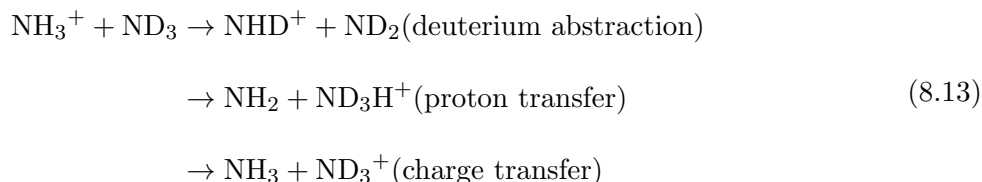
translational energies were tunable over the range of 0.4-4 K, depending on the buffer gas species. The resulting dependence of the reaction rate was plotted with respect to temperature, as shown in Figure 8.17c. Five points within the translation range are fit to a log plot, with a data point at 300 K that is the average of three thermal measurements from other systems. [363, 361, 100] The fit in this graph corresponds to a best fit line of $2.1(6) \times 10^{-9} \left(\frac{T}{300}\right)^{-0.21} \text{cm}^3 \text{s}^{-1}$. This fit does have an inverse dependence on temperature, but not quite the expected $T^{-0.5}$ dependence. It is possible the dipole enhancement effects are not as evident due to the broader rotational temperatures, which exceeded those of the translational temperatures.

From a kinetics perspective, the proposed $\text{NH}_3^+ + \text{ND}_3$ reaction has an interesting place in the context of this prior research on ammonia-ammonia ion-neutral reactions. As mentioned before, the extensive measurements of thermal rates allow some firm expectations on the measured reaction rate constant at room temperature. In addition, we can compare our 1-40 K results with the low-temperature results of Smith et al. (although the rotational temperatures will be different.) One important contrast from all the aforementioned reaction studies is that our proposed reaction is with a different isotopologue.

The isotopologue combination has important ramifications for identification of competing reaction mechanisms. The $\text{NH}_3^+ + \text{NH}_3 \rightarrow \text{NH}_4^+ + \text{NH}_2$ may technically proceed as a proton transfer or a hydrogen abstraction, and both are identified as NH_4^+ . In addition, charge exchange is energetically possible, but experimentally undetectable without isotope substitution. For the reaction of $\text{ND}_3^+ + \text{NH}_3$, SIFT experiments showed a branching of 0.85 to products $\text{NH}_3\text{D}^+ + \text{ND}_2$ and 0.15 to $\text{ND}_3\text{H}^+ + \text{NH}_2$. This has suggested the precedence of proton transfer over hydrogen abstraction in the ammonia ion reaction with ammonia. [363]

Our proposed reaction is split into three possible products, each of which associated with a

unique reaction mechanism:



To my knowledge, there are two groups that have studied our proposed isotopologue combination. One group is that of Shinji Tomoda in Japan, who studied the reaction with TESICO (threshold electronsecondary ion coincidence) measurements, with accompanying theory. [368, 369] The second is the group of Richard Zare at Stanford, where the reactions were conducted with a guided ion beam setup. [370, 24] Both groups studied the dependence of the translational energy and vibrational excitation of the ν_2 “umbrella mode.” While slight discrepancies in the studies exist at high kinetic energies (≥ 3 eV,) the results agree well at low temperatures, and the insights regarding the reaction mechanisms are in agreement.

I will primarily focus on the most recent measurement, which is one of the guided ion beam experiments conducted by Posey et al. in 1994. [24] While they did not measure a reaction rate constant, their reported branching ratio dependence on internal and external energy is noteworthy. Figure 8.18(left) demonstrates the dependence of the branching ratios on vibrational excitement. The excitation of the ν_2 vibrational mode correlated with an enhancement of the deuterium abstraction and a suppression of the proton transfer. This is consistent with a mechanistic model in which the deuterium abstraction is facilitated by out-of-plane bend of the planar NH_3^+ to abstract a deuterium atom from the neutral ND_3 . A possible intermediate complex for such a mechanism is sketched in Figure 8.18d. In the case that a proton is transferred from the ion to attach to the exposed lone pair on the neutral ND_3 (Figure 8.18e), excitation of the umbrella mode would be orthogonal to the active reaction coordinate. This model is consistent with suppression of this product branching with increasing vibrational excitement. [24, 368, 369] In the case of charge exchange, the addition of both internal and external energy is expected to increase the charge transfer cross-section, as there is expected to be a small barrier to nearly isothermal charge transfer process.

The dependence on vibrational excitation support these proposed reaction mechanisms, although the absolute branching ratio comparisons require more computational and experimental work for rigorous assessment.

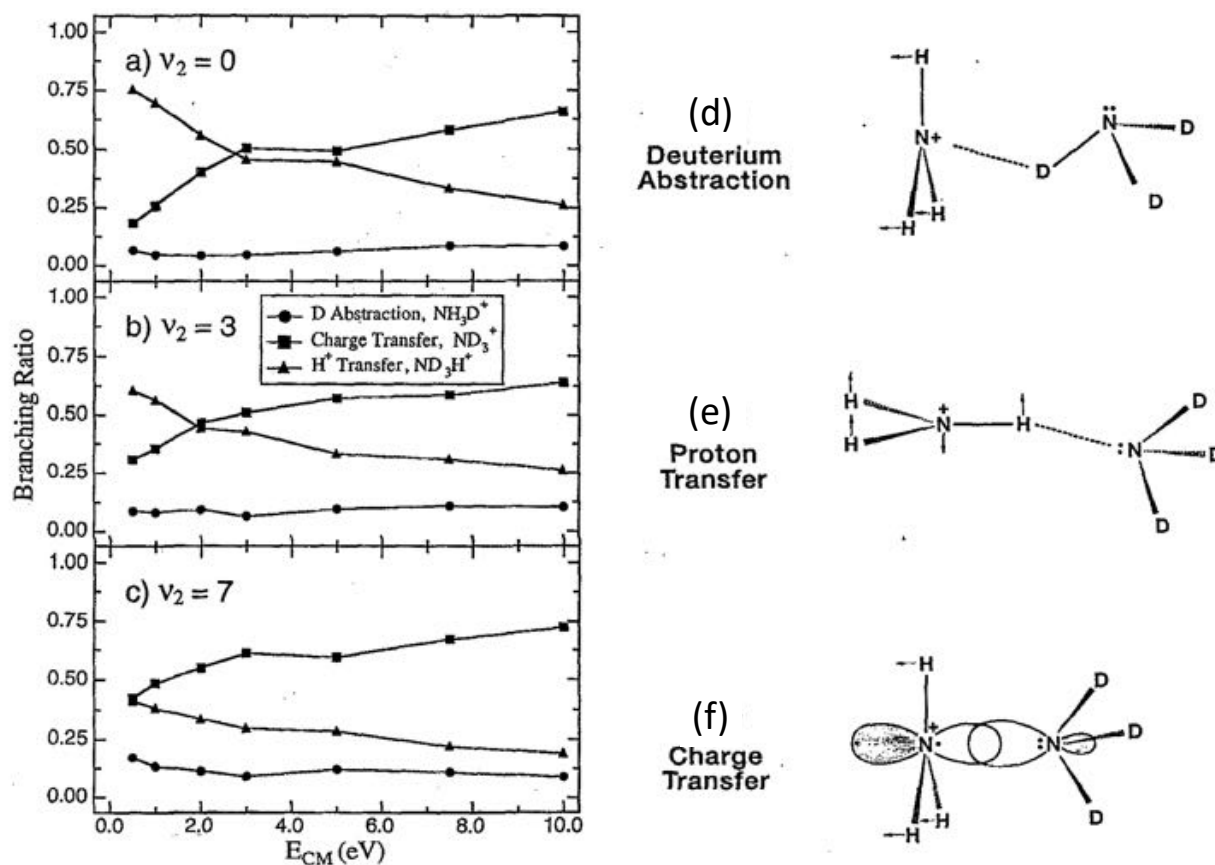


Figure 8.18: **(left)** Branching ratios for the three products of $NH_3^+ + ND_3$ as they depend on vibrational excitation and kinetic energy. **(a)** With vibrationally relaxed NH_3^+ , the proton transfer product is enhanced at thermal kinetic energies. Conversely, the charge transfer product is significantly enhanced at higher energy. The deuterium abstraction is relatively independent of kinetic energy. **(b,c)** The aforementioned trends persist with the excitation of the ammonia umbrella mode. Overall, the proton transfer mechanism decreases with vibrational excitation, while the deuterium abstraction and charge transfer cross-sections increase with increasing internal excitation. **(right)** Illustrations of possible direct models for **(d)** deuterium abstraction, **(e)** proton transfer, and **(f)** charge transfer. Figure adapted from Posey (1994.)[\[24\]](#)

There are a few places that a reaction in our Coulomb crystal could supplement previous study. One reason for further need of experimental investigation on the relative branching ratios is due to possible inconsistency in the guided ion beam transfer efficiency. The guided beam setup of

Zare's group in 1987 reported a product ion transfer efficiency that was dependent on the reaction mechanism. This was remedied by the addition of an octopole ion guide to the collision region, which purportedly removes dynamic-dependent collection efficiency. However, in their 1994 work, the TOF signal profile was dependent on the reaction mechanism. They reported much greater widths for the proton transfer and charge transfer products over deuterium abstraction product. In their work, they attribute this to incomplete momentum transfer in these two mechanisms relative to deuterium abstraction, suggesting that this was indicative of the short-lived nature of the reaction complex.

An additional avenue to investigate is the report of a secondary reaction product ND_4^+ . However, the authors explicitly state that its population could not be compared to other products due to product transfer efficiency inconsistencies with the secondary product ions. This also implies that the source of this secondary ion product, the ND_3^+ primary product, is likely under-reported in the branching ratio to an unknown degree. Both of these possible complications with the accurate measurement of branching ratios will not be present in our combined setup. As we can control the amount of reaction time the ions have with the neutral gas, we can easily delineate primary and secondary products. In addition, all of our ions of all product orders have an equivalent detection efficiency. This will allow us to add insights to previous measurements of this reaction.

Of course, we will extend prior work by tuning collisional energies, with well-defined rotational state populations. The Stark decelerator will allow us to identify the relative impacts of translational energy on each of these mechanisms independently as well as in comparison. The fact that energy dependence for the mechanism has already been indicated for this reaction recommends it for further study. The $\text{NH}_3^+ + \text{ND}_3$ reaction rate will be interesting to study at low temperatures as well. While prior studies of energy-dependent reaction rates of $\text{NH}_3^+ + \text{NH}_3$ have been primarily warmer than room temperature, there is a large expected enhancement of the reaction of ion-dipole reaction rate at lower temperatures. The temperature dependence of the overall reaction rate, as well as the temperature dependence of each product, will be extremely interesting to study. The "warm" collision range that we will reach, 1-40 K, has historically been extremely difficult to

address with the experimental techniques available. Instead of extrapolating between very cold and room temperature or measurements at higher kinetic energy, these rates will be directly measured within this range.

In addition to its importance for illuminating reaction mechanisms and capture rates, measurements of $\text{NH}_3^+ + \text{ND}_3$ over this critical range of temperatures will be relevant for astrochemical applications. Given the importance of the isotopologues of ammonia to astrochemical reactions, it should be unsurprising that an accurate measurement of this reaction may have a high impact on models of the ISM. Ammonia has been discovered from distant galaxies,[\[324\]](#) to our own,[\[323, 329, 325, 326\]](#) and from dense cores[\[327\]](#) to T Tauri stars.[\[328\]](#) It is very well studied throughout the cosmos for its ability to indicate the temperature in regions of space,[\[331, 332\]](#) as well as its chemical reactivity in molecular clouds, protoplanetary disks, and prebiotic chemistry.[\[328, 330, 371, 26\]](#) We hope that an energy-dependent measurement of the reaction rate of $\text{NH}_3^+ + \text{ND}_3$ will be the first of many ammonia reactions measured by our group at important interstellar temperatures.

Chapter 9

Summary & Outlook

“A ship in port is safe, but that’s not what ships are built for. Sail out to sea and do new things.”

– Admiral Grace Murray Hopper, Address at Trinity College, 1987

9.1 Summary

This dissertation presented experimental and theoretical methodologies for investigating cold, ion-neutral, gas-phase chemical reactions. I described our LIT-TOFMS system, which is well-suited for extremely high resolution and well-controlled chemical reactions at constrained, warm, collision energies.

I have presented three reactions studied in such a system. This includes two studies focused on the role and reactivity of the CCl^+ ion with two astrochemically relevant molecules, CH_3CN , C_6H_6 . Both reactions demonstrated fast kinetic rates branching to multiple cosmically viable ionic products. The $\text{CCl}^+ + \text{CH}_3\text{CN}$ reaction was accompanied by a detailed potential energy surface to identify potential reaction pathways. The computed PES demonstrated a reaction mechanism heavily influenced by the electronegativity of the chlorine atom, and the nucleophilic nature of the nitrogen involved. When paired with RRKM statistical transition rate theory, the predicted branching ratios from this surface agreed well with the nearly equivalent branching to the two ionic products, NCCl^+ and C_2H_3^+ .

In the case of $\text{CCl}^+ + \text{C}_6\text{H}_6$, the reaction produced four cationic products. When supplemented with quantum-chemical calculations, nearly all were found to be cyclic isomers, a required set by thermodynamic constraints. In addition, the C_7H_5^+ product represented nearly half the branching ratio, with multiple possible highly exothermic ionic isomers. These possible C_7H_5^+ product isomers included many with single or double rings, recommending this reaction as a plausible early step for polycyclic aromatic hydrocarbon formation. Another interesting result was the increased reaction rate when the heavier isotope of chlorine was substituted in the ionic reactant. Overall, our work with CCl^+ established two fast, viable reactions with which this ion may react. Such studies are important for establishing the role and reactivity of this halogenated carbocation in astrochemistry throughout the ISM.

The final reaction is that of $\text{C}_2\text{H}_2^+ + \text{CH}_3\text{CN}$. Both ions are quite relevant for astrochemistry, being well established in many regions of space. This reaction had three primary products, C_3H_3^+ , C_3H_4^+ , C_2NH_3^+ and one secondary product, C_2NH_4^+ . All of these products are identified and suspected participants of chemistry in the ISM. The identification of these products was possible due to combinations of isotope substitution with deuterated reactants. This technique also aided in complications due to the mass overlap of some products with the trapped Ca^+ . This study was accompanied by a full potential energy surface, which computationally demonstrated the thermodynamic viability of each product in our cold Coulomb crystal environment.

A second phase of this dissertation turned to the characterization of a traveling-wave Stark decelerator, and its coupling to our ion trap system. This process physically combined the two operational experiments, coupling a velocity-tunable neutral beam source to our trap of cold ions with a hexapole. The development of the optimum operation parameters of this hexapole is underway and nearing completion. This optimization was interrupted by the need for upgrades to the amplifiers, which provide high voltage to the TWSD. These upgrades are thoroughly outlined in this dissertation, and should promote the longevity and stability of these critical components of the new, combined apparatus.

9.2 Outlook

On the not-so-distant horizon is the realization of the first reaction of decelerated molecules with ions in a Coulomb crystal. This will introduce a Stark decelerator as a molecular source for energy-tunable ion-neutral chemical reactions in an ion trap. The LIT-TWSD apparatus will be capable of reaching collision energies that are important for testing classical capture theories for polar molecules, as well as relevant for chemistry in many regions of the ISM. The proposed first reaction, $\text{NH}_3^+ + \text{ND}_3$, has additional applications for studying the energetic dependence of the branching ratio of this key reaction among three unique reaction mechanisms. This has broader applications for this astrochemically abundant molecule, as well as fundamental chemical dynamics within this system. Further reactions with ND_3 and other polar molecules, such as OH, [\[321\]](#), [\[314\]](#) will keep the lab busy for years to come.

Bibliography

- [1] James Greenberg. Cold, Controlled, Ion-Molecule Reactions. PhD thesis, University of Colorado, Boulder, 2020.
- [2] Yomay Shyur. Stark Deceleration Methods for Cold Molecule Experiments. PhD thesis, University of Colorado, 2018.
- [3] Paul et al. ‘apparatus for separating charged particles of different specific charges’, Jun 1960. Patent number: 2939952.
- [4] Raymond E. March. An Introduction to Quadrupole Ion Trap Mass Spectrometry. Journal of Mass Spectrometry, 32(4):351–369, apr 1997.
- [5] William D. Phillips. Laser cooling and trapping of neutral atoms. Reviews of Modern Physics, 70(3):721–741, 1998.
- [6] Andrés Villani Davila. Impact of Non-Laser Cooled Species in the Average Kinetic Energy of Coulomb Crystals. Undergraduate Honors Thesis, University of Colorado, Boulder, 2021.
- [7] P. C. Schmid, J. Greenberg, T. L. Nguyen, J. H. Thorpe, K. J. Catani, O. A. Krohn, M. I. Miller, J. F. Stanton, and H. J. Lewandowski. Isomer-selected ion-molecule reactions of acetylene cations with propyne and allene. Physical Chemistry Chemical Physics, 22(36):20303–20310, 2020.
- [8] Julian Schmidt, Daniel Hönig, Pascal Weckesser, Fabian Thielemann, Tobias Schaetz, and Leon Karpa. Mass-selective removal of ions from Paul traps using parametric excitation. Applied Physics B, 126(11):176, 2020.
- [9] Rüdiger Paschotta. Microchannel plates, Jun 2023.
- [10] Michael T Bowers. Gas Phase Ion Chemistry: Volume 1, volume 1. Academic Press, 1979.
- [11] Timothy Su and Michael T. Bowers. Ion-polar molecule collisions: the effect of ion size on ion-polar molecule rate constants; the parameterization of the average-dipole-orientation theory. International Journal of Mass Spectrometry and Ion Physics, 12(4):347–356, 1973.
- [12] Errol Lewars. Computational chemistry : introduction to the theory and applications of molecular and quantum mechanics, jan 2010.
- [13] B. Weiner, C. J. Williams, D. Heaney, and M. C. Zerner. Structures of $C_5H_3^+$. J. Phys. Chem., 94:7001–7007, 1990.

- [14] K. Lammertsma and P. v. R. Schleyer. Structures and energies of $C_6H_6^{+2}$ isomers. fragmentation into $C_5H_3^+$ and CH_3^+ . J. Am. Chem. Soc., 105:1049–1051, 1983.
- [15] J. Fulara, A. Chakraborty, A. Nagy, K. Filipkowski, and J. P. Maier. Electronic transitions of $C_5H_3^+$ and C_5H_3 : Neon matrix and caspt2 studies. J. Phys. Chem. A, 119:2338–2343, 2015.
- [16] Noah J Fitch. Traveling-wave Stark-decelerated molecular beams for cold collision experiments. PhD thesis, University of Colorado, 2013.
- [17] Yomay Shyur, Jason A Bossert, and HJ Lewandowski. Pulsed operation of a ring stark decelerator. J. Phys. B, 51(16):165101, 2018.
- [18] James Greenberg, O. A. Krohn, Jason A. Bossert, Yomay Shyur, David Macaluso, N. J. Fitch, and H. J. Lewandowski. Velocity-tunable beam of continuously decelerated polar molecules for cold ion-molecule reaction studies. Rev. Sci. Instr., 92(10):103202, 2021.
- [19] Yomay Shyur, N. J. Fitch, Jason A. Bossert, Terry Brown, and H. J. Lewandowski. A high-voltage amplifier for traveling-wave stark deceleration. Rev. Sci. Instr., 89(8):084705, 2018.
- [20] Comsol multiphysics v. 5.4. COMSOL AB, Stockholm, Sweden.
- [21] K. R. Ryan. Ionic Collision Processes in Gaseous Ammonia. The Journal of Chemical Physics, 53(10):3844–3848, nov 1970.
- [22] Rose Marx and Gérard Mauclaire. Ion cyclotron resonance study of positive and negative ion-molecule reactions in ammonia. International Journal of Mass Spectrometry and Ion Physics, 10(3):213–226, 1973.
- [23] Mark A. Smith and Michael Hawley. Ion/molecule reaction rate coefficients at translational temperatures below 5 K: selected bimolecular reactions of $C_2H_2^+$ and NH_4^+ . International Journal of Mass Spectrometry and Ion Processes, 149-150(C):199–206, 1995.
- [24] Lynmarie A. Posey, Robert D. Guettler, Nicholas J. Kirchner, and Richard N. Zare. Influence of vibrational excitation and collision energy on the ion-molecule reaction $NH_3^+(\nu_2)+ND_3$. The Journal of Chemical Physics, 101(5):3772–3786, 1994.
- [25] A. G.G.M. Tielens. The molecular universe. Reviews of Modern Physics, 85(3):1021–1081, 2013.
- [26] Lucy M. Ziurys. Interstellar molecules and their prebiotic potential. Handbook of Astrobiology, 2:147–164, 2018.
- [27] Cristina Puzzarini and Vincenzo Barone. A never-ending story in the sky: The secrets of chemical evolution. Physics of Life Reviews, 32:59–94, 2020.
- [28] Brett A. McGuire. 2021 Census of Interstellar, Circumstellar, Extragalactic, Protoplanetary Disk, and Exoplanetary Molecules. The Astrophysical Journal Supplement Series, 259(2):30, 2022.
- [29] V. Wakelam, E. Herbst, J. C. Loison, I. W.M. Smith, V. Chandrasekaran, B. Pavone, N. G. Adams, M. C. Bacchus-Montabonel, A. Bergeat, K. Béroff, V. M. Bierbaum, M. Chabot, A. Dalgarno, E. F. Van Dishoeck, A. Faure, W. D. Geppert, D. Gerlich, D. Galli, E. Hébrard,

- F. Hersant, K. M. Hickson, P. Honvault, S. J. Klippenstein, S. Le Picard, G. Nyman, P. Pernot, S. Schlemmer, F. Selsis, I. R. Sims, D. Talbi, J. Tennyson, J. Troe, R. Wester, and L. Wiesenfeld. A kinetic database for astrochemistry (KIDA). *Astrophysical Journal, Supplement Series*, 199(1), 2012.
- [30] V. G. Anicich. Evaluated Bimolecular Ion-Molecule Gas Phase Kinetics of Positive Ions for Use in Modeling Planetary Atmospheres, Cometary Comae, and Interstellar Clouds. *J. Phys. Chem. Ref. Data*, 22(6):1469–1569, 1993.
- [31] V. Wakelam, E. Herbst, and F. Selsis. The effect of uncertainties on chemical models of dark clouds. *Astronomy and Astrophysics*, 451(2):551–562, may 2006.
- [32] V. Wakelam, I. W.M. Smith, E. Herbst, J. Troe, W. Geppert, H. Linnartz, K. Öberg, E. Roueff, M. Agúndez, P. Pernot, H. M. Cuppen, J. C. Loison, and D. Talbi. Reaction networks for interstellar chemical modelling: Improvements and challenges. *Space Science Reviews*, 156(1-4):13–72, 2010.
- [33] Ian W.M. Smith. Laboratory astrochemistry: Gas-phase processes. *Annual Review of Astronomy and Astrophysics*, 49:29–66, 2011.
- [34] Theodore P. Snow and Veronica M. Bierbaum. Ion chemistry in the interstellar medium. *Annual Review of Analytical Chemistry*, 1(1):229–259, 2008.
- [35] David Smith. The Ion Chemistry of Interstellar Clouds. *Chemical Reviews*, 92(7):1473–1485, 1992.
- [36] Wolf D. Geppert and Mats Larsson. Experimental investigations into astrophysically relevant ionic reactions. *Chemical Reviews*, 113(12):8872–8905, 2013.
- [37] Andriana Tsikritea, Jake A. Diprose, Timothy P. Softley, and Brianna R. Heazlewood. Capture theory models: An overview of their development, experimental verification, and applications to ion-molecule reactions. *Journal of Chemical Physics*, 157(6), 2022.
- [38] Paul M. Langevin. Une formule fondamentale de theorie cinetique. *Annales de Chimie et de Physique, series, T5*:245–288, 1905.
- [39] Timothy Su and Walter J. Chesnavich. Parametrization of the ion-polar molecule collision rate constant by trajectory calculations. *The Journal of Chemical Physics*, 76(10):5183–5185, 1982.
- [40] T. Su and M. T. Bowers. Theory of ionpolar molecule collisions. comparison with experimental charge transfer reactions of rare gas ions to geometric isomers of difluorobenzene and dichloroethylene. *J. Chem. Phys.*, 58(7):3027–3037, 1973.
- [41] D C Clary. Calculations of rate constants for ion-molecule reactions using a combined capture and centrifugal sudden approximation. *Molecular Physics*, 54(3):605–618, 1985.
- [42] J. Troe. Statistical adiabatic channel model for ion-molecule capture processes. *The Journal of Chemical Physics*, 87(5):2773–2782, 1987.
- [43] R. V. Krems. Cold controlled chemistry. *Physical Chemistry Chemical Physics*, 10(28):4079–4092, 2008.

- [44] Moshe Shapiro and Paul Brumer. Principles of the quantum control of molecular processes. 2003.
- [45] J. Toscano, H. J. Lewandowski, and B. R. Heazlewood. Cold and controlled chemical reaction dynamics. Phys. Chem. Chem. Phys., 22:9180–9194, 2020.
- [46] Brianna R Heazlewood and Timothy P Softley. Towards chemistry at absolute zero. Nat. Rev. Chem., 5(2):125–140, 2021.
- [47] Martin T. Bell and Timothy P. Softley. Ultracold molecules and ultracold chemistry. Molecular Physics, 107(2):99–132, 2009.
- [48] Diethard K. Böhme. Experimental studies of positive ion chemistry with flow-tube mass spectrometry: Birth, evolution, and achievements in the 20th century. International Journal of Mass Spectrometry, 200(1-3):97–136, 2000.
- [49] N. G. Adams and D. Smith. The selected ion flow tube (SIFT); A technique for studying ion-neutral reactions. International Journal of Mass Spectrometry and Ion Physics, 21(3-4):349–359, 1976.
- [50] Alexey Potapov, André Canosa, Elena Jiménez, and Bertrand Rowe. Uniform Supersonic Chemical Reactors: 30 Years of Astrochemical History and Future Challenges. Angewandte Chemie - International Edition, 56(30):8618–8640, 2017.
- [51] B. R. Rowe and J. B. Marquette. CRESU studies of ion/molecule reactions. International Journal of Mass Spectrometry and Ion Processes, 80(C):239–254, 1987.
- [52] Roland Wester. Velocity map imaging of ion-molecule reactions. Physical Chemistry Chemical Physics, 16(2):396–405, 2014.
- [53] Eduardo Carrascosa, Jennifer Meyer, and Roland Wester. Imaging the dynamics of ion-molecule reactions. Chemical Society Reviews, 46(24):7498–7516, 2017.
- [54] Pitt Allmendinger, Johannes Deiglmayr, Otto Schullian, Katharina Höveler, Josef A. Agner, Hansjürg Schmutz, and Frédéric Merkt. New Method to Study IonMolecule Reactions at Low Temperatures and Application to the $H_2^{++}H_2H_3^{++}H$ Reaction. ChemPhysChem, 17(22):3596–3608, 2016.
- [55] Dieter Gerlich. Experimental investigations of ion-molecule reactions relevant to interstellar chemistry. Journal of the Chemical Society, Faraday Transactions, 89(13):2199–2208, 1993.
- [56] Roland Wester. Radiofrequency multipole traps: Tools for spectroscopy and dynamics of cold molecular ions. Journal of Physics B: Atomic, Molecular and Optical Physics, 42(15), 2009.
- [57] G. H. Dunn. Ion-electron and ion-neutral collisions in ion traps. Physica Scripta, 1995(T59):249–255, 1995.
- [58] K. Okada, M. Wada, T. Takayanagi, S. Ohtani, and H. A. Schuessler. Characterization of ion Coulomb crystals in a linear paul trap. Physical Review A - Atomic, Molecular, and Optical Physics, 81(1):1–10, 2010.
- [59] Stefan Willitsch. Coulomb-crystallised molecular ions in traps: Methods, applications, prospects. International Reviews in Physical Chemistry, 31(2):175–199, 2012.

- [60] Brianna R. Heazlewood and Timothy P. Softley. Low-Temperature Kinetics and Dynamics with Coulomb Crystals. Annual Review of Physical Chemistry, 66(1):475–495, 2015.
- [61] M. Drewsen, I. Jensen, J. Lindballe, N. Nissen, R. Martinussen, A. Mortensen, P. Sta anum, and D. Voigt. Ion Coulomb crystals: A tool for studying ion processes. International Journal of Mass Spectrometry, 229(1-2):83–91, 2003.
- [62] B R Heazlewood. Cold ion chemistry within Coulomb crystals. Mol. Phys., 117(14):1934–1941, 2019.
- [63] Brianna R Heazlewood and Heather J Lewandowski. Chemistry Using Coulomb Crystals. In Emerging Trends in Chemical Applications of Lasers, volume 1398 of ACS Symposium Series, pages 17–389. American Chemical Society, oct 2021.
- [64] Stefan Willitsch. Chemistry With Controlled Ions. In S. A. Rice Dinner and A. R., editors, Advances in Chemical Physics, volume 162, pages 307–340. John Wiley & Sons, oct 2017.
- [65] P. C. Schmid, J. Greenberg, M. I. Miller, K. Loeffler, and H. J. Lewandowski. An ion trap time-of-flight mass spectrometer with high mass resolution for cold trapped ion experiments. Review of Scientific Instruments, 88(12), 2017.
- [66] Michael Drewsen. Ion Coulomb crystals and some applications. volume 135, pages 135–144, 2003.
- [67] P. F. Sta anum, K. Højbjerg, R. Wester, and M. Drewsen. Probing isotope effects in chemical reactions using single ions. Phys. Rev. Lett., 100(24):243003, 2008.
- [68] L. S. Petralia, A. Tsikritea, J. Loreau, T. P. Softley, and B. R. Heazlewood. Strong inverse kinetic isotope effect observed in ammonia charge exchange reactions. Nat. Comm., 11(1):1–7, 2020.
- [69] A. Tsikritea, K. Park, P. Bertier, J. Loreau, T. P. Softley, and B. R. Heazlewood. Inverse kinetic isotope effects in the charge transfer reactions of ammonia with rare gas ions. Chemical Science, 12(29):10005–10013, 2021.
- [70] TJ Millar, A Bennett, and Eric Herbst. Deuterium fractionation in dense interstellar clouds. Astrophysical Journal, Part 1 (ISSN 0004-637X), vol. 340, May 15, 1989, p. 906-920. Research supported by SERC., 340:906–920, 1989.
- [71] J. Greenberg, P. C. Schmid, J. H. Thorpe, T. L. Nguyen, K. J. Catani, O. A. Krohn, M. I. Miller, J. F. Stanton, and H. J. Lewandowski. Using isotopologues to probe the potential energy surface of reactions of $C_2H_2^+ + C_3H_4$. J. Chem. Phys., 154:124310, 2021.
- [72] Tiangang Yang, Anyang Li, Gary K. Chen, Qian Yao, Arthur G. Suits, Hua Guo, Eric R. Hudson, and Wesley C. Campbell. Isomer-specific kinetics of the $C^+ + H_2O$ reaction at the temperature of interstellar clouds. Science Advances, 7(2):3–8, 2021.
- [73] Yuan Pin Chang, Karol Długołęcki, Jochen Küpper, Daniel Rösch, Dieter Wild, and Stefan Willitsch. Specific chemical reactivities of spatially separated 3-aminophenol conformers with cold Ca^+ ions. Science, 342(6154):98–101, 2013.

- [74] Ardita Kilaj, Jia Wang, Patrik Straák, Max Schwilk, Uxía Rivero, Lei Xu, O. Anatole von Lilienfeld, Jochen Küpper, and Stefan Willitsch. Conformer-specific polar cycloaddition of dibromobutadiene with trapped propene ions. Nature Communications, 12(1):1–8, 2021.
- [75] Alexander D. Gingell, Martin T. Bell, James M. Oldham, Timothy P. Softley, and Jeremy N. Harvey. Cold chemistry with electronically excited Ca^+ Coulomb crystals. Journal of Chemical Physics, 133(19), 2010.
- [76] Martin T. Bell, Alexander D. Gingell, James M. Oldham, Timothy P. Softley, and Stefan Willitsch. Ion-molecule chemistry at very low temperatures: cold chemical reactions between coulomb-crystallized ions and velocity-selected neutral molecules. Faraday Discuss., 142:73–91, 2009.
- [77] K. Okada, T. Suganuma, T. Furukawa, T. Takayanagi, M. Wada, and H. A. Schuessler. Cold ion–polar-molecule reactions studied with a combined stark-velocity-filter–ion-trap apparatus. Phys. Rev. A, 87:043427, 2013.
- [78] Kunihiro Okada, Kazuhiro Sakimoto, Yusuke Takada, and Hans A. Schuessler. A study of the translational temperature dependence of the reaction rate constant between CH_3CN and Ne^+ at low temperatures. Journal of Chemical Physics, 153(12), 2020.
- [79] Chloé Miossec, Michal Hejduk, Rahul Pandey, Neville J A Coughlan, and Brianna R Heazlewood. Design and characterization of a cryogenic linear Paul ion trap for ionneutral reaction studies. Review of Scientific Instruments, 93(3):33201, 2022.
- [80] Charles R. Markus, Charles R. Markus, Oskar Asvany, Thomas Salomon, Philipp C. Schmid, Sandra Brünken, Filippo Lipparini, Filippo Lipparini, Jürgen Gauss, and Stephan Schlemmer. Vibrational Excitation Hindering an Ion-Molecule Reaction: The $\text{c-C}_3\text{H}_2^+ - \text{H}_2$ Collision Complex. Physical Review Letters, 124(23):233401, 2020.
- [81] Dieter Gerlich. Ion-neutral collisions in a 22-pole trap at very low energies. Physica Scripta, 1995(T59):256–263, 1995.
- [82] R Plasil, T Mehner, P Dohnal, T Kotrik, J Glosik, and D Gerlich. REACTIONS OF COLD TRAPPED CH^+ IONS WITH SLOW H ATOMS. The Astrophysical Journal, 737(2):60, aug 2011.
- [83] Valentina Zhelyazkova, Fernanda B.V. Martins, Josef A. Agner, Hansjürg Schmutz, and Frédéric Merkt. Multipole-moment effects in ion-molecule reactions at low temperatures: Part I-ion-dipole enhancement of the rate coefficients of the $\text{He}^{++} - \text{NH}_3$ and $\text{He}^{++} - \text{ND}_3$ reactions at collisional energies: $E_{\text{coll}}/k_B \rightarrow 0$ K. Physical Chemistry Chemical Physics, 23(38):21606–21622, 2021.
- [84] Katharina Höveler, Johannes Deiglmayr, and Frédéric Merkt. Deviation of the rate of the reaction from Langevin behaviour below 1 K, branching ratios for the and product channels, and product-kinetic-energy distributions. Molecular Physics, 119(17-18), 2021.
- [85] Baruch Margulis, Julia Narevicius, and Edvardas Narevicius. Direct observation of a Feshbach resonance by coincidence detection of ions and electrons in Penning ionization collisions. Nature Communications, 11(1):1–6, 2020.

- [86] Baruch Margulis, Karl P. Horn, Daniel M. Reich, Meenu Upadhyay, Nitzan Kahn, Arthur Christianen, Ad van der Avoird, Gerrit C. Groenenboom, Markus Meuwly, Christiane P. Koch, and Edvardas Narevicius. Tomography of Feshbach resonance states. Science, 380(6640):77–81, 2023.
- [87] Chloé Miossec, Lok Yiu Wu, Paul Bertier, Michal Hejduk, Jutta Toscano, and Brianna R Heazlewood. A stand-alone magnetic guide for producing tuneable radical beams. The Journal of Chemical Physics, 153(10):104202, 2020.
- [88] Dominik Haas, Claudio von Planta, Thomas Kierspel, Dongdong Zhang, and Stefan Willitsch. Long-term trapping of Stark-decelerated molecules. Communications Physics, 2(1), 2019.
- [89] Wolfgang Paul. Electromagnetic traps for charged and neutral particles. Rev. Mod. Phys., 62:531–540, Jul 1990.
- [90] P K Ghosh. Ion traps, Dec 1995.
- [91] C E Pearson, D R Leibbrandt, W S Bakr, W J Mallard, K R Brown, and I L Chuang. Experimental investigation of planar ion traps. Phys. Rev. A, 73(3):32307, mar 2006.
- [92] M E Poitzsch, J C Bergquist, W M Itano, and D J Wineland. Cryogenic linear ion trap for accurate spectroscopy. Review of Scientific Instruments, 67(1):129–134, 1996.
- [93] Kunihiro Okada, Kazuhiro Yasuda, Toshinobu Takayanagi, Michiharu Wada, Hans A Schuessler, and Shunsuke Ohtani. Crystallization of Ca^+ ions in a linear rf octupole ion trap. Phys. Rev. A, 75(3):33409, mar 2007.
- [94] Madison M Foreman, Maristella Alessio, Anna I Krylov, and J Mathias Weber. Influence of Transition Metal Electron Configuration on the Structure of MetalEDTA Complexes. The Journal of Physical Chemistry A, 127(10):2258–2264, mar 2023.
- [95] Dongdong Zhang and Stefan Willitsch. Cold ion chemistry. 2017.
- [96] S. E. Barlow, J. A. Luine, and G. H. Dunn. Measurement of ion/molecule reactions between 10 and 20 K. International Journal of Mass Spectrometry and Ion Processes, 74(1):97–128, 1986.
- [97] M. M. Schauer, S. R. Jefferts, S. E. Barlow, and G. H. Dunn. Reactions of H_2 with He^+ at temperatures below 40 K. The Journal of Chemical Physics, 91(8):4593–4596, oct 1989.
- [98] S E Barlow, G. H. Dunn, and M Schauer. Radiative association of CH_3^+ and H_2 at 13 K. Physical Review Letters, 52(11):902–905, mar 1984.
- [99] T. B. McMahon and J. L. Beauchamp. A versatile trapped ion cell for ion cyclotron resonance spectroscopy. Review of Scientific Instruments, 43(3):509–512, 1972.
- [100] W. T. Huntress and R. F. Pinizzotto. Product distributions and rate constants for ionmolecule reactions in water, hydrogen sulfide, ammonia, and methane. The Journal of Chemical Physics, 59(9):4742–4756, 1973.

- [101] M.T. Bowers, P.V. Neilson, P.R. Kemper, and A.G. Wren. Temperature dependence of ion-molecule collision phenomena: An application of ion cyclotron resonance spectroscopy to the determination of reactive and momentum transfer rate constants. International Journal of Mass Spectrometry and Ion Physics, 25(1):103–116, sep 1977.
- [102] A. G. Wren, P. Gilbert, and M. T. Bowers. New design of an ion cyclotron resonance cell capable of temperature variation over the range 80T450 K. Review of Scientific Instruments, 49(4):531–536, 1978.
- [103] D. Kielpinski, C. Monroe, and D. J. Wineland. Qccd. Nature, 417(6890):709–711, 2002.
- [104] D. Stick, W. K. Hensinger, S. Olmschenk, M. J. Madsen, K. Schwab, and C. Monroe. Ion trap in a semiconductor chip. Nature Physics, 2(1):36–39, 2006.
- [105] Dieter Gerlich and Stevan Horning. Experimental Investigations of Radiative Association Processes as Related to Interstellar Chemistry. Chemical Reviews, 92(7):1509–1539, 1992.
- [106] I Savic and D. Gerlich. Temperature variable ion trap studies of $C_3H_n^+$. Physical Chemistry Chemical Physics, 7:1026–1035, 2005.
- [107] Stephan Schlemmer, Emmanuelle Lescop, Jan Von Richthofen, Dieter Gerlich, and Mark A. Smith. Laser induced reactions in a 22-pole ion trap: $C_2H_2^{++} + h\nu \rightarrow C_2H_3^{++} + H$. Journal of Chemical Physics, 117(5):2068–2075, 2002.
- [108] Raymond E March. Quadrupole ion traps. Mass Spectrometry Reviews, 28(6):961–989, 2009.
- [109] Dieter Gerlich. Inhomogeneous rf fields: a versatile tool for the study of processes with slow ions. Advances in chemical physics, 82:1–176, 1992.
- [110] A. Ashkin. Trapping of atoms by resonance radiation pressure. Physical Review Letters, 40(12):729–732, 1978.
- [111] T.W. Hänsch and A.L. Schawlow. Cooling of gases by laser radiation. Optics Communications, 13(1):68–69, jan 1975.
- [112] Stig Stenholm. The semiclassical theory of laser cooling. Reviews of Modern Physics, 58(3):699–739, 1986.
- [113] D. J. Wineland and Wayne M. Itano. Laser cooling of atoms. Physical Review A, 20(4):1521–1540, 1979.
- [114] D. J. Wineland, J. Dalibard, and C. Cohen-Tannoudji. Sisyphus cooling of a bound atom. Journal of the Optical Society of America B, 9(1):32, 1992.
- [115] Y. Castin, H. Wallis, and J. Dalibard. Limit of Doppler cooling. Journal of the Optical Society of America B, 6(11):2046, 1989.
- [116] E. S. Shuman, J. F. Barry, and D. Demille. Laser cooling of a diatomic molecule. Nature, 467(7317):820–823, 2010.
- [117] N. J. Fitch and M. R. Tarbutt. Laser-cooled molecules, volume 70. Elsevier Inc., 1 edition, 2021.

- [118] Daniel McCarron. Laser cooling and trapping molecules. Journal of Physics B: Atomic, Molecular and Optical Physics, 51(21), 2018.
- [119] M. Schubert, I. Siemers, R. Blatt, W. Neuhauser, and P. E. Toschek. Transient internal dynamics of a multilevel ion. Physical Review A, 52(4):2994–3006, 1995.
- [120] H. J. Metcalf and P. van der Straten. Laser cooling and trapping of atoms. Journal of the Optical Society of America B, 20(5):887, may 2003.
- [121] Nathaniel B. Vilas, Christian Hallas, Loïc Anderegg, Paige Robichaud, Andrew Winnicki, Debayan Mitra, and John M. Doyle. Magneto-optical trapping and sub-Doppler cooling of a polyatomic molecule. Nature, 606(7912):70–74, 2022.
- [122] Pauline Yzombard, Mehdi Hamamda, Sebastian Gerber, Michael Doser, and Daniel Comparat. Laser cooling of molecular anions. Physical Review Letters, 114(21):1–5, 2015.
- [123] E. Bentine, C. J. Foot, and D. Trypogeorgos. (py)LIon: A package for simulating trapped ion trajectories. Computer Physics Communications, 253:107187, 2020.
- [124] "A. P. Thompson, H. M. Aktulga, R. Berger, D. S. Bolintineanu, W. M. Brown, P. S. Crozier, P. J. in 't Veld, A. Kohlmeyer, S. G. Moore, T. D. Nguyen, R. Shan, M. J. Stevens, J. Tranchida, C. Trott, and S. J. Plimpton". "LAMMPS - a flexible simulation tool for particle-based materials modeling at the atomic, meso, and continuum scales". Comp. Phys. Comm., 271:108171, 2022.
- [125] C. B. Zhang, D. Offenber, B. Roth, M. A. Wilson, and S. Schiller. Molecular-dynamics simulations of cold single-species and multispecies ion ensembles in a linear Paul trap. Physical Review A - Atomic, Molecular, and Optical Physics, 76(1):1–13, 2007.
- [126] Bernhard Roth and Stephan Schiller. Sympathetically cooled molecular ions: from principles to first applications. In Cold Molecules, pages 683–736. CRC Press, 2009.
- [127] B. Roth, P. Blythe, and S. Schiller. Motional resonance coupling in cold multispecies coulomb crystals. Phys. Rev. A, 75:023402, Feb 2007.
- [128] Kunihiro Okada, Masanari Ichikawa, and Michiharu Wada. Characterization of ion Coulomb crystals for fundamental sciences. Hyperfine Interactions, 236(1):87–94, 2015.
- [129] Stephan Schiller and Claus Lämmerzahl. Molecular dynamics simulation of sympathetic crystallization of molecular ions. Physical Review A - Atomic, Molecular, and Optical Physics, 68(5):5, 2003.
- [130] Travis C. Briles. Production, Deceleration, And Detection Of Oh Radicals. PhD thesis, University of Colorado, Boulder, 2015.
- [131] Andrew J Orr-Ewing, Ross A Morgan, Steven HS Wilson, Claire L Reed, and Michael NR Ashfold. (1+1) resonance-enhanced multiphoton ionization spectroscopy of jet-cooled C₂H₂, C₂HD and C₂D₂ in the range 46 400-48 400 cm⁻¹. J. Chem. Soc. Faraday Trans., 91(19):3327–3337, 1995.
- [132] A A Herod, A G Harrison, and N A McAskill. IonMolecule Reactions in Methyl Fluoride and Methyl Chloride. Canadian Journal of Chemistry, 49(13):2217–2222, 1971.

- [133] D. Smith and N. G. Adams. Production and loss process for HCl in interstellar clouds: some relevant laboratory measurements. *Astrophys. J.*, 298:827–829, 1985.
- [134] N A McAskill. Ion-molecule reactions in Trihalo- and Tetrahalo-methanes. *Australian Journal of Chemistry*, 23(5):893–903, 1970.
- [135] G. A. Blake, V. G. Anicich, and W. T. Huntress. Chemistry of chlorine in dense interstellar clouds. *Astrophys. J.*, 300(1):415–419, 1986.
- [136] K. Okada, M. Wada, L. Boesten, T. Nakamura, I. Katayama, and S. Ohtani. Acceleration of the chemical reaction of trapped Ca⁺ ions with H₂O molecules by laser excitation. *J. Phys. B: At., Mol. Opt. Phys.*, 36(1):33–46, 2003.
- [137] Fabian Schmid, Johannes Weitenberg, Jorge Moreno, Theodor W. Hänsch, Thomas Udem, and Akira Ozawa. Number-resolved detection of dark ions in Coulomb crystals. *Physical Review A*, 106(4):1–7, 2022.
- [138] Tiangang Yang, Anyang Li, Gary K. Chen, Changjian Xie, Arthur G. Suits, Wesley C. Campbell, Hua Guo, and Eric R. Hudson. Optical Control of Reactions between Water and Laser-Cooled Be⁺ Ions. *Journal of Physical Chemistry Letters*, 9(13):3555–3560, 2018.
- [139] WC Wiley and Ii H McLaren. Time-of-flight mass spectrometer with improved resolution. *Review of scientific instruments*, 26(12):1150–1157, 1955.
- [140] Joseph Ladislav Wiza. Microchannel plate detectors. *Nuclear Instruments and Methods*, 162(1):587–601, 1979.
- [141] S Matsuura, S Umebayashi, C Okuyama, and K Oba. Current Status of the Micro Channel Plate. *IEEE Transactions on Nuclear Science*, 31(1):399–403, 1984.
- [142] Richard Cordia Taylor, Michael C Hettrick, and Roger F Malina. Maximizing the quantum efficiency of microchannel plate detectors: The collection of photoelectrons from the inter-channel web using an electric field. *Review of Scientific Instruments*, 54(2):171–176, 1983.
- [143] L Wilhelmy. Temperature dependence to rate theories. *Pogg. Ann.*, 81:422–499, 1850.
- [144] Jacobus Henricus Van't Hoff. *Etudes de dynamique chimique*. Frederik Muller, 1884.
- [145] Keith J. Laidler. The development of the arrhenius equation. *Journal of Chemical Education*, 61(6):494–498, 1984.
- [146] Svante Arrhenius. Über die Reaktionsgeschwindigkeit bei der Inversion von Rohrzucker durch Säuren. *Zeitschrift für Physikalische Chemie*, 4U(1):226–248, 1889.
- [147] Keith J. Laidler and M. Christine King. Development of transition-state theory. *The Journal of Physical Chemistry*, 87(15):2657–2664, jul 1983.
- [148] H Eyring and M Polanyi. On Simple Gas Reactions. *Zeitschrift für Physikalische Chemie*, 227(9-11):1221–1246, jan 2013.
- [149] Henry Eyring. The activated complex in chemical reactions. *The Journal of Chemical Physics*, 3(2):63–71, 1935.

- [150] Henry Eyring. The Activated Complex and the Absolute Rate of Chemical Reactions. Chemical Reviews, 17(1):65–77, aug 1935.
- [151] Max Trautz. Das Gesetz der Reaktionsgeschwindigkeit und der Gleichgewichte in Gasen. Bestätigung der Additivität von $Cv^{3/2}R$. Neue Bestimmung der Integrationskonstanten und der Moleküldurchmesser. Zeitschrift für anorganische und allgemeine Chemie, 96(1):1–28, 1916.
- [152] W. C. McC. Lewis. No Title. J Chem. Soc., 113(471), 1918.
- [153] Henry Eyring, J. O. Hirschfelder, and Hugh S. Taylor. The Theoretical Treatment of Chemical Reactions Produced by Ionization Processes Part I. The Ortho-Para Hydrogen Conversion by Alpha-Particles. Journal of Chemical Physics, 4(8):479–491, 1936.
- [154] Mark Brouard and Claire Vallance. Tutorials in molecular reaction dynamics. Royal Society of Chemistry, 2015.
- [155] Lowell P. Theard and William H. Hamill. The Energy Dependence of Cross Sections of Some Ion-Molecule Reactions1. Journal of the American Chemical Society, 84(7):1134–1139, 1962.
- [156] Thomas F. Moran and William H. Hamill. Cross sections of ion-permanent-dipole reactions by mass spectrometry. The Journal of Chemical Physics, 39(6):1413–1422, 1963.
- [157] John V Dugan and John L Magee. Capture Collisions between Ions and Polar Molecules. The Journal of Chemical Physics, 47(9):3103–3112, nov 1967.
- [158] Walter J. Chesnavich, Timothy Su, and Michael T. Bowers. Collisions in a noncentral field: A variational and trajectory investigation of ion-dipole capture. The Journal of Chemical Physics, 72(4):2641–2655, 1980.
- [159] Walter J. Chesnavich and Michael T. Bowers. Theory of translationally driven reactions. Journal of Physical Chemistry, 83(8):900–905, 1979.
- [160] Timothy Su and Michael T. Bowers. Ion-polar molecular collisions: the average quadrupole orientation theory. International Journal of Mass Spectrometry and Ion Physics, 17(3):309–319, 1975.
- [161] Timothy Su, Elkie C.F. Su, and Michael T. Bowers. Ion-polar molecule collisions. Conservation of angular momentum in the average dipole orientation theory. The AADO theory. The Journal of Chemical Physics, 69(5):2243–2250, 1978.
- [162] Alexander Balint-Kurti, Gabriel G. ; P. Palov. Rate Constants, Cross Sections and Reactive Scattering. In Theory of Molecular Collisions. The Royal Society of Chemistry, 2015.
- [163] David C. Clary. Rate constants for the reactions of ions with dipolar polyatomic molecules. Journal of the Chemical Society, Faraday Transactions 2: Molecular and Chemical Physics, 83(1):139–148, 1987.
- [164] R Thomas, K O Roberts, E Tiesinga, A C J Wade, P B Blakie, A B Deb, and N Kjaergaard. Multiple scattering dynamics of fermions at an isolated p-wave resonance. Nature Communications, 7(1):12069, 2016.

- [165] Hyungmok Son, Juliana J Park, Yu-Kun Lu, Alan O Jamison, Tijs Karman, and Wolfgang Ketterle. Control of reactive collisions by quantum interference. Science, 375(6584):1006–1010, 2022.
- [166] Matthew Chilcott, Ryan Thomas, and Niels Kjaergaard. Experimental observation of the avoided crossing of two S -matrix resonance poles in an ultracold atom collider. Phys. Rev. Res., 3(3):33209, sep 2021.
- [167] Alaina Green, Hui Li, Jun Hui See Toh, Xinxin Tang, Katherine C McCormick, Ming Li, Eite Tiesinga, Svetlana Kotochigova, and Subhadeep Gupta. Feshbach Resonances in p -Wave Three-Body Recombination within Fermi-Fermi Mixtures of Open-Shell ${}^6\text{Li}$ and Closed-Shell ${}^{173}\text{Yb}$ Atoms. Phys. Rev. X, 10(3):31037, aug 2020.
- [168] Juliana J Park, Yu-Kun Lu, Alan O Jamison, Timur V Tscherebul, and Wolfgang Ketterle. A Feshbach resonance in collisions between triplet ground-state molecules. Nature, 614(7946):54–58, 2023.
- [169] Yu Liu and Kang Kuen Ni. Bimolecular Chemistry in the Ultracold Regime. Annual Review of Physical Chemistry, 73:73–96, 2022.
- [170] Baruch Margulis, Prerna Paliwal, Wojciech Skomorowski, Mariusz Pawlak, Piotr S Zuchowski, and Edvardas Narevicius. Observation of the p -wave shape resonance in atom-molecule collisions. Phys. Rev. Res., 4(4):43042, oct 2022.
- [171] E. Lavert-Ofir, Y. Shagam, A. B. Henson, S. Gersten, J. Klos, P. S. Żuchowski, J. Narevicius, and E. Narevicius. Observation of the isotope effect in sub-kelvin reactions. Nat. Chem., 6(4):332–335, 2014.
- [172] Valentina Zhelyazkova, Fernanda B.V. Martins, Josef A. Agner, Hansjurg Schmutz, and Frederic Merkt. Ion-Molecule Reactions below 1 K: Strong Enhancement of the Reaction Rate of the Ion-Dipole Reaction $\text{He}^{++}\text{CH}_3\text{F}$. Physical Review Letters, 125(26):1–6, 2020.
- [173] P. Puri, M. Mills, I. Simbotin, J. A. Montgomery, R. Côté, C. Schneider, A. G. Suits, and E. R. Hudson. Reaction blockading in a reaction between an excited atom and a charged molecule at low collision energy. Nat. Chem., 11(7):615–621, 2019.
- [174] A. D. Dörfler, P. Eberle, D. Koner, M. Tomza, M. Meuwly, and S. Willitsch. Long-range versus short-range effects in cold molecular ion-neutral collisions. Nat. Comm., 10(1):5429, 2019.
- [175] Raphael D Levine. Molecular reaction dynamics / Raphael Levine., jan 2005.
- [176] M. J. Frisch, G. W. Trucks, H. B. Schlegel, G. E. Scuseria, M. A. Robb, J. R. Cheeseman, G. Scalmani, V. Barone, G. A. Petersson, H. Nakatsuji, X. Li, M. Caricato, A. V. Marenich, J. Bloino, B. G. Janesko, R. Gomperts, B. Mennucci, H. P. Hratchian, J. V. Ortiz, A. F. Izmaylov, J. L. Sonnenberg, D. Williams-Young, F. Ding, F. Lipparini, F. Egidi, J. Goings, B. Peng, A. Petrone, T. Henderson, D. Ranasinghe, V. G. Zakrzewski, J. Gao, N. Rega, G. Zheng, W. Liang, M. Hada, M. Ehara, K. Toyota, R. Fukuda, J. Hasegawa, M. Ishida, T. Nakajima, Y. Honda, O. Kitao, H. Nakai, T. Vreven, K. Throssell, J. A. Montgomery, Jr., J. E. Peralta, F. Ogliaro, M. J. Bearpark, J. J. Heyd, E. N. Brothers, K. N. Kudin, V. N. Staroverov, T. A. Keith, R. Kobayashi, J. Normand, K. Raghavachari, A. P. Rendell, J. C.

- Burant, S. S. Iyengar, J. Tomasi, M. Cossi, J. M. Millam, M. Klene, C. Adamo, R. Cammi, J. W. Ochterski, R. L. Martin, K. Morokuma, O. Farkas, J. B. Foresman, and D. J. Fox. Gaussian16 Revision C.01, 2016. Gaussian Inc. Wallingford CT.
- [177] Robert M. Parrish, Lori A. Burns, Daniel G. A. Smith, Andrew C. Simmonett, A. Eugene De-Prince, Edward G. Hohenstein, Uğur Bozkaya, Alexander Yu. Sokolov, Roberto Di Remigio, Ryan M. Richard, Jérôme F. Gonthier, Andrew M. James, Harley R. McAlexander, Ashutosh Kumar, Masaaki Saitow, Xiao Wang, Benjamin P. Pritchard, Prakash Verma, Henry F. Schaefer, Konrad Patkowski, Rollin A. King, Edward F. Valeev, Francesco A. Evangelista, Justin M. Turney, T. Daniel Crawford, and C. David Sherrill. Psi4 1.1: An open-source electronic structure program emphasizing automation, advanced libraries, and interoperability. *J. Chem. Theory Comput.*, 13(7):3185–3197, 2017.
- [178] Ruben Van de Vijver and Judit Zádor. KinBot: Automated stationary point search on potential energy surfaces. *Computer Physics Communications*, 248:106947, 2020.
- [179] Judit Zádor, Carles Martí, Ruben Van de Vijver, Sommer L. Johansen, Yoona Yang, Hope A. Michelsen, and Habib N. Najm. Automated Reaction Kinetics of Gas-Phase Organic Species over Multiwell Potential Energy Surfaces. *Journal of Physical Chemistry A*, 127(3):565–588, 2023.
- [180] Frank Jensen. *Introduction to Computational Chemistry*. John Wiley & Sons, Incorporated, Newark, UNITED STATES, 2017.
- [181] David C Young. *Computational chemistry : a practical guide for applying techniques to real world problems*. Wiley, jan 2001.
- [182] Donald A (Donald Allan) McQuarrie. *Physical chemistry : a molecular approach*. Sausalito, Calif. : University Science Books, [1997] ©1997, 1997.
- [183] W. Kohn and L. J. Sham. Self-consistent equations including exchange and correlation effects. *Phys. Rev.*, 140:A1133–A1138, Nov 1965.
- [184] Frédéric Castet and Benoît Champagne. Assessment of DFT Exchange-Correlation Functionals for Evaluating the Multipolar Contributions to the Quadratic Nonlinear Optical Responses of Small Reference Molecules. *J. Chem. Theory Comput.*, 8(6):2044–2052, Jun 2012.
- [185] Jeffrey I Steinfeld. *Chemical kinetics and dynamics* / Jeffrey I. Steinfeld, Joseph S. Francisco, William L. Hase., jan 1989.
- [186] James A Miller and Stephen J Klippenstein. Master Equation Methods in Gas Phase Chemical Kinetics. *The Journal of Physical Chemistry A*, 110(36):10528–10544, sep 2006.
- [187] David L Osborn. Reaction Mechanisms on Multiwell Potential Energy Surfaces in Combustion (and Atmospheric) Chemistry. *Annual Review of Physical Chemistry*, 68(1):233–260, 2017.
- [188] Thanh Lam Nguyen and John F Stanton. A Steady-State Approximation to the Two-Dimensional Master Equation for Chemical Kinetics Calculations. *The Journal of Physical Chemistry A*, 119(28):7627–7636, 2015.

- [189] Martin Stei, Eduardo Carrascosa, Alexander Dörfler, Jennifer Meyer, Balázs Olasz, Gábor Czako, Anyang Li, Hua Guo, and Roland Wester. Stretching vibration is a spectator in nucleophilic substitution. *Science Advances*, 4(7), 2018.
- [190] O. A. Krohn, K. J. Catani, J. Greenberg, S. P. Sundar, G. da Silva, and H. J. Lewandowski. Isotope-specific reactions of acetonitrile (CH_3CN) with trapped, translationally cold CCl^+ . *J. Chem. Phys.*, 154:074305, 2021.
- [191] Lewis E. Snyder and David Buhl. Observations of Radio Emission from Interstellar Hydrogen Cyanide. *Astrophys. J. Lett.*, 163:L47, January 1971.
- [192] K. B. Jefferts, A. A. Penzias, and R. W. Wilson. Deuterium in the Orion Nebula. *Astrophys. J. Lett.*, 179:L57, January 1973.
- [193] B. A. McGuire, A. M. Burkhardt, S. Kalenskii, C. N. Shingledecker, A. J. Remijan, E. Herbst, and M. C. McCarthy. Detection of the aromatic molecule benzonitrile ($c\text{-C}_6\text{H}_5\text{CN}$) in the interstellar medium. *Science*, 359(6372):202–205, 2018.
- [194] J. H. Waite, D. T. Young, T. E. Cravens, A. J. Coates, F. J. Crary, B. Magee, and J. Westlake. The process of tholin formation in titan’s upper atmosphere. *Science*, 316(5826):870–875, 2007.
- [195] A. Ali, E. C. Sittler, D. Chornay, B. R. Rowe, and C. Puzzarini. Organic chemistry in Titan’s upper atmosphere and its astrobiological consequences: I. Views towards Cassini plasma spectrometer (CAPS) and ion neutral mass spectrometer (INMS) experiments in space. *Planet. Space Sci.*, 109-110(1):46–63, 2015.
- [196] P. M. Solomon, K. B. Jefferts, A. A. Penzias, and R. W. Wilson. Detection of Millimeter Emission Lines from Interstellar Methyl Cyanide. *Astrophys. J.*, 168:L107, 1971.
- [197] H. E. Matthews and T. J. Sears. Detection of the $J = 1 \rightarrow 0$ transition of CH_3CN . *Astrophys. J. Lett.*, 267:L53–L57, April 1983.
- [198] C. Codella, M. Benedettini, M. T. Beltrán, F. Gueth, S. Viti, R. Bachiller, M. Tafalla, S. Cabrit, A. Fuente, and B. Lefloch. Methyl cyanide as tracer of bow shocks in L1157-B1. *Astron. Astrophys.*, 507(2):L25–L28, 2009.
- [199] S. E. Bisschop, J. K. Jørgensen, T. L. Bourke, S. Bottinelli, and E. F. van Dishoeck. An interferometric study of the low-mass protostar iras 16293-2422: small scale organic chemistry*. *Astron. Astrophys.*, 488(3):959–968, 2008.
- [200] S. Cazaux, A. G. G. M. Tielens, C. Ceccarelli, A. Castets, V. Wakelam, E. Caux, B. Parise, and D. Teyssier. The hot core around the low-mass protostar IRAS 16293-2422: Scoundrels rule! *Astrophys. J.*, 593(1):L51–L55, Jul 2003.
- [201] S. E. Bisschop, J. K. Jørgensen, E. F. van Dishoeck, and E. B. M. de Wachter. Testing grain-surface chemistry in massive hot-core regions*. *Astron. Astrophys.*, 465(3):913–929, 2007.
- [202] J Kissel and F R Krueger. The organic component in dust from comet Halley as measured by the PUMA mass spectrometer on board Vega 1. *Nature*, 326(6115):755–760, 1987.

- [203] Nicolas Biver, Dominique Bockelée-Morvan, Pierre Colom, Jacques Crovisier, John K. Davies, William R. F. Dent, Didier Despois, Eric Gérard, Emmanuel Lellouch, Heike Rauer, Raphael Moreno, and Gabriel Paubert. Evolution of the outgassing of comet hale-bopp (c/1995 o1) from radio observations. *Science*, 275(5308):1915–1918, 1997.
- [204] A. D. Morse and Q. H. S. Chan. Observations of Cometary Organics: A Post Rosetta Review. *ACS Earth Space Chem.*, 3(9):1773–1791, sep 2019.
- [205] M. Gerin, F. Combes, G. Wlodarczak, T. Jacq, M. Guelin, P. Encrenaz, and C. Laurent. Interstellar detection of deuterated methyl cyanide. *Astron. Astrophys.*, 259:L35–L38, Jun 1992.
- [206] A. Belloche, H. S. P. Müller, R. T. Garrod, and K. M. Menten. Exploring molecular complexity with alma (emoca): Deuterated complex organic molecules in sagittarius b2(n2). *Astron. Astrophys.*, 587:A91, 2016.
- [207] B. A. McGuire. 2018 Census of Interstellar, Circumstellar, Extragalactic, Protoplanetary Disk, and Exoplanetary Molecules. *Astrophys. J., Suppl. Ser.*, 239(2):17, 2018.
- [208] Edith C Fayolle, Karin I Öberg, Jes K Jørgensen, Kathrin Altwegg, Hannah Calcutt, Holger S P Müller, Martin Rubin, Matthijs H D van der Wiel, Per Bjerkerli, Tyler L Bourke, Audrey Coutens, Ewine F van Dishoeck, Maria N Drozdovskaya, Robin T Garrod, Niels F W Ligterink, Magnus V Persson, Susanne F Wampfler, H Balsiger, J J Berthelier, J De Keyser, B Fiethe, S A Fuselier, S Gasc, T I Gombosi, T Sémon, C Y. Tzou, and the ROSINA Team. Protostellar and cometary detections of organohalogens. *Nat. Astro.*, 1(10):703–708, 2017.
- [209] D. C. Lis, J. C. Pearson, D. A. Neufeld, P. Schilke, H. S. P. Müller, H. Gupta, T. A. Bell, C. Comito, T. G. Phillips, E. A. Bergin, C. Ceccarelli, P. F. Goldsmith, G. A. Blake, A. Bachmann, A. Baudry, M. Benedettini, A. Benz, J. Black, A. Boogert, S. Bottinelli, S. Cabrit, P. Caselli, A. Castets, E. Caux, J. Cernicharo, C. Codella, A. Coutens, N. Crimier, N. R. Crockett, F. Daniel, K. Demyk, C. Dominic, M. L. Dubernet, M. Emprechtinger, P. Encrenaz, E. Falgarone, A. Fuente, M. Gerin, T. F. Giesen, J. R. Goicoechea, F. Helmich, P. Hennebelle, Th. Henning, E. Herbst, P. Hily-Blant, Å. Hjalmarsen, D. Hollenbach, T. Jack, C. Joblin, D. Johnstone, C. Kahane, M. Kama, M. Kaufman, A. Klotz, W. D. Langer, B. Larsson, J. Le Bourlot, B. Lefloch, F. Le Petit, D. Li, R. Liseau, S. D. Lord, A. Lorenzani, S. Maret, P. G. Martin, G. J. Melnick, Menten, K. M., P. Morris, J. A. Murphy, Z. Nagy, B. Nisini, V. Ossenkopf, S. Pacheco, L. Pagani, B. Parise, M. Pérault, R. Plume, S.-L. Qin, E. Roueff, M. Salez, A. Sandqvist, P. Saraceno, S. Schlemmer, K. Schuster, R. Snell, J. Stutzki, A. Tielens, N. Trappe, F. F. S. van der Tak, M. H. D. van der Wiel, E. van Dishoeck, C. Vastel, S. Viti, V. Wakelam, A. Walters, S. Wang, F. Wyrowski, H. W. Yorke, S. Yu, J. Zmuidzinas, Y. Delorme, J.-P. Desbat, R. Güsten, J.-M. Krieg, and B. Delforge. Herschel/hifi discovery of interstellar chloronium (h2cl+). *Astron. Astrophys.*, 521:L9, 2010.
- [210] David A. Neufeld, Evelyne Roueff, Ronald L. Snell, Dariusz Lis, Arnold O. Benz, Simon Bruderer, John H. Black, Massimo De Luca, Maryvonne Gerin, Paul F. Goldsmith, Harshal Gupta, Nick Indriolo, Jacques Le Bourlot, Franck Le Petit, Bengt Larsson, Gary J. Melnick, Karl M. Menten, Raquel Monje, Zsófia Nagy, Thomas G. Phillips, Aage Sandqvist, Paule Sonnentrucker, Floris van der Tak, and Mark G. Wolfire. HERSCHELOBSERVATIONS OF INTERSTELLAR CHLORONIUM. *Astrophys. J.*, 748(1):37, mar 2012.

- [211] D. A. Neufeld and M. G. Wolfire. The chemistry of interstellar molecules containing the halogen elements. *Astrophys. J.*, 706(2):1594–1604, dec 2009.
- [212] J. Glosik, D. Smith, P. Španěl, W. Freysinger, and W. Lindinger. SIFDT studies of the reactions of C^+ , CH^+ and CH_2^+ with HCl and CO_2 , and CH_3^+ with HCl. *Int. J. Mass Spectrom. Ion Processes*, 129(C):131–143, 1993.
- [213] K. J. Catani, J. Greenberg, B. V. Saarel, and H. J. Lewandowski. Reactions of translationally cold trapped ccl^+ with acetylene (c_2h_2). *J. Chem. Phys.*, 152(23):234310, 2020.
- [214] V. G. Anicich, W. T. Huntress, and M. J. McEwan. Ion-molecule reactions of hydrocarbon ions in acetylene and hydrocyanic acid. *J. Phys. Chem.*, 90(11):2446–2450, 1986.
- [215] A. S. Blair and A. G. Harrison. Bimolecular reactions of trapped ions. vi. ion-molecule reactions involving CH_5^+ and $C_2H_5^+$. *Can. J. Chem.*, 51(10):1645–1654, 1973.
- [216] David Smith, Patrik Španěl, and Christopher A. Mayhew. A selected ion-flow tube study of the reactions of O^+ , H^+ and HeH^+ with several molecular gases at 300 k. *Int. J. Mass Spectrom. Ion Processes*, 117:457 – 473, 1992.
- [217] A. Petrank, M. Iraqi, I. Dotan, and C. Lifshitz. Proton transfer reactions of $C_2H_4^+$: the bond energy $d(C_2H_3-H)$. *Int. J. Mass Spectrom. Ion Processes*, 117:223 – 236, 1992.
- [218] M. Iraqi, A. Petrank, M. Peres, and C. Lifshitz. Proton transfer reactions of $C_2H_2^{\bullet+}$: the bond energy $d_0(C_2H-H)$. *Int. J. Mass Spectrom. Ion Processes*, 100:679 – 691, 1990.
- [219] Masaharu Tsuji, Masato Aizawa, Hiroki Ujita, and Yukio Nishimura. Mass-spectrometric study on ion-molecule reactions of cf_3^+ with nitrogen-containing benzene derivatives, pyridine, pyrrole, and acetonitrile at near-thermal energy. *Bull. Chem. Soc. Jpn.*, 68(8):2385–2392, 1995.
- [220] D. Smith and N.G. Adams. The selected ion flow tube (sift): Studies of ion-neutral reactions. *Adv. At. Mol. Phys.*, 24:1–49, 1988.
- [221] J L Beauchamp. Ion cyclotron resonance spectroscopy. *Annual Review of Physical Chemistry*, 22(1):527–561, 1971.
- [222] K. Okada, Y. Takada, N. Kimura, M. Wada, and H. A. Schuessler. Development of a wavy stark velocity filter for studying interstellar chemistry. *Rev. Sci. Instr.*, 88(8):083106, 2017.
- [223] A. Kilaj, H. Gao, D. Rösch, U. Rivero, J. Küpper, and S. Willitsch. Observation of different reactivities of para and ortho-water towards trapped diazenylium ions. *Nat. Comm.*, 9(1):2096, 2018.
- [224] P. C. Schmid, M. I. Miller, J. Greenberg, T. L. Nguyen, J. F. Stanton, and H. J. Lewandowski. Quantum-state-specific reaction rate measurements for the photo-induced reaction $Ca^+ + O_2 \rightarrow CaO^+ + O$. *Mol. Phys.*, 117(21):3036–3042, 2019.
- [225] J. Greenberg, P. C. Schmid, M. Miller, J. F. Stanton, and H. J. Lewandowski. Quantum-state-controlled reactions between molecular radicals and ions. *Phys. Rev. A*, 98:032702, 2018.

- [226] Peter F Staantum, Klaus Højbjerg, Peter S Skyt, Anders K Hansen, and Michael Drewsen. Rotational laser cooling of vibrationally and translationally cold molecular ions. *Nat. Phys.*, 6(4):271–274, 2010.
- [227] Yuntao Xu, Bo Xiong, Yih Chung Chang, and Cheuk-Yiu Ng. Quantum-State-Selected Integral Cross Sections and Branching Ratios for the Ion–Molecule Reaction of $N_2+(X^2\Sigma_g^+; \nu_+ = 0-2) + C_2H_4$ in the Collision Energy Range of 0.05–10.00 eV. *J. Phys. Chem. A*, 122(32):6491–6499, aug 2018.
- [228] C. Q. Jiao, D. R. A. Ranatunga, W. E. Vaughn, and B. S. Freiser. A pulsed-leak valve for use with ion trapping mass spectrometers. *J. Am. Soc. Mass Spectrom.*, 7(1):118–122, Jan 1996.
- [229] K Jousten. Gauges for fine and high vacuum. *CAS Cern Accelerator School*, 2007.
- [230] John R. Barker, T. L. Nguyen, J. F. Stanton, C. Aieta, M. Ceotto, F. Gabas, T. J. D Kumar, C. G. L. Li, L. L. Lohr, A Maranzana, N. F Ortiz, J. M. Preses, J. M. Simmie, J. A. Sonk, and P. J. Stimac. Multiwell-2020 software suite. <http://clasp-research.engin.umich.edu/multiwell/>, 2020.
- [231] John R Barker. Multiple-well, multiple-path unimolecular reaction systems. i. multiwell computer program suite. *Int. J. Chem. Kinet.*, 33(4):232–245, 2001.
- [232] John R Barker. Energy transfer in master equations simulations: A new approach. *Int. J. Chem. Kinet.*, 41:748–763, 2009.
- [233] G. da Silva, B. B. Kirk, C. Lloyd, A. J. Trevitt, and S. J. Blanksby. Concerted HO_2 elimination from alpha-aminoalkylperoxyl free radicals: Experimental and theoretical evidence from the gas-phase $NH_2CHCO_2^- + O_2$ reaction. *J. Phys. Chem. Lett.*, 3:805–811, 2012.
- [234] K. J. Catani, G. Muller, G. da Silva, and E. J. Bieske. Electronic spectrum and photodissociation chemistry of the linear methyl propargyl cation $H_2C_4H_3^+$. *J. Chem. Phys.*, 146:044307, 2017.
- [235] J. N. Bull, M. S. Scholz, E. Carrascosa, G. da Silva, and E. J. Bieske. Double molecular photoswitch driven by light and collisions. *Physical Review Letters*, 120:223002, 2018.
- [236] G. P. Smith and D. M. Golden. Application of rrkm theory to the reactions $OH + NO_2 + N_2 \rightarrow HONO_2 + N_2$ (1) and $clo + NO_2 + N_2 \rightarrow ClONO_2 + N_2$ (2); a modified gorin model transition state. *Int. J. Chem. Kinet.*, 10:489–501, 1978.
- [237] A. K. Y. Lam, C. Li, G. Khairallah, B. B. Kirk, S. J. Blanksby, A. J. Trevitt, U. Wille, R. A. J. O’Hair, and G. da Silva. Gas-phase reactions of aryl radicals with 2-butyne: An experimental and theoretical investigation employing the n-methyl-pyridinium-4-yl radical cation. *Phys. Chem. Chem. Phys.*, 14:2417–2426, 2012.
- [238] J. A. Burt, J. L. Dunn, M. J. McEwan, M. M. Sutton, A. E. Roche, and H. I. Schiff. Some ion–molecule reactions of h_3^+ and the proton affinity of h_2 . *J. Chem. Phys.*, 52(12):6062–6075, 1970.
- [239] Brian T Psciuk, Victor A Benderskii, and H Bernhard Schlegel. Protonated acetylene revisited. *Theor. Chem. Acc.*, 118(1):75–80, 2007.

- [240] Mark W. Crofton, MaryFrances Jagod, Brent D. Rehfuss, and Takeshi Oka. Infrared spectroscopy of carbo-ions. v. classical vs nonclassical structure of protonated acetylene c_2h+3 . J. Chem. Phys., 91(9):5139–5153, 1989.
- [241] Amit R. Sharma, Jiayan Wu, Bastiaan J. Braams, Stuart Carter, Ralf Schneider, Ben Shepler, and Joel M. Bowman. Potential energy surface and multimode vibrational analysis of c_2h_3+ . J. Chem. Phys., 125(22):224306, 2006.
- [242] O. A. Krohn, K. J. Catani, and H. J. Lewandowski. Formation of astrochemically relevant molecular ions: Reaction of translationally cold CCl^+ with benzene in a linear ion trap. Physical Review A, 105(2):1–6, 2022.
- [243] Theodore P Snow, Valery Le Page, Yeghis Keheyan, and Veronica M Bierbaum. The interstellar chemistry of PAH cations. Nature, 391(6664):259–260, 1998.
- [244] V. Vuitton, R. V. Yelle, and J. Cui. Formation and distribution of benzene on titan. J. Geophys. Res. Planets, 113(E5), 2008.
- [245] A.G.G.M. Tielens. Interstellar polycyclic aromatic hydrocarbon molecules. Annu. Rev. Astron. Astrophys., 46(1):289–337, 2008.
- [246] Eric Herbst and Ewine F. van Dishoeck. Complex organic interstellar molecules. Annu. Rev. Astron. Astrophys., 47(1):427–480, 2009.
- [247] J. H. Westlake, J. H. Waite Jr., N. Carrasco, M. Richard, and T. Cravens. The role of ion-molecule reactions in the growth of heavy ions in titan’s ionosphere. J. Geophys. Res. Space Physics, 119:5951–5963, 2014.
- [248] Bruno Bézard, Pierre Drossart, Thérèse Encrenaz, and Helmut Feuchtgruber. Benzene on the giant planets. Icarus, 154(2):492–500, 2001.
- [249] E K Campbell, M Holz, D Gerlich, and J P Maier. Laboratory confirmation of C_{60}^+ as the carrier of two diffuse interstellar bands. Nature, 523(7560):322–323, 2015.
- [250] Christian P Endres, Stephan Schlemmer, Peter Schilke, Jürgen Stutzki, and Holger SP Müller. The cologne database for molecular spectroscopy, cdms, in the virtual atomic and molecular data centre, vamdc. J. Mol. Spectrosc., 327:95–104, 2016.
- [251] Eric Herbst. The synthesis of large interstellar molecules. Int. Rev. Phys. Chem., 36:287–331, 2017.
- [252] E. K. Campbell. Spectroscopy of astrophysically relevant ions in traps. Mol. Phys., 118:1–12, 2020.
- [253] Diethard K. Bohme. Pah and fullerene ions and ion/molecule reactions in interstellar and circumstellar chemistry. Chem. Rev., 92:1487–1508, 1992.
- [254] D. Calzetti, R. C. Kennicutt, C. W. Engelbracht, C. Leitherer, B. T. Draine, L. Kewley, J. Moustakas, M. Sosey, D. A. Dale, K. D. Gordon, G. X. Helou, D. J. Hollenbach, L. Armus, G. Bendo, C. Bot, B. Buckalew, T. Jarrett, A. Li, M. Meyer, E. J. Murphy, M. Prescott, M. W. Regan, G. H. Rieke, H. Roussel, K. Sheth, J. D. T. Smith, M. D. Thornley, and F. Walter. The calibration of mid-infrared star formation rate indicators. Astrophys. J., 666(2):870–895, sep 2007.

- [255] J. D. T. Smith, B. T. Draine, D. A. Dale, J. Moustakas, Jr. R. C. Kennicutt, G. Helou, L. Armus, H. Roussel, K. Sheth, G. J. Bendo, B. A. Buckalew, D. Calzetti, C. W. Engelbracht, K. D. Gordon, D. J. Hollenbach, A. Li, S. Malhotra, E. J. Murphy, and F. Walter. The mid-infrared spectrum of star-forming galaxies: Global properties of polycyclic aromatic hydrocarbon emission. *Astrophys. J.*, 656(2):770–791, feb 2007.
- [256] Jacqueline Kessler-Silacci, Jean-Charles Augereau, Cornelis P. Dullemond, Vincent Geers, Fred Lahuis, Neal J. Evans II, Ewine F. van Dishoeck, Geoffrey A. Blake, A. C. Adwin Boogert, Joanna Brown, Jes K. Jorgensen, Claudia Knez, and Klaus M. Pontoppidan. C2d spitzer irs spectra of disks around t tauri stars. i. silicate emission and grain growth. *Astrophys. J.*, 639(1):275–291, Mar 2006.
- [257] L. Verstraete, J. L. Puget, E. Falgarone, S. Drapatz, C. M. Wright, and R. Timmermann. SWS spectroscopy of small grain features across the M17-Southwest photodissociation front. *Astron. Astrophys.*, 315:L337–L340, November 1996.
- [258] A. Omont. Physics and chemistry of interstellar polycyclic aromatic molecules. *Astron. Astrophys.*, 164:159–178, August 1986.
- [259] A. Leger and J. L. Puget. Identification of the “unidentified” IR emission features of interstellar dust? *Astron. Astrophys.*, 500:279–282, 1984.
- [260] J. L. Puget and A. Leger. A new component of the interstellar matter: small grains and large aromatic molecules. *Annu. Rev. Astron. Astrophys.*, 27:161–198, 1989.
- [261] José Cernicharo, Ana M. Heras, A. G. G. M. Tielens, Juan R. Pardo, Fabrice Herpin, Michel Guélin, and L. B. F. M. Waters. Infrared space observatory’s discovery of C_4H_2 , C_6H_2 , and benzene in CRL 618. *Astrophys. J.*, 546(2):L123–L126, 2001.
- [262] J. Bernard-Salas, E. Peeters, G. C. Sloan, J. Cami, S. Guiles, and J. R. Houck. The spitzer IRS spectrum of SMP LMC 11. *Astrophys. J.*, 652(1):L29–L32, 2006.
- [263] Simon Petrie, Gholamreza Javahery, and Diethard K. Bohme. Gas-phase reactions of benzenoid hydrocarbon ions with hydrogen atoms and molecules: uncommon constraints to reactivity. *J. Am. Chem. Soc.*, 114(23):9205–9206, 1992.
- [264] Graham B. I. Scott, David A. Fairley, Colin G. Freeman, Murray J. McEwan, Nigel G. Adams, and Lucia M. Babcock. $C_mH_n^+$ reactions with h and H_2 : An experimental study. *J. Phys. Chem. A*, 101(27):4973–4978, 1997.
- [265] Serge A. Krasnokutski and Friedrich Huisken. Ultra-low-temperature reactions of $c(3p0)$ atoms with benzene molecules in helium droplets. *J. Chem. Phys.*, 141(21):214306, 2014.
- [266] Steven J. Sibener, Richard J. Buss, Piergiorgio Casavecchia, Tomohiko Hirooka, and Yuan T. Lee. A crossed molecular beams investigation of the reactions $o(3p)+c_6h_6$, c_6d_6 . *The Journal of Chemical Physics*, 72(8):4341–4349, 1980.
- [267] AJ Colussi, DL Singleton, RS Irwin, and RJ Cvetanovic. Absolute rates of oxygen ($3p$) atom reactions with benzene and toluene. *The Journal of Physical Chemistry*, 79(18):1900–1903, 1975.

- [268] D. Ascenzi, P. Franceschi, T.G.M. Freearge, P. Tosi, and D. Bassi. Cn bond formation in the reaction of nitrogen ions $n+$ with benzene molecules. Chemical Physics Letters, 346(1):35–40, 2001.
- [269] Kinsuk Acharyya and Eric Herbst. Gas-grain fluorine and chlorine chemistry in the interstellar medium. Astrophys. J., 850:105, 2017.
- [270] A. Ali, E.C. Sittler, D. Chornay, B.R. Rowe, and C. Puzzarini. Cyclopropenyl cation – the simplest huckel’s aromatic molecule – and its cyclic methyl derivatives in titan’s upper atmosphere. Planetary and Space Science, 87:96 – 105, 2013.
- [271] Vincent G. Anicich, Daniel B. Milligan, David A. Fairley, and Murray J. McEwan. Termolecular Ion–Molecule Reactions in Titan’s Atmosphere, I: Principal Ions with Principal Neutrals. Icarus, 146(1):118 – 124, 2000.
- [272] A Korth, M L Marconi, D A Mendis, F R Krueger, A K Richter, R P Lin, D L Mitchell, K A Anderson, C W Carlson, H Rème, J A Sauvaud, and C D’Uston. Probable detection of organic-dust-borne aromatic $C_3H_3^+$ ions in the coma of comet Halley. Nature, 337(6202):53–55, 1989.
- [273] Daniel Hauser, Seunghyun Lee, Fabio Carelli, Steffen Spieler, Olga Lakhmanskaya, Eric S Endres, Sunil S Kumar, Franco Gianturco, and Roland Wester. Rotational state-changing cold collisions of hydroxyl ions with helium. Nature Physics, 11(6):467–470, 2015.
- [274] Stefan Willitsch, Martin T. Bell, Alexander D. Gingell, and Timothy P. Softley. Chemical applications of laser- and sympathetically-cooled ions in ion traps. Phys. Chem. Chem. Phys., 10:7200–7210, 2008.
- [275] Yan Zhao and Donald G. Truhlar. The m06 suite of density functionals for main group thermochemistry, thermochemical kinetics, noncovalent interactions, excited states, and transition elements: two new functionals and systematic testing of four m06-class functionals and 12 other functionals. Theor. Chem. Acc., 120(1):215–241, 2008.
- [276] Thom H Dunning Jr. Gaussian basis sets for use in correlated molecular calculations. i. the atoms boron through neon and hydrogen. J. Chem. Phys., 90(2):1007–1023, 1989.
- [277] Rick A Kendall, Thom H Dunning Jr., and Robert J Harrison. Electron affinities of the first-row atoms revisited. systematic basis sets and wave functions. J. Chem. Phys., 96(9):6796–6806, 1992.
- [278] David E Woon and Thom H Dunning Jr. Gaussian basis sets for use in correlated molecular calculations. iii. the atoms aluminum through argon. J. Chem. Phys., 98(2):1358–1371, 1993.
- [279] A. Halkier, T. Helgaker, P. Jørgensen, W. Klopper, and J. Olsen. Basis-set convergence of the energy in molecular hartree–fock calculations. Chem. Phys. Lett., 302:437–446, 1999.
- [280] Richard D. Smith and James J. DeCorpo. A study of the mechanism of (2p) carbon ion reactions with benzene at 1.0 to 12 ev. J. Phys. Chem., 80(26):2904–2910, 1976.
- [281] Richard D. Smith and Jean H. Futrell. Reactions of thermal energy (2p) C^+ ions with several molecules. Int. J. Mass Spectrom. Ion Phys., 26(2):111–113, 1978.

- [282] R. I. Kaiser, I. Hahndorf, L. C. L. Huang, Y. T. Lee, H. F. Bettinger, P. v. R. Schleyer, H. F. Schaefer, and P. R. Schreiner. Crossed beams reaction of atomic carbon, $C(^3P_j)$, with d6-benzene, C_6D_6 ($X \cdot^1 A_{1g}$): Observation of the per-deutero-1,2-didehydro-cycloheptatrienyl radical, C_7D_5 ($X \cdot^2 B_2$). J. Chem. Phys., 110:6091–6094, 1999.
- [283] D.K. Bohme, A.B. Rakshit, and H.I. Schiff. Reactions of $^{12}C^+$ with hydrocarbons at 296 k:carbon-carbon bond formation. Chem. Phys. Lett., 93(6):592–597, 1982.
- [284] O. Asvany, C. R. Markus, K. Nagamori, H. Kohguchi, J. Furuta, K. Kobayashi, S. Schlemmer, and S. Thorwirth. Pure rotational spectrum of CCl^+ . Astrophys. J., 910(1):15, mar 2021.
- [285] O A Krohn, K J Catani, Srivathsan P. Sundar, James Greenberg, G da Silva, and H J Lewandowski. Reactions of Acetonitrile with Trapped, Translationally Cold Acetylene Cations. The Journal of Physical Chemistry A, 127(24):5120–5128, jun 2023.
- [286] John M. Goodings, Scott D. Tanner, and Diethard K. Bohme. Hydrocarbon ions in fuel-rich, CH_4 - C_2H_2 - O_2 flames as a probe for the initiation of soot: interpretation of the ion chemistry. Can. J. Chem., 60(22):2766–2776, 1982.
- [287] Michael Frenklach. Reaction mechanism of soot formation in flames. Phys. Chem. Chem. Phys., 4(11):2028–2037, 2002.
- [288] D. G. Keil, R. J. Gill, D. B. Olson, and H. F. Calcote. Ionization and soot formation in premixed flames. Symp. (Int.) Combust., [Proc.], 20(1):1129–1137, 1985.
- [289] H F Calcote and D G Keil. The role of ions in soot formation. Pure & Appl. Chem., 62(5):815–824, 1990.
- [290] H F Calcote and D G Keil. Ion-molecule reactions in sooting acetylene-oxygen flames. Combust. Flame, 74(2):131–146, 1988.
- [291] H F Calcote. Mechanisms of soot nucleation in flames—a critical review. Combust. Flame, 42:215–242, 1981.
- [292] AB Fialkov, AN Hayhurst, SG Taylor, and SB Newcomb. Shapes of soot particles, both charged and uncharged, after molecular beam sampling a premixed oxyacetylene flame, burning at atmospheric pressure. Combust. Sci. Technol., 185(12):1762–1776, 2013.
- [293] Allan N Hayhurst and Howard R N Jones. Ions and soot in flames. J. Chem. Soc., Faraday Trans. 2, 83(1):1–27, 1987.
- [294] N M Semo and W S Koski. Some ion-molecule reactions pertinent to combustion. J. Phys. Chem., 88:5320–5324, 1984.
- [295] H. I. Schiff and D. K. Bohme. An ion-molecule scheme for the synthesis of hydrocarbon-chain and organonitrogen molecules in dense interstellar clouds. Astrophys. J., 232:740–746, 1979.
- [296] J. J. Myher and A. G. Harrison. Ion-molecule reactions in acetylene and acetylene-methane mixtures. Can. J. Chem., 46(10):1755–1762, 1968.
- [297] Hartmut Palm, Christian Alcaraz, Philippe Millié, and Odile Dutuit. State-selected $C_2H_2^+ + C_2H_4$ reaction: Controlled by dynamics or statistics? Int. J. Mass Spectrom., 249-250:31–44, 2006.

- [298] Martin F. Jarrold, Lewis M. Bass, Paul R. Kemper, Petra A. M. van Koppen, and Michael T. Bowers. Unimolecular and bimolecular reactions in the $C_4H_6^+$ system: Experiment and theory. *J. Chem. Phys.*, 78(6):3756–3766, 1983.
- [299] Vincent G. Anicich, Paul F. Wilson, and Murray J. McEwan. An ict study of ion-molecules reactions relevant to titan’s atmosphere: An investigation of binary hydrocarbon mixtures up to 1 micron. *J. Am. Soc. Mass Spectrom.*, 17(4):544–561, 2006.
- [300] K. Mølhave and M. Drewsen. Formation of translationally cold mgh^+ and mgd^+ molecules in an ion trap. *Phys. Rev. A*, 62:011401, Jun 2000.
- [301] Emma E. Rennie, Louise Cooper, Larisa G. Shpinkova, David M.P. Holland, David A. Shaw, and Paul M. Mayer. Threshold photoelectron photoion coincidence spectroscopy sheds light on the dissociation of pyrrole and thiophene molecular ions. *Int. J. of Mass Spectrom.*, 290(2):142–144, 2010.
- [302] Gary D. Willett and Tomas Baer. Thermochemistry and dissociation dynamics of state-selected c_4h_4x ions. 3. $c_4h_5n^+$. *J. Am. Chem. Soc.*, 102(22):6774–6779, 1980.
- [303] E.E. Rennie, C.A.F. Johnson, J.E. Parker, R. Ferguson, D.M.P. Holland, and D.A. Shaw. A photoabsorption and mass spectrometry study of pyrrole. *Chem. Phys.*, 250(2):217–236, 1999.
- [304] J. C. Van Craen, M. Herman, R. Colin, and J. K. G. Watson. The $\tilde{a} - \tilde{x}$ band system of acetylene: Analysis of medium-wavelength bands, and vibration-rotation constants for the levels $n\nu'_3$ ($n = 4 - 6$), $\nu'_2 + n\nu'_3$ ($n = 3 - 5$), and $\nu'_1 + n\nu'_3$ ($n = 2, 3$). *J. Mol. Spectrosc.*, 111(1):185–197, 1985.
- [305] Gabriel da Silva. G3x-k theory: A composite theoretical method for thermochemical kinetics. *Chem. Phys. Lett.*, 558:109–113, 2013.
- [306] K Okada, M Wada, L Boesten, T Nakamura, I Katayama, and S Ohtani. Acceleration of the chemical reaction of trapped ca ions with h2o molecules by laser excitation. *J. Phys. B: At. Mol. Opt. Phys.*, 36:33–46, 2002.
- [307] M. Peri, B. Engels, and M. Hanrath. Ab initio study of the electronic spectrum of $c_2h_2^{+}$: I. vertical spectrum and angular potential curves. *Chem. Phys.*, 238(1):33–46, 1998.
- [308] Ralph C. Gillen, Bojana Ostojic, and Wolfgang Domcke. Theoretical investigation of a_2g+x_2u vibronic-coupling and ultrafast internal-conversion dynamics in the acetylene cation. *Chem. Phys.*, 272(1):1–14, 2001.
- [309] G. Chambaud, R. Van den Boom, and P. Rosmus. On the mechanism of the energy redistribution in the $a_2g(2g^+)$ state of the $hcch^+$ ion. *Chem. Phys. Lett.*, 247(1):79–84, 1995.
- [310] John M Gray, Jason Bossert, Yomay Shyur, Ben Saarel, Travis C Briles, and HJ Lewandowski. Characterization of a vacuum ultraviolet light source at 118 nm. *J. Chem. Phys.*, 154(2):024201, 2021.
- [311] Andreas Osterwalder, Samuel A. Meek, Georg Hammer, Henrik Haak, and Gerard Meijer. Deceleration of neutral molecules in macroscopic traveling traps. *Phys. Rev. A*, 81:051401, May 2010.

- [312] Marina Quintero-Pérez, Paul Jansen, Thomas E. Wall, Joost E. van den Berg, Steven Hoekstra, and Hendrick L. Bethlem. Static trapping of polar molecules in a traveling wave decelerator. Phys. Rev. Lett., 110:133003, Mar 2013.
- [313] Giacinto Scoles. Atomic and molecular beam methods. Oxford University Press, 1988.
- [314] Sebastiaan Y.T. Van De Meerakker, Hendrick L. Bethlem, Nicolas Vanhaecke, and Gerard Meijer. Manipulation and control of molecular beams. Chemical Reviews, 112(9):4828–4878, 2012.
- [315] Stephen D. Hogan, Michael Motsch, and Frédéric Merkt. Deceleration of supersonic beams using inhomogeneous electric and magnetic fields. Physical Chemistry Chemical Physics, 13(42):18705–18723, 2011.
- [316] Jon B Cross and James J Valentini. High repetition rate pulsed nozzle beam source. Review of Scientific Instruments, 53(1):38–42, 1982.
- [317] D Proch and T Trickl. A high-intensity multi-purpose piezoelectric pulsed molecular beam source. Review of Scientific Instruments, 60(4):713–716, 1989.
- [318] Wolfgang Christen and Klaus Rademann. Cooling and slowing in high-pressure jet expansions. Phys. Rev. A, 77:012702, Jan 2008.
- [319] Matteo Leone, Alessandro Paoletti, and Nadia Robotti. A Simultaneous Discovery: The Case of Johannes Stark and Antonino Lo Surdo. Physics in Perspective, 6(3):271–294, 2004.
- [320] Johannes Stark. 'the synthesis of ammonia from its elements. Nobelprize.org, 1919.
- [321] John M Gray. Measurement of Cold Molecular Collisions between co-trapped OH and Rb. PhD thesis, University of Colorado, 2022.
- [322] Fritz Haber. 'the synthesis of ammonia from its elements. Nobelprize.org, 1920.
- [323] A. C. Cheung, D. M. Rank, C. H. Townes, D. D. Thornton, and W. J. Welch. Detection of NH₃ molecules in the interstellar medium by their microwave emission. Physical Review Letters, 21(25):1701–1705, 1968.
- [324] R. Martin and P. Ho. Detection of extragalactic ammonia. Astronomy and Astrophysics, 1979.
- [325] W Hermsen, T. L. Wilson, C. M. Walmsley, and W. Batrla. N-15H₃ in Orion-KL. The hot core is not so hot. Astron. Astrophys., 146:134–138, 1985.
- [326] Patrick G.J. Irwin, Neil Bowles, Ashwin S. Braude, Ryan Garland, and Simon Calcutt. Analysis of gaseous ammonia (NH₃) absorption in the visible spectrum of Jupiter. Icarus, 302:426–436, 2018.
- [327] E Roueff, D C Lis, F van der Tak, M Gerin, and P F Goldsmith. Interstellar deuterated ammonia: from NH₃ to ND₃. Astron. Astrophys., 438(2):585–598, 2005.
- [328] Vachail N. Salinas, Michiel R. Hogerheijde, Edwin A. Bergin, L. Ilse de Cleves, Christian Brinch, Geoffrey A. Blake, Dariusz C. Lis, Gary J. Melnick, Olja Panić, John C. Pearson, Lars Kristensen, Umut A. Yildiz, and Ewine F. van Dishoeck. First detection of gas-phase ammonia in a planet-forming disk. Astronomy & Astrophysics, 591:A122, 2016.

- [329] A. C. CHEUNG, D. M. RANK, C. H. TOWNES, and W. J. WELCH. Further Microwave Emission Lines and Clouds of Ammonia in our Galaxy. Nature, 221(5184):917–919, mar 1969.
- [330] Paul T P Ho and Charles H Townes. Interstellar Ammonia. Annual Review of Astronomy and Astrophysics, 21(1):239–270, 1983.
- [331] G. Danby, D. R. Flower, P. Valiron, P. Schilke, and C. M. Walmsley. A recalibration of the interstellar ammonia thermometer. Monthly Notices of the Royal Astronomical Society, 235(1):229–238, nov 1988.
- [332] S. Maret, A. Faure, E. Scifoni, and L. Wiesenfeld. On the robustness of the ammonia thermometer. Monthly Notices of the Royal Astronomical Society, 399(1):425–431, 2009.
- [333] Hendrick L. Bethlem, Giel Berden, Floris M. H. Cromptvoets, Rienk T. Jongma, André J. A. van Rooij, and Gerard Meijer. Electrostatic trapping of ammonia molecules. Nature, 406(6795):491–494, aug 2000.
- [334] Floris M.H. Cromptvoets, Hendrick L. Bethlem, Rienk T. Jongma, and Gerard Meijer. A prototype storage ring for neutral molecules. Nature, 411(6834):174–176, 2001.
- [335] Floris M.H. Cromptvoets, Hendrick L. Bethlem, and Gerard Meijer. A Storage Ring for Neutral Molecules. Advances in Atomic, Molecular and Optical Physics, 52(05):209–287, 2005.
- [336] Hendrick L. Bethlem, Floris M.H. Cromptvoets, Rienk T. Jongma, Sebastiaan Y.T. van de Meerakker, and Gerard Meijer. Deceleration and trapping of ammonia using time-varying electric fields. Physical Review A - Atomic, Molecular, and Optical Physics, 65(5):20, 2002.
- [337] Sebastiaan YT van de Meerakker, Nicolas Vanhaecke, Hendrick L Bethlem, and Gerard Meijer. Transverse stability in a stark decelerator. Physical Review A, 73(2):023401, 2006.
- [338] David L Reens. Pushing the Limits for Directly Cooled Molecules. PhD thesis, University of Colorado, 2019.
- [339] Ludwig Scharfenberg, Henrik Haak, Gerard Meijer, and Sebastiaan YT van de Meerakker. Operation of a stark decelerator with optimum acceptance. Physical Review A, 79(2):023410, 2009.
- [340] LP Parazzoli, N Fitch, DS Lobser, and HJ Lewandowski. High-energy-resolution molecular beams for cold collision studies. New Journal of Physics, 11(5):055031, 2009.
- [341] Moritz Kirste, Xingan Wang, H. Christian Schewe, Gerard Meijer, Kopin Liu, Ad Van Der Avoird, Liesbeth M.C. Janssen, Koos B. Gubbels, Gerrit C. Groenenboom, and Sebastiaan Y.T. Van De Meerakker. Quantum-state resolved bimolecular collisions of velocity-controlled OH with NO radicals. Science, 338(6110):1060–1063, 2012.
- [342] Eric R. Hudson, H. J. Lewandowski, Brian C. Sawyer, and Jun Ye. Cold molecule spectroscopy for constraining the evolution of the fine structure constant. Physical Review Letters, 96(14):1–4, 2006.
- [343] JA Hernandez and Andre Koch Torres Assis. Electric potential for a resistive toroidal conductor carrying a steady azimuthal current. Phys. Rev. E, 68(4):046611, 2003.

- [344] M. I. Fabrikant, Tian Li, N. J. Fitch, N. Farrow, Jonathan D. Weinstein, and H. J. Lewandowski. Method for traveling-wave deceleration of buffer-gas beams of ch. Phys. Rev. A, 90:033418, Sep 2014.
- [345] Marina Quintero-Prez, Thomas E. Wall, Steven Hoekstra, and Hendrick L. Bethlem. Preparation of an ultra-cold sample of ammonia molecules for precision measurements. Journal of Molecular Spectroscopy, 300:112–115, 2014. Spectroscopic Tests of Fundamental Physics.
- [346] Congsen Meng, Aernout P. P. van der Poel, Cunfeng Cheng, and Hendrick L. Bethlem. Femtosecond laser detection of stark-decelerated and trapped methylfluoride molecules. Phys. Rev. A, 92:023404, Aug 2015.
- [347] Paul Jansen, Marina Quintero-Pérez, Thomas E. Wall, Joost E. van den Berg, Steven Hoekstra, and Hendrick L. Bethlem. Deceleration and trapping of ammonia molecules in a traveling-wave decelerator. Phys. Rev. A, 88:043424, Oct 2013.
- [348] Victoria A Cho and Richard B Bernstein. Tight focusing of beams of polar polyatomic molecules via the electrostatic hexapole lens. J. Phys. Chem., 95(21):8129–8136, 1991.
- [349] Philip R. Brooks, Eugene M. Jones, and K. E.N. Surra. Orienting polar molecules in molecular beams. Symmetric tops. The Journal of Chemical Physics, 51(7):3073–3081, 1969.
- [350] Philip R. Brooks and Eugene M. Jones. Reactive scattering of K atoms from oriented CH₃I molecules. The Journal of Chemical Physics, 45(9):3446–3448, 1966.
- [351] K. H. Kramer and R. B. Bernstein. Focusing and orientation of symmetric-top molecules with the electric six-pole field. The Journal of Chemical Physics, 42(2):767–770, 1965.
- [352] Floris M. H. Cromptvoets, Rienk T. Jongma, Hendrick L. Bethlem, André J. A. van Roij, and Gerard Meijer. Longitudinal focusing and cooling of a molecular beam. Phys. Rev. Lett., 89:093004, Aug 2002.
- [353] Yi Ke, Xiao Bing Deng, and Zhong Kun Hu. Low chromatic aberration hexapole for molecular state selection. Journal of Physics B: Atomic, Molecular and Optical Physics, 49(2), 2015.
- [354] Benjamin Bertsche and Andreas Osterwalder. State-selective detection of velocity-filtered ND₃ molecules. Physical Review A - Atomic, Molecular, and Optical Physics, 82(3):1–8, 2010.
- [355] Cynthia E. Heiner, David Carty, Gerard Meijer, and Hendrick L. Bethlem. A molecular synchrotron. Nature Physics, 3(2):115–118, 2007.
- [356] Cynthia E. Heiner, Hendrick L. Bethlem, and Gerard Meijer. A synchrotron for neutral molecules. Chemical Physics Letters, 473(1-3):1–9, 2009.
- [357] T. Suganuma, K. Okada, N. Kimura, K. Shiina, M. Wada, and H. A. Schuessler. A Stark velocity filter for studying cold polar molecule-molecular ion reactions. Journal of Physics: Conference Series, 388(PART 10):2–4, 2012.
- [358] L. D. Van Buuren, C. Sommer, M. Motsch, S. Pohle, M. Schenk, J. Bayerl, P. W.H. Pinkse, and G. Rempe. Electrostatic extraction of cold molecules from a cryogenic reservoir. Physical Review Letters, 102(3):2–5, 2009.

- [359] Dudley Herschbach. Molecular collisions, from warm to ultracold. Faraday Discussions, 142:9–23, 2009.
- [360] Wesley T. Huntress, Michael M. Mosesman, and Daniel D. Elleman. Relative rates and their dependence on kinetic energy for ion-molecule reactions in ammonia. The Journal of Chemical Physics, 54(3):843–849, 1971.
- [361] R. S. Hemsforth, J. D. Payzant, H. I. Schiff, and D. K. Bohme. Rate constants at 297K for proton transfer reactions with NH_3 . Comparisons with classical theories and exothermicity. Chemical Physics Letters, 26(3):417–421, 1974.
- [362] F. C. Fehsenfeld and E. E. Ferguson. Thermal energy positive ion reactions in a wet atmosphere containing ammonia. The Journal of Chemical Physics, 6276(1973):6272–6276, 1973.
- [363] Nigel G Adams, David Smith, and John F Paulson. An experimental survey of the reactions of NH_n^+ ions ($n = 0$ to 4) with several diatomic and polyatomic molecules at 300 K. The Journal of Chemical Physics, 72(1):288–297, jan 1980.
- [364] Keith R. Ryan and Jean H. Futrell. Effect of Translational Energy on Ion-Molecule Reaction Rates. I. The Journal of Chemical Physics, 42(3):824–829, feb 1965.
- [365] Keith R. Ryan and Jean H. Futrell. Effect of Translational Energy on Ion-Molecule Reaction Rates. II. The Journal of Chemical Physics, 43(9):3009–3014, nov 1965.
- [366] G. A.W. Derwish, A. Galli, A. Giardini-Guidoni, and G. G. Volpi. Ion-molecule reactions in gaseous ammonia. The Journal of Chemical Physics, 39(6):1599–1605, 1963.
- [367] PC Dorfman, Leon M and Noble. Reactions of gaseous ions. Ammonium ion formation in ionized ammonia. The Journal of Physical Chemistry, 63(6):980–982, 1959.
- [368] Shinji Tomoda, Shinzo Suzuki, and Inosuke Koyano. State selected ion-molecule reactions by a coincidence technique. XV. Hydrogen atom abstraction as an electron jump followed by proton transfer in the $\text{ND}_3^+(v)+\text{NH}_3$ and $\text{NH}_3^+(v)+\text{ND}_3$ reactions. The Journal of Chemical Physics, 89(12):7268–7276, 1988.
- [369] Hiroto Tachikawa and Shinji Tomoda. A theoretical study on the vibrationally state-selected hydrogen transfer reaction: $\text{NH}_3^+(\nu) + \text{NH}_3 \rightarrow \text{NH}_4^+ + \text{NH}_2$. An ab initio MR-SD-CI and classical trajectory approach. Chemical Physics, 182(2-3):185–194, 1994.
- [370] William E Conaway, Takayuki Ebata, and Richard N Zare. Vibrationally state selected reactions of ammonia ions. III. NH_3^+ . Journal of Chemical Physics, 87(3):3453–3460, 1987.
- [371] Vincent G. Anicich. Evaluated Bimolecular Ion-Molecule Gas Phase Kinetics of Positive Ions for Use in Modeling Planetary Atmospheres, Cometary Comae, and Interstellar Clouds. Journal of Physical and Chemical Reference Data, 22(6):1469–1569, 1993.

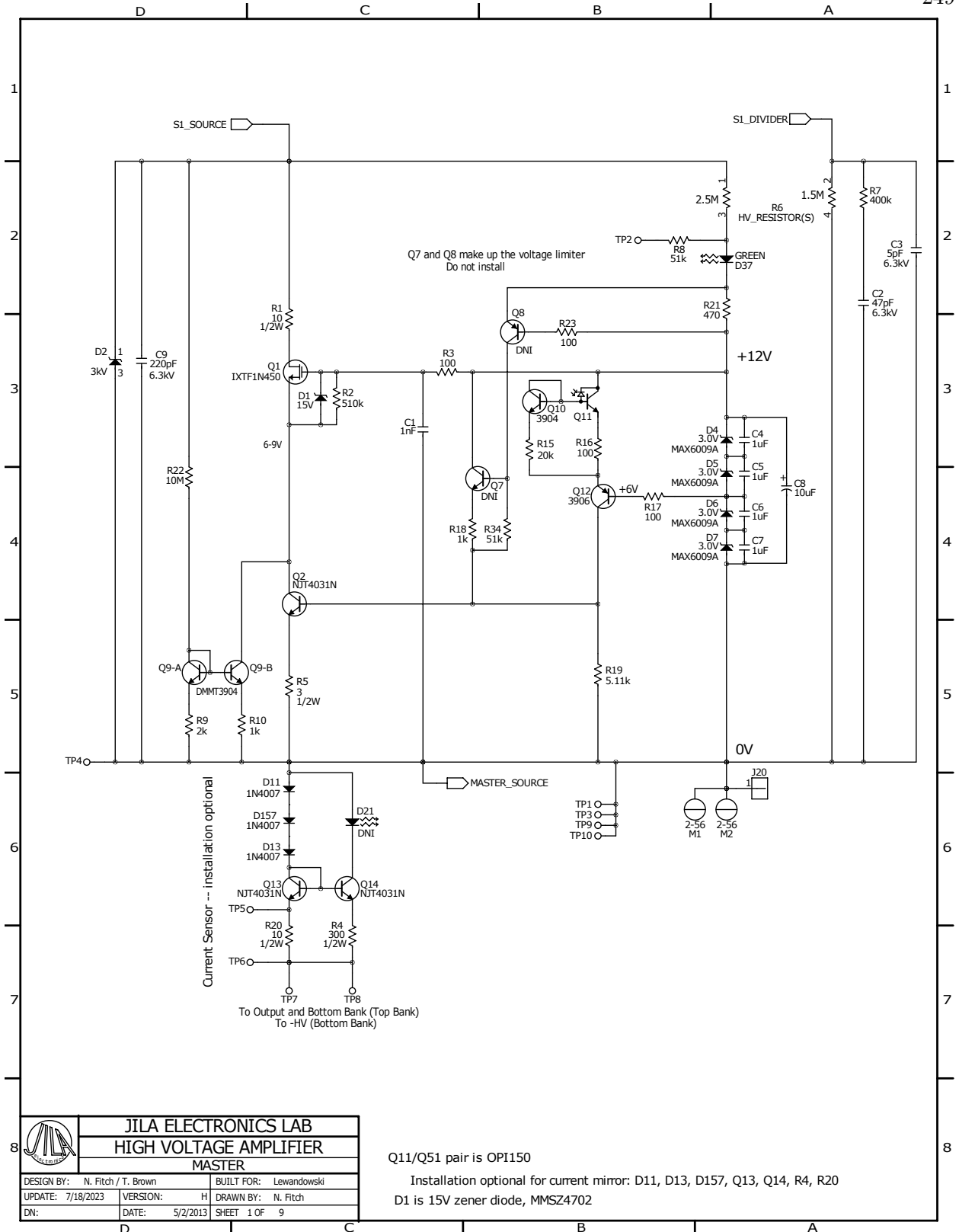
Appendix A

TWSD Amplifier Schematics

This appendix includes circuit for the amplifier banks, updated from those given in Shyur (2018). [2] This includes contributions from Jason Bossert’s work on the optoisolators, as well as our troubleshooting that determined the IXTF1N400 FETs could be replaced with IXTF1N450 FETs. A table of the changes is reproduced here from section 7.3.2:

Table A.1: Summary of changes to amplifier electronics since Yomay’s thesis. [2]

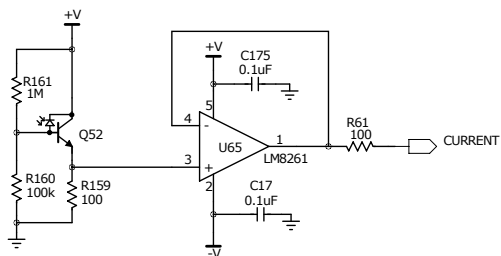
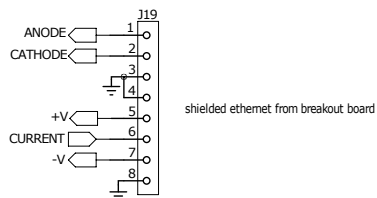
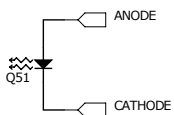
Original Component	New Component	Component number	Comment
OPI120	OPI150	Q11/Q51	new optoisolator
10 k Ω RES	20 k Ω RES	R15	new optoisolator driving circuitry
470 Ω RES	430 Ω RES	R21	new optoisolator driving circuitry
	DNI	Q52/D21	current monitor circuitry, no longer in use
	DNI/ optional	LM8261,C17,C175,R61 R159,R160,R161	current monitor circuitry, no longer in use
IXTF1N400	IXTF1N450	Q1,Q15,Q19,Q23,Q27 Q31,Q35,Q39,Q43,Q47	old component is now obsolete



	JILA ELECTRONICS LAB	
	HIGH VOLTAGE MASTER AMPLIFIER	
	MASTER	
	DESIGN BY: N. Fitch / T. Brown	BUILT FOR: Lewandowski
UPDATE: 7/18/2023	VERSION: H	DRAWN BY: N. Fitch
DN:	DATE: 5/2/2013	SHEET 1 OF 9

Q11/Q51 pair is OPI150
 Installation optional for current mirror: D11, D13, D157, Q13, Q14, R4, R20
 D1 is 15V zener diode, MMSZ4702

OPTOCOUPLER CONNECTIONS
(elevated off board)

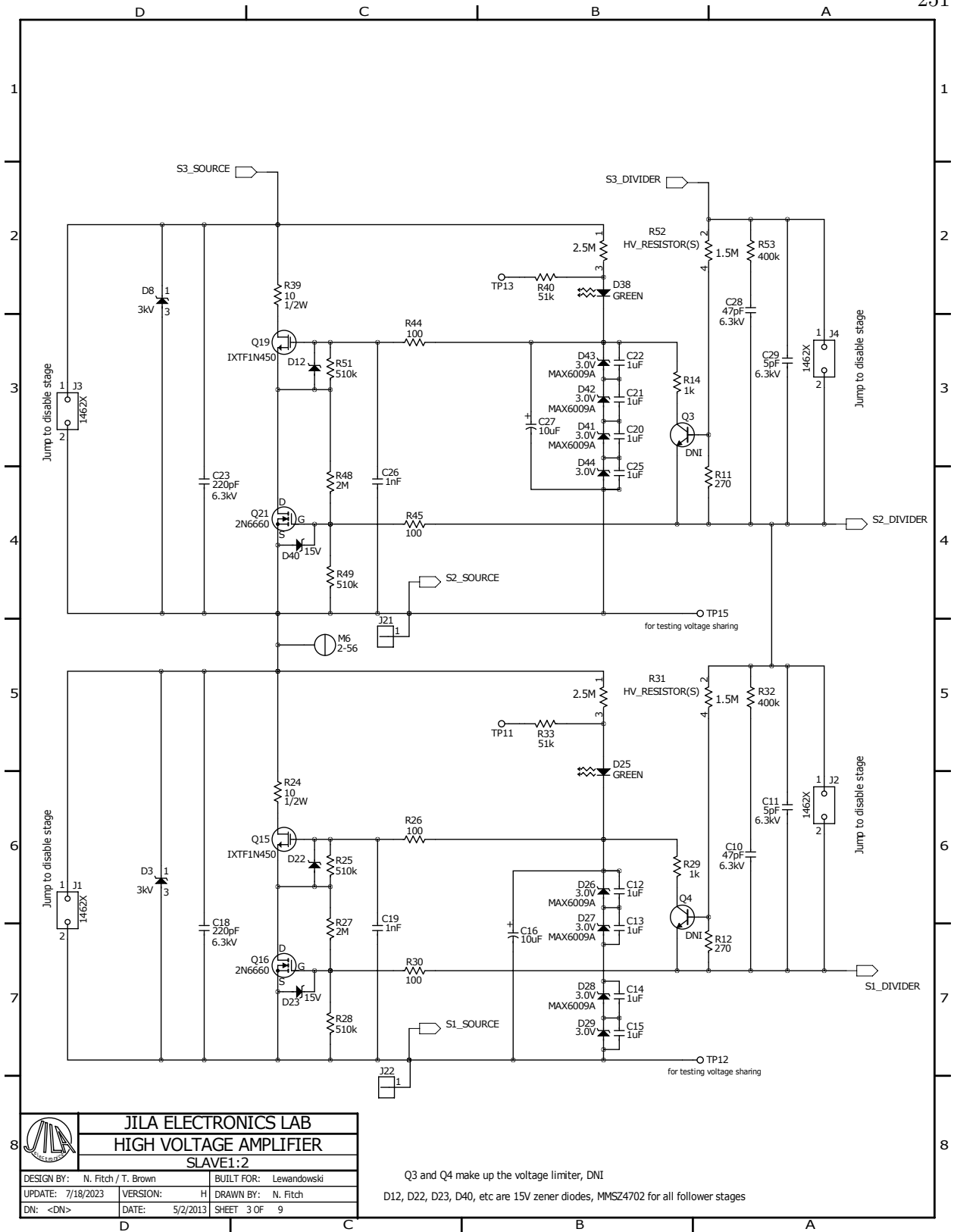


Q11/Q51 pair is OPI150
Installation optional for current mirror circuit: LM8261, C17, C175, R61, R159, R160, R161. DNI Q52



JILA ELECTRONICS LAB
HIGH VOLTAGE AMPLIFIER
OPTOCOUPLERS

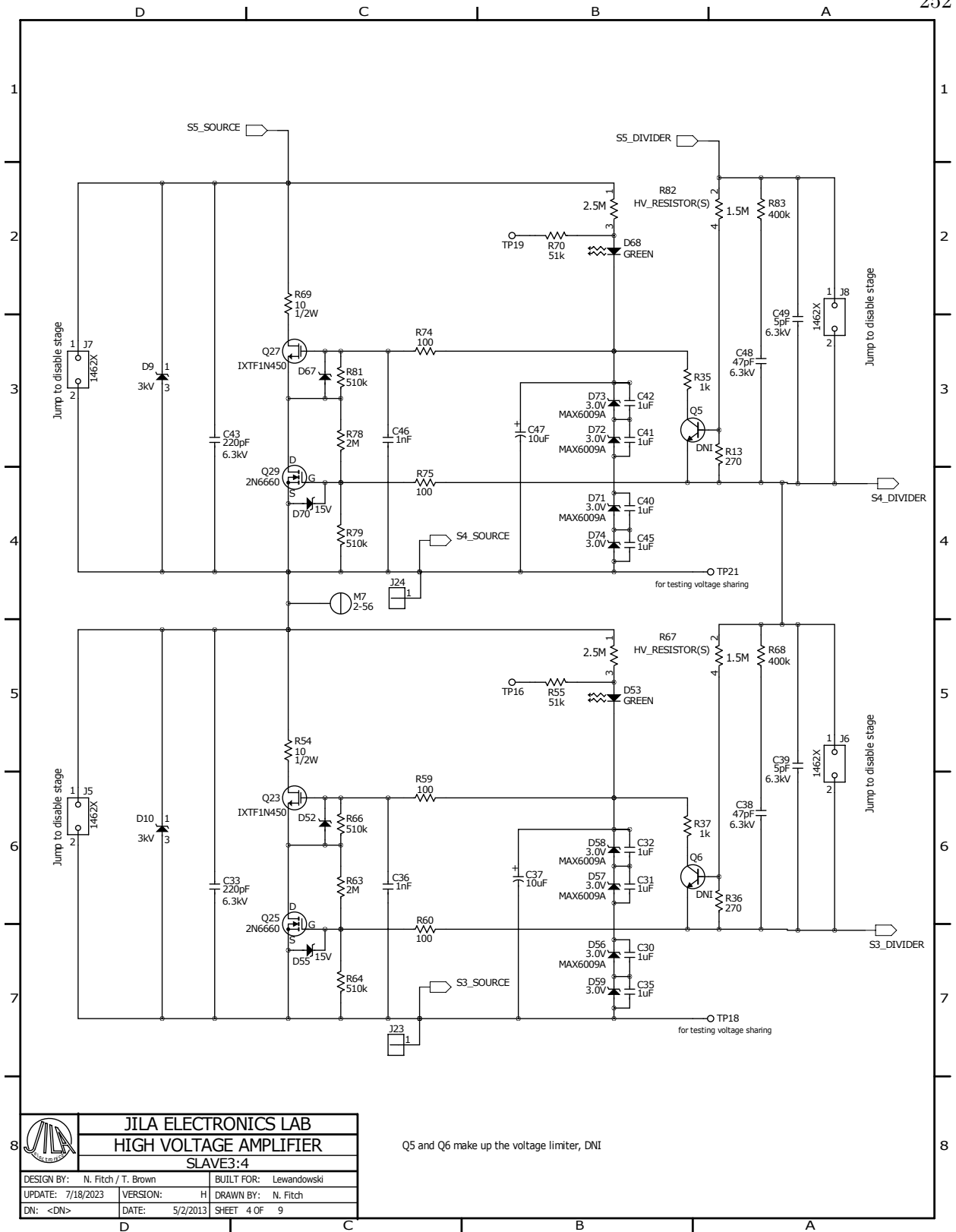
DESIGN BY: N. Fitch / T. Brown	BUILT FOR: Lewandowski
UPDATE: 7/18/2023	VERSION: H DRAWN BY: N. Fitch
DN: <DN>	DATE: 5/2/2013 SHEET 2 OF 9




JILA ELECTRONICS LAB
HIGH VOLTAGE AMPLIFIER
SLAVE1:2

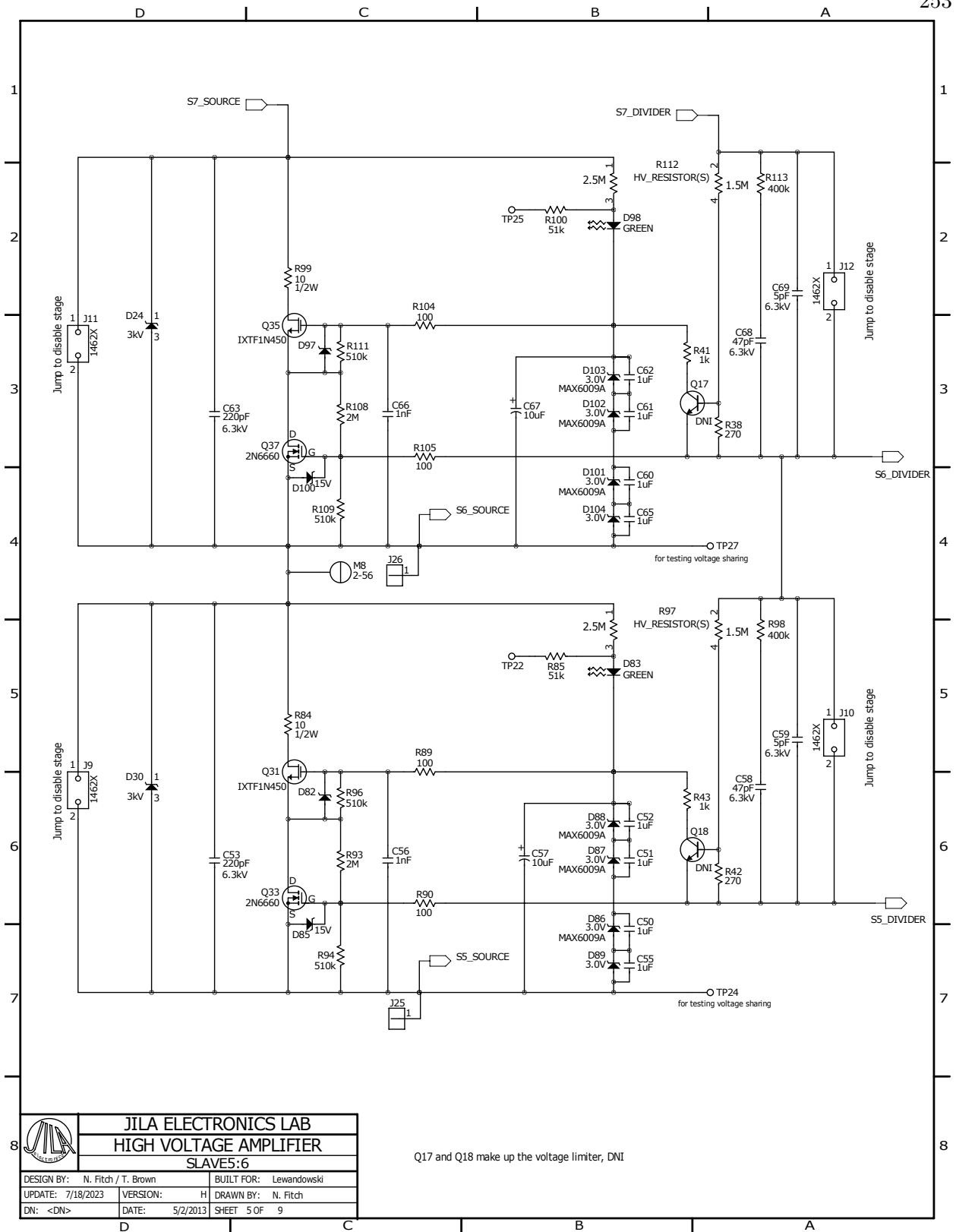
DESIGN BY: N. Fitch / T. Brown	BUILT FOR: Lewandowski
UPDATE: 7/18/2023	VERSION: H DRAWN BY: N. Fitch
DN: <DN>	DATE: 5/2/2013 SHEET 3 OF 9


Q3 and Q4 make up the voltage limiter, DNI
 D12, D22, D23, D40, etc are 15V zener diodes, MMSZ4702 for all follower stages



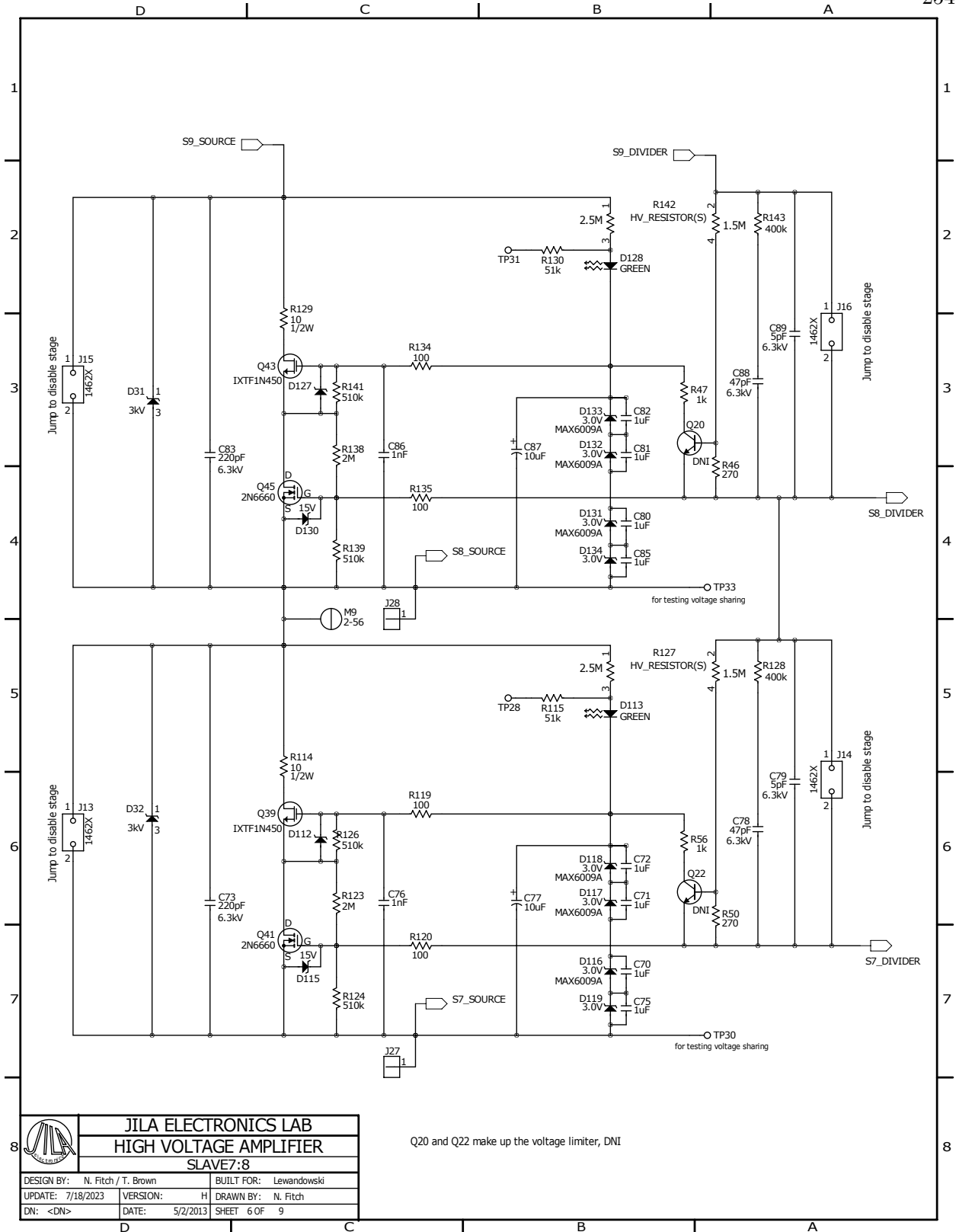
			
JILA ELECTRONICS LAB HIGH VOLTAGE AMPLIFIER SLAVE3:4			
DESIGN BY:	N. Fitch / T. Brown	BUILT FOR:	Lewandowski
UPDATE:	7/18/2023	VERSION:	H
DN:	<DN>	DATE:	5/2/2013
		SHEET:	4 OF 9


Q5 and Q6 make up the voltage limiter, DNI



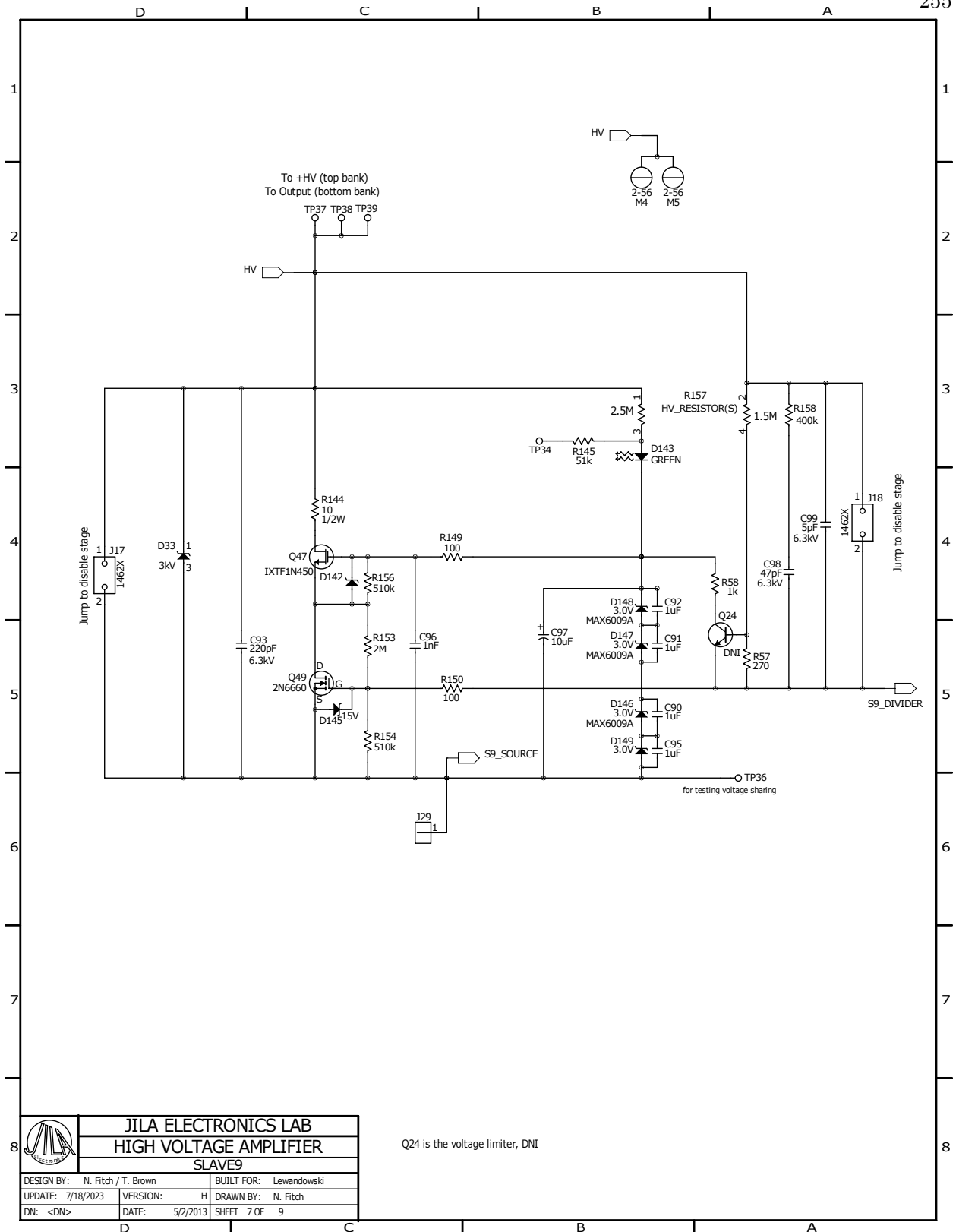
	JILA ELECTRONICS LAB HIGH VOLTAGE AMPLIFIER SLAVE5:6		
	DESIGN BY: N. Fitch / T. Brown	BUILT FOR: Lewandowski	
UPDATE: 7/18/2023	VERSION: H	DRAWN BY: N. Fitch	
DN: <DN>	DATE: 5/2/2013	SHEET 5 OF 9	


Q17 and Q18 make up the voltage limiter, DNI



	JILA ELECTRONICS LAB HIGH VOLTAGE AMPLIFIER SLAVE7:8	
	DESIGN BY: N. Fitch / T. Brown UPDATE: 7/18/2023 DN: <DN>	BUILT FOR: Lewandowski VERSION: H DATE: 5/2/2013 SHEET 6 OF 9

Q20 and Q22 make up the voltage limiter, DNI



	JILA ELECTRONICS LAB	
	HIGH VOLTAGE AMPLIFIER	
	SLAVE9	
	DESIGN BY: N. Fitch / T. Brown	BUILT FOR: Lewandowski
UPDATE: 7/18/2023	VERSION: H	DRAWN BY: N. Fitch
DN: <DN>	DATE: 5/2/2013	SHEET 7 OF 9

Q24 is the voltage limiter, DNI

Appendix B

Mathematica code for calculating collision energies of $\text{NH}_3^+ + \text{ND}_3$ reaction

This appendix include code written to perform convolutions on two three-dimensional velocity distributions, calculating a center-of-mass collisional energy distribution as it depends on the final velocity out of the decelerator. This code is written for distributions described by Gaussians by can be modified for any distribution with a finite integral.

```
In[114]:= ClearAll["Global`*"];
```

Setup

Conversions and definitions

```
In[115]:=
kbeV = 8.617333262 * 10^(-5);
kb = 1.38064852 * 10^(-23);
mND3 = 20 * 1.66054 * 10^(-27);
G[meanv_, deltav_, x_] =
  1/deltav/Sqrt[2 Pi] * E^(-0.5 * (x - meanv)^2/deltav^2);
mb[T_, m_, x_] = Sqrt[2/Pi * (m/kb/T)^3] * x^2 * Exp[-m * x^2 / (2 kb * T)];
FWHMtoSDEV[fwhm_] = fwhm / (2 * Sqrt[2. * Log[2]]);
TEMPtoSDEV[T_, m_] = Sqrt[kb * T/m];
SDEVtoTEMP[sig_, m_] = sig^2/kb * m;
```

Defining reaction-specific variables, including standard deviation of velocities for longitudinal and transverse directions of the beam, and radial and axial (Z) directions for the crystal

```
In[123]:= vlspread = 4.1; (*longitudinal s.d. of decelerated beam from dynamic syms*)
vtspread = 3; (*transverse s.d. of decelerated beam from dynamic syms *)
Ionspread = 20.2; (*radial s.d. of Coulomb crystal*)
IonspreadZ = 3.1; (*axial s.d. of Coulomb crystal*)
mu = mND3/2; (*radial s.d. of Coulomb crystal*)
decellongMEAN = {240, 200, 160, 120, 100, 80, 60, 40, 20, 10};
(*selection of final decelerated velocities*)
(*decellongSD = {FWHMtoSDEV[14.82], FWHMtoSDEV[13.36], FWHMtoSDEV[12.10],
  FWHMtoSDEV[11.08], FWHMtoSDEV[10.66], FWHMtoSDEV[10.31],FWHMtoSDEV[10.04] ,
  FWHMtoSDEV[9.84], FWHMtoSDEV[9.72], FWHMtoSDEV[9.68]};*)
(*longitudinal spreads taken from LPSA model,
converted from FWHM standard deviations;
this makes some assumptions about the filling of the phase space*)
```

Integral checks -- make sure gaussians and M-Bs are properly normalized to 1

2 | FinalCollisionalEnergies.nb

```
In[127]:= Integrate[G[meanv, deltav, v], {v, -Infinity, Infinity}]
Integrate[mB[T, m, v], {v, 0, Infinity}]
```

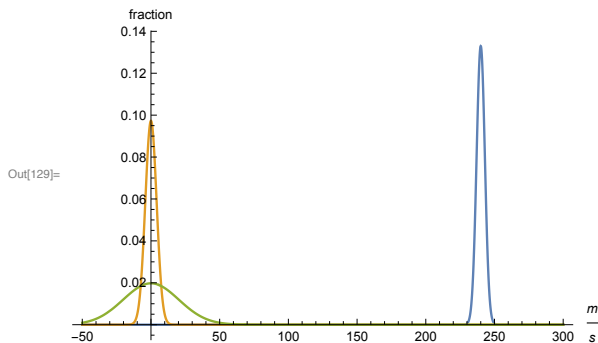
Out[127]=
$$\frac{1.}{\sqrt{\frac{1}{\text{deltav}^2}}} \text{deltav} \quad \text{if } \text{Re}[\text{deltav}^2] > 0$$

Out[128]=
$$\frac{1. \sqrt{\frac{m^3}{T^3}}}{\left(\frac{m}{T}\right)^{3/2}} \quad \text{if } \text{Re}\left[\frac{m}{T}\right] > 0$$

Plotting check, gets estimates and visualizations of curves

```
In[129]:= Plot[{G[240, vtspread, v], G[0, vlspeed, v], G[0, Ionspread, v]},
{v, -50, 300}, PlotRange -> Full, AxesLabel -> {m/s, fraction}]
```

General: Exp[-4671.99] is too small to represent as a normalized machine number; precision may be lost.



```
In[130]:= Plot[{Integrate[G[0, vtspread, vx - vxp] * G[0, Ionspread, vxp],
{vxp, -Infinity, Infinity}], G[0, vtspread, vx], G[0, Ionspread, vx]},
{vx, -300, 300}, PlotRange -> Full, AxesLabel -> {m/s, fraction}]
```

You can see the broadening of the profile as the crystal velocities are taken into effect for the relative velocity, and the summing of the mean values for the two gaussians

Summing & Output “Temperatures”

We now have the relative velocities in all three directions. So for a few difference v_{dec} , we can get the energy of the center of mass frame, $1/2 * \mu * \langle v_{rel}^2 \rangle$, with $\mu = mND/2$. We get out “temperature” E/kb

1. Integrate over $\langle v^2 \rangle$ for all three dimensions given the center velocities and spreads with a convolution of the two distributions. The decelerator beam distribution is defined as ‘x’ axis, the axial direction

of the trap is 'z' axis.

```
In[130]= f[vdec_, vlspr_] = 1/2 * mu *
  (Integrate[vx^2 * Integrate[G[vdec, vtspr, vx - vxp] * G[0, Ionspr, vxp],
    {vxp, -Infinity, Infinity}], {vx, -Infinity, Infinity}] +
  Integrate[vy^2 * Integrate[G[0, vlspr, vy - vyp] * G[0, Ionspr, vyp],
    {vyp, -Infinity, Infinity}], {vy, -Infinity, Infinity}] +
  Integrate[vz^2 * Integrate[G[0, vlspr, vz - vzp] * G[0, IonsprZ, vzp],
    {vzp, -Infinity, Infinity}], {vz, -Infinity, Infinity}]) / kb;
```

vlspr was determined by a fit of numerical calculations of 160m/s. The LPSA for our velocities has used to determine the maximum longitudinal spread as per phasespace_vs_vfinal.nb. This is used as a normalization to compare other velocities to 160m/s

```
In[131]= LPSAweight =
  {14.817182523349384 / 12.103928724123168, 13.358414143522442 / 12.103928724123168,
  12.103928724123168 / 12.103928724123168, 11.078285836246522 / 12.103928724123168,
  10.66071447634202 / 12.103928724123168, 10.312004176311255 / 12.103928724123168,
  10.036008139975674 / 12.103928724123168, 9.83613041143648 / 12.103928724123168,
  9.715052982466025 / 12.103928724123168, 9.684644725894202 / 12.103928724123168}
```

```
Out[131]= {1.22416, 1.10364, 1., 0.915264, 0.880765,
  0.851955, 0.829153, 0.812639, 0.802636, 0.800124}
```

```
In[132]= vlspr = vlspr * LPSAweight
```

```
Out[132]= {5.01907, 4.52494, 4.1, 3.75258, 3.61114, 3.49302, 3.39953, 3.33182, 3.29081, 3.28051}
```

drumroll for the major result.....

```
In[133]= TempOutions = {f[240, vlspr[[1]]], f[200, vlspr[[2]]], f[160, vlspr[[3]]],
  f[120, vlspr[[4]]], f[100, vlspr[[5]]], f[80, vlspr[[6]]],
  f[60, vlspr[[7]]], f[40, vlspr[[8]]], f[20, vlspr[[9]]], f[10, vlspr[[10]]]}
```

```
Out[133]= {35.1707, 24.5811, 15.917, 9.17851,
  6.53126, 4.36534, 2.68076, 1.47748, 0.755521, 0.575031}
```

Relative uncertainty in the Collisional temperature calculations based on the fit uncertainty for the ion distribution fit and a transverse velocity fit

```
In[134]= Sqrt[(1.3/20.2)^2 + (0.2/3.1 * LPSAweight)^2]
```

```
Out[134]= {0.101879, 0.095977, 0.0911267, 0.0873417, 0.0858526,
  0.0846338, 0.0836859, 0.0830089, 0.0826028, 0.0825013}
```

```
In[135]= Sqrt[(0.5/26)^2 + (0.03/3)^2] * TempOutions
```

```
Out[135]= {0.762339, 0.532804, 0.345008, 0.198948, 0.141568,
  0.0946205, 0.0581064, 0.032025, 0.0163762, 0.012464}
```

To compare to our temperatures without the Coulomb crystal energies being considered, i.e. the math with "0 K" ions. I left the option to have different transverse spreads for each final velocity that won't

be used at this time.

```
In[136]:= g[vdec_, decspread_] =
  1/2 * mu * (Integrate[vx^2 * G[vdec, decspread, vx], {vx, -Infinity, Infinity}] +
    Integrate[vy^2 * G[0, vlsread, vy], {vy, -Infinity, Infinity}] +
    Integrate[vz^2 * G[0, vlsread, vz], {vz, -Infinity, Infinity}]) / kb;

In[137]:= TempOutnoIons = {g[decellongMEAN[[1]], vlsread], g[decellongMEAN[[2]], vlsread],
  g[decellongMEAN[[3]], vlsread], g[decellongMEAN[[4]], vlsread],
  g[decellongMEAN[[5]], vlsread], g[decellongMEAN[[6]], vlsread],
  g[decellongMEAN[[7]], vlsread], g[decellongMEAN[[8]], vlsread],
  g[decellongMEAN[[9]], vlsread], g[decellongMEAN[[10]], vlsread]}

Out[137]:= {34.6688, 24.0848, 15.4252, 8.68994, 6.04395,
  3.87905, 2.19523, 0.992506, 0.270872, 0.0904629}

SD of the convolution for all the velocities for a energy resolution estimation

In[138]:= SDEVtoTEMP[
  Sqrt[vlsread * LPSAweight^2 + vtsread^2 + 2 * Ionsread^2 + IonsreadZ^2], mu]

Out[138]:= {1.01129, 1.00991, 1.00883, 1.00803,
  1.00773, 1.00748, 1.00729, 1.00716, 1.00708, 1.00706}
```